UNIVERSITY OF GENOVA
DEPARTMENT OF MECHANICAL ENGINEERING, ENERGY,
MANAGEMENT AND TRANSPORTS

TUNING OF DATA-DRIVEN ALGEBRAIC TURBULENCE MODELS TO IMPROVE RANS PREDICTION IN SEPARATED FLOWS

This dissertation is submitted for the degree of
Doctor of Philosophy

Andrea Carlucci

Supervisor:
Davide Lengani

May 27, 2026

Nomenclature

Latin symbols

a	Anisotropy tensor [Jkg^{-1}]
b^*	Normalized extra-anisotropy tensor [-]
c_x	Axial chord [m]
G	Output function
h, m_0	Hyperparameters
k	Turbulent kinetic energy [Jkg^{-1}]
L_{II}	II-type Marginal likelihood
P	Pressure [Pa]
p	Probability distribution
S_{ij}	Mean strain rate tensor [s^{-1}]
t	Time [s]
U	Mean velocity [ms^{-1}]
u	Velocity component [ms^{-1}]
u'	Fluctuating velocity [ms^{-1}]
w	Model coefficient
s	Frobenius norm of the mean velocity gradient tensor [s^-1]

Greek symbols

α, σ_n	Model hyperparameters

ε Turbulent dissipation $[m^2 s^{-3}]$

γ Intermittency [-]

λ Model penalty term

μ Dynamic viscosity [Pa s]

μ Gaussian mean [-]

ν Kinematic viscosity $[m^2 s^{-1}]$

$\nu_t', \nu_t'', \nu_t'''$ EARSM turbulent viscosities $[m^2 s^{-1}]$

ν_t Turbulent viscosity [m^2 s^{-1}]

Ω_{ij} Mean rotation rate tensor [s^{-1}]

Φ Dissipation function $[m^2 s^{-3}]$

Π, η Predictor groups

ρ Density [kg m^{-3}]

Σ Gaussian covariance [-]

σ_w Standard deviation

τ_{ij}^R Reynolds stress tensor $[Jkg^{-1}]$

Acronyms / Abbreviations

Re Flow Reynolds number [-]

ANN Artificial Neural Network

BFS Backward-Facing step

BMSA Bayesian Model-Scenario Averaging

CFD Computational Fluid Dynamics

DA Data Assimilation

DNN Deep Neural Networks

DNS Direct Numerical Simulation

EARSM Explicit Algebraic Reynolds Stress Models

F.A.S.P. Flux of Average Stagnation Pressure

F.T.K.E. Flux of Turbulent Kinetic Energy

FIML Field Inversion and Machine Learning

GEP Gene-Expression Programming

GPE Gaussian Process Emulator

KNN K-Nearest Neighbours

LES Large Eddy Simulation

LEVM Linear Eddy Viscosity Models

LKE Laminar Kinetic Energy

LPT Low pressure Turbine

ML Machine Learning

RANS Reynolds-Averaged Navier-Stokes Equations

SBL Sparse Bayesian Learning

SMA Sequential Model Aggregation

SpaRTA Sparse Regression of Turbulent Stress Anisotropy

TKE Turbulent Kinetic Energy

TR-PIV Time-Resolved Particle Image Velocimetry

URANS Unsteady Reynolds-Averaged Navier-Stokes Equations

X-MA Model Aggregation

XGB eXtreme Gradient Boosting

Contents

Abstract . . . XIII

1 Introduction **1**

2 Fundamentals of Turbulent Flows **8**
2.1 What is Turbulence? . . . 8
2.2 The Physics of Turbulence . . . 9
2.2.1 From Isotropic to Shear-Strained Turbulence: Correlations and Momentum Transfer . . . 15
2.2.2 Turbulence Forcing and Kinetic Energy Production . . . 16
2.3 Boundary Layer Transition . . . 17
2.3.1 Basic Concepts of the Boundary Layer . . . 17
2.3.2 Transition Mechanisms . . . 20
2.3.3 Separated flow transition . . . 21

3 Importance of Turbulence Modelling **24**
3.1 Navier-Stokes equations . . . 24
3.2 A numerical attempt to solve the NSE . . . 26
3.2.1 Reynolds Averaged Navier Stokes Equations (RANS) . . . 26
3.3 The Problem of Loss Evaluation . . . 28

4 Reynolds Stress Tensor Modelling **34**
4.1 The Eddy Viscosity . . . 34
4.2 One and Two-Equations Models . . . 36
4.3 EARSM Models . . . 37
4.4 Model Aggregation . . . 39
4.5 State of Art in Modelling Separated Flows . . . 41

5 Datasets available for model tuning **48**
5.1 Laminar Separation Bubble Experimental Dataset (EXP-FP) . . . 48
5.1.1 Test Facility . . . 48
5.1.2 Particle Image Velocimetry . . . 53

5.1.3 Test Conditions . . . 55
5.1.4 Incoming Flow and Edge Velocity Characterization . . . 55
5.1.5 Time-mean velocity . . . 57
5.1.6 Reynolds Stress Tensor Components . . . 58
5.2 LES Rounded-Nose Flat Plate Dataset (LES-T3L) . . . 64
5.3 DNS compressor dataset (DNS-CDA) . . . 67

6 Sparse Bayesian Learning **72**
6.1 An Overview on Machine Learning . . . 72
6.2 Regression Methods . . . 73
6.3 Sparse Bayesian Learning Algorithm . . . 75
6.3.1 Cross-Validation . . . 79

7 Results **80**
7.1 Tuning of an Algebraic Model for the Prediction of Long Bubbles . . . 80
7.2 Tuning of Algebraic Models for the Prediction of Short and Long Bubbles 85
7.2.1 Long and Short Bubble Models . . . 89
7.2.1.1 Long Bubble Model . . . 90
7.2.1.2 Short Bubble Model . . . 92
7.2.2 Comparison with the literature . . . 94
7.3 Aggregated Model for Long and Short Bubbles . . . 99
7.3.1 Tuning of the Two Sub-models . . . 99
7.3.2 Aggregation Procedure of Long and Short Bubble Sub-models . . 100
7.3.3 Results of Model Aggregation . . . 103
7.4 Tuning of Aggregated Turbulence Model for Separated Flows from Different Datasets . . . 108
7.4.1 Methodology . . . 109
7.4.2 Flow Features Analysis . . . 110
7.4.3 EXP-FP and LES-T3L Models . . . 112
7.4.4 Aggregation Procedure of the EXP-FP and LES-T3L Sub-models 114
7.4.5 Distribution of the Modelled Weighing Functions and Reynolds Stress Tensor Components . . . 117
7.5 Intermittency-Weighted Model . . . 122
7.5.1 Intermittency Function . . . 122
7.5.2 Reynolds Stress Tensor Model . . . 125
7.5.3 Tuning of the Intermittency Model . . . 126
7.5.4 Validation on the Flat-Plate Dataset . . . 127
7.5.5 Test on CDA . . . 130
7.6 Comparison with Existing Constitutive Models . . . 133

8 Conclusions **137**

List of Figures

2.1 Example of vortexes developing inside a turbulent flow [65] 9
2.2 Probability-density function of the fluctuating streamwise velocity component from a DNS simulation [65]. 11
2.3 Energy density (a) and turbulent dissipation as a function of the wavenumber κ [65]. 12
2.4 Qualitative variation of R_{11} as a function of the distance from the eddy centre. 15
2.5 Schematic representation of the boundary layer transition. The laminar (on the left) and turbulent (on the right) velocity profiles are also reported. 17
2.6 Blasius self-similar velocity profile for a laminar boundary layer developing on a flat plate at zero angle of incidence. 18
2.7 Classification of boundary layer regions: viscous sublayer ($y^+ < 5$), buffer layer ($5 < y^+ < 30$), fully turbulent/log-law region ($y^+ > 30$). 20

3.1 Sketch of the LES domain. 33
3.2 Cumulatives of the terms of Eq. 3.28 computed for each zone of the domain. 33

4.1 Profiles of tangential velocity component at various positions along the airfoil surface ($x/c = 0.675, 0.731, 0.786, 0.842, 0.897, 0.953$) [101]. . . 43
4.2 Computed velocity profiles in the case of periodic hill geometry at different locations (Re = 10595) [103]. 44
4.3 Comparison of different ANN architectures in terms of wall isentropic Mach number distribution on the T106c at Re_{2s} = 810^4(a) and Re_{2s} = 2.510^5(b) [105]. 44
4.4 TKE profiles for the periodic hill configuration [20]. 46

5.1 Drawing of the fan installed in the wind tunnel. 49
5.2 Settling chamber: (a) top view, (b) side view of the settling chamber and the convergent section of the wind tunnel. The location of turbulence generating grids is highlighted in the figure. 50
5.3 Sketch of the flat-plate test section with main dimensions quoted in mm. . 50

5.4 Scheme of the turbulence generating grids installed in the test section. . . 51
5.5 Example of location of the bubbles on the flat plate 52
5.6 Typical components of a dual-laser single module used in PIV setups. . . 54
5.7 Functional scheme of a Particle Image Velocimetry system. 54
5.8 Inlet turbulence decay for the cases at Tu=1.5%, Tu=2.5% and Tu=3.5% (on the left) and freestream velocity distributions for the 7°, 9° and 12° cases (on the right). 57
5.9 Normalized time-mean streamwise velocity (U/U_e) for different Reynolds numbers at fixed $Tu = 1.5\%$ and $AP = -0.41$. The white curve corresponds to the isoline U/U_e=0. 58
5.10 Normalized time-mean streamwise velocity (U/U_e) for different Reynolds numbers at fixed $Tu = 3.5\%$ and $AP = -0.41$.The white curve corresponds to the isoline U/U_e=0. 59
5.11 Normalized time-mean streamwise velocity (U/U_e) for different Reynolds numbers at fixed $Tu = 1.5\%$ and $AP = -0.18$.The white curve corresponds to the isoline U/U_e=0. 59
5.12 Normalized Reynolds stress tensor components for different Reynolds numbers at fixed $Tu = 1.5\%$ and $AP = -0.41$. The isolines correspond to $U/U_e = 0$, 0.5 and 0.9 (from the bottom to the top). 61
5.13 Normalized Reynolds stress tensor components for different Reynolds numbers at fixed $Tu = 3.5\%$ and $AP = -0.41$. The isolines correspond to $U/U_e = 0$, 0.5 and 0.9 (from the bottom to the top). 62
5.14 Normalized Reynolds stress tensor components for different Reynolds numbers at fixed $Tu = 1.5\%$ and $AP = -0.18$. The isolines correspond to $U/U_e = 0$, 0.5 and 0.9 (from the bottom to the top). 63
5.15 Sketch of the computational domain. The location of a separation bubble is highlighted through the streamwise mean velocity. 65
5.16 Normalized streamwise mean velocity for two flow conditions within the LES-T3L dataset. 66
5.17 Normalized Reynolds stress tensor components for a LES-T3L condition at $Re_D = 1725$ and Tu = 0.65%. The contour lines correspond to $U/Ue =$ 0, 0.5 and 0.9 (from the bottom to the top). 66
5.18 Normalized Reynolds stress tensor components for a LES-T3L condition at $Re_D = 3450$ and Tu = 2.3%. The contour lines correspond to $U/Ue =$ 0, 0.5 and 0.9 (from the bottom to the top). 67
5.19 Example of the mesh used to generate the present dataset [126] 68
5.20 Loading coefficient for different Reynolds number 69
5.21 Streamwise mean-velocity component for the two DNS-CDA separated conditions 69

5.22 Distributions of the Reynolds stress tensor components for the DNS CDA case at Re = 34000 and $Tu = 8\%$. 70
5.23 Distributions of the Reynolds stress tensor components for the DNS CDA case at Re = 68000 and $Tu = 8\%$. 70
5.24 Vorticity Reynolds number at the separation point and turbulent kinetic energy Reynolds number at reattachment position for separation bubbles of different datasets. 71

6.1 Sketch for the minimization problem in the Lasso regression. 75
6.2 Prior and posterior probability distribution of a retained coefficient (a) and of a skipped one (b). 78
6.3 Accuracy and generalizability in function of the model complexity 79

7.1 Mean Square Error (MSE) as a function of λ. 82
7.2 Number of predictors as a function of λ. 83
7.3 Uncertainty related to the coefficients of the survived predictors of the selected model. 85
7.4 Measured (top) and modelled (bottom) components of Reynolds stress tensor for the Validation case (made dimensionless with the external velocity). 86
7.5 Measured (top) and modelled (bottom) components of Reynolds stress tensor for the Test case (made dimensionless with the external velocity). . . 87
7.6 MSE (left) and number of the survived predictors (right) vs. λ for the long bubble models. 90
7.7 MSE (left) and number of the survived predictors (right) vs. λ for the short bubble models 90
7.8 Comparison between the measured (on the top) and the modelled (on the bottom) anisotropy tensor components for the long bubble model for the condition $Re = 34600$, $Tu = 2.5\%$ and $AP = -0.41$. The contour lines correspond to $U/U_e = 0$, 0.5 and 0.9 (from the bottom to the top). 93
7.9 Comparison between the measured (on the left) and the modelled (on the right) anisotropy tensor components for the long bubble model for the condition $Re = 22200$, $Tu = 1.5\%$ and $AP = -0.41$. The contour lines correspond to $U/U_e = 0$, 0.5 and 0.9 (from the bottom to the top). 94
7.10 Comparison between the measured (on the left) and the modelled (on the right) anisotropy tensor components for the short bubble model for the condition $Re = 61800$, $Tu = 3.5\%$ and $AP = -0.41$. The contour lines correspond to $U/U_e = 0$, 0.5 and 0.9 (from the bottom to the top). 96

7.11 Comparison between the measured (on the left) and the modelled (on the right) anisotropy tensor components for the short bubble model for the condition $Re = 52200$, $Tu = 2.5\%$ and $AP = -0.27$. The contour lines correspond to $U/U_e = 0$, 0.5 and 0.9 (from the bottom to the top). 97
7.12 MSE on the diagonal components (blue bars) and MSE on the shear stress (red bars) for validation sets of long (left) and short (right) bubbles for different constitutive models. 98
7.13 MSE of the long and short bubble models as functions of λ. 100
7.14 Comparison between the measured and the modelled shear stress component a_{12} for a long bubble case not used for training. 101
7.15 Comparison between the measured and the modelled shear stress component a_{12} for a short bubble case not used for training. 101
7.16 Measured distributions of $\tilde{w}_{SB}$ varying σ. 103
7.17 Modelled distributions of w_{SB} varying λ. 106
7.18 Measured time-mean anisotropy tensor components. 106
7.19 Time-mean anisotropy tensor components modelled with the long bubble model. 107
7.20 Time-mean anisotropy tensor components modelled with the short bubble model. 107
7.21 Time-mean anisotropy tensor components modelled with the merged model. 108
7.22 Probability density functions of the values assumed by flow features in the separated shear layer region for the different datasets. 111
7.23 Spatial distribution of Re_Ω for four different cases from EXP-FP and LES-T3L datasets 112
7.24 Model terms and coefficients (on the left) and reconstruction errors (on the right) for EXP-FP models with different levels of sparsity. 113
7.25 Model terms and coefficients (on the left) and reconstruction errors (on the right) for LES-T3L models with different levels of sparsity. 113
7.26 Comparison between estimated and modelled distributions of the weighting function for two cases among the EXP-FP and T3L datasets. 116
7.27 Modelled weight distributions $w_1(\underline{x})$ for the CDA cases at different Reynolds numbers. 116
7.28 Comparison between measured (top) and modelled (bottom) distributions of the Reynolds stress tensor components for a validation case of the EXP-FP dataset. 118
7.29 Comparison between high fidelity (top) and modelled (bottom) distributions of the Reynolds stress tensor components for a validation case of the LES-T3L dataset. 119

7.30 Comparison between high fidelity (top) and modelled (bottom) distributions of the Reynolds stress tensor components for the DNS-CDA case at $Re = 68000$. 120
7.31 Comparison between high fidelity (top) and modelled (bottom) distributions of the Reynolds stress tensor components for the DNS-CDA case at $Re = 34000$. 121
7.32 MSE computed applying the two sub-models and the aggregated model on a set of validation conditions for the three datasets. 122
7.33 Intermittency distribution for different flow conditions. 124
7.34 Time-mean Reynolds stress tensor components for a long bubble case. The black lines correspond to the isolines at $U/U_e = 0, 0.5, 0.9$ (from the bottom to the top). 124
7.35 Time-mean Reynolds stress tensor components for a short bubble case. The black lines correspond to the isolines at $U/U_e = 0, 0.5, 0.9$ (from the bottom to the top) 125
7.36 Measured distribution of the Intermittency function for three flow conditions within the validation set 128
7.37 Modelled distribution of the Intermittency function for three flow conditions within the validation set 129
7.38 Comparison between measured (top) and modelled (bottom) distributions of the Reynolds stress tensor components for the experimental case at Re = 56700, $Tu = 3.5\%$ and AP = -0.41. 130
7.39 Comparison between measured (top) and modelled (bottom) distributions of the Reynolds stress tensor components for the experimental case at Re = 30700, $Tu = 2.5\%$ and AP = -0.41. 131
7.40 Comparison between measured (top) and modelled (bottom) distributions of the Reynolds stress tensor components for the experimental case at Re = 43100, $Tu = 2.5\%$ and AP = -0.18. 132
7.41 Comparison between measured (top) and modelled (bottom) distributions of the Reynolds stress tensor components for the DNS CDA case at Re = 34000 and $Tu = 8\%$. 133
7.42 Comparison between measured (top) and modelled (bottom) distributions of the Reynolds stress tensor components for the DNS CDA case at Re = 68000 and $Tu = 8\%$. 134
7.43 MSE of the diagonal (blue) and shear (red) Reynolds stress components for the CDA DNS dataset for different constitutive models. 135
7.44 Normalized Reynolds stress profiles at a fixed streamwise location for the DNS-CDA case at $Re = 68k$. 136

List of Tables

4.1 Flow Features for SBL. 40

5.1 Details about the turbulence grids. 51
5.2 A list of all the tested conditions. The **bold** Re_L values correspond to long bubbles, the others to short bubbles. 56
5.3 Free-stream Reynolds number and turbulence intensity characterizing all the computed cases. The cases highlighted in bold represent the original ERCOFTAC conditions. 65

7.1 Flow conditions adopted to train, validate and test the model 81
7.2 Flow features for SBL 81
7.3 Coefficients and predictors of the best model. (n) indicates the progressive number associated to the predictor. 84
7.4 Validation cases used for long and short bubble models, ordered by increasing Re_L. The **bold** Re_L values correspond to long bubbles. 88
7.5 Invariants and flow features for SBL. 89
7.6 Long bubble model predictors. 92
7.7 Short bubble model predictors. 95
7.8 Common predictors for long and short bubble models. 95
7.9 Long bubble model predictors. 101
7.10 Short bubble model predictors. 102
7.11 Flow features for SBL. 104
7.12 Comparison between MSE values. 105
7.13 Weighting function model predictors 108
7.14 Flow features for SBL. 110
7.15 Pressure-induced laminar separation bubbles model predictors. 126

Abstract

The present thesis aims at the development of data-driven Explicit Algebraic Reynolds Stress Models (EARSM) to improve the prediction of the Reynolds stress tensor in separated flows, with particular attention to separation-induced transition phenomena relevant to turbomachinery applications. A comprehensive experimental database, consisting of 87 laminar separation bubbles measured through Time-Resolved Particle Image Velocimetry (TR-PIV) at the University of Genoa, was first employed for model training. Sparse Bayesian Learning (SBL) was used to identify parsimonious models able to reproduce the anisotropy properties of the Reynolds stress tensor based on both classical invariants and extended flow-feature libraries. Starting from a baseline model with 37 predictors, reduced models containing 13 and 15 predictors were obtained for long and short separation bubbles, respectively. The inclusion of flow features among the predictor library will show improved accuracy compared to invariant-based formulations. To enhance model generalizability across different flow regimes, a space-dependent Model Aggregation (X-MA) [1] strategy was introduced. This method employs SBL not only for turbulence model calibration but also for determining spatially varying weights that combine the predictions of individually trained models. Initially, the technique was applied to weight the solutions of a model specific for long bubbles and one for short bubbles. The goal was to extend the generalizability of the aggregated model to long and short bubbles as well as to bubbles exhibiting intermediate behavior between the two.
The aggregation procedure was further extended by combining the predictive capabilities of two models trained on two different datasets: on the experimental flat-plate dataset without a distinction in bubble size and on a second numerical LES dataset. The latter included 15 separation-bubble conditions evolving over a flat plate with a rounded-nose leading edge. In the first case, separation is mainly driven by the pressure gradient, whereas in the second case it is instead related to the geometry of the plate leading edge. The aggregated model exhibited improved predictive capabilities when applied to a third unseen flow configuration that did not participate to the training.
Finally, an algebraic model for intermittency was calibrated using the experimental laminar separation bubble dataset. When coupled with the trained turbulence model, this intermittency model dampens low-frequency oscillations in the upstream part of the separated shear layer, ensuring that non-zero Reynolds stress values arise only where true turbulence is present.
Overall, the outcomes of this work demonstrate the potential of ML-driven turbulence modelling to bridge the gap between high-fidelity simulations and practical RANS solvers. The developed models contribute to a more accurate and efficient prediction of separated and transitional flows, paving the way for next-generation data-informed tools in aerodynamic design and sustainable propulsion system development.

Acknowledgments

I would like to sincerely thank my supervisor, Prof. Davide Lengani, as well as Prof. Daniele Simoni, Prof. Francesca Satta and Prof. Dario Barsi for their guidance, support, and valuable scientific advice throughout my PhD journey and during the development of this work.
A special acknowledgment goes to Daniele Petronio, Matteo Dellacasagrande, Pawel Przytarski and Matteo Russo for their contribution to this research and for the many fruitful discussions and collaborative work.
I also wish to thank Virginia Bologna, Daniele Biassoni and all the other colleagues and new members of the group for their support and for contributing not only to a stimulating research environment, but also to an atmosphere of friendship and collaboration.

Funding

This thesis has been developed within the PRIN 2022 Project MILESTONE approved by the Italian Ministry of University and Research (Project ID 2022K28PHK). The author gratefully acknowledges all the participants of the project for their scientific contribution.

Chapter 1

Introduction

The rapid advancement of artificial intelligence, and in particular of Machine Learning (ML) methodologies, is leading to a groundbreaking transformation in scientific and technological research. Sophisticated and powerful computational tools are now being employed to tackle complex problems that were once considered intractable, opening new frontiers in data-driven modelling, prediction, and decision-making.

ML techniques are able to handle large volumes of data and modelling highly complex systems. Unlike traditional modelling approaches, ML algorithms can learn the behavior of a system directly from experimental or simulated data, without requiring explicit governing equations or detailed prior knowledge [2]. This data-driven paradigm is particularly advantageous in scenarios where physical models are incomplete, difficult to calibrate, or computationally expensive. For these reasons, the use of ML is spreading rapidly across scientific and engineering disciplines.

Moreover, the progressive development of high-performance computing also enables the generation of large high-fidelity datasets from numerical simulations. Together with experimental data, these simulation-based datasets are essential for training accurate and generalizable ML models. Indeed, ML offers efficient tools for the analysis and interpretation of these vast datasets. Its integration into engineering design processes can significantly enhance performance: it allows for the rapid exploration of wide design spaces, accelerates optimization procedures, and reduces both development time and computational costs compared to traditional approaches.

These new data-driven methodologies can contribute significantly to addressing one of the major challenges of the new millennium for modern engineering: the reduction of the environmental impact of the transportation sector. Among the various modes of transport, aviation plays a significant role, contributing notably to global CO_2 emissions. In 2018, air transport emissions represented 2.4% of global fossil fuel emissions [3], and this share is expected to grow in parallel with the increase in traffic and transported volumes. In response, the aeronautical industry has committed to ambitious sustainability targets, first and foremost the goal of achieving net-zero CO_2 emissions by 2050 [4]. Meeting such

goal will require coordinated efforts across multiple disciplines. These include improving aircraft aerodynamics to reduce drag and fuel consumption, enhancing propulsion system efficiency through advanced design, and developing innovative technologies. A holistic approach—combining advancements in materials, system integration, and flight operations—will be essential to meet the environmental expectations of the future.
Focusing now on the aspect related to the improvement of the propulsion system efficiency, it is clear that the primary objective is to reduce the energy losses that the flow inevitably undergoes while passing through the engine. However, before this goal can be achieved, it is necessary to have tools that enable an accurate estimation of such losses, together with an accurate analysis of the flow behavior. The most intuitive approach, carrying out experiments, has historically been widely employed and has provided valuable insights into the behavior of propulsion systems. However, conducting experiments involves cost-related issues and can demand considerable engineering effort.
Beginning in the 1960s and 1970s, alongside experimental work, Computational Fluid Dynamics (CFD) started to emerge, driven by the development of computer technology and numerical methods for solving the Navier–Stokes equations. Initially confined to research centers due to computational limitations, CFD progressively expanded during the 1980s and became widely adopted in the 1990s, eventually establishing itself as a standard tool in the aerospace industry, reducing the reliance on costly experimental campaigns. With the exponential growth of computational power over the past decades, high-fidelity approaches such as Direct Numerical Simulations (DNS) and Large Eddy Simulations (LES) have become increasingly accessible for studying complex flow phenomena. These methods are well recognized for their ability to capture the intricate dynamics of transitional and turbulent flows, yet their application in industrial practice remains limited. DNS, in particular, offers the most accurate description of turbulence by resolving all spatial and temporal scales without modelling assumptions, but the associated computational burden restricts its use to academic research and relatively simple geometries at low Reynolds numbers. As a result, routine industrial design still relies primarily on low-fidelity approaches such as Reynolds-Averaged Navier–Stokes (RANS) and Unsteady RANS (URANS) simulations, which are more affordable and better suited for systematic engineering workflows. The main limitation of RANS lies in the fact that solving the governing equations of the method requires modelling a specific term, the Reynolds stress tensor. Accurately modelling this term is by no means straightforward, particularly under complex flow conditions. However, the advantages in terms of computational efficiency ensure that research aimed at developing new models to improve RANS remains very active. At the industrial level, the turbulence models most commonly implemented in CFD solvers are Linear-Eddy-Viscosity Models (LEVM) relying on the Boussinesq's hypothesis, which establish a linear relationship between the Reynolds stress and strain-rate tensors via a turbulent viscosity. This hypothesis is directly implemented in widely used numerical schemes such as the Spalart-Allmaras (*S&A*, [5]), the $k-\varepsilon$ (Launder and

Spalding [6]), and the $k-\omega$ (Menter [7]) models. However, as shown by Wilcox [8] and Schmitt [9], the assumption that the Reynolds stress and the strain-rate tensors are perfectly aligned does not hold even in relatively simple flows. To improve predictions in complex flow conditions, various approaches have introduced nonlinear terms. The Explicit Algebraic Reynolds Stress Model (EARSM, Pope [10]) overcomes Boussinesq hypothesis by introducing a tensorial expansion of the strain and rotation tensors, allowing the principal axes of the modelled Reynolds stress tensor to deviate from those of the strain-rate tensor. Like turbulent viscosity in LEVM models, EARSM requires determination of multiplicative coefficients for each term, interpreted as higher-order turbulent viscosities. Numerous implementations have been developed: Rodi [11] for fully turbulent flows at high Reynolds numbers; Shih *et al.* [12] tuned a model that relies on a quadratic expansion of the strain and rotation tensors; the LienCubicKE model (Lien [13]) is based on a cubic formulation. Other EARSM are provided by Gibson and Launder [14], Gatski and Speziale [15], Craft *et al.* [16], Wallin and Johansson [17], Menter *et al.* [18] and Pacciani *et al.* [19].
This is exactly the point at which modern machine learning techniques become relevant in this field. The remarkable amount of data available today, derived from both high-fidelity simulations and detailed time-resolved experiments, offers significant opportunities to advance turbulence and transition modelling, enhancing the accuracy of RANS/URANS while maintaining low computational costs. By applying machine learning techniques, it becomes possible to calibrate model constants and blending functions to better reproduce high-quality reference data. This approach particularly opens new perspective for the development of specialized models for different flow scenarios, such as jets, shear layers, and separated flows, which can be locally activated through Model Aggregation (MA) within an improved low-cost CFD solver. It should be emphasized that, through this process, high-fidelity simulations and experiments do not need to be employed systematically. Instead, they can be carried out in a limited scope to generate databases aimed at improving lower-fidelity simulations, which, in contrast, are well suited for everyday use.

In line with this perspective, numerous studies have been proposed in recent literature. For example, Schmelzer *et al.* [20] and Cherroud *et al.* [21] applied Sparse Symbolic Regression and Sparse Bayesian Learning (SBL) to learn apparent viscosities in Pope's expansion from high-fidelity data for three separated flow configurations. Their research investigated three specific types of separated flow configurations: periodic hills, a converging- diverging channel, and a curved backward-facing step. Gene-Expression Programming (GEP) has been employed by Akolekar *et al.* [22], [23] and Fang *et al.* [24] to improve LKE models. While GEP offers greater flexibility but at a high computational cost, SBL provides direct sparsity control, yielding parsimonious models. If the combinations of candidate functions of SBL are well defined, both algorithms should provide two solutions characterized by a similar structure. Marioni *et al.* [25] assessed a neural network framework trained on DNS data to activate improved models in specific flow regions. Physics-Informed Neural Networks have also been widely applied to turbulence modelling, for instance in Wang *et al.* [26], for both model development (Yazdani and Tahani [27]) and solver enhancement (Pioch *et al.* [28] and Patel *et al.* [29]). Further efforts to improve EARSM models can be found in Sandberg *et al.* [30], Davidson [31], and Pacciani *et al.* [32].

The models discussed above, regardless of their formulation or training methodology, are generally nonlocal. This can influence predictions even in regions where the baseline LEVM already performs accurately. Furthermore, these models tend to be effective only within specific flow types and conditions, often requiring retraining for new scenarios. A promising strategy to enhance predictions across a wider range of flows is to combine models trained under different settings, using space-dependent weights to prioritize the best-performing models at each spatial location. Following this approach, Yuksel *et al.* [33] provide a comprehensive survey of Mixture Models. This methodology enables partitioning the input feature space and assigning greater weights to the models that achieve the best performance within each partition. Furthermore, the Sequential Model Aggregation (SMA) method has been proposed with the aim of enhancing accuracy by merging predictions from multiple models, often referred to as experts or forecasters (see [34]–[36], for instance). A stochastic variant of SMA, the Bayesian Model-Scenario Averaging (BMSA), has been investigated in recent years by Edeling *et al.* [37] to calibrate and combine predictions from a set of competing baseline LEVM models, each trained on different datasets. Another example is provided in De Zordo-Banliat *et al.* [38], where a novel strategy termed space-dependent Model Aggregation (X-MA) is introduced, in which predictions from established LEVM models in the literature are blended using weights regressed through Random Forests. Expanding on this framework, Cherroud *et al.* [1] presents an extension where baseline LEVM are replaced with data-driven EARSM models trained via SBL.
An other fundamental aspect, particularly relevant when modelling transitional flows, as often encountered in turbomachinery, is instead related to the need for an appropriate activation strategy for the turbulence model. Transition models, usually linked to the concept of intermittency, are introduced to this end. The γ-Re_θ model [39], for example, is based on two additional transport equations, one for the intermittency function (γ) and the other for the momentum-thickness Reynolds number (Re_θ). Intermittency acts as a blending function (equal to 0 in laminar boundary layers and 1 in fully-turbulent flows), generally applied to the production term appearing in the turbulent kinetic energy (TKE) equation. The momentum-thickness Reynolds number, on the other hand, provides the threshold that characterizes the passage between the laminar and the turbulent states. Recent works (e.g., [40]) replaced the Re_θ with a Reynolds number based on the vorticity (Re_Ω), which is defined with local boundary layer parameters that allows for a parallelized computations. More recently, algebraic models have been proposed directly for the intermittency function (see [40]–[42] for example), to avoid the resolution of additional differential

equations. These models have been shown to provide accurate predictions of the transition process in specific flow cases. The growing use of machine-learning-based tools may help to enlarge algebraic model applicability in an increasingly broad range of flow configurations. In this sense, additional examples of high-fidelity data used to extract new correlations can be found in [43]–[46].

However, the effectiveness of applying machine learning techniques is closely linked to the availability of high-quality data. Datasets specifically assembled for modelling purposes are available, for instance, in the ERCOFTAC [47] database, while other attempts of sharing large-scale dataset have been carried out by Bonnet *et al.* [48] and Towne *et al.* [49]. Many of the previously cited works rely on high-fidelity simulations, yet detailed time-resolved experimental datasets can also serve to the same purpose. Compared with DNS and LES, experiments offer the important advantage of acquiring a variety of flow cases more rapidly, thereby facilitating the exploration of wide design spaces under varying influential parameters. However, experimental measurements are inevitably affected by noise, and their spatial resolution may be limited. Examples of publicly released experimental data include the works of Bridges and Wernet [50] and Bridges and Wernet [51] on near-sonic asymmetric jets, Naughton *et al.* [52] on wall-mounted hump separated flow, and Towne *et al.* [49] on turbulent boundary layers and airfoils encountering gusts, while datasets on laminar separation bubbles are provided in Laurent *et al.* [53] and Carlucci *et al.* [54].

Among the various flow scenarios, separation-induced transition represents a particularly relevant research topic, as it is one of the main mechanisms responsible for loss generation, especially in internal aerodynamics such as turbomachinery (Mayle [55]). Under strong adverse pressure gradients and at low Reynolds numbers, flow separation can occur. The resulting separation bubbles are prone to bursting (see, e.g., Marxen and Henningson [56]), where a short bubble abruptly develops into a long one as flow parameters change. This phenomenon has been extensively studied in the classical works of Von Doenhoff [57], Owen and Klanfer [58], Crabtree [59], Gaster [60], and more recently in Dellacasagrande et al. [61].

Accurately predicting separation-induced transition remains a challenge for current CFD solvers based on LEVM. In particular, when boundary layer separation is involved, these models often suffer from excessive turbulence diffusion in the attached boundary layer and struggle to capture the development of the shear layer in the upper part of the bubble [62], [63]. As a result, LEVM predictions of aerodynamic performance downstream of separation bubbles are frequently compromised.

In this work, applications of machine learning tools for training EARSM models to represent the Reynolds stress tensor in separated flows are presented. In particular, a large experimental dataset acquired at the laboratories of the University of Genoa (see Dellacasagrande *et al.* [64]) was first employed. This dataset, acquired through TR-PIV measurements, comprises 87 different laminar separation bubbles developing over a flat plate with adjustable endwalls. The flow cases were obtained under varying flow parameters such as Reynolds number, freestream turbulence level, and adverse pressure gradient. The range of flow conditions is chosen to simulate the operating conditions of a low-pressure turbine (LPT) blade. This dataset includes both long and short separation bubbles, and also allows the observation of the bursting phenomenon. The machine learning algorithm adopted is SBL, which is able to identify the dominant predictors within predefined library. Unlike Pope's baseline theory, which assumes turbulent viscosities to be functions of the invariants of the strain and rotation tensors only, here the possibility of introducing combinations of flow features into the predictor library has been investigated. The selection of the features has been conducted following a literature review and physical considerations. As a first step, a model composed of 37 predictors was calibrated for long separation bubbles. Subsequently, with the aim of extending the work and pursuing increasingly parsimonious models, two new models were calibrated for the prediction of long and short separation bubbles, consisting of 13 and 15 predictors, respectively. For an equal number of predictors, the actual improvement brought by the introduction of flow features compared to the use of invariants alone was also demonstrated. Finally, the predictive capabilities of the obtained models were compared with those of models already widely used in the literature, showing improvements. At a later stage, the possibility of extending the generalizability of the models was investigated by aggregating models calibrated on individual flow conditions through spatially dependent weights. To this end, the SBL algorithm has been employed also for the modelling of the weights. Following this approach, an aggregated model was first calibrated by weighting the individual solutions of models specifically trained for long and short bubbles. Given the effectiveness of the procedure but the excessive similarity between long and short bubbles, the technique was then extended to merge two models trained on completely different datasets. Specifically, a model for the prediction of experimental separation bubbles was combined with a model trained on an LES dataset including 15 separation bubbles developing over a rounded-nose flat plate. Unlike the experimental dataset, where bubble formation is mainly caused by the adverse pressure gradient, in the numerical dataset separation is induced by the geometry of the plate leading edge. The aggregated model thus obtained was further tested on a third DNS dataset including two separation bubbles forming on the suction side of a compressor blade, showing improved prediction capabilities. Finally, after computing the 2D intermittency distribution for all the laminar separation bubbles within the experimental dataset, an algebraic model for the intermittency function was also calibrated using SBL. When coupled with the EARSM model, this intermittency models selectively activates the turbulence production after the bubble maximum height, i.e., where non-zero regions of the filtered tensor components effectively correspond to turbulent flow fluctuations. Indeed, this procedure allows damping low-frequency fluctuations in the upstream portion of the separated shear layer, which are mainly due to the formation of streaky structures and low-frequency oscillation of the bubble.

The overall results demonstrate the strong potential of the present models for effective integration into RANS frameworks, enabling a more faithful and physically consistent description of separated-flow dynamics. This advancement paves the way for more reliable design and analysis of turbomachinery blades, where accurate representation of laminar–turbulent transition and flow separation plays a decisive role in performance assessment and operational robustness.

Chapter 2

Fundamentals of Turbulent Flows

2.1 What is Turbulence?

Turbulence can be regarded as the unstable response of a fluid to external forcing, such as the shear stress generated by the presence of a solid wall, or to small velocity perturbations and pressure forcing. The action of this stress, in combination with vorticity, tends to make the fluid prone to instabilities whenever the damping effect of viscosity is too weak. As a result, vorticity becomes fragmented and redistributed into chaotic three-dimensional vortices of various scales, which evolve and interact with one another.

To fully characterize a turbulent flow, one would ideally need an analytical solution of the Navier–Stokes equations, which describe the motion of viscous fluids, or, from an experimental or numerical standpoint, access to an infinite sequence of snapshots of the three-dimensional velocity field. This clearly represents a major obstacle to any attempt at providing a general description of turbulent flows.

Despite significant progress in both mathematical analysis and high-fidelity simulations enabled by high-performance computing, a complete description of turbulence remains elusive. It is no coincidence that the German physicist Werner Heisenberg, who, before devoting himself to quantum mechanics, also worked on turbulence, is said to have remarked:

> *"If I could ask God two questions, one would be 'Why relativity?' and the other would be 'Why turbulence?' ' I really believe he will have an answer for the first.'*

From an engineering perspective, an accurate characterization of turbulence is essential. Many of the phenomena under investigation are, in fact, governed by turbulent dynamics. Consider, for example, its influence on boundary layer separation under an adverse pressure gradient, on turbomachinery losses, on jet and wake development, and on the convective heat transfer coefficient, to name just a few.

Fortunately, engineers are not necessarily concerned with the detailed mechanisms of turbulence, but rather with its practical implications. In most cases, the focus lies on its macroscopic and integral behavior, which emerges from a statistical analysis of the turbulent field. This approach enables the interpretation of complex phenomena whose intrinsic mechanisms are not yet fully understood. Nevertheless, a solid understanding of turbulence physics and its interaction with the surrounding environment remains crucial, at the very least, to gain deeper insight into the engineering tools used for turbulence analysis [65].

2.2 The Physics of Turbulence

When approaching the study of turbulence, it is almost instinctive to associate it with an image of chaos and randomness. Yet, like any phenomenon in fluid dynamics, turbulence is ultimately governed by precise mathematical laws: the Navier–Stokes equations. In principle, once the initial state of a flow is known, it is always possible, at least theoretically, to determine its exact evolution in both space and time. The perception of chaos arises instead from the extraordinary number of degrees of freedom that characterize such a system, together with its marked sensitivity to initial conditions: even the smallest variation can lead to outcomes that differ substantially, while still remaining strictly deterministic.

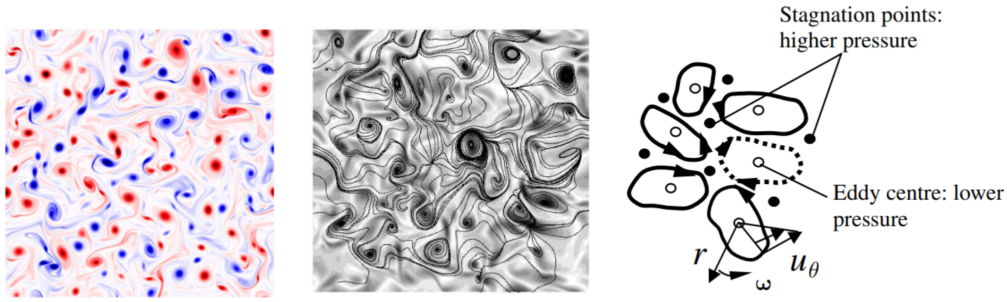

Figure 2.1: Example of vortexes developing inside a turbulent flow [65]

A key element that illustrates this ordered-complexity is provided by the vorticity field. Far from being entirely disordered, turbulence often organizes itself through the formation of eddies spanning a wide range of scales. These coherent structures are among the most distinctive features of turbulent flows, and they provide a tangible manifestation of the dynamics described by the Navier–Stokes equations. To satisfy the continuity constraint, neighboring eddies are counter-rotating, at least in the simplified case of two-dimensional turbulence (see Fig. 2.1). The constant interplay between apparent disorder

and underlying structure lies at the very heart of what makes turbulence such a fascinating yet challenging phenomenon to study.
For a two-dimensional flow field characterized by the velocity components $u(x,y)$ and $v(x,y)$ in the x- and y-directions, respectively, the vorticity is defined as:

$$\Omega_{xy} = \frac{1}{2}\left(\frac{\partial u}{\partial y} - \frac{\partial v}{\partial x}\right) \tag{2.1}$$

To better relate this definition to the rotational velocity of a fluid element, one may imagine that, to a first approximation, the motion in the vicinity of the center of an eddy resembles that of a solid body. In this case, the tangential velocity u_θ can be expressed as:

$$u_\theta = \omega r. \tag{2.2}$$

Decomposing u_θ and r into their $x-y$ components, i.e., $u = -\omega \sin\theta$, $v = \omega\cos\theta$, $x = r\cos\theta$ and $y = r\sin\theta$, and substituting this decomposition into Eq. (2.1), we otain

$$\Omega_{xy} = -\omega. \tag{2.3}$$

From this expression, it becomes evident how vorticity quantifies the rotation rate of eddies, and thus the rotational property of the fluid element.
In real flows, the velocity field induced by each eddy tends to affect the motion of neighboring eddies. This mutual interaction not only alters the velocity field of the eddies but also causes them to deform and stretch each other. Such dynamic interactions are fundamental in determining the evolution of vortex structures. Another typical feature of turbulence eddies is that to occur at very different sizes, with a range that, as will be detailed later, can be extremely wide. For this reason, turbulence is regarded as a multiscale phenomenon.
The considerations introduced above make it clear that the velocity in a turbulent flow is strongly time-dependent. Let us now consider the fluctuating velocity component along the Cartesian coordinate x, defined by subtracting from the instantaneous velocity $u(t)$ its time average, i.e., $u'(t) = u(t) - \overline{u(t)}$. The probability density function (Pdf), defined by evaluating the proportion, either in terms of time or number of realizations, in which a measured event falls within a given velocity interval, yields the curve shown in Fig. 2.2. The area obtained by summing the elements of the histogram, which for a sufficiently small velocity increment can be expressed as the integral $\int_{-\infty}^{+\infty} Pdf(u')du'$, must be equal to 1, since it represents the probability that the velocity fluctuation lies between $-\infty$ and $+\infty$. Similarly, the turbulent kinetic energy associated with the x-wise velocity component is expressed as:

$$\overline{u'^2} = \int_{-\infty}^{\infty} u'^2 Pdf(u')du' \tag{2.4}$$

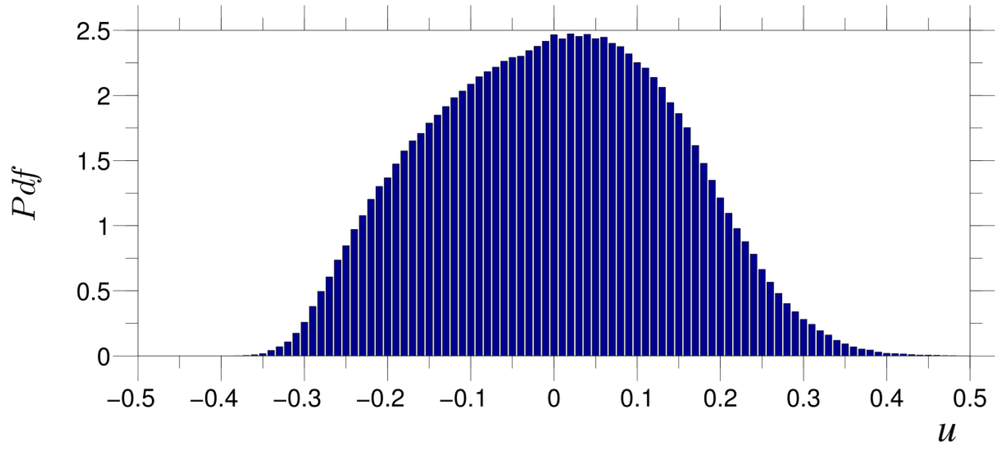

Figure 2.2: Probability-density function of the fluctuating streamwise velocity component from a DNS simulation [65].

By summing the same quantity evaluated for the other two fluctuating velocity components, the turbulent kinetic energy k can be obtained:

$$k = 0.5(\overline{u'^2} + \overline{v'^2} + \overline{w'^2}). \tag{2.5}$$

Turbulent kinetic energy is a particularly important quantity in the characterization of turbulence. From it, the turbulent velocity scale $\sqrt{k}$ can also be derived, which is useful to provide an average characterization of the fluctuating velocity field.
As mentioned earlier, the size of vortices is highly variable. To characterize this aspect, it is useful to define the wavenumber $\kappa = 2\pi/\ell$, where ℓ is the characteristic size of a given vortex. Another important quantity characterizing turbulence is the energy density E, defined as the energy contained within each eddy-size increment, divided by the increment itself. By this definition, the integral of E with respect to κ yields the total turbulent kinetic energy:

$$k = \int_{\kappa_\Lambda}^{\kappa_\eta} E(\kappa) d\kappa \tag{2.6}$$

The two terms κ_Λ and κ_η represent the wavelengths associated with the largest and smallest eddies, whose sizes are denoted by Λ and η, respectively. It is reasonable to assume that the size of the largest eddies is roughly comparable to, or in any case smaller than, the perimeter confining the flow. The size of the smallest eddies, on the other hand, cannot be intuitively estimated and instead requires a more detailed discussion.
As can be observed from Fig. 2.3 (a), the trend of E as a function of κ tends to exhibit a universal behavior, provided that the Reynolds number is sufficiently high. Within the range of scales depicted in the Figure, three distinct subranges can be identified. On the left lies subrange A, which corresponds to the largest eddies (characterized by a length

scale Λ) and contains the majority of the energy. In the center is subrange B, the so-called *inertial subrange*. This region is particularly relevant from a modelling perspective, since in this wavelength interval vortexes, due to mutual interactions, stretch along their axis and subsequently break down into smaller eddies. Understanding and correctly modelling this process is indeed fundamental to an accurate representation of turbulence itself. Within subrange C, on the other hand, whose representative scale corresponds to the smallest eddies (η), viscosity becomes predominant, so that the energy of the eddies is dissipated into heat.

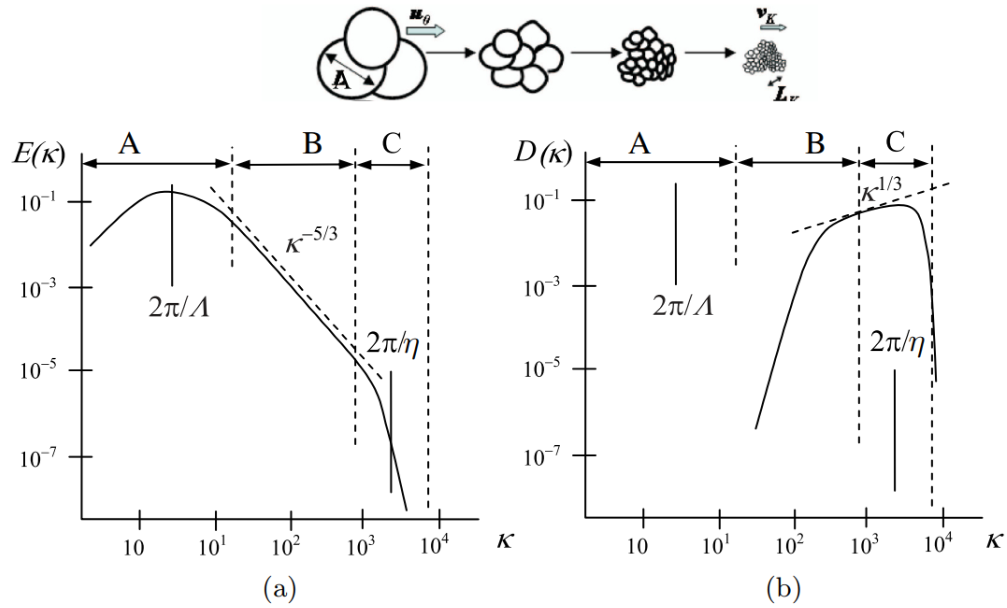

Figure 2.3: Energy density (a) and turbulent dissipation as a function of the wavenumber κ [65].

Coming back to to subrange B, it can be observed that the distribution of E as a function of k is governed by the rate at which energy is transferred across scales. Since the eddies are still too large to be directly damped by viscosity, no explicit dependence on viscosity is expected within this range. Instead, the distribution depends on the rate at which energy is transferred from subrange A to subrange C, where it is eventually dissipated. Consequently, it is a function of ε, the kinematic rate of turbulence-energy dissipation. This consideration justifies the possibility to define $E(\kappa) = f(\kappa, \varepsilon)$, from which, by means of dimensional consistency arguments, one arrives at the expression:

$$E(\kappa) = c_k \varepsilon^{\frac{2}{3}} \kappa^{-\frac{5}{3}} \tag{2.7}$$

This relation was first introduced by the Soviet mathematician Andrei Kolmogorov [66], who in particular showed that $c_k = 1.5$ in the specific case of spatially homogeneous and

isotropic turbulence.
In other words, the large-scale eddies characteristic of subrange A, which are the first to form when the flow encounters an obstacle along its path (such as a grid), tend to break down into smaller eddies through a "cascade" process. The rate at which energy is transferred from subrange A to subrange C is constant and equal to the rate at which energy is dissipated by viscous friction within subrange C. To describe the dependence of the dissipation rate on the wavenumber within subrange C, another function $D(k)$ is defined, whose distribution is shown in Fig. 2.3 (b). The dissipation must depend on viscosity, so the functional dependence of $D(\kappa)$ is of the form: $D(\kappa) = g(\nu, \kappa, \varepsilon)$. Following again a dimensional analysis we obtain:

$$D(\kappa) = c_\varepsilon \nu \varepsilon^{\frac{2}{3}} \kappa^{\frac{1}{3}}. \tag{2.8}$$

In this case, Kolmogorov derived $c_\varepsilon = 2 \cdot c_k$. The behavior described by Eq. (2.7) has an almost universal significance and can also be observed, at least qualitatively, in non-homogeneous flows characterized by non-homogeneous turbulence.
This preliminary description of the main characteristics of turbulence leads to a fundamental issue. While, as mentioned, it is possible to estimate the size of the largest eddies by relating them to some characteristic length of the flow, the same cannot be done for the smallest eddies. Moreover, one may also wonder what determines the ratio $\frac{\Lambda}{\eta}$. The estimation of the scale η can be derived from the following considerations:

- The order of the energy-transfer rate towards subrange C, according to dimensional analysis, must be $u^2(u/\ell)$, which represents the kinematic energy per unit time. Here, u is the turbulent-velocity scale at the length scale ℓ.
- The energy transfer rate is equal to the kinematic rate of turbulence-energy dissipation, i.e., $u^2(u/\ell) = \varepsilon$.
- At the smallest scale ($\ell \to \eta$) viscous effects are of the same order of inertial effects, so $Re_\eta = \frac{u_\eta \eta}{\nu} \approx 1$.

Thus, imposing $\ell = \eta$ and $u = u_\eta$, from the second consideration we obtain $\eta = \frac{u_\eta^3}{\varepsilon}$. Hence, expressing u_η from Re_η and substituting it into the previous equation leads to:

$$\eta = \left(\frac{\nu^3}{\varepsilon}\right)^{\frac{1}{4}}. \tag{2.9}$$

From the assumption on Re_η, it immediately follows that the velocity scale of the length scale η is:

$$u_\eta = (\nu\varepsilon)^{\frac{1}{4}}, \tag{2.10}$$

while the corresponding time scale is:

$$\tau_\eta = \frac{\eta}{u_\eta} = \left(\frac{\nu}{\varepsilon}\right)^{\frac{1}{2}}. \tag{2.11}$$

Focusing now on the derivation of the ratio Λ/η, one can similarly define a Reynolds number associated with the scale of the largest eddies, Λ:

$$Re_\Lambda = \frac{u_\Lambda \Lambda}{\nu}. \tag{2.12}$$

Considering, for example, the case of a fluid flowing over a flat plate, it is reasonable to assume that the scale of the largest eddies is approximately equal to that of the boundary layer developing on the plate ($\Lambda \approx \delta$). The corresponding velocity scale, u_Λ, will therefore be roughly 10% of the freestream velocity, and consequently the associated Reynolds number will also be about 10% of the Reynolds number based on the mean velocity. To estimate $\frac{\Lambda}{\eta}$ one can rely on the Kolmogorov cascade concept, which implies that $u_\Lambda^2(u_\Lambda/\Lambda) \approx \varepsilon$. Substituting it into Eq. 2.9 then leads to:

$$\frac{\Lambda}{\eta} = Re_\Lambda^{\frac{3}{4}} \tag{2.13}$$

Moreover, form Eqs. (2.10) and (2.11) it is easy to derive:

$$\frac{u_\Lambda}{u_\eta} = Re_\Lambda^{\frac{1}{4}}, \tag{2.14}$$

$$\frac{\tau_\Lambda}{\tau_\eta} = Re_\Lambda^{\frac{1}{2}}. \tag{2.15}$$

From Eq. (2.13) thus becomes evident that the ratio between the volumes of the largest and smallest eddies is proportional to $Re^{9/4}$, whereas, from Eq. (2.15) the ratio of the time scales varies with $Re^{1/2}$. This highlights how computationally challenging is the resolution of the whole turbulence spectrum. Close to the wall, the situation becomes even more complex: the dissipation rate ε increases due to the steep velocity gradients, and as a consequence the Kolmogorov scale decreases further. This means that the smallest turbulent structures, already difficult to resolve in the bulk flow, become even finer and more demanding to be captured in the near-wall region. As a result, at seemingly modest Reynolds number, for instance 10^5, combined with a length scale of the solid surface confining the flow of the order of centimeters, would already require a mesh composed of billions of cells. RANS approaches, on the other hand, aim to avoid this issue by modelling the entire turbulence field rather than resolving it directly. Of course, such an approach is not without drawbacks, as the challenge is shifted to the development and validation of appropriate turbulence models.

2.2.1 From Isotropic to Shear-Strained Turbulence: Correlations and Momentum Transfer

The comparison between freely evolving turbulence and shear-strained turbulence highlights a fundamental difference in the organization of eddies. In the absence of mean shear, turbulence can be represented schematically as a collection of nearly isotropic eddies. However, when a mean shear is applied, the larger eddies deform and align with the shear direction. The small eddies, on the other hand, remain largely unaffected because their characteristic scale is much smaller than that of the mean shear, for instance the shear-layer thickness δ. This separation of scales prevents a direct interaction, which is consistent with the idea that small-scale eddies are universal and insensitive to the details of the large-scale flow. This universality is one of the fundamental assumptions of the Kolmogorov's theory.

Another important aspect is that turbulent motions are not independent from point to point, but rather spatially correlated. If $u_i(x)$ denotes the fluctuating velocity component at a location x, then the velocity fluctuations at x are correlated with those at $x+r$ over distances r of the order of the large-eddy size. The correlation function can be written as

$$R_{ij}(r) = \frac{\overline{u_i(x)u_j(x+r)}}{\overline{u_i(x)u_j(x)}}, \tag{2.16}$$

which decays gradually with r, starting from unity at $r=0$ (see 2.4). This correlation demonstrates that turbulence is not a purely local process, but instead exhibits spatial organization that must be considered in any analysis or modelling.

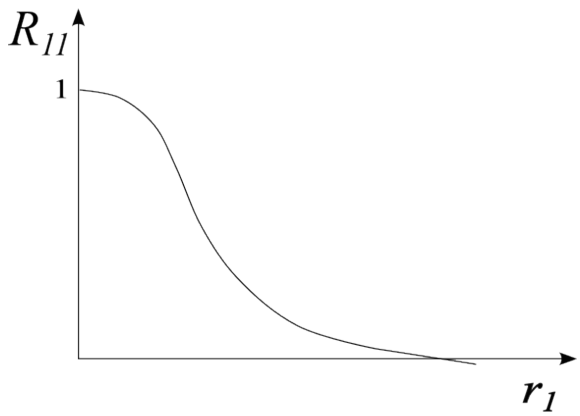

Figure 2.4: Qualitative variation of R_{11} as a function of the distance from the eddy centre.

A particularly relevant feature of shear turbulence is the nonzero correlation between different velocity components. In a flow sheared in the $x-y$ plane, the product $\overline{uv}$, where $u=u_1$ and $v=u_2$, is negative. This can be understood by considering the motion of the eddies: on average, rotational motions carry low-momentum fluid from lower regions upward and high-momentum fluid from upper regions downward. As a consequence, a negative fluctuation in v (downward motion) is typically associated with a positive fluctuation in u (streamwise velocity higher than the mean), whereas a positive v (upward motion) is correlated with a negative u. This systematic coupling implies that

$$\overline{uv} < 0 \quad \text{for} \quad \frac{\partial U}{\partial y} > 0, \tag{2.17}$$

while the opposite sign in the velocity correlation arises if $\frac{\partial U}{\partial y} < 0$.

This correlation has a clear physical interpretation: it represents a flux of momentum caused by the turbulent eddies, redistributing mean momentum across the shear layer. In fact, $\overline{uv}$ acts as a turbulent stress that opposes the mean velocity gradient, in analogy with the viscous stress $\mu \frac{\partial U}{\partial y}$, but typically much larger in magnitude. This mechanism explains how turbulence enhances momentum transfer far beyond what viscosity alone could induce.

Finally, it is important to note that streamwise fluctuations u tend to be much larger than wall-normal fluctuations v, especially in shear flows. This disparity marks the onset of anisotropy, the departure from isotropic turbulence, which is an inherent characteristic of turbulence subjected to mean strain.

2.2.2 Turbulence Forcing and Kinetic Energy Production

When turbulence evolves in an unforced environment like behind a grid, it inevitably decays because turbulent kinetic energy is progressively converted into heat by viscous dissipation. To sustain turbulence, a continuous source of forcing is required, among which straining, and in particular shear, represents the most effective and widely encountered mechanism.

Shear arises most clearly in wall-bounded flows as a consequence of the no-slip condition imposed at solid surfaces. At the wall, the velocity of the fluid must match that of the surface, which in most cases is zero, while farther from the wall the fluid is free to move at a higher velocity. This contrast generates a velocity gradient normal to the surface. As a result, adjacent layers of fluid slide past each other, transferring momentum and creating a mechanism through which the kinetic energy of the mean flow is continuously converted into turbulent fluctuations. Fig. 2.5 shows the shape of the velocity profiles in a laminar and a turbulent boundary layer, highlighting the velocity gradient at the wall (for a deeper description of the boundary layer see Sec. 2.3.1).

This mechanism is responsible for the production term of the turbulent kinetic energy equation:

$$P_{k,\text{shear}} = -\overline{uv}\,\frac{\partial U}{\partial y}, \tag{2.18}$$

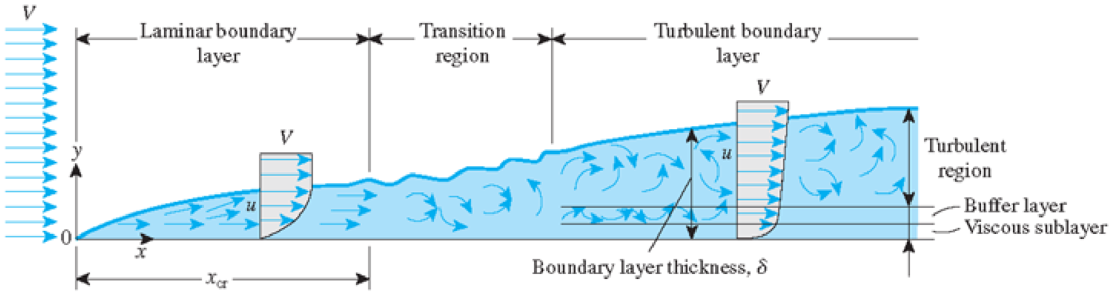

Figure 2.5: Schematic representation of the boundary layer transition. The laminar (on the left) and turbulent (on the right) velocity profiles are also reported.

where $-\overline{uv}$ represents the Reynolds shear stress and $\frac{\partial U}{\partial y}$ is the mean velocity gradient. Their product provides the energy transfer rate from the mean flow to the turbulent field. Physically, this term counteracts viscous dissipation contributing to sustain the turbulence field. In canonical shear flows such as boundary layers, free jets, or mixing layers, production and dissipation tend to balance, as already introduced by discussing Fig. 2.3. This leads to a statistical steady state often referred to as local turbulence–energy equilibrium, which will be better examined in Section 3.3. Within this regime, the energy supplied by shear does not accumulate indefinitely but instead cascades to progressively smaller scales until it is ultimately dissipated to heat by viscosity.

2.3 Boundary Layer Transition

As will be highlighted in the following Chapters, one of the major challenges in turbulence modelling lies in accurately representing the transition between laminar and turbulent boundary layers. These two regimes behave very differently: the laminar boundary layer is characterized by lower surface friction and therefore lower aerodynamic losses, but it tends to separate easily under adverse pressure gradients. In contrast, the turbulent boundary layer exhibits higher friction but enhanced internal mixing, which allows it to keep attached to the surface for longer distance. In the case of an airfoil, for example, this increases the resistance to stall, enabling higher angles of incidence without loss of lift. For this reason, correctly identifying the transition point is fundamental for reliable numerical simulations and for understanding how the flow will respond under different operating conditions.

2.3.1 Basic Concepts of the Boundary Layer

The boundary layer concept allows accounting for viscous effects in fluid motion, namely the property of fluids to transmit shear stresses between regions with different velocities

[67]. The velocity gradients that occur in flows over a solid surface are responsible for the generation of wall shear stresses, which are defined as:

$$\tau_w = \mu \left(\frac{du}{dy}\right)_{y=0} \tag{2.19}$$

where μ is the dynamic viscosity, and the derivative of the streamwise velocity component (u) with respect to the wall-normal direction (y) is evaluated at the wall ($y = 0$). It can be seen that higher gradients or viscosity values lead to greater shear stresses. Close to the surface, viscous effects dominate, reducing the velocity of flow particles from the free-stream value to zero at the wall. This is due to electrostatic forces causing the no-slip condition on the solid surface. Outside the boundary layer edge, viscous effects become negligible. Friction acts to transmit shear stresses, increasing the velocity of fluid particles near the wall while slowing down those in faster regions farther from the wall. The portion of fluid that contains 99% of the velocity variation compared to the free-stream velocity defines the boundary layer thickness $\delta_{99}(x)$.

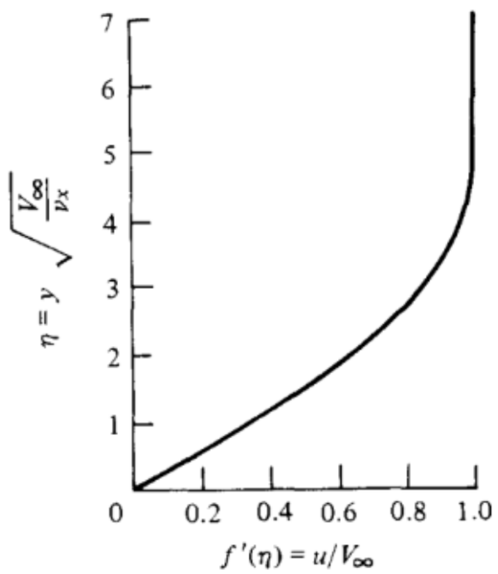

Figure 2.6: Blasius self-similar velocity profile for a laminar boundary layer developing on a flat plate at zero angle of incidence.

To better illustrate the effects of transition on boundary layer growth and viscous stresses, the simplified Blasius solution, obtained for flat plates under zero pressure gradient, is briefly recalled here. For two-dimensional flows over a flat plate, Blasius [68] obtained the self-similar solution shown in Fig. 2.6, where η and $f'(\eta)$ are similarity variables [68]. In this simplified case, the values of δ_{99} and the skin friction coefficient C_f can be exactly predicted as a function of the distance x from the leading edge of the plate.

The skin friction coefficient, defined as the ratio between the wall shear stress τ_w and the dynamic pressure $1/2\rho_\infty U_\infty^2$, is found to depend on the local Reynolds number according to:

$$C_{f_{lam}} = \frac{0.664}{\sqrt{Re_x}} \tag{2.20}$$

That is, C_f decreases with the square root of the distance from the leading edge. According to the Blasius solution, the laminar boundary layer thickness is given by:

$$\delta_{lam} = \frac{5.0x}{\sqrt{Re_x}} \tag{2.21}$$

i.e., the laminar boundary layer thickness over a flat plate grows proportionally to $x^{1/2}$. It is important to underline that the previous relations are valid only for laminar boundary layers. As the flow develops downstream along the plate, the local Reynolds number eventually becomes high enough to induce transition, leading to the onset of a turbulent boundary layer. In this case, the Blasius solution no longer applies, and empirical correlations are typically used to estimate δ_{99} and C_f for a fully developed turbulent boundary layer:

$$\delta_{turb} = \frac{0.37x}{Re_x^{1/5}} \tag{2.22}$$

$$C_{f_{turb}} = \frac{0.074}{Re_x^{1/5}} \tag{2.23}$$

The turbulent boundary layer thickness scales as $x^{4/5}$, meaning it grows more rapidly than the laminar one. This faster growth is due to enhanced mixing between adjacent fluid layers. The friction coefficient is instead proportional to $Re^{-1/5}$, as stated by Prandtl's law, and results in a higher friction drag. The lack of an exact similarity solution for the turbulent boundary layer arises from the presence of a viscous sublayer near the wall, where viscous effects are still dominant.

More precisely, three distinct regions can be identified in a turbulent boundary layer, each with different velocity profiles and growth characteristics: the viscous sublayer, the buffer layer, and the logarithmic layer, as illustrated in Fig. 2.7. These regions are typically defined as a function of the wall-normal distance expressed in dimensionless form as $y^+ = \frac{y}{\nu}\sqrt{\frac{\tau_w}{\rho}}$. The corresponding dimensionless velocity is expressed as $u^+ = u\sqrt{\frac{\rho}{\tau_w}}$, where $\sqrt{\frac{\tau_w}{\rho}}$ is the so-called friction velocity, u_τ, so that $u^+ = \frac{u}{u_\tau}$. In the viscous sublayer ($y^+ < 5$), u^+ is linearly proportional to y^+, indicating a laminar-like behavior due to the dominance of viscosity. For $y^+ > 30$, the logarithmic region is reached, where the flow becomes fully turbulent and is characterized by strong fluctuations in both intensity and direction. In this region, the log-law applies, and u^+ follows:

$$u^+ = \frac{1}{k}\ln(y^+) + C^+ \tag{2.24}$$

where k and C^+ are the von Kármán constants. The buffer layer, which lies between the viscous and logarithmic regions, exhibits transitional behavior and does not conform to either of the previous laws.

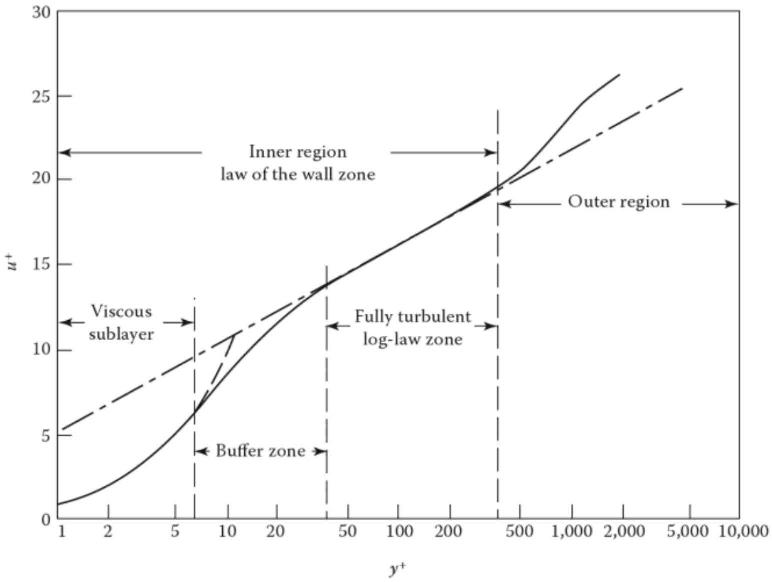

Figure 2.7: Classification of boundary layer regions: viscous sublayer ($y^+ < 5$), buffer layer ($5 < y^+ < 30$), fully turbulent/log-law region ($y^+ > 30$).

2.3.2 Transition Mechanisms

Boundary layer transition may occur through different mechanisms depending on the free-stream turbulence level and on the unsteadiness of the external flow. Among the various transition mechanism, this work focuses particularly on separation-induced transition. Indeed, boundary layer separation can drastically alter the performance of any object exposed to a fluid. Referring again to an airfoil, its lift collapses if the boundary layer separates prematurely, or, in the case of a turbine blade, separation on the suction side leads to a significant increase in losses. Except for separation-induced transition, addressed separately in Sec. 2.3.3, the main transition scenarios can be summarized as follows:

- **Natural transition** (low free-stream turbulence, $Tu < 0.5\%$). In very low-disturbance environments, transition is driven by instabilities intrinsic to the boundary layer.

Two-dimensional Tollmien–Schlichting (T–S) waves grow while propagating downstream and, once their amplitude exceeds a critical threshold, secondary three-dimensional instabilities arise. This process leads to the formation of turbulent spots that progressively merge into a fully turbulent boundary layer. Natural transition is gradual and spatially extended, but highly sensitive to external disturbances, which makes its prediction particularly challenging in external aerodynamics applications [69]. However, turbine-relevant conditions are characterized by moderate to high free-stream turbulence levels, so natural transition will therefore not be further addressed.

- **Bypass transition** (moderate to high free-stream turbulence, $0.5 < Tu < 1\%$). When the incoming turbulence level is sufficiently high, classical T–S waves are effectively bypassed. Transition is instead driven by the transient amplification of streamwise-elongated disturbances, known as streaks or Klebanoff modes [70]. These structures arise from the lift-up effect generated by counter-rotating streamwise vortices and may reach large amplitudes before undergoing secondary instability and breakdown into turbulent spots [71], [72]. Bypass transition is typically faster and occurs at Reynolds numbers significantly lower than those predicted by modal stability theory.

- **Wake-induced transition** (periodically unsteady inflow). In turbomachinery, wakes shed by upstream blades periodically impinge on downstream boundary layers. If wake disturbances are weak, the mechanism resembles bypass transition, with localized acceleration of the process under the wake trajectory and delayed transition between wakes, often accompanied by a calming effect. For stronger wake interactions, transient adverse pressure gradients may develop, promoting rapid breakdown through Kelvin–Helmholtz-type instabilities. The resulting transition can be significantly faster than in statistically steady conditions [70].

The present work specifically focuses on separation-induced transition under turbine-relevant flow conditions, where laminar separation and subsequent shear-layer instability govern the onset of turbulence.

2.3.3 Separated flow transition

When the flow is subjected to a sufficiently strong adverse pressure gradient, the boundary layer developing along a solid wall may no longer remain attached. In such circumstances, a reverse-flow region forms, where the fluid particles near the surface move opposite to the outer flow. Separation can affect both laminar and turbulent boundary layers, although in the latter case a higher adverse pressure gradient is generally required. The point of separation is conventionally defined as the wall location where the fluid adjacent to the surface is forced to reverse direction with respect to the external stream [73]. At this coordinate, the streamline of zero velocity detaches from the wall. Before separation occurs, the velocity gradient at the wall is positive, and shear stress resists the main flow direction; once the layer has separated, the gradient becomes negative, and the shear stress changes both sign and orientation. Hence, the separation point is identified as the position where the wall shear stress vanishes:

$$\tau_w = \mu \left(\frac{\partial u}{\partial y} \right)_{y=0} = 0 \tag{2.25}$$

In turbomachinery, such separation-driven transitions often appear on high-lift turbine blade profiles, strongly influencing the surface pressure distribution (see Fig. 2.5).

Although detachment disrupts the boundary layer, the flow can reattach when laminar-to-turbulent transition develops inside the separated shear layer. Downstream of the separation point, disturbances are amplified by the inviscid Kelvin–Helmholtz instability [74], [75]. Their growth continues until the bubble reaches its maximum thickness, where saturation occurs [76]. At this location, the shear layer rolls into vortices, leading to an intense vortex shedding process [77]. The subsequent breakdown of these large coherent structures promotes transition and reattachment, as reported by Marxen and Henningson [56] and by Simoni et al. [78].

The stability of the separated boundary layer can be interpreted qualitatively by a free-shear layer analogy. Once detached from the surface, the strong velocity gradients across the shear layer make it prone to instabilities. In this context, Rayleigh's inviscid theory helps explain how small perturbations evolve: only disturbances within a certain range of scales can grow, while others remain neutral or decay [79]. The unstable ones amplify rapidly, feeding on the velocity difference across the layer, until they roll up into vortices that drive transition to turbulence.

Depending on the Reynolds number, turbulence intensity, and adverse pressure gradient (Re, Tu, AP), the resulting separation bubble may remain short or extend into a long bubble configuration [60]. A first distinction lies in their impact on the pressure field: short bubbles cause only local deviations, leaving the upstream and downstream distributions close to inviscid predictions, whereas long bubbles alter the entire surface pressure distribution significantly. A change in flow conditions, such as angle of incidence or velocity (hence Reynolds number), may force the bubble to expand from the short to the long type, increasing aerodynamic losses and modifying blade loading. This transition is commonly referred to as bursting. From a dynamical standpoint, short and long pressure-induced bubbles are not merely geometrically different. In short bubbles, the separated shear layer is dominated by convective Kelvin–Helmholtz instabilities that grow spatially while being advected downstream, promoting an efficient momentum transfer and a rapid turbulent reattachment [80]. When bursting occurs, the instability mechanism progressively shifts toward a more globally amplified behaviour, closer to absolute instability conditions. Disturbances grow predominantly in time, the recirculation region becomes more actively involved, and the resulting vortical structures are larger but less effective in sustaining reattachment, leading to a thicker and longer bubble [81]. Thus, the short-to-long transition reflects a qualitative modification of the shear-layer stability properties rather than a simple elongation of the separated region.

It is worth noting that not all separation bubbles originate from an adverse pressure gradient. In geometry-induced configurations, such as flows over rounded leading edges, separation is enforced by curvature effects rather than by pressure. While at low free-stream turbulence intensity these bubbles also exhibit classical Kelvin–Helmholtz rollers and separation-induced transition, increasing turbulence intensity may progressively suppress the coherent shear-layer instability. In such cases, the transition mechanism shifts toward bypass-dominated dynamics, characterized by streamwise streaks, even in separated flows [82]. This behaviour differs from pressure-induced bubbles, where Kelvin–Helmholtz instabilities typically remain dynamically relevant over a broader range of operating conditions. Consequently, despite similar mean-flow features, pressure-induced and geometry-induced bubbles can follow substantially different transition pathways [83].

Chapter 3

Importance of Turbulence Modelling

3.1 Navier-Stokes equations

In the description of the main features of turbulence reported above, implicit reference was made to the Navier–Stokes equations (NSE), which govern fluid motion. In order to delve into the details of transition modelling, it is essential to provide a more thorough description of them.
These equations, developed by the French engineer and physicist Claude-Louis Navier and the mathematician George Gabriel Stokes between 1822 and 1850, represent a cornerstone of fluid dynamics, providing a fundamental framework for describing the behavior of Newtonian fluids. These equations govern the motion of fluids by expressing the balance of momentum and mass, and they are widely used in engineering, meteorology, oceanography, and many other fields where fluid flow plays a central role. Despite their importance and apparent simplicity, the mathematical understanding of the Navier–Stokes equations is still incomplete. In particular, one of the most profound open questions is whether, given smooth initial conditions, a unique and smooth solution (i.e. infinitely differentiable) always exists. This issue is not only of theoretical interest, but also has deep implications for the predictability and reliability of numerical simulations of fluid flows, especially in turbulent regimes. Due to its significance, the problem was selected in the year 2000 as one of the seven Millennium Prize Problems by the Clay Mathematics Institute, which offered a prize of one million dollars for a correct solution. Resolving this question would constitute a major breakthrough in the mathematical theory of partial differential equations and in our understanding of fluid motion.
The Navier–Stokes equations are derived from the momentum balance over an arbitrary control volume. This leads to the Cauchy momentum equation, which, in index notation, reads:

$$\rho \left(\frac{\partial u_i}{\partial t} + u_j \frac{\partial u_i}{\partial x_j} \right) = \rho g_i + \frac{\partial \sigma_{ij}}{\partial x_j} \tag{3.1}$$

where:

- ρ is the fluid density;
- u_i are the components of the velocity vector $\vec{u} = (u_1, u_2, u_3) = (u, v, w)$;
- g_i are the components of the gravitational acceleration vector;
- σ_{ij} are the components of the Cauchy stress tensor.

The indexes $i = 1, 2, 3$ denotes the Cartesian directions x, y, z.
Introducing now the continuity equation for a compressible fluid:

$$\frac{\partial \rho}{\partial t} + \frac{\partial(\rho u_j)}{\partial x_j} = 0, \tag{3.2}$$

we can see that, together, equations (3.1) and (3.2) form a system with 10 unknowns: the scalar density ρ, the three components of the velocity u_i, and the six independent components of the symmetric stress tensor σ_{ij}. Self-evidently, this system is underdetermined and requires a constitutive relation to express σ_{ij} in terms of the other unknowns.

To close the system, the stress tensor is decomposed into pressure and viscous contributions:

$$\sigma_{ij} = -p\delta_{ij} + \mu\tau_{ij} \tag{3.3}$$

where:

- p is the thermodynamic pressure;
- δ_{ij} is the Kronecker delta;
- τ_{ij} are the components of the deviatoric (viscous) stress tensor, defined for a Newtonian fluid as:

$$\tau_{ij} = \mu(\frac{\partial u_i}{\partial x_j} + \frac{\partial u_j}{\partial x_i}) \tag{3.4}$$

Thus, the full constitutive equation becomes:

$$\sigma_{ij} = -p\delta_{ij} + \mu\left(\frac{\partial u_i}{\partial x_j} + \frac{\partial u_j}{\partial x_i}\right) \tag{3.5}$$

Substituting equation (3.5) into the momentum equation (3.1) and considering an incompressible flow (i.e., $\frac{\partial u_i}{\partial x_i} = 0$), the Navier–Stokes equations in index form become:

$$\rho\left(\frac{\partial u_i}{\partial t} + u_j\frac{\partial u_i}{\partial x_j}\right) = -\frac{\partial p}{\partial x_i} + \rho g_i + \mu\frac{\partial^2 u_i}{\partial x_j \partial x_j} \tag{3.6}$$

Coupling these equations with the continuity equation, which, for a three-dimensional incompressible flow, simplifies to $\vec{\nabla} \cdot \vec{u} = 0$, we obtain a subsystem of 4 equations in 4 unknowns [84]. Solving this system, with appropriate boundary conditions, allows for the pointwise determination of the four key fluid dynamic quantities: the fluid pressure and the three components of the velocity field.

3.2 A numerical attempt to solve the NSE

Computational Fluid Dynamics (CFD) comprises numerical approaches for solving the Navier–Stokes equations on a discretized computational domain. Depending on the level of turbulence resolution, different strategies can be adopted, including Direct Numerical Simulation (DNS), Large Eddy Simulation (LES), and Reynolds-Averaged Navier–Stokes (RANS) methods. DNS provides the highest level of fidelity but at high computational cost, while LES offers an intermediate compromise. In industrial applications, however, RANS remains the most widely used approach due to its computational efficiency. The present section therefore focuses on the formulation and closure of the RANS equations.

3.2.1 Reynolds Averaged Navier Stokes Equations (RANS)

One of the most widely used techniques for solving the equations governing turbulent flow, introduced by Osborne Reynolds in a paper presented to the Royal Society of London in 1885, involves averaging these equations over a certain time interval. In particular, Reynolds proposed to decompose the velocity field. To do this, he considered turbulent flows as the superposition of a mean motion, averaged over a long sampling period, and a fluctuating motion function of time:

$$u = \overline{u} + u' \tag{3.7}$$

However, to derive the equations in their most widely recognized form today, one may start from the general case in which the time average is taken over a finite time interval T. In this case, the following decomposition is introduced [65]:

$$u_i = \tilde{u}_i + u_i' \quad , \quad p = \tilde{p} + p' \tag{3.8}$$

The use of tilde indicates that the velocity and the pressure are averaged over a finite period T:

$$\tilde{u}_i(t) = \frac{1}{T} \int_{\frac{t-T}{2}}^{\frac{t+T}{2}} u_i(t)dt. \tag{3.9}$$

This definition makes it evident that the averaged value depends on the length of the period T. Applying the decomposition to the NS equations (Eq. (3.6)), again neglecting the body forces, we derive:

$$\frac{\partial \rho(\tilde{u}_i+u'_i)}{\partial t}+\frac{\partial \rho(\tilde{u}_i+u'_i)(\tilde{u}_j+u'_j)}{\partial x_j}=\frac{\partial(\tilde{p}+p')}{\partial x_i}+\frac{\partial}{\partial x_j}\mu\Big(\frac{\partial(\tilde{u}_i+u'_i)}{\partial x_j}+\frac{\partial(\tilde{u}_j+u'_j)}{\partial x_i}\Big) \tag{3.10}$$

Then, the whole equation Eq. (3.10) is averaged over the same period T. The inclusion of the approximations $\tilde{u'_i}=0$ and $\tilde{p'}=0$, together with the relations $\tilde{\tilde{u}}_i=\tilde{u}_i$ and $\tilde{\tilde{p}}=\tilde{p}$, then yields:

$$\begin{aligned}\frac{\partial \rho\tilde{u}_i}{\partial t}+\frac{\rho\tilde{u}_i\tilde{u}_j}{\partial x_j}=&-\frac{\partial \tilde{p}}{\partial x_i}+\frac{\partial}{\partial x_j}\mu\Big(\frac{\partial \tilde{u}_i}{\partial x_j}+\frac{\partial \tilde{u}_j}{\partial x_i}\Big)-\frac{\partial}{\partial x_j}\big(\rho\widetilde{\tilde{u}_i\tilde{u}_j}-\rho\tilde{u}_i\tilde{u}_j\big)\\&-\frac{\partial}{\partial x_j}\big(\rho\widetilde{\tilde{u}_iu'_j}+\rho\widetilde{\tilde{u}_ju'_i}\big)-\frac{\partial}{\partial x_j}\rho\widetilde{u'_iu'_j},\end{aligned} \tag{3.11}$$

in which $\tilde{u}_i$ is the unknown of the equation.
The equation just introduced has a general validity, as it holds for both steady and unsteady flow conditions. According to this formulation, the mean velocity is in fact a function of time, accounting for the fact that not all temporal variations of the velocity are related to turbulence, but may also be associated with periodic oscillations of the mean flow. Examples include the vortices generated downstream of a cylinder that is exposed to a flow (the vortex shedding phenomenon), or the wake produced by a turbine blade impinging on the adjacent row in relative motion. In all these cases, in addition to the inherent turbulence that characterizes the actual flow field, there is a component associated with the unsteadiness of the mean flow. However, this consideration entails a fundamental ambiguity, stemming from the arbitrary choice of the integration period T. This choice determines the separation between what is regarded as turbulence, represented in the term u'_i, and what is instead the unsteadiness of the flow, which is included in $\tilde{u}_i$. Moreover, this formulation includes three terms, namely $\widetilde{\tilde{u}_i\tilde{u}_j}$, $\widetilde{\tilde{u}_iu'_j}$, and $\widetilde{u'_iu'_j}$, which, in order to close the equation, need to be correlated to the velocity $\tilde{u}_i$ through appropriate models. Without addressing the details of the issues associated with the so-called unsteady RANS (URANS), this discussion will be restricted to the case of steady flow.
The problem now becomes simpler, since there is no longer any interest in evaluating the temporal variation of the mean velocity. The integration interval T is extended so as to be much larger than the largest turbulence scales. To indicate that the averaging operation is performed over a very long time, the averaging operator can be denoted by an overbar ($\tilde{u}_i=\overline{u_i}$).

$$\frac{\partial \rho\overline{u_i}\,\overline{u_j}}{\partial x_j}=-\frac{\partial \overline{p}}{\partial x_i}+\frac{\partial}{\partial x_j}\mu\Big(\frac{\partial \overline{u_i}}{\partial x_j}+\frac{\partial \overline{u_j}}{\partial x_i}\Big)-\frac{\partial}{\partial x_j}\rho\overline{u'_iu'_j}. \tag{3.12}$$

Although Eq. (3.11) is evidently simplified, the presence of the term $\overline{u_iu_j}$, which arises from the product of the fluctuating velocity components (the time average of the product is different from zero), still prevents direct closure of the problem. This term corresponds to the Reynolds Stress Tensor τ_{ij}^R:

$$\boldsymbol{\tau}_{ij}^R \equiv \overline{u_i'u_j'} \equiv \begin{pmatrix} \overline{u_1'^2} & \overline{u_1'u_2'} & \overline{u_1'u_3'} \\ \overline{u_2'u_1'} & \overline{u_2'^2} & \overline{u_2'u_3'} \\ \overline{u_3'u_1'} & \overline{u_3'u_2'} & \overline{u_3'^2} \end{pmatrix}. \tag{3.13}$$

Since τ_{ij}^R is a symmetric tensor, i.e., $\overline{u_1'u_2'} = \overline{u_2'u_1'}$, $\overline{u_1'u_3'} = \overline{u_3'u_1'}$ and $\overline{u_2'u_3'} = \overline{u_3'u_2'}$, only six components are independent. Moreover, looking at Eq. (3.12), one can see that, grouping the last two terms, τ_{ij}^R acts as the turbulence-equivalent of the viscous term $\mu\left(\frac{\partial\overline{u_i}}{\partial x_j} + \frac{\partial\overline{u_j}}{\partial x_i}\right)$. The formulation in Eq. (3.13) can be simplified for two-dimensional flows. In a flow where the mean velocity component $\overline{u_3} = 0$, the corresponding fluctuation u_3' may still be nonzero, as oscillations in the x_3 direction are not excluded. Nevertheless, the off-diagonal terms $\overline{u_1'u_3'}$ and $\overline{u_2'u_3'}$ vanish, since no correlation is expected between u_3' and the other two fluctuating components.
The predictive capability of a RANS approach fundamentally relies on the definition of an appropriate model able to express the components of the Reynolds stress tensor as a functions of the mean velocity components. In this way, the system can be closed, since the additional unknowns are related to the other variables of the problem, thereby making the set of equations well posed. The ultimate goal of turbulence modelling is the definition of a model able to accurately represent the Reynolds stress tensor even under highly complex flow conditions, an issue that is far from trivial. The problem of Reynolds stress modelling will be further discussed in Chapter 4.

3.3 The Problem of Loss Evaluation

As mentioned in the Introduction, the design process of any component that operates in contact with a fluid, whether a simple duct or an aircraft engine blade, has as its primary objective the minimization of energy losses. However, in order to pursue this goal, it is essential that such losses be correctly assessed, even when relying on computational tools such as RANS, which are unable to resolve the instantaneous flow field. In this section, the way losses are defined and evaluated will be shown, ultimately highlighting once again the importance of an accurate modelling of the Reynolds stress tensor.

From a theoretical point of view, in order to quantify mechanical energy losses within a generic flow, one must evaluate the effect of the irreversibilities. Irreversibilities are responsible for entropy increase that, by means of the Gibbs' equation, can be formulated according to Eq. 3.14.

$$T_t \frac{DS}{Dt} = \frac{Dh_t}{Dt} - \frac{1}{\rho_t}\frac{Dp_t}{Dt}, \tag{3.14}$$

where, for an incompressible low speed flow, $\rho_t \approx \rho$.
The two terms on the right hand side of Eq. 3.14 can be expanded by means of the transport equation of the instantaneous kinetic energy of the flow K:

$$K = \frac{1}{2}\rho ||\vec{V}||^2 = \frac{1}{2}\rho\left(u^2 + v^2 + w^2\right). \tag{3.15}$$

The corresponding transport equation is obtained multiplying the momentum equation by the corresponding velocity component:

$$u\mathrm{NSE}(u) + v\mathrm{NSE}(v) + w\mathrm{NSE}(w) = 0, \tag{3.16}$$

where NSE(u) is the Navier-Stokes equation related to the u velocity component. After some algebra, the following equation is obtained:

$$\frac{DK}{Dt} = -\vec{V}\cdot\nabla p + \mu\left(u\nabla^2 u + v\nabla^2 v + w\nabla^2 w\right), \tag{3.17}$$

or, for incompressible flows in terms of total pressure p_t (i.e., $p_t = p + \frac{1}{2}\rho(u^2+v^2+w^2)$):

$$\frac{Dp_t}{Dt} = \frac{\partial p}{\partial t} + \mu\left(u\nabla^2 u + v\nabla^2 v + w\nabla^2 w\right). \tag{3.18}$$

Now, a dissipation function Φ is defined as the difference between the net external work and the friction work:

$$\Phi = \nabla\cdot\left(\boldsymbol{\tau}\vec{V}\right) - \mu\left(u\nabla^2 u + v\nabla^2 v + w\nabla^2 w\right). \tag{3.19}$$

Thus, Eq. 3.18 can be reformulated as:

$$\frac{Dp_t}{Dt} = \frac{\partial p}{\partial t} + \nabla\cdot\left(\boldsymbol{\tau}\vec{V}\right) - \Phi. \tag{3.20}$$

The term $\nabla\cdot(\tau\vec{V})$ also appears inside the total enthalpy equation:

$$\rho\frac{Dh_t}{Dt} = \frac{\partial p}{\partial t} - \nabla\cdot\vec{q} + \nabla\cdot\left(\boldsymbol{\tau}\vec{V}\right) \tag{3.21}$$

Combining this equation with Eq. (3.20) we obtain:

$$\rho\frac{Dh_t}{Dt} = \frac{Dp_t}{Dt} - \nabla\cdot\vec{q} + \Phi \tag{3.22}$$

In the context of a turbomachinery experimental campaign or numerical simulations a non-work exchanging steady (or time-averaged) adiabatic flow is usually considered, i.e.:

$\nabla \cdot \vec{q} = 0$ and $\frac{Dh_t}{Dt} = 0$. Introducing these assumptions and combining Eq. (3.14) with Eq. (3.22), the following relation is derived:

$$T_t \frac{DS}{Dt} = \frac{1}{\rho_t}\Phi = -\frac{1}{\rho_t}\frac{Dp_t}{Dt}. \tag{3.23}$$

Additionally, since we are interested in temporally-averaged quantities, we can write the averaged alternative formulation of the Gibbs' equation:

$$\overline{T_t \frac{DS}{Dt}} = \overline{\frac{1}{\rho_t}\Phi} = -\overline{\frac{1}{\rho_t}\frac{Dp_t}{Dt}}. \tag{3.24}$$

This expression highlights that losses can be locally related to a variation in total pressure. To evaluate the overall losses generated within a domain, it is necessary to integrate the substantial derivative of the total pressure across the domain. However, a direct evaluation of $\overline{\frac{Dp_t}{dt}}$ is not feasible through RANS simulation, since computing the instantaneous total pressure would require knowledge of both the instantaneous velocity and static pressure fields. In the following, it will be shown that, through suitable assumptions, it is possible to express $\overline{\frac{Dp_t}{Dt}}$ and, consequently, also $\overline{\Phi}$ as a function of the mean velocity components and on the Reynolds stress tensor, and therefore suitable for a solution within the RANS framework.
In order to derive the time-averaged stagnation pressure transport equation, we recall the definition of the substantial derivative of the total pressure:

$$\frac{Dp_t}{Dt} = \frac{\partial p_t}{\partial t} + \overline{u}_i \frac{\partial p_t}{\partial x_i} \tag{3.25}$$

Then, by means of the Reynolds decomposition of both velocity and static pressure contributing to p_t, after some algebra we obtain:

$$\overline{\frac{Dp_t}{Dt}} = \underbrace{\overline{u}_i \frac{\partial \overline{p}}{\partial \overline{x}_i} + \frac{D}{Dt}\left(\frac{1}{2}\overline{\rho}\,\overline{u}_i\overline{u}_i\right) + \frac{D}{Dt}\left(\frac{1}{2}\overline{\rho}\,\overline{u'_i u'_i}\right)}_{\frac{D\overline{p_t}}{Dt}} + \frac{\partial}{\partial x_j}\left[\overline{u}_i\left(\overline{\rho u'_i u'_j}\right)\right] + \overline{\frac{\partial \rho u'_i k}{\partial x_i}} + \overline{\frac{\partial u'_i p'}{\partial x_i}}. \tag{3.26}$$

The equation for $\frac{D\overline{p_t}}{Dt}$ can be derived summing together Eq. (3.27) and Eq. (3.28), which represent a pseudo-p_t transport equation (computed only from time-averaged quantities) and the turbulent kinetic energy transport equation, respectively.

$$\underbrace{\overline{u}_i \cdot \nabla\left(\overline{p} + \tfrac{1}{2}\rho\overline{V}^2\right)}_{\text{F.A.S.P.}} = -\underbrace{\overline{\tau}_{ij}\frac{\partial \overline{u}_i}{\partial x_j}}_{\Phi_m} - \underbrace{\left(-\overline{\rho u'_i u'_j}\frac{\partial \overline{u}_i}{\partial x_j}\right)}_{P_k} - \underbrace{\frac{\partial \overline{\tau}_{ij}\overline{u}_i}{\partial x_j}}_{\text{V.D.}} - \underbrace{\frac{\partial}{\partial x_j}\left[\overline{u}_i\left(\overline{\rho u'_i u'_j}\right)\right]}_{\text{T.D.}}, \tag{3.27}$$

where P_k is the turbulent kinetic energy production, Φ_m the mean flow dissipation rate, while V.D. and T.D. viscous and turbulent diffusion, respectively.

$$\underbrace{\overline{u}_i \cdot \nabla \overline{k}}_{\text{F.T.K.E.}} = \underbrace{\nu \frac{\partial^2 k}{\partial x_j^2}}_{\text{V.D.}_{\cdot k}} + \underbrace{\left(-\overline{u_i' u_j'} \frac{\partial \overline{u}_i}{\partial x_j} \right)}_{P_k} - \underbrace{\frac{\partial \overline{u_i' k}}{\partial x_i}}_{\text{T.D.}_{\cdot k}} - \underbrace{\frac{1}{\rho} \frac{\partial \overline{u_i' p'}}{\partial x_i}}_{\text{P.D.}_{\cdot k}} - \frac{1}{\rho} \underbrace{\overline{\tau_{ij}' \frac{\partial u_i'}{\partial x_j}}}_{\overline{\Phi}_f} . \quad (3.28)$$

Here, V.D.$_{\cdot k}$, T.D.$_{\cdot k}$ and P.D.$_{\cdot k}$ correspond to the viscous, turbulent and pressure diffusion of k, respectively, while $\overline{\Phi_f}$ is the turbulent dissipation rate.
Moreover, considering an adiabatic non-work exchanging flow, the terms V.D. and V.D.$_{\cdot k}$ are null. Hence, adding together these two equations we obtain the balance equation for the mean total pressure (Eq. (3.28) must be multiplied by ρ):

$$\frac{D\overline{p_t}}{Dt} = -\overline{\tau}_{ij} \frac{\partial \overline{u}_i}{\partial x_j} - \frac{\partial}{\partial x_j} \left[\overline{u}_i \left(\overline{\rho u_i' u_j'} \right) \right] - \frac{\overline{\partial u_i' p'}}{\partial x_i} - \overline{\tau_{ij}' \frac{\partial u_i'}{\partial x_j}} \quad (3.29)$$

Finally, substituting Eq. (3.29) into Eq. (3.26), one can obtain that the time-averaged substantial derivative of p_t is equal to dissipation terms:

$$\overline{\frac{Dp_t}{Dt}} = -\overline{\tau}_{ij} \frac{\partial \overline{u}_i}{\partial x_j} - \overline{\tau_{ij}' \frac{\partial u_i'}{\partial x_j}} \quad (3.30)$$

The former result states that entropy production can be locally evaluated from the sum of the mean flow viscous dissipation and the turbulent dissipation:

$$\Phi_m = \overline{\tau}_{ij} \frac{\partial \overline{u}_i}{\partial x_j} \qquad , \qquad \overline{\Phi}_f = \overline{\tau_{ij}' \frac{\partial u_i'}{\partial x_j}} \quad (3.31)$$

Recalling Eq. (3.23), it can be observed that the sum of Φ_m and $\overline{\Phi}_f$ represents a formulation of $\overline{\Phi}$, namely the dissipation function to which the Reynolds decomposition has been applied:

$$\overline{\Phi} = \Phi_m + \overline{\Phi}_f, \quad (3.32)$$

The term $\overline{\Phi}_f$ represents the dissipation of both the turbulent kinetic energy (Φ_k) and the off-diagonal entries (Φ_τ) of the stress tensor:

$$\overline{\Phi}_f = \overline{\Phi}_k + \overline{\Phi}_\tau, \quad (3.33)$$

being:

$$\overline{\Phi}_k = \mu \overline{\frac{\partial u_i'}{\partial x_j} \frac{\partial u_i'}{\partial x_j}} \quad , \quad \overline{\Phi}_\tau = \mu \overline{\frac{\partial u_i'}{\partial x_j} \frac{\partial u_j'}{\partial x_i}} \quad \text{for} \quad i \neq j \quad (3.34)$$

The term $\overline{\Phi}_\tau$ is identically zero for non-work exchanging flows, thus the entropy variation is equal to the sum of the of the mean flow viscous dissipation and the turbulent dissipation

$$\overline{T_t \frac{DS}{Dt}} = \frac{1}{\rho_t}\overline{\Phi} = \frac{1}{\rho_t}\left(\Phi_m + \overline{\Phi}_k\right). \tag{3.35}$$

The local evaluation of losses through the sum of these two terms is a common practice in RANS simulations. In particular, Φ_m depends on the mean velocity distribution. Therefore, the numerical simulation must be able to well capture the mean velocity profile of the boundary layer, where the strong gradients of the velocity field make this term relevant. The term $\overline{\Phi}_f$, instead, is only related to the fluctuating velocity field. Thus, an exact evaluation can be obtained only by means of DNS, which provides a complete resolution of all turbulence scales. LES, as already mentioned, is able to capture only the largest flow structures, and consequently, part of the fluctuating field remains unresolved and must be modeled. In the case of RANS, instead, a direct evaluation is not feasible. To overcome this limitation, one may rely on the transport equation of turbulent kinetic energy (Eq. (3.28)). Indeed, if the turbulence is in equilibrium (i.e., the term on the left-hand side of the equation is zero) and the diffusion terms (i.e., V.D.$_k$, T.D.$_k$ and P.D.$_k$) can be neglected, it follows that the production term of turbulent kinetic energy, under such conditions, is entirely balanced by dissipation, with no significant contributions from transport or diffusion (Eq. 3.36). In other words, the energy generated by turbulent motions is immediately converted into viscous heat, making the turbulent flow energetically steady. The resulting advantage is therefore the possibility of estimating dissipation by computing the production of turbulent kinetic energy, which depends on the mean flow and the Reynolds stress tensor, i.e., on terms that can be evaluated through a RANS approach.

$$\underbrace{\left(-\overline{u'_i u'_j}\frac{\partial \overline{u}_i}{\partial x_j}\right)}_{P_k} = \underbrace{\frac{1}{\rho}\overline{\tau'_{ij}\frac{\partial u'_i}{\partial x_j}}}_{\overline{\Phi}_f}. \tag{3.36}$$

However, in real flows turbulence is rarely in equilibrium. Nevertheless, Russo et al. [85] have shown that, for a LES simulation performed on a domain such as that in Fig. 3.1, which includes the flow developing through a low-pressure turbine cascade, the cumulative contribution of the left-hand side terms of Eq. (3.36) is one order of magnitude smaller than the production and dissipation terms. Additionally, the magnitude of $\overline{\Phi}_k$ is underestimated, since the LES simulation, is not able to resolve the smallest scales. The estimation of P_k, on the other hand, is accurate since P_k is mainly related to the larger scales of turbulence, which are well resolved by LES.
Finally, the three diffusive terms are found to be two orders of magnitude smaller than the latter. Fig. 3.2 reports the cumulative contribution of the diffusive terms of equation (3.36) integrated over the eight zones that make up the domain sketched in Fig. 3.1. As

can be observed, the cumulative sum of those terms, integrated over the various regions of the domain, never deviates significantly from zero and, in any case, remains negligible in magnitude when compared with the cumulative values of P_k and $\overline{\Phi}_k$.
This discussion highlights once again why accurate modelling of the Reynolds stress tensor is essential. It affects the calculation of losses in two ways: indirectly, by providing closure for the computation of the mean flow, and directly, by appearing in the expression for P_k.

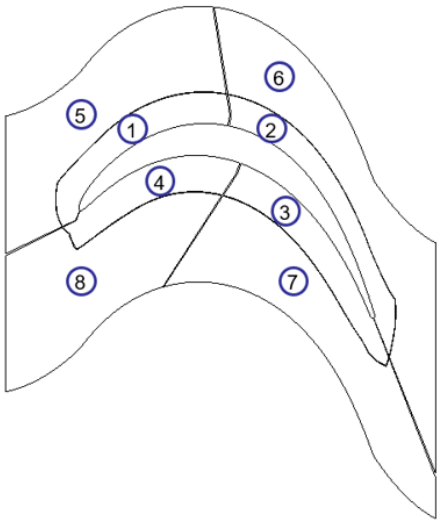

Figure 3.1: Sketch of the LES domain.

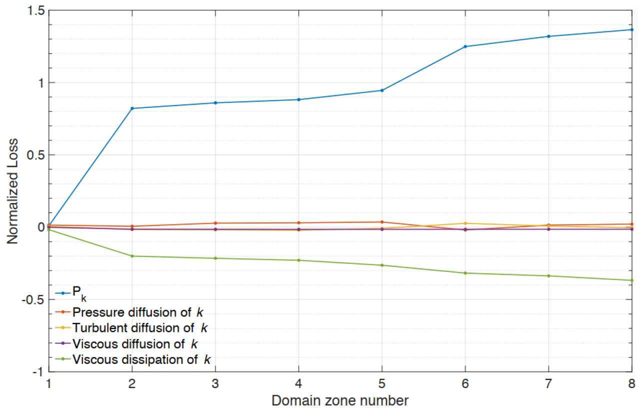

Figure 3.2: Cumulatives of the terms of Eq. 3.28 computed for each zone of the domain.

Chapter 4

Reynolds Stress Tensor Modelling

4.1 The Eddy Viscosity

As discussed in Chapter 2, the main challenge in turbulence modelling is the determination of the Reynolds stress tensor $\tau_{ij}^R = \overline{u_i' u_j'}$ in RANS equations. Although one could, in principle, attempt to write and solve the transport equations of the Reynolds stress tensor, this approach is extremely complex and inefficient, since additional terms would appear in the transport equations that require further modeling, effectively shifting the closure problem rather than resolving it. Even after achieving closure, the resulting system of highly coupled, nonlinear equations is often more computationally demanding than solving the RANS equations themselves. Early turbulence modelling therefore pursued simpler approaches, particularly for canonical shear flows.

A highly influential and widely used simplification was introduced by the French mathematician Joseph Valentin Boussinesq in *Essai sur la théorie des eaux courantes* (1877) through the eddy-viscosity concept. The underlying idea is that turbulent motions diffuse momentum in a way analogous to molecular viscosity, albeit with an additional flow-dependent turbulent viscosity. For example, in a simple shear layer, the shear stress can be expressed as:

$$\nu \frac{d\bar{u}}{dy} - \overline{u_1' u_2'} = (\nu + \nu_t) \frac{d\bar{u}}{dy}, \tag{4.1}$$

where ν_t is the turbulent viscosity, generally dependent on local flow properties. This formulation expresses the concept that turbulent diffusion is proportional to the gradient of the mean velocity, similar to the action of molecular viscosity in laminar flows.

Although this expression provides insight into the mechanism of turbulent diffusion, it does not constitute a full closure, since the unknown turbulent viscosity ν_t must still be modelled. Dimensional arguments reinforce the analogy between Reynolds stresses and viscous stresses, as can be seen by rewriting the RANS momentum equation as:

$$\frac{\partial(\overline{u}_i\overline{u}_j)}{\partial x_j} = -\frac{1}{\rho}\frac{\partial \overline{p}}{\partial x_i} + \frac{\partial}{\partial x_j}\left[\nu\left(\frac{\partial \overline{u}_i}{\partial x_j} + \frac{\partial \overline{u}_j}{\partial x_i}\right) - \tau_{ij}^R\right]. \tag{4.2}$$

This similarity suggests the generalization of the eddy-viscosity concept to all components of the Reynolds stress tensor. Hence, Eq. 4.1 can be written as:

$$-\tau_{ij}^R = \nu_t\left(\frac{\partial \overline{u}_i}{\partial x_j} + \frac{\partial \overline{u}_j}{\partial x_i}\right). \tag{4.3}$$

The term in parentheses, $\frac{\partial \overline{u}_i}{\partial x_j} + \frac{\partial \overline{u}_j}{\partial x_i}$, is the strain rate tensor S_{ij}. The Boussinesq hypothesis postulate that the Reynolds stress tensor aligns with this tensor, establishing a linear relationship between the two. However, differently from Eq. 4.1, a single function ν_t is now demanded to satisfy all components of the tensor simultaneously, so this approach inevitably introduces errors, particularly in complex shear flows.

To account for the presence of turbulent fluctuations even in the absence of mean strain, the eddy-viscosity model is augmented as:

$$-\tau_{ij}^R = \nu_t\left(\frac{\partial \overline{u}_i}{\partial x_j} + \frac{\partial \overline{u}_j}{\partial x_i}\right) - \frac{2}{3}\delta_{ij}k, \tag{4.4}$$

where k is the turbulent kinetic energy:

$$k = \frac{1}{2}\left(\overline{u_1^2} + \overline{u_2^2} + \overline{u_3^2}\right). \tag{4.5}$$

This formulation implies that, in the absence of normal straining, all normal-stress components relax toward isotropy,

$$\overline{u_1^2} = \overline{u_2^2} = \overline{u_3^2} = \frac{2}{3}k, \tag{4.6}$$

while the eddy-viscosity term accounts only for the deviatoric components of the stress tensor, i.e., the anisotropy stress tensor $a_{ij} = -\nu_t\left(\frac{\partial \overline{u}_i}{\partial x_j} + \frac{\partial \overline{u}_j}{\partial x_i}\right)$. This allows the model to incorporate, at least partially, non-local effects, such as turbulence convected from upstream regions, which are not captured by local velocity gradients. One practical example of turbulence generation in the absence of velocity gradients occurs downstream of a grid in a wind tunnel, where upstream agitation produces vortical structures and turbulent fluctuations that are then convected forward. Although turbulence intensity decreases over time due to viscous dissipation, a significant turbulent kinetic energy k remains present, justifying the augmentation of the Boussinesq model.

Despite its usefulness, the linear eddy-viscosity model has important limitations. In pure shear flows, it predicts isotropic normal stresses, which contradicts experimental observations showing significant anisotropy in jets, free shear layers, and boundary layers. Moreover, at high strain rates, the model can produce nonphysical stresses. Above all, however, eddy-viscosity model fails to account for the coupling between stress components and strain rates, by imposing an alignment between the two tensors that often does not occur in real flows.

4.2 One and Two-Equations Models

As highlighted in the previous section, the Boussinesq hypothesis does not by itself provide closure to the RANS equations. Although it introduces a major simplification by relating the Reynolds stresses to the mean strain rate, it leaves the eddy viscosity ν_t undefined. A turbulence model is therefore required to supply an appropriate expression for ν_t. The fundamental assumption of eddy-viscosity models is that ν_t can be expressed dimensionally as the product of a characteristic turbulent velocity scale and a characteristic length scale. A natural choice for the velocity scale is $\sqrt{k}$, where k is the turbulent kinetic energy. The main difficulty lies in defining a suitable turbulence length scale, since no exact transport equation exists for it. Early approaches relied on algebraic prescriptions of the length scale, which limited their applicability in complex flows where convection and diffusion of turbulence play an essential role. This motivated the development of transport-equation-based models. In one-equation models, a single additional transport equation is solved, typically for k or directly for ν_t. A well-known example about the second strategy is the Spalart–Allmaras model [5], widely adopted in external aerodynamics. However, models that directly transport ν_t are not based on a fully rigorous physical formulation and therefore risk being limited to the flow conditions for which they were originally calibrated. Similarly, models that transport k still require empirical formulations for the turbulence length scale, which restricts generality. To overcome this limitation, two-equation models were introduced. These models solve two additional transport equations: one for the turbulent kinetic energy k, and another for a variable related to the turbulence time or length scale. In the standard k–ε model, the second variable is the dissipation rate ε, representing the rate at which turbulent kinetic energy is converted into thermal energy at the smallest scales. On dimensional grounds, a turbulence length scale can be defined as $l \sim \frac{k^{3/2}}{\varepsilon}$, leading to the classical formulation $\nu_t = C_\mu \frac{k^2}{\varepsilon}$. The k–ε [6] model is robust and performs well in free-shear and fully turbulent flows, but its near-wall behaviour is less accurate and often requires wall functions. An alternative approach is provided by the k–ω model [86], in which the second transported variable is the specific dissipation rate $\omega = \varepsilon/k$. In this case, the turbulent viscosity is written as $\nu_t = \frac{k}{\omega}$. The k–ω formulation offers improved near-wall resolution and does not necessarily rely on wall functions, making it particularly suitable for boundary layer flows under adverse pressure gradients. However, it is known to be sensitive to the prescribed free-stream value of ω. The Shear Stress Transport (SST) [7] model combines the advantages of both formulations. It employs a k–ω model in the near-wall region, where its accuracy is beneficial, and gradually blends into a k–ε formulation in the outer flow, where the latter shows greater robustness.

Moreover, the SST model introduces a limiter on the turbulent shear stress, improving the prediction of separation under adverse pressure gradients. For flows characterized by strong pressure gradients and possible separation, such as those encountered in turbomachinery, the choice among k–ε, k–ω, and SST models significantly affects the accuracy of separation and transition predictions.

4.3 EARSM Models

The models introduced above are based on the Boussinesq hypothesis. Although they have been refined to increasingly complex flow conditions, they still suffer from the inherent limitation of assuming an alignment between the strain-rate tensor and the Reynolds stress tensor. This is a limiting assumption for many flow cases ([8], [9]), including separated shear layers. Thus, a more general relation is needed. Over the years, many attempts have been made to overcome this issue. Among them, in 1975 the British engineer Stephen B. Pope proposed [10] a new formulation. Let now consider the anisotropy tensor, defined as:

$$a_{ij} = \tau^R_{ij} - \frac{2k}{3}\delta_{ij} \tag{4.7}$$

In Pope's theory, the normalized anisotropy tensor, i.e., $a^*_{ij} = \frac{a_{ij}}{k}$, is expressed not only as a function of the mean strain rate tensor S_{ij}, but also of the mean rotation rate tensor $\Omega_{ij} = \frac{1}{2}(\frac{\partial U_i}{\partial x_j} - \frac{\partial U_j}{\partial x_i})$, which is anti-symmetric and its diagonal elements are zero:

$$a^*_{ij} = a^*_{ij}(S^*_{ij}, \Omega^*_{ij}) \tag{4.8}$$

In the most general expression of EARSM models, Eq. (4.8) can be formulated as a tensor polynomial expansion of the normalized strain and rotation rate tensors S^*_{ij} and Ω^*_{ij}. They are commonly made non-dimensional by the turbulent time scale $\omega^{-1} = \frac{k}{\varepsilon}$, being ε the turbulent dissipation rate ([15], [87]). The form of the tensor expansion can be defined thanks to the Cayley-Hamilton theorem which states that, for 3D flows, only ten second-order tensors and five invariants of S_{ij} and Ω_{ij} are actually independent. The problem simplifies for 2D flows, where only three second-order tensors are independent and only two invariants are nonzero:

$$\begin{cases} T^1_{ij} = S^*_{ij} \\ T^2_{ij} = S^*_{ik}\Omega^*_{kj} - \Omega^*_{ik}S^*_{kj} \\ T^3_{ij} = S^*_{ik}S^*_{ki} - \frac{1}{3}\delta_{ij}S^*_{mn}S^*_{mn} \\ I_1 = S^*_{mn}S^*_{mn} \\ I_2 = \Omega^*_{mn}\Omega^*_{mn} \end{cases} \tag{4.9}$$

Therefore, a^*_{ij} can be expressed as:

$$a^*_{ij} = \nu'_t T^1_{ij} + \nu''_t T^2_{ij} + \nu'''_t T^3_{ij} \tag{4.10}$$

where ν'_t, ν''_t and ν'''_t are apparent viscosities, formulated as polynomial expansions of the invariants of the strain and rotation tensors I_1 and I_2 (Eq. 4.11).

$$(\nu'_t, \nu''_t, \nu'''_t) = f(I_1, I_2) \tag{4.11}$$

It is emphasized that the anisotropy tensor a^*_{ij} and all the tensors T^1_{ij}, T^2_{ij} and T^3_{ij} are traceless and symmetric. The term T^1_{ij} corresponds to the non-dimensional strain rate tensor S^*_{ij}, thus it is equivalent to the Boussinesq constitutive relation. The higher order terms T^2_{ij} and T^3_{ij} are corrections to the Boussinesq hypothesis, and they act misaligning the principal axis of a^*_{ij} with respect to those of T^1_{ij} (and consequently of S_{ij}). In 2D flows, T^2_{ij} has a matrix form similar to T^1_{ij}, having opposite diagonal elements and non zero symmetric off-diagonal terms. Performing the tuning with only these two tensors would still force the resulting tensor a^*_{ij} to have opposite diagonal elements. The formulation is further decoupled through the introduction of T^3_{ij} which, conversely, has equal diagonal elements and null off-diagonal terms, hence allowing different magnitudes on the diagonal terms of a^*_{ij}. Therefore, Eq. 4.10, differently from Eq. 4.4, allows the independent tuning of the a^*_{ij} components.
In the research activities presented in this thesis, however, certain hypotheses and assumptions were made that slightly deviate from the underlying theory.

- The hypothesis $\overline{u'^2_3} = \overline{u'^2_2}$ has been made to calculate the turbulent kinetic energy $k = \frac{1}{2}(\overline{u'^2_1} + \overline{u'^2_2} + \overline{u'^2_3})$.This is needed since turbulence is 3D even if the mean flow is 2D and, at the same time, the component $\overline{u'^2_3}$ is not available from TR-PIV measurements. The motivation of this hypothesis stems from the fact that, for separation bubbles under high freestream turbulence levels, $\overline{u'^2_1}$ plays a central role due to the formation of streaky structures, while $\overline{u'^2_2}$ and $\overline{u'^2_3}$ are expected to be almost of the same magnitude (see [88], [89] and [90]). It is worth noting that this assumption concerns the definition of turbulent kinetic energy, but does not affect the mathematical rigor of Eq. 4.10 since a^*_{ij} is traceless by definition (i.e., the equation for a^*_{33} is linearly dependent on the equation for a^*_{11} and a^*_{22}). Thus, Eq. 4.10 can be only solved for $\overline{u'^2_1}$, $\overline{u'^2_2}$ and $\overline{u'_1 u'_2}$, limiting all the tensors to their 2D representation.

- The Frobenius norm of the mean velocity gradient tensor $s = \sqrt{||\Delta U||^2}$ has been used to make the strain and rotation tensors non-dimensional, in place of the dissipation frequency ω. This follows the approach presented in [91] and [92]. It has been adopted because ω (and equivalently ε) can not be evaluated with accuracy from TR-PIV data.

- The formulation of the turbulent viscosities provided by Eq. (4.11) has been generally enlarged to include not only the invariants I_1 and I_2, but also other physical-based dimensionless flow features (see [93]). The idea of deviating from the mathematical rigor of the baseline EARSM relies on the fact that these models are suitable for fully turbulent flows, while it was considered reasonable to investigate new solutions in the case of transitional flow.

With the exception of some occasional variations, described in detail in the following, the main flow features adopted in the present works are reported in Table 4.1. For clarity, here $||x||$ is the Frobenius norm of the generic quantity x. The selection of the features has been conducted following a literature review and physical considerations. The Reynolds numbers based on turbulent kinetic energy Re_k and vorticity Re_Ω have been considered, since they have been shown in the literature to be involved in the transition process ([94]). The π-groups Π_2, Π_5 and Π_6 have been defined in [23], where the authors used dimensionless features to capture the effect of the main local independent variables on the transition process. In particular, Π_2 and Π_6 represent local scales for the separated shear layer thickness, while Π_5 is used as transition sensor function in a variety of models ([70]). Π_k has been developed from a dimensional analysis on the expression of turbulent kinetic energy production in RANS-based solver, i.e., $P_k = \frac{K^2}{\varepsilon}\left(\frac{\partial U_i}{\partial x_j}\right)^2$. Two considerations led to the definition of Π_k. The first assumes that $\left(\frac{\partial U_i}{\partial x_j}\right)^2 \simeq ||S_{ij}||^2$. The second, defining $\varepsilon = \frac{k^{\frac{3}{2}}}{l_0}$, with l_0 the turbulent integral length scale, supposes l_0 of the order of y, since in a laminar separation bubble l_0 is proportional to the size of the vortices originated in the high shear region, which in turn is related to the local y-coordinate. Finally, η_1 and η_2, introduced first in [1], correspond to the normalized Q-criterion and to the turbulence intensity, respectively. Therefore, unlike what is provided by Eq. (4.11), the dependence of $\nu_t', \nu_t'', \nu_t'''$ has been formulated as:

$$(\nu_t', \nu_t'', \nu_t''') = f(I_1, I_2, flowfeatures), \tag{4.12}$$

implying that turbulent viscosities are functions of predictors composed not only of combinations of invariants but also of physical features. Then, ML techniques can be applied for model tuning to identify the leading predictors. In this work, as will be detailed in Chapters 6 and 7, the SBL algorithm was used to obtain compact and physically interpretable models.

4.4 Model Aggregation

To complete the theoretical framework related to Reynolds stress tensor modelling, this section presents the Model Aggregation (MA) technique. It enables the development

Table 4.1: Flow Features for SBL.

Feature	Definition	Description
I_1	$S^*_{mn}S^*_{mn}$	Mean strain rate tensor invariant
I_2	$\Omega^*_{mn}\Omega^*_{mn}$	Mean rotation rate tensor invariant
Re_k	$\frac{\sqrt{k}y}{\nu}$	Reynolds number based on turbulent kinetic energy
Re_Ω	$\frac{\sqrt{I_2}y^2}{\nu}$	Reynolds number based on vorticity
Π_2	$\frac{\lVert\Omega\rVert y}{\lVert U\rVert}$	Local scale for the separated shear layer thickness based on the mean rotation rate tensor
Π_5	$\frac{k}{\nu\lVert\Omega\rVert}$	Transition sensor function
Π_6	$\frac{\lVert S\rVert y}{\lVert U\rVert}$	Local scale for the separated shear layer thickness based on the mean strain rate tensor
Π_k	$\frac{\lVert S\rVert y}{\sqrt{k}}$	Non dimensional group based on turbulent kinetic energy production in RANS
η_1	$\frac{\lVert\Omega\rVert^2-\lVert S\rVert^2}{\lVert\Omega\rVert^2+\lVert S\rVert^2}$	Normalized Q-criterion
η_2	$\frac{k}{0.5U_iU_i+k}$	Turbulence intensity

of models with robust generalization properties, capable of accurately predicting flow conditions that can vary widely in nature. The idea is to assign a higher weight to the model which performs better in a single spatial point, and, consequently, a lower weight to the others. Following the Mixture-of-Experts concept proposed in [33], the ensemble solution $a^{AG}_{ij}(x)$ is obtained by aggregating the individual predictions $a^n_{ij}(x)$ provided by the N models, such that:

$$a^{AG}_{ij}(x) = \sum_{n=1}^{N} w_n(x)\, a^n_{ij}(x) \tag{4.13}$$

where $w_n(x)$ indicates the weighting function assigned to the n-th model. As already introduced in [21], [38], the weighting functions satisfy the following conditions:

$$\begin{cases} 0 \leq w_n(x) \leq 1 \quad \forall n \in \{1, \dots, N\} \\ \sum_{n=1}^{N} w_n(x) = 1 \end{cases} \tag{4.14}$$

Then, the Exponentially Weighted Average (EWA) has been computed for the prediction errors with respect to the measured anisotropy tensor components a_{ij}. In this framework, the weight assigned to the n-th model is defined as:

$$w_n(x, \sigma_w) = \frac{g_n(x, \sigma_w)}{\sum_{m=1}^{N} g_m(x, \sigma_w)} \tag{4.15}$$

where σ_w is a hyperparameter, while g_n is the gating function associated with the n-th model, given by:

$$g_n(x, \sigma_w) = \exp\left(-\frac{1}{2\sigma_w^2} \sum_{i=1}^{2} \sum_{j=1}^{2} \left(p_{ij} \left(a_{ij}^n(x) - a_{ij}(x) \right)^2 \right) \right) \tag{4.16}$$

The gating function has a Gaussian distribution with standard deviation σ_w, the hyperparameter which determines the sensitivity of the weighting function. For a fixed value of σ_w, the weight w_n tends to 1 if the n-th model significantly outperforms the others (i.e., $g_n \gg g_m$, $m \neq n$). In the opposite condition, the weight will approach 0, whereas if all the models exhibit similar performance, the weights will tend to be uniformly distributed (i.e., $w_n \approx 1/N$), regardless of their absolute accuracy. In order to use this technique for prediction, however, it is necessary to train $N-1$ models specifically for the weighting functions. Before doing so, it is first necessary to compute the weights themselves for a set of conditions used as the training set. As will be detailed in Chapter 7, in this work the MA technique was applied to aggregate two different models, reducing the number of models required for the weights to one. Following the example of [21], a library of predictors was defined in this work that includes only combinations of physical features. The SBL algorithm was then applied again for training the models.

4.5 State of Art in Modelling Separated Flows

Traditional RANS models, such as the one-equation Spalart–Allmaras [5] model and the two-equation models k–ε [6], k–ω [86] have long been the standard tools for industrial simulations of turbulent flows. As pointed out in this work, the simplification introduced by the Boussinesq hypothesis ensures robustness and computational efficiency, but it inherently limits the capability of these models to reproduce complex turbulence dynamics, particularly in non-equilibrium and highly anisotropic conditions. In attached boundary layers or mildly separated flows, baseline models can provide satisfactory predictions of mean flow quantities. However, in the presence of strong adverse pressure gradients, massive separation, or transitional behavior, these models often fail to accurately capture the onset, extent, and reattachment of the separated region. Some attempt were made during the year to improve standard models. The k-ω SST model [7] refines the standard k-ω formulation by incorporating turbulence shear stress transport, improving its applicability to separated flows. However, it is primarily suited for fully turbulent regimes. Advanced transitional models based on the k-ω SST formulation, such as the low-Reynolds number correction model (LowRe), γ-Re_θ [95], γ [96], and k-k_l-ω [97], [98], have been developed to better predict laminar separation, transition, and reattachment, with the γ-Re_θ model showing the best performance at higher Reynolds numbers and lower angles of attack [99]. This model is based on two additional transport equations, for the intermittency and for the momentum thickness Reynolds number. The second allows the definition of threshold function identifying transition onset, while intermittency acts as a blending function (0 in laminar boundary layer, 1 in turbulent flow) applied to the turbulent kinetic energy production term. Nevertheless, these models still struggle with massively separated flows, and their accuracy often remains case-dependent [100].

As a result, traditional RANS approaches often provide inaccurate pressure and velocity distributions in separated regions, compromising the prediction of lift, drag, and losses in aerodynamic and turbomachinery blade flow prediction. This motivates the growing interest in data-driven and hybrid modelling frameworks, which aim to incorporate physical insights or high-fidelity data to correct RANS deficiencies and enhance their performance in separated and transitional flow regimes.

The increasing availability of experimental and high-fidelity simulation data, combined with advances in machine learning, has opened new path for improving RANS turbulence models. In this section, an overview of the recent literature regarding the use of machine learning routines to improve turbulence modelling in separated flows is provided.

One promising approach is to revisit classical models from a data-driven perspective. For instance, the work of Jiang *et al.* [101] treats traditional eddy viscosity models as "black boxes," consisting of some transport equations where the strain rate S is the input and the eddy viscosity ν_t the output. This methodology emphasizes the importance of the second length-scale variable, particularly for separated flows, and led to the development of a new two-equation model, the k–$\sqrt{\omega}$ model. This model retains the simplicity and robustness of standard k–ε and k–ω formulations while improving predictions of separated flows, as confirmed by tests on an asymmetric diffuser and a NACA 4412 airfoil. Fig. 4.1 shows that, unlike the baseline models, the k–$\sqrt{\omega}$ model is able to correctly reproduce the separation occurring near the trailing edge of the airfoil.

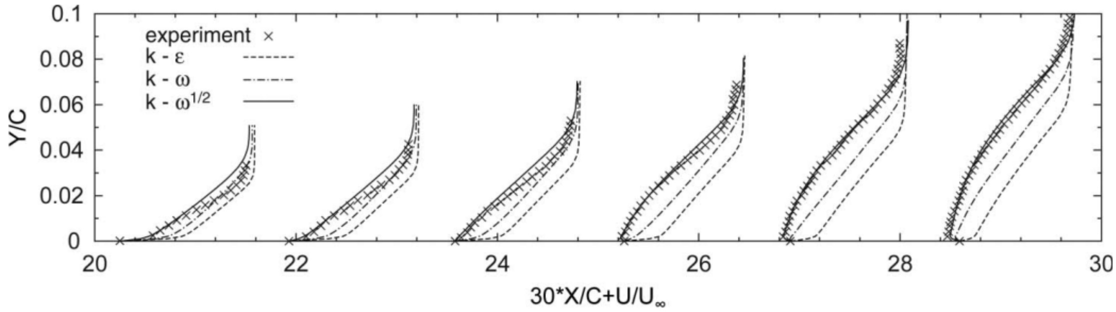

Figure 4.1: Profiles of tangential velocity component at various positions along the airfoil surface ($x/c = 0.675, 0.731, 0.786, 0.842, 0.897, 0.953$) [101].

Several studies applied the Field Inversion and Machine Learning (FIML) framework to enhance the predictive capability of the *S&A* [5] turbulence model for separated and transitional flows. Field Inversion is a technique used to infer spatially varying corrective terms for a baseline RANS model by solving an inverse problem. Given experimental or high-fidelity data, such as lift or surface pressure, field inversion adjusts model terms, typically as multipliers of production, dissipation, or transport terms in eddy-viscosity models, so that the simulated outputs match the observed data. Singh *et al.* [102] developed a data-driven framework combining full-field inversion and machine learning to infer and reconstruct model discrepancies from experimental lift data. This approach was applied to separated airfoil flows, improving predictions of lift, drag, and stall onset while maintaining accuracy in attached-flow regions. Yan *et al.* [103] extended this methodology to several separated flow cases, including the S809 airfoil, a periodic hill, and the GLC305 airfoil with ice accretion, demonstrating that the augmented model can reproduce key flow quantities with high accuracy and generalization capability, while remaining consistent with the physics of nonequilibrium turbulence. An improved prediction of the velocity profiles in the case of the periodic hill configuration can be observed in Fig. 4.2.

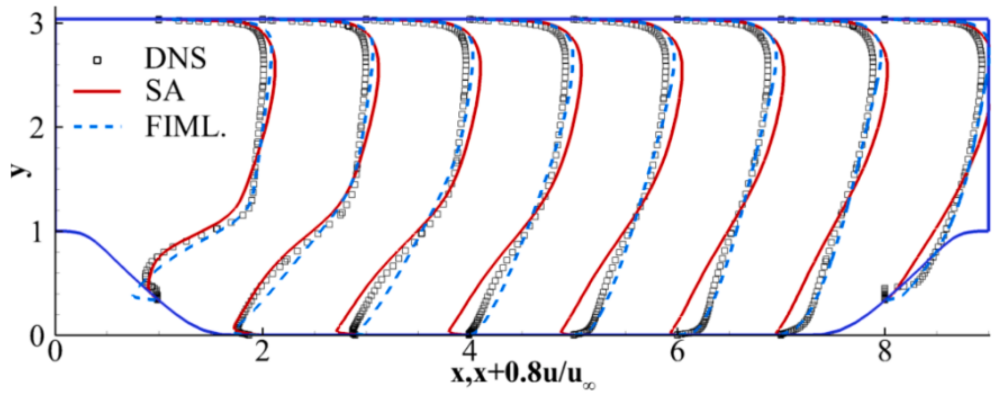

Figure 4.2: Computed velocity profiles in the case of periodic hill geometry at different locations (Re = 10595) [103].

A complementary approach has been proposed by Shan *et al.* [104] combining data assimilation (DA) and deep neural networks (DNNs) to improve the accuracy of traditional models in the case of separated flows over an airfoil. DA integrates experimental data with numerical models to optimize turbulence parameters, while DNNs are trained on high-fidelity data to directly predict eddy viscosity. Focusing on turbomachinery applications, Ferrero *et al.* [105] applied the FIML framework to low-pressure turbine cascades, including the T106c and T2 geometries. In these transitional and separated flows, field inversion was used to locally correct the production term, and an Artificial Neural Network (ANN) generalized the corrections. The resulting ANN-augmented model improved predictions of wall isentropic Mach number distributions (see Fig. 4.3), exit flow angles, and kinetic energy losses, while preserving robustness and avoiding overfitting.

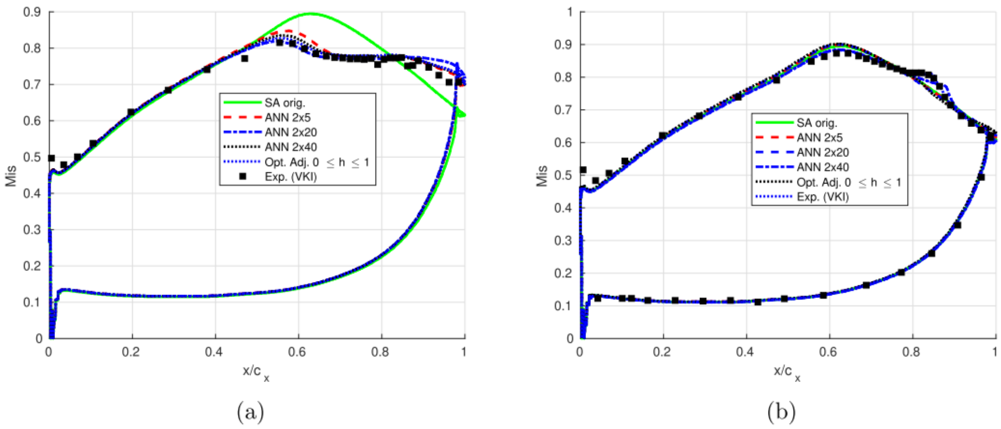

Figure 4.3: Comparison of different ANN architectures in terms of wall isentropic Mach number distribution on the T106c at $Re_{2s} = 810^4$(a) and $Re_{2s} = 2.510^5$(b) [105].

Other examples of the application of DA and FIML to separated flows can be also found in Volpiani *et al.* [106].
Field inversion, combined with an ensemble of Gaussian Process Emulators (GPEs), has also been used by Ho *et al.* [107] to augment the k–ω SST turbulence model, improving predictions for separated flows and enhancing the generalization of learned corrections. The GPE ensemble handles heterogeneous datasets and quantifies model uncertainty, improving turbulent kinetic energy and separation predictions while reverting to the baseline in regions outside the training data. Its probabilistic formulation identifies areas of extrapolation and uncertainty, preventing overconfident or erroneous model activation and supporting reliable data-driven turbulence modelling. A convolutional machine learning model based on convolutional layers was developed by Choi *et al.* [108] to predict velocity fields in backward-facing step (BFS) flows with varying step angles. The model was trained on three-dimensional large-eddy simulation data for step angles of 20° and 30°, using a loss function that combines mean-squared error with a boundary loss to enforce velocity constraints at walls and step surfaces. An ANN captures the spatial correlations in the flow and reconstructs the velocity and turbulence intensity fields for unseen step angles case (15°, 25°, and 45°) that did not participate to the training. Validation against experimental data showed good agreement for velocity profiles, turbulence intensity, and reattachment lengths, with only slight delays in the reattachment position. The ML approach demonstrated strong generalization across different step angles and shows potential for extension to varying Reynolds numbers, geometries, and reduced-order input strategies to further improve predictive efficiency. An other example which demonstrate the potential of data-driven surrogate turbulence models for the case of the BFS is provided by Wu *et al.* [109]. In this work, to enhance the efficiency and accuracy of RANS simulations, five machine learning (ML) algorithms, i.e., Random Forests, eXtreme Gradient Boosting (XGB), K-Nearest Neighbours (KNN), Support Vector Machine, and ANN, were employed to construct surrogate models of the *S&A* turbulence model. These models establish a nonlinear mapping between the mean flow field and the steady-state eddy viscosity. All ML-based surrogates effectively capture the complex relationship between flow features and eddy viscosity, achieving good predictive accuracy while significantly reducing computational cost. Among the tested algorithms, XGB, KNN, and ANN showed the best trade-off between accuracy, memory usage, and computational time, demonstrating the potential of data-driven surrogate turbulence models for accelerating industrial-scale CFD simulations. The modelling of separated flows has also been addressed through Gene Expression Programming (GEP), as done by Weatheritt and Sandberg [110]. In this work, a novel approach is presented using GEP for tensor regression, leveraging high-fidelity data and uncertainty measures to generate constraint-free, non-linear models of the turbulent stress tensor aimed at improving separated flow predictions. The resulting models are effective as a posteriori predictive tools even on flows different from the training data, demonstrating the potential of evolutionary, data-driven

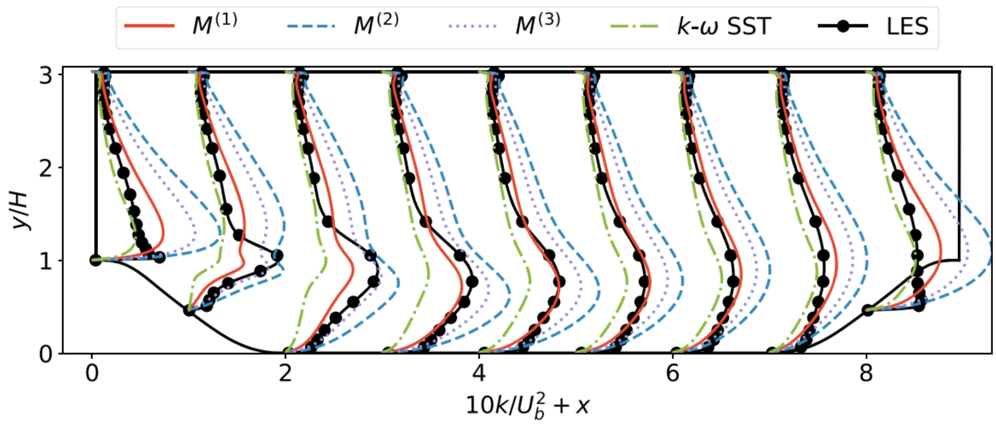

Figure 4.4: TKE profiles for the periodic hill configuration [20].

methods to discover functional forms without imposing prior assumptions. This proof-of-concept highlights the flexibility of GEP for future turbulence model development, particularly for complex flow regimes. Other examples of GEP applied to separated flows can be found in Fang *et al.* [24], [111].

Promising developments in modelling separated flows also come from EARSM (Explicit Algebraic Reynolds Stress Models). For example, Schmelzer *et al.* [112] applied the SpaRTA (Sparse Regression of Turbulent Stress Anisotropy) framework, which introduces a deterministic symbolic regression approach to infer algebraic stress models directly from LES or DNS data. Using elastic-net regularization, the method identifies sparse, data-driven corrections to the k–ω SST model, particularly effective in capturing separated flows such as periodic hills, converging-diverging channels, and curved backward-facing steps. Fig. 4.4, for example, shows the improvements in terms of TKE profiles obtained by the models $M^{(1)}$, $M^{(2)}$, and $M^{(3)}$, which correspond to EARSM models defined with a decreasing number of predictors, compared to the baseline k–ω SST for the periodic hill case. The discovered models significantly improve RANS predictions, even for higher Reynolds numbers, demonstrating SpaRTA's ability to rapidly derive robust corrections for separated-flow regimes without requiring inversion procedures. Building on the deterministic SpaRTA framework Cherroud *et al.* [21] advances in modelling separated flows have been achieved through Sparse Bayesian Learning (SBL) for stochastic EARSM closures. SBL-SpaRTA represents corrections to the k-ω SST model as sparse, physically interpretable tensor polynomials learned from high-fidelity data, with assigned posterior probability distributions to quantify uncertainty of the coefficients. Applied to 2D separated flows, the method improved predictions of velocity and skin friction over baseline models, and the uncertainty estimates highlighted regions of lower model reliability. In [54], the SBL algorithm is employed to calibrate two EARSM models specifically tailored for the prediction of long and short separation bubbles, respectively. The dataset was acquired through PIV measurements over a flat plate (see Sec. 5.1 and Sec. 7.2). This work investigates the inclusion of physically meaningful flow features among the predictors used to model the turbulent viscosities, demonstrating promising improvements in predictive performance. In Frey Marioni *et al.* [113] the use of DNS data and machine learning to improve RANS turbulence models is investigated. High-fidelity DNS were generated for a turbulent channel flow and a stationary serpentine passage, and neural networks were trained to develop alternative Reynolds stress anisotropy formulations, replacing the standard Boussinesq approximation. Clustering of flow features was applied to focus the tuning process on selected regions. The resulting models were implemented in the Rolls-Royce HYDRA solver, showing significant improvements in velocity profiles, wall shear stress, and separation bubble predictions compared to baseline k–ω SST, with velocity discrepancies reduced by up to 88%. In Frey Marioni *et al.* [114], instead, a DNS–Machine Learning framework was developed to improve turbulence closures for low-pressure turbine (LPT) profiles in RANS simulations. EARSM models were trained with shallow neural networks on DNS data, separately for low and high Reynolds numbers, and then merged into a single blended model. The approach was tested on multiple computational domains, including the full airfoil and transitional regions, and implemented in the HYDRA solver. The data-driven closures improved velocity profiles, TKE production, and mixing losses compared to the baseline k–ω SST, with discrepancies reduced by over 60% and an increase of about 1% in overall turbine efficiency.

Chapter 5

Datasets available for model tuning

From the previous Chapters it has become clear the importance of an accurate modelling of transition in the case of separated flows, which, due to their nonlinear nature and sensitivity to external conditions, represents one of the most challenging configurations to be reproduced. It has also been highlighted that the increasing availability of both numerical and experimental data, together with the growing variety of advanced machine learning models, represents a turning point for research in this field. This Chapter is dedicated to the description of the datasets employed in this work for the calibration of turbulence and transition models. In particular, Sec. 5.1 provides an extensive discussion of the dataset most widely used throughout the study, namely an experimental dataset of separation bubbles developing on a flat plate with adverse pressure gradients. Secs. 5.2 and 5.3, on the other hand, are dedicated to two additional numerical datasets: a LES dataset of geometry-induced separation bubbles over a flat plate and a DNS dataset of bubbles developing on the suction side of a compressor blade.

5.1 Laminar Separation Bubble Experimental Dataset (EXP-FP)

5.1.1 Test Facility

To analyze the transition and separation processes of the boundary layer under different combinations of freestream Reynolds number, turbulence intensity (Tu), and adverse pressure gradient (AP), a flat plate test section was designed and installed at the Laboratory of Aerodynamics and Turbomachinery of the University of Genova. The variable area opening section allows for investigation of the effects induced by different AP. Its core consists of a thick flat plate, which, due to the simplified geometry, facilitates a detailed characterization of the development of the boundary layer. The setup supports both intrusive and non-intrusive instrumentation for thorough analysis of the transition process.

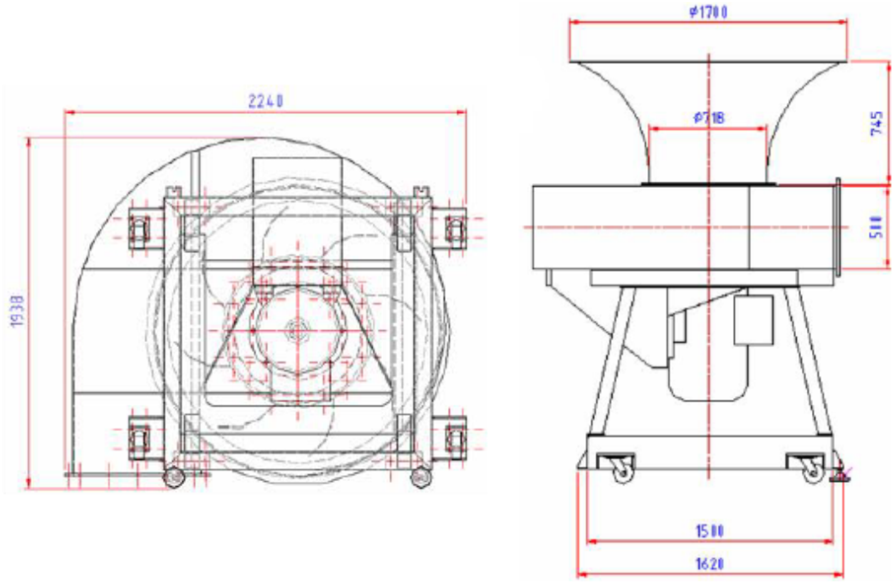

Figure 5.1: Drawing of the fan installed in the wind tunnel.

The wind tunnel is an open-circuit, low-speed facility. Airflow is driven by a 55 kW centrifugal fan powered by an asynchronous three-phase electric motor, whose speed is controlled via an inverter with 0.01 Hz resolution. Adjusting the inverter frequency allows precise control of the fan rotation, and thus the flow velocity and Reynolds number inside the tunnel. A bell mouth located above the fan (see Fig. 5.1) includes a filter to prevent dust and impurities from entering the tunnel, which could otherwise affect optical measurements by generating bright reflections on the test section walls.

Between the fan and the test section, a settling chamber is installed to control the flow uniformity and reduce uncontrolled fluctuating events produced by the fan (see Fig. 5.2). The chamber contains five metal screens and a honeycomb. The screens, made of thin metal mesh, reduce both large- and small-scale turbulent structures, while the honeycomb, composed of small hexagonal cells, aligns the flow axially, further reducing the turbulence level.

A converging duct connects the settling chamber to the test section. With a length of 420 mm and an area ratio of 2.77, it accelerates the flow. This acceleration also reduces the thickness of the sidewall boundary layers. Additionally, a continuous suction slot upstream of the test section removes part of the boundary layer developing on the sidewalls. Turbulence-generating grids can be positioned at the inlet of the test section to impose a controlled turbulence level and decay rate, as illustrated in Figs. 5.2 and 5.3. Turbulence intensity is a key parameter influencing boundary layer development and transition.

The grids, manufactured by laser cutting from steel sheets, are composed of rectangular bars arranged to form a mesh, as shown in Fig. 5.4. All grids used to generate the

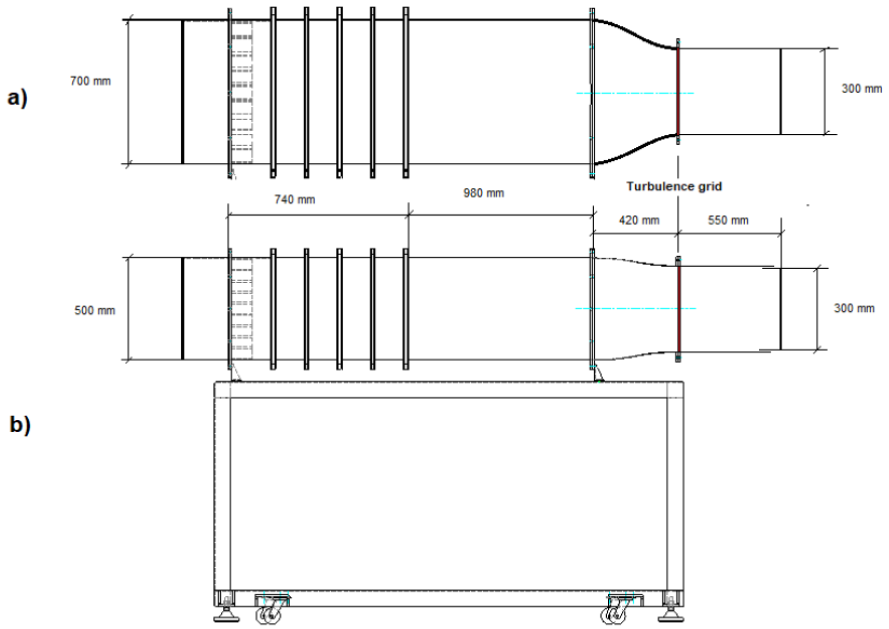

Figure 5.2: Settling chamber: (a) top view, (b) side view of the settling chamber and the convergent section of the wind tunnel. The location of turbulence generating grids is highlighted in the figure.

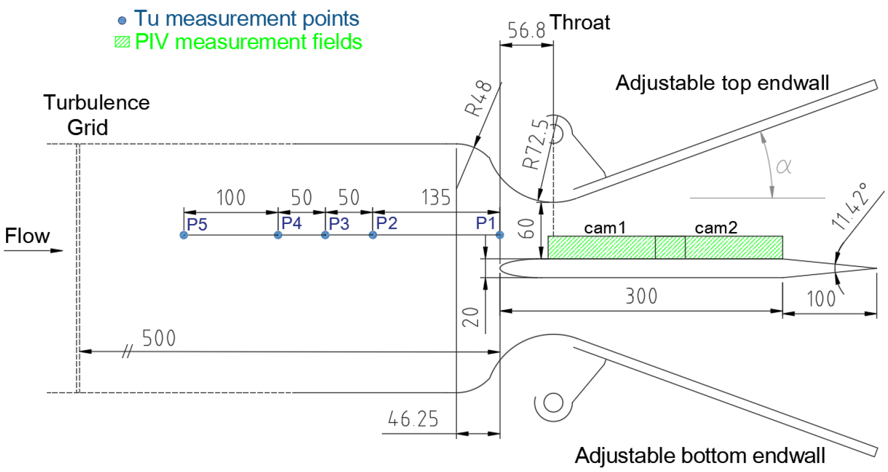

Figure 5.3: Sketch of the flat-plate test section with main dimensions quoted in mm.

present dataset share the same overall dimension. The grids are rigidly fixed to suppress vibrations that could otherwise affect the turbulence levels. Their geometry is mainly characterized by the porosity factor, defined as

$$\beta = \left(1 - \frac{s}{m}\right)^2, \tag{5.1}$$

which represents the ratio between the open surface and the total mesh area. Three configurations were adopted: the no-grid case (NG), the low-turbulence condition (LTU) and the high-turbulence condition (HTU). The corresponding porosity values and turbulence intensities, along with further details of the turbulence grids such as the bar and the mesh size (s, m) and the streamwise integral lenghtscale L_x are summarized in Tab. 5.1. In particular, L_x was computed by means of the autocorrelation function of Hot-Wire (HW) data involving the Taylor's hypothesis of frozen turbulence.

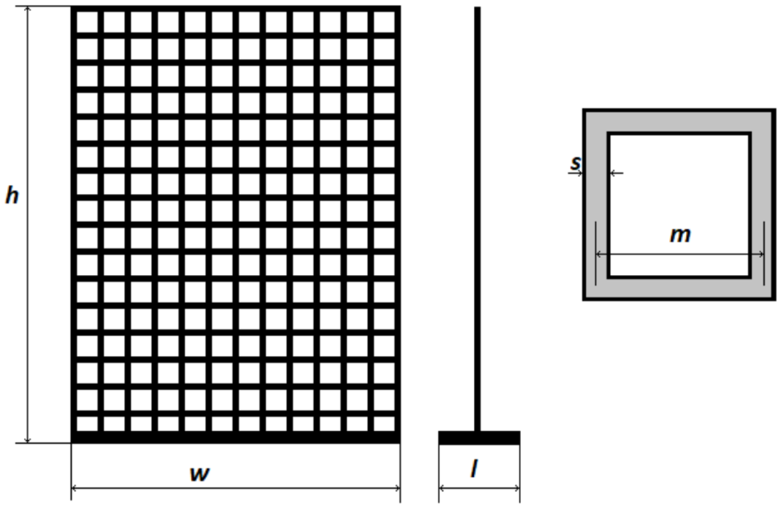

Figure 5.4: Scheme of the turbulence generating grids installed in the test section.

Table 5.1: Details about the turbulence grids.

Tu [-]	Grid Size [mm]	β	L_x [mm]
1.5% (P1)	no grid	-	6.2 (P1)
2.5% (P1)	s=2, m=8	0.56	11.5 (P1)
3.5% (P1)	s=4, m=8	0.25	13.2 (P1)

Fig. 5.3 provides a schematic view of the test section, which consists of the flat plate installed in a variable area opening endwall channel. In particular, the flat plate is 300 mm long and 300 mm wide, ensuring 2D time-mean flow at mid-span. A 3:1 elliptic leading

edge has been adopted to mitigate possible occurrence of leading-edge separation that may introduce uncontrolled wave packets into the flat plate boundary layer, thus altering the transition process. With the aim of studying the combined effects of *Re* and *Tu* for different AP, the test section is equipped with moving endwalls, allowing the acquisition of a large number of flow conditions with a wide and independent variation of the flow parameters. Moreover, the adjustable endwalls can be set in non-symmetric positions to control the incidence angle on the leading edge of the flat plate, preventing the occurrence of BL separation on the top endwall of the test section. The setting and control of the proper angle of attack for the different conditions is monitored by several pressure taps (17) on the top and the bottom sides of the leading edge. In the straight part of the plate, 51 pressure taps have been installed to provide the characterization of the pressure gradient imposed by the different endwall settings. The pressure taps are connected to the acquisition system by means of a scannivalve, which allows the acquisition of the signals coming from all the pressure taps with a reduced number of pressure transducers.
Downstream of the test section, air is expelled from the laboratory, with a valve on the exit duct allowing adjustment of the downstream pressure.

The facility is also equipped with optical accesses allowing measurements with Particle Image Velocimetry (PIV) and Laser Doppler Velocimetry (LDV). Moreover, to better visualize the position of the bubbles inside the facility, Fig. 5.5 shows an exemplary distribution of the streamwise velocity, highlighting the bubble size and position (i.e., by the blue area in the plot).

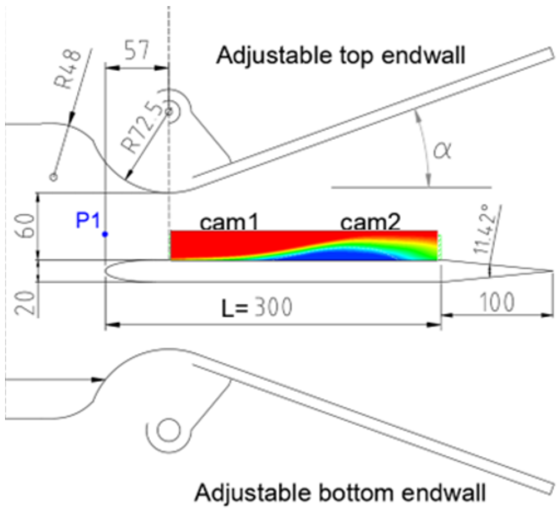

Figure 5.5: Example of location of the bubbles on the flat plate

5.1.2 Particle Image Velocimetry

Particle Image Velocimetry (PIV) is a non-intrusive optical technique that allows the reconstruction of a two-dimensional velocity vector field in a single acquisition, providing an accurate description of the flow and its fluctuations [115].

A typical PIV system consists of:

- a high-power pulsed laser,
- a CCD camera,
- a synchronizer,
- a data processing unit.

The operating principle relies on a pulsed light source which, through an optical system, generates a thin light sheet to illuminate a cross-section of the seeded flow. Short light pulses are essential to "freeze" the particle images and prevent streaking, which makes pulsed lasers the natural choice for PIV. The most common sources are Nd:YAG lasers, emitting infrared radiation at 1064 nm; in PIV applications the wavelength is halved to 532 nm, producing visible green light. To ensure powerful pulses and a wide range of time separations, dual-cavity lasers are employed. These are housed in a single module together with the optical components required for light sheet generation (see Fig. 5.6). Its geometry (thickness and spreading angle) is controlled by a combination of cylindrical and spherical lenses: the first expands the beam into a sheet, while the following ones regulate its thickness and divergence.

The camera, mounted perpendicularly to the light sheet, records the entire flow field. A synchronizer coordinates the timing between laser pulses and the camera acquisition sequence so that each frame is properly exposed. Modern cross-correlation cameras, based on high-performance CCD sensors, immediately convert the captured light into digital signals stored in the internal memory. The first laser pulse generates the first frame, which is transferred to storage, while the second pulse produces the second frame containing the updated particle positions. For data processing, the images are divided into interrogation regions (usually square, as shown in Fig. 5.7), which may partially overlap to improve spatial resolution. Each region of the first image is compared with its counterpart in the second one, and the mean particle displacement is determined by cross-correlation. In general, the cross-correlation function Φ is defined as

$$\Phi = \int f_1(x + \Delta x) \, f_2(x) \, dx, \tag{5.2}$$

where f_1 and f_2 are the image intensity functions at times t and $t + \Delta t$, respectively. In its discrete formulation, more suitable for digital processing, the cross-correlation can be expressed as

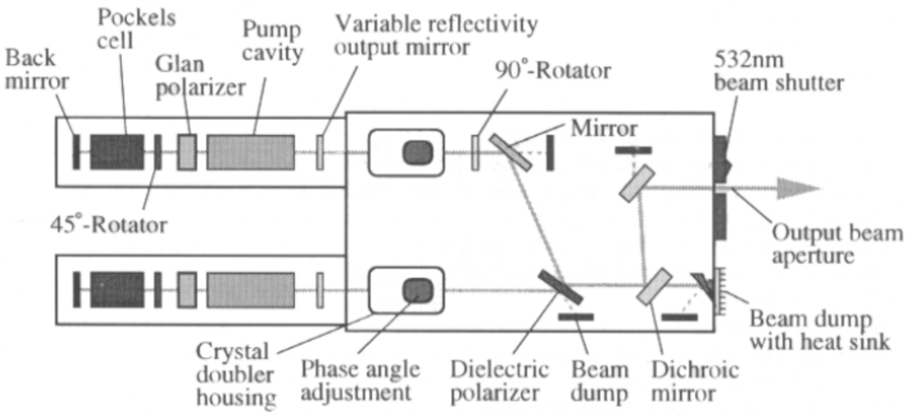

Figure 5.6: Typical components of a dual-laser single module used in PIV setups.

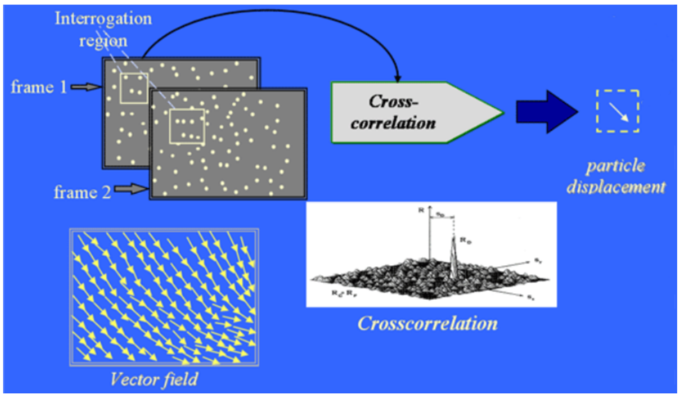

Figure 5.7: Functional scheme of a Particle Image Velocimetry system.

$$\Phi = \sum_m \sum_n f_1(m+i, n+j)\, f_2(m,n). \tag{5.3}$$

The peak of the function Φ provides the most probable displacement $\Delta x = (\delta i, \delta j)$, which is then converted into velocity by applying the scaling factor between pixel coordinates and the real dimensions of the flow field. This factor is determined using a calibration target installed inside the test section. The computed vectors are finally validated: outliers in terms of magnitude and direction are filtered out and usually replaced by a moving average estimation, ensuring continuity of the velocity field.

In the present dataset, a fast-response DANTEC time-resolved PIV system was used, consisting of a dual-cavity Nd:YLF pulsed laser (Litron LDY 300, 30 mJ per pulse, 1000 Hz, 527 nm) and a high-sensitivity SpeedSense M340 digital camera (2560 $\times$ 1600 pixels, cooled sensor). The optical system generates a 1 mm thick light sheet, while vaseline oil droplets were used as seeding particles.

The seeding system is essential for non-intrusive optical measurements, as it introduces tracer particles into the wind tunnel flow, making the phenomena in the test section visible.

In this study, vaseline oil droplets with a mean diameter of $1.5\,\mu$m were used, as their low density reduces inertial effects and allows them to rapidly follow flow variations.

5.1.3 Test Conditions

The overall database includes 87 flow cases acquired for different combinations of Reynolds numbers, freestream turbulence levels and pressure gradients. Specifically, it accounts for about 10 Reynolds numbers for every combination of the three different freestream turbulence levels and the three tailboard opening angles. The Reynolds number ($Re_L = \frac{U_{e,1}L}{\nu}$, where $U_{e,1}$ is the freestream velocity in correspondence of the plate leading edge, i.e. at point P1 in Fig. 5.3, and ν the kinematic viscosity) has been varied from $Re \approx 15k$ to $Re \approx 80k$. Three turbulence levels ($Tu = \frac{u_{rms}}{U_{e,1}}$ = 1.5%, 2.5% and 3.5% evaluated at point P1), obtained without the grid and with two different turbulence grids characterized by different bar width have been tested. The opening angle has been fixed to 7°, 9° and 12°. Different opening angles impose a mean diffusion over the plate that can be quantified by values of $AP = \frac{L}{U_{e,o}}\frac{\Delta U_e}{\Delta x} = -0.18, -0.27$ and -0.41, which refers to the free-stream velocity at the throat of the channel $U_{e,o}$ and the mean velocity gradient between the throat and the end of the plate $\frac{\Delta U_e}{\Delta x}$. To provide comparison with the typical parameter adopted in turbomachinery applications, these values of AP can be translated into the diffusion rate $Ds' = (\frac{U_{e,0}}{U_2})/(\frac{\Delta x_{decel}}{L})$, where U_2 is the freestream velocity at the end of the plate and Δx_{decel} the length of the decelerating portion of the plate. In particular, the three values of AP correspond to $Ds' = 0.25, 0.40$ and 0.60, respectively, that are typical values of front, mid and aft loaded turbine blades.

Table 5.2 reports the entire test matrix, with the values of the Re_L tested for the different combinations of AP and Tu. The table also indicates which bubbles can be considered of the long type and which are short, according to the classification method provided in [61].

5.1.4 Incoming Flow and Edge Velocity Characterization

In order to characterize the turbulent field at the entrance of the test section for proper initialization of CFD simulations, Hot wire (HW) measurements have been performed in different spatial positions (points from P1 to P5 in Fig. 5.3). This allowed the evaluation of inlet turbulence intensity and decay rate. For this purpose, a Dantec single-sensor probe (type 55P14) has been adopted in the constant temperature mode. The signal has been sampled at 10 kHz, collecting $1.2 \cdot 10^6$ points with a DAQ-NI acquisition board. The left panel of Fig. 5.8 reports the turbulence decay observed for the cases at Tu=1.5%, Tu=2.5% and Tu=3.5% for two Reynolds numbers (Re_L=140k and 220k). In particular,

Table 5.2: A list of all the tested conditions. The **bold** Re_L values correspond to long bubbles, the others to short bubbles.

AP	-0.18	-0.18	-0.18	-0.27	-0.27	-0.27	-0.41	-0.41	-0.41
Tu	1.5%	2.5%	3.5%	1.5%	2.5%	3.5%	1.5%	2.5%	3.5%
Re_L	29600	28800	24800	**13400**	**16100**	**15400**	**15800**	**14800**	**10600**
Re_L	34700	33200	27500	**22700**	**20700**	**16800**	**22200**	**17100**	**14300**
Re_L	39100	38100	33700	**24300**	**23800**	**22800**	**26300**	**22200**	**17200**
Re_L	41000	43100	36700	**31800**	**28200**	**25200**	**32900**	**25900**	**29500**
Re_L	49000	45400	41000	**40300**	32600	**29200**	**42800**	**30700**	38400
Re_L	53300	50900	49900	**50600**	37500	35100	**54400**	**34600**	56700
Re_L	71500	56800	53200	**62200**	42100	40500	**59800**	**38500**	61800
Re_L	76500	63600	56100	64600	47200	45000	64700	44000	65800
Re_L	-	68800	57000	72800	52200	51400	71600	52000	-
Re_L	-	75100	66500	75600	57400	52700	78400	63300	-
Re_L	-	-	71600	-	-	-	-	-	-

data are available from P1 to P5 for the cases with the turbulence grid installed (Tu=2.5% and Tu=3.5%), and in P1 and P2 for the case without the grid (Tu=1.5%). Re_L is higher with respect to the PIV measurements to minimize the uncertainty in the Tu evaluation, since the effect of this parameter will be shown to be small. For the cases with the grid, the turbulence decay follows a power law with $(x/M)^{-5/7}$ according to [116], and tends to 2.5% and 3.5% in correspondence of the plate leading edge. For the case without the grid, the Tu is instead almost constant with a value close to 1.5%. The Reynolds number exhibits a minor effect on the Tu decay. In particular, lower values of the Reynolds number lead to a slightly stronger Tu decay, especially for the case at $Tu = 3.5\%$. Moreover, being in line with the Roach's trend [116], the Tu at point P1 does not seem to be affected by local flow acceleration due to the convergent section, which is instead expected to have an impact further downstream.

On the other hand, to specify the effects induced by the different opening angles, the right panel of Fig. 5.8 shows the distributions of the free-stream velocity along the plate for the three opening angles. The curves are provided by PIV data at the highest Re_L number tested ($Re_L \approx 80k$), which is the one where blockage effects due to the laminar separation bubble forming on the plate are minimized. The channel throat here is at $x/L \approx 0.19$. Downstream of the throat the flow deceleration is almost linear and proportional to the tailboard opening angle, with a slight bump due to the very small separation bubble, which slightly increases at higher opening angles. The values previously quoted for the $AP = -0.18, -0.27$ and -0.41 are based on these distributions.

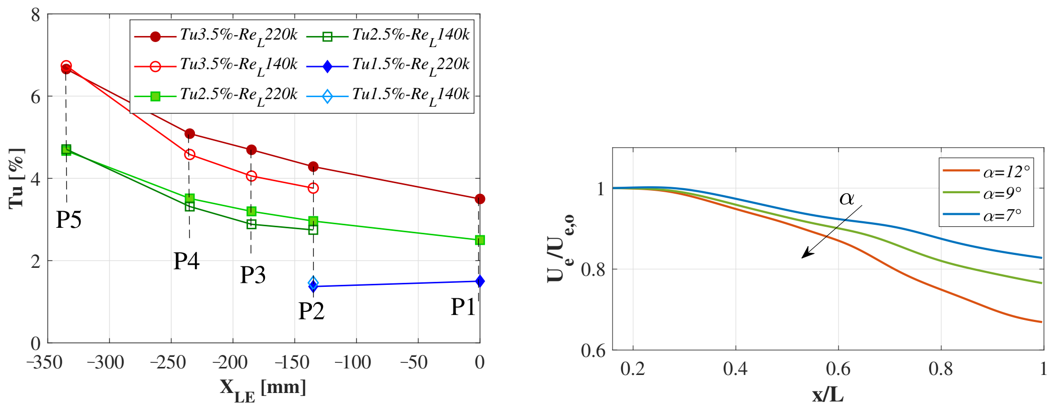

Figure 5.8: Inlet turbulence decay for the cases at Tu=1.5%, Tu=2.5% and Tu=3.5% (on the left) and freestream velocity distributions for the 7°, 9° and 12° cases (on the right).

5.1.5 Time-mean velocity

With the aim of showing the influence of the flow parameter variation on the behavior of the laminar separation bubble, a set of 18 flow conditions among the overall database have been reported here. They accounts for 6 almost equally-spaced Reynolds numbers for the following Tu and AP combinations: $Tu = 1.5\%$ and $AP = -0.41$, $Tu = 3.5\%$ and $AP = -0.41$, and $Tu = 1.5\%$ and $AP = -0.18$. The time-mean streamwise velocity distributions for these flow conditions are shown in Figs. 5.9, 5.10 and 5.11, respectively. All the distributions have been normalized by the corresponding free-stream velocity $U_e(x/L)$, evaluated at the top of the experimental domain. The white line evidences the isoline at $U/U_e = 0$ that includes the reverse flow region, highlighting the extension of the bubble from the separation point to the reattachment position. The isoline has not been reported for those conditions where the image resolution did not allow to distinguish a clear separated flow region.

Fig. 5.9 shows the Reynolds number effect at the lowest turbulence level and highest adverse pressure gradient. It can be readily observed that the bubble size increases as the Reynolds number decreases. Particularly, the Reynolds number variation has a low effect on the separation position (about $x/L \approx 0.45$), while it evidently influences the reattachment position, clearly shifted downstream as Re_L decreases. A criterion to identify the bursting process for the present bubble distributions has been provided by [61]. Here, bursting occurs at $Re_L \approx 50k$ (between the third and the fourth plots of the figure) where a change in the bubble growth rate can be observed. The Reynolds number variation shows similar effects also at higher Tu levels (Fig. 5.10) and lower AP (Fig. 5.11). In Fig. 5.10 the bursting process occurs at $Re_L \approx 30k$, while it is not observed in Fig. 5.11 due to the significantly smaller pressure gradient. Thus, at AP=−0.18 all separation bubbles are of

the short type.
The comparison between Fig. 5.9 and 5.10 provides the effect of the Tu variation on the bubble size. An increase of the freestream turbulent intensity results in smaller bubble extension. This is clear looking at the most similar Reynolds numbers acquired for these two flow cases, like for the second and the fourth plots in the figures. In particular, the turbulent reattachment shifts upstream at high Tu level due to an earlier transition process induced by higher freestream disturbances which are amplified in the separated shear layer (see [80] for instance).
The effect of the AP variation can instead be seen by comparing Fig. 5.9 and Fig. 5.11. For less aggressive adverse pressure gradients the bubble dimensions are strongly reduced. Moreover, the position of the bubble is clearly shifted downstream due to the different channel diffusion, with separation point at $x/L \approx= 0.7$. At high Re_L and small AP (Fig. 5.11, last plot), the transition process shifts toward the bypass type, with the laminar separation bubble that practically disappears.

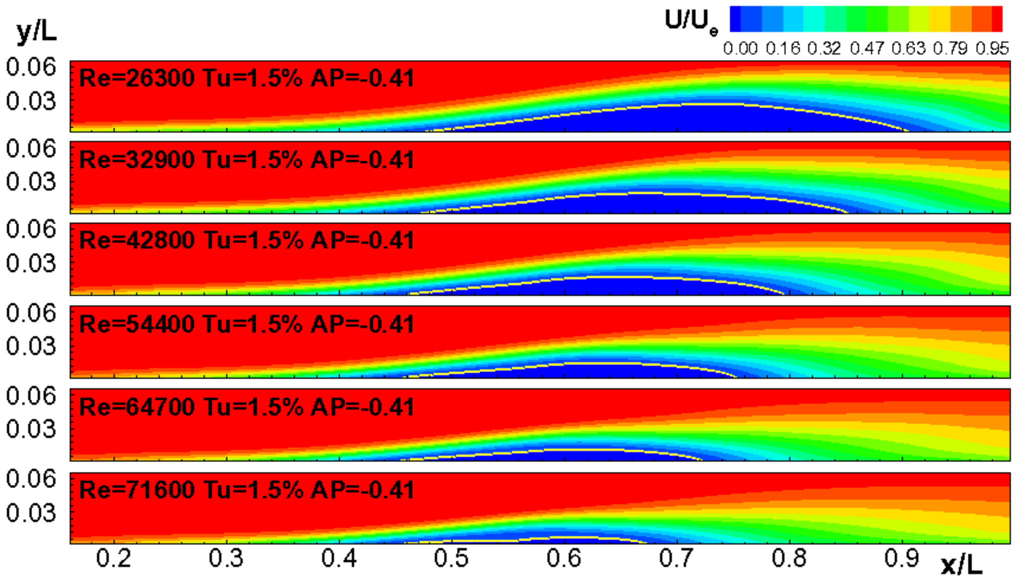

Figure 5.9: Normalized time-mean streamwise velocity (U/U_e) for different Reynolds numbers at fixed $Tu = 1.5\%$ and $AP = -0.41$. The white curve corresponds to the isoline U/U_e=0.

5.1.6 Reynolds Stress Tensor Components

The streamwise, wall-normal and shear components of the Reynolds stress tensor:

$$\tau_{ij} = \overline{u_i' u_j'} \tag{5.4}$$

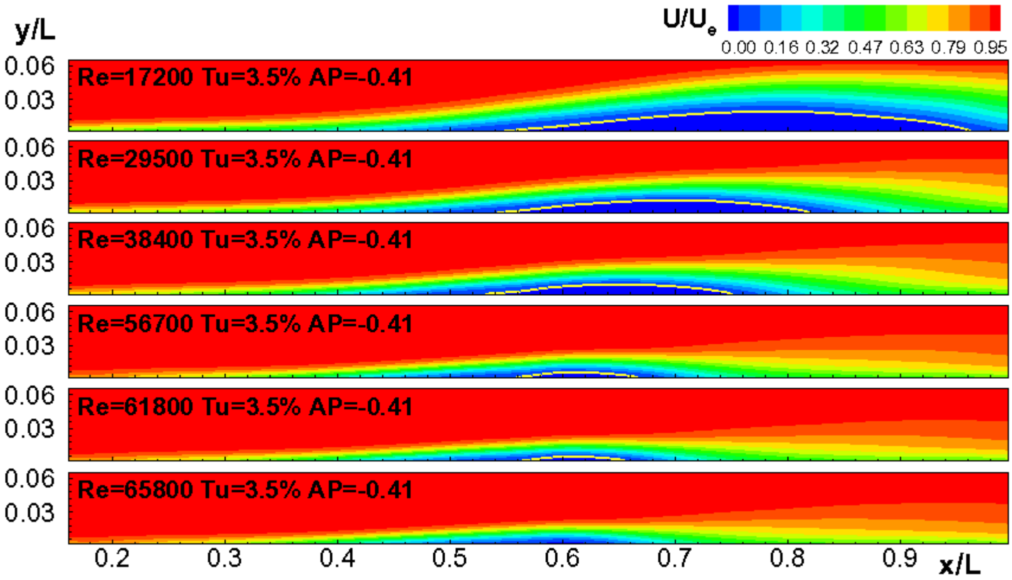

Figure 5.10: Normalized time-mean streamwise velocity (U/U_e) for different Reynolds numbers at fixed $Tu = 3.5\%$ and $AP = -0.41$.The white curve corresponds to the isoline U/U_e=0.

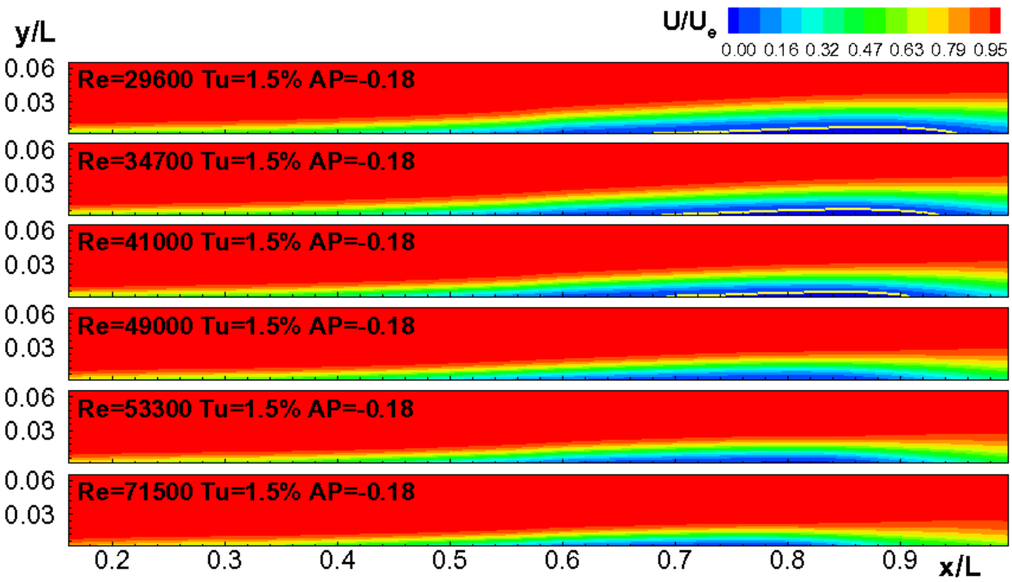

Figure 5.11: Normalized time-mean streamwise velocity (U/U_e) for different Reynolds numbers at fixed $Tu = 1.5\%$ and $AP = -0.18$.The white curve corresponds to the isoline U/U_e=0.

being u'_i and u'_j the ith and jth fluctuating velocity component, have been computed from PIV data. Their distributions are shown in Figs. 5.12, 5.13 and 5.14 for the flow cases previously presented. For each figure, 6 conditions with varying Reynolds numbers are shown, while the values of Tu and AP are constant at $Tu = 1.5\%$ and $AP = -0.41$ in Fig. 5.12, $Tu = 3.5\%$ and $AP = -0.41$ in Fig. 5.13 and $Tu = 1.5\%$ and $AP = -0.18$ in Fig. 5.14. All the plots have been normalized by U_e^2 and a zoomed view limited to the flow region $0.4 \leq x/L \leq 1$ is used for a better visualization. Moreover, contour lines at constant time-mean velocity $U/U_e = 0, 0.5, 0.9$ have been superimposed to the Reynolds stress tensor components to track the position of the separation bubble.

The plots show that the streamwise component τ_{11} starts rising just downstream of the separation position, and increases almost along the isoline at $U/U_e = 0.5$. It reaches the maximum value just downstream of the bubble maximum height position, prior to reattachment. This velocity fluctuation growth can be ascribed to low-frequency oscillation of the bubble and streamwise oscillations induced by the propagation of streaky structures within the separated shear layer, as documented in [117] and [118]. This is characteristic of laminar separation bubbles developing under high freestream turbulence intensities, as documented in the same test section in the previous work of [90] and also for other flow configuration by [80], for examples.

Conversely, the wall-normal and shear components τ_{22} and τ_{12} are null in the fore part of the separated shear layer. They start rising only downstream of the bubble maximum height position and reach their maximum around the position of the flow reattachment. This is due to the vortex shedding process that dominates the flow motion downstream of the bubble [119]. The strong difference in shape and magnitude between τ_{11} and τ_{22} reveals a strong anisotropic character of the Reynolds stress tensor along the separated shear layer.

Furthermore, comparing Figs. 5.12, 5.13 and 5.14, it is also possible to observe the main differences between the stress tensor component distributions characterizing bubbles of different sizes and types. In particular, the positions corresponding to the maximum value of all the three Reynolds stress tensor components shift upstream in case of shorter bubbles, according to the reduced size of the bubble. The intensity of the velocity fluctuations is also scaled with respect to the bubble size, resulting higher in case of long bubbles (top plots of Figs. 5.12 and 5.13). This is probably due to the occurrence of significantly stronger vortical structures leading to transition [120]. For the low AP case (Fig. 5.14), fluctuations are mainly limited to the streamwise velocity and they start growing significantly downstream compared to the other flow cases. Additionally, Reynolds shear stress appears in the rear part of the plate ($x/L > 0.8$), where the bypass type of transition (or the mixed scenario) induces smaller magnitude for this stress component.

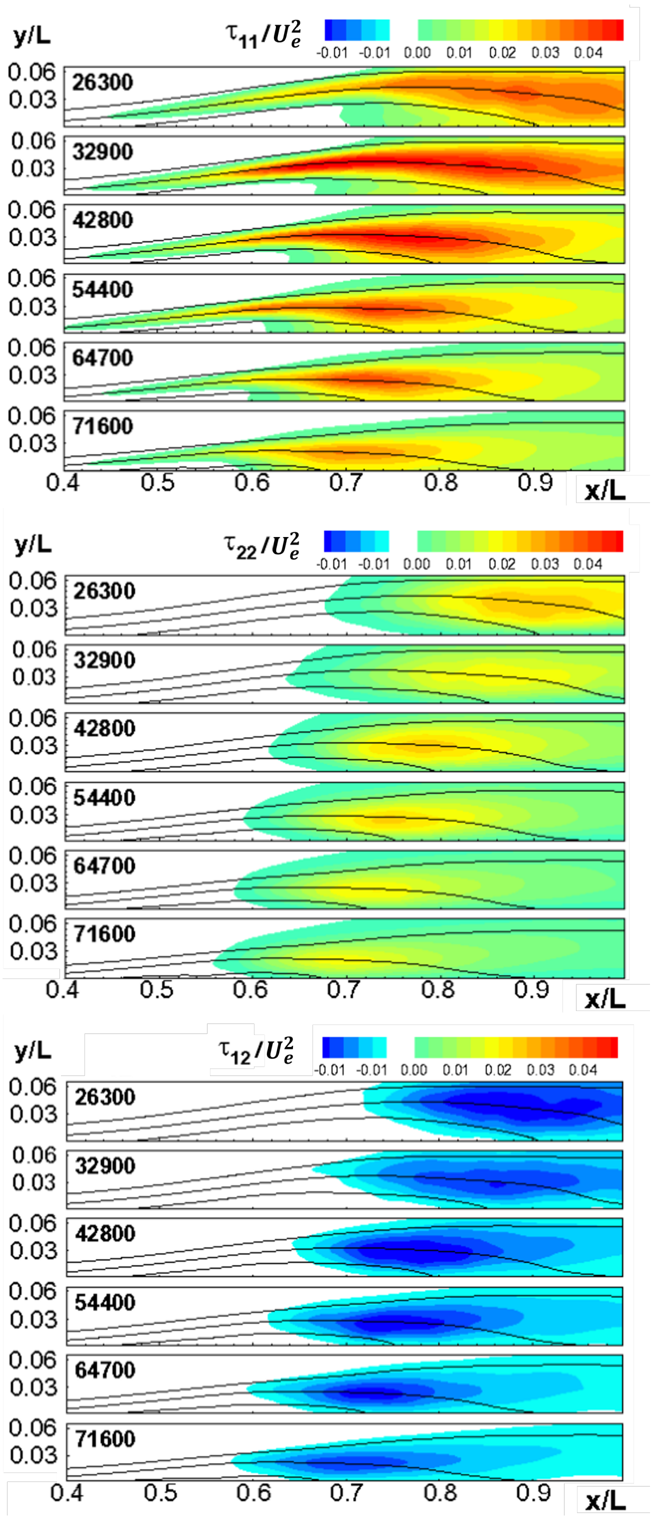

Figure 5.12: Normalized Reynolds stress tensor components for different Reynolds numbers at fixed $Tu = 1.5\%$ and $AP = -0.41$. The isolines correspond to $U/U_e = 0$, 0.5 and 0.9 (from the bottom to the top).

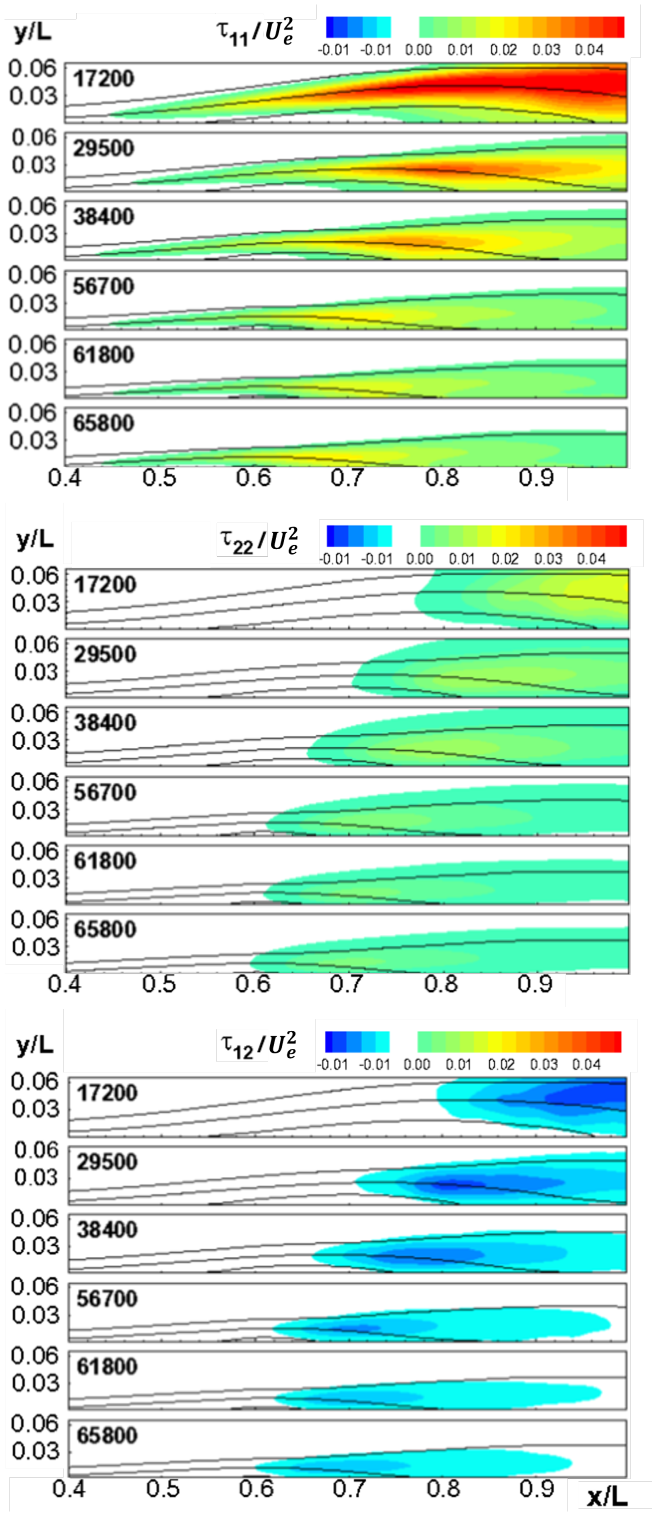

Figure 5.13: Normalized Reynolds stress tensor components for different Reynolds numbers at fixed $Tu = 3.5\%$ and $AP = -0.41$. The isolines correspond to $U/U_e = 0$, 0.5 and 0.9 (from the bottom to the top).

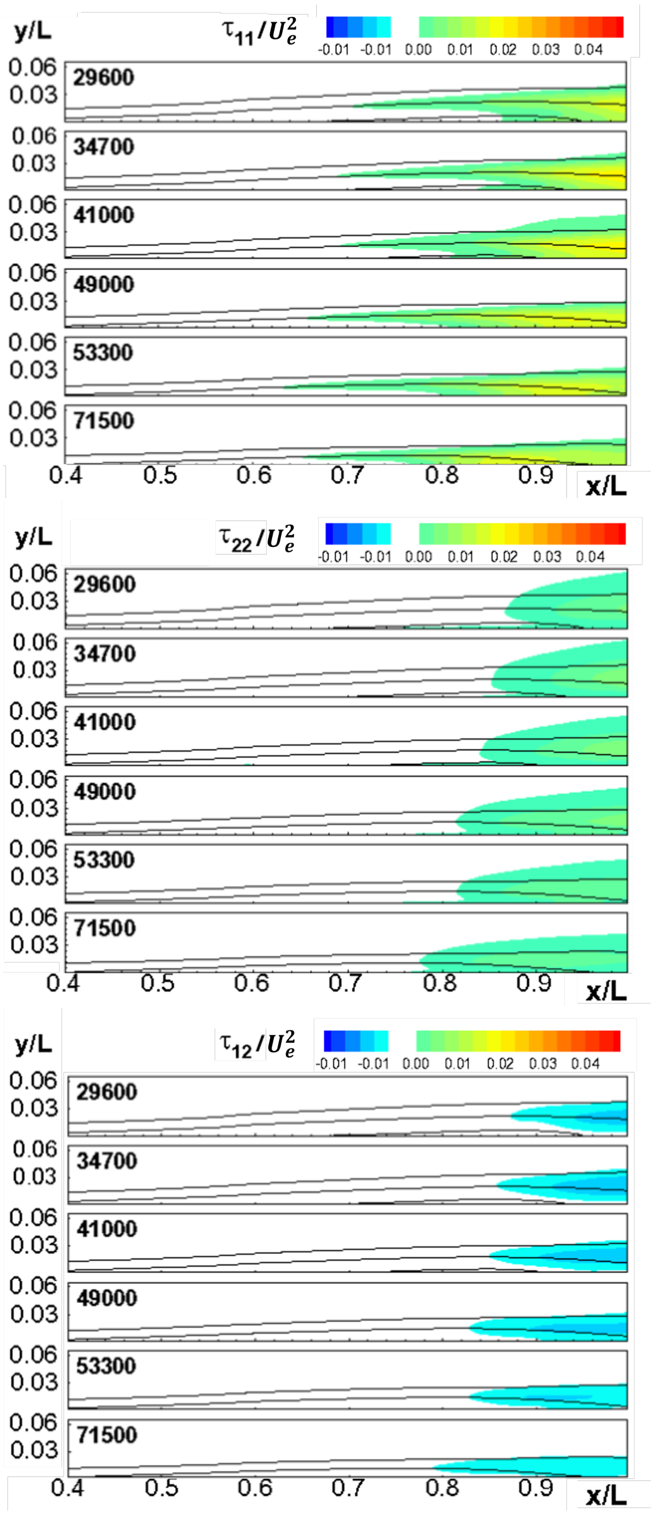

Figure 5.14: Normalized Reynolds stress tensor components for different Reynolds numbers at fixed $Tu = 1.5\%$ and $AP = -0.18$. The isolines correspond to $U/U_e = 0$, 0.5 and 0.9 (from the bottom to the top).

5.2 LES Rounded-Nose Flat Plate Dataset (LES-T3L)

A total number of 15 high-fidelity numerical simulations, based on Implicit Large Eddy Simulations (ILES), were conducted by Gianmaria Noventa (University of Brescia) and Andrea Crivellini (Marche Polytechnic University) [121], [122] on the ERCOFTAC reference case T3L, i.e., the transitional flow over a flat plate with a rounded leading edge. The simulation were obtained using a discontinuous Galerkin solver. The case study consists of a flat plate, theoretically infinite in the streamwise direction, equipped with a rounded leading edge of diameter D. This configuration is particularly suitable for investigating separation and transition phenomena, as the curvature discontinuity at the leading edge naturally induces the formation of a laminar separation bubble, whose evolution strongly depends on the free-stream conditions. Unlike the experimental dataset, where, due to the elliptical leading edge, the separation was caused by the adverse pressure gradient, in this case it is induced by the plate geometry.
In Fig. 5.15 a sketch of the domain is provided, together with a view of the location of the bubbles with respect to the plate. In the figure, D is the diameter of the leading edge of the plate, while L_x represents the distance between the leading edge and the inflow boundary. The dataset is composed of several freestream conditions obtained by varying two main parameters: the reference Reynolds number, $\mathrm{Re}_\infty = 1725, 3450, 6900$, and the incoming turbulence intensity, $\mathrm{Tu}_\infty = 0.0\%, 0.2\%, 0.65\%, 2.3\%, 5.6\%$. The set of cases includes both the official ERCOFTAC configurations (T3L1–T3L6) [83] and additional simulations, allowing for a systematic exploration of the influence of inflow parameters. In Tab. 5.3 a list of all the conditions is provided. For each configuration, once statistically stationary conditions were reached, data were collected over more than 300 characteristic times D/u_∞. The results comprise first- and second-order statistics, including mean velocity and RMS fluctuations of all three velocity components and pressure, averaged both in time and in the spanwise direction. Figure 5.16 shows the normalized streamwise mean velocity component for two different flow conditions. The separated region is identified by the white dashed line, which correspond to $\frac{U}{U_e} = 0$. The upper condition, characterized by low turbulence levels and low Reynolds number, results in the formation of a long bubble, whereas the lower condition, with high turbulence intensity and high Reynolds number, corresponds to a short bubble. Unlike the experimental dataset, the onset point of separation depends solely on the plate geometry; therefore, it remains constant and is independent of variations in the flow parameters. Figures 5.17 and 5.18 report the corresponding normalized Reynolds stress tensor components. Similarly to the EXP-FP dataset, all three components of the tensor reach their maximum magnitude after the maximum height of the bubble. Now, however, the anisotropy is reduced particularly in the separated shear layer. The τ_{11} component, indeed, does not appear to grow in this region, but rather intensifies in the rear part of the bubble, along with the other two components. Another important difference is that, in this case, the intensity of the components is in-

versely proportional to the size of the bubble. As a result, the long bubble corresponds to a lower maximum intensity of the components compared to the short bubble. The models trained on this dataset must therefore be able to effectively reproduce the differences that characterize this dataset with respect to the experimental one.

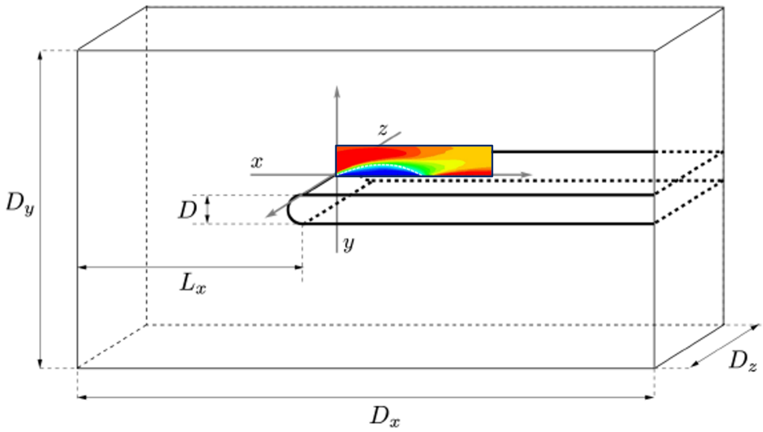

Figure 5.15: Sketch of the computational domain. The location of a separation bubble is highlighted through the streamwise mean velocity.

Re_D \ Tu_∞	0%	0.2%	0.65%	2.3%	6.5%
1725	T3L0L	T3L1L	T3L2L	**T3L5**	T3L4L
3450	T3L0	**T3L1**	**T3L2**	**T3L3**	**T3L4**
6900	T3L0H	T3L1L	T3L2H	**T3L6**	T3L4H

Table 5.3: Free-stream Reynolds number and turbulence intensity characterizing all the computed cases. The cases highlighted in bold represent the original ERCOFTAC conditions.

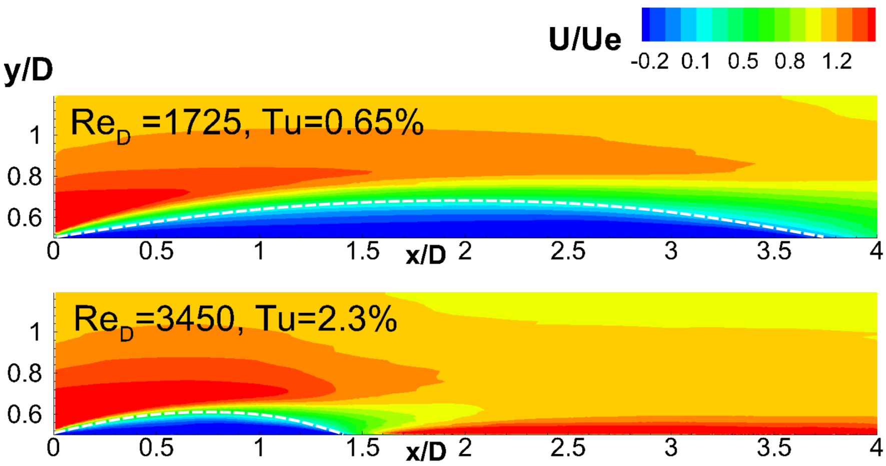

Figure 5.16: Normalized streamwise mean velocity for two flow conditions within the LES-T3L dataset.

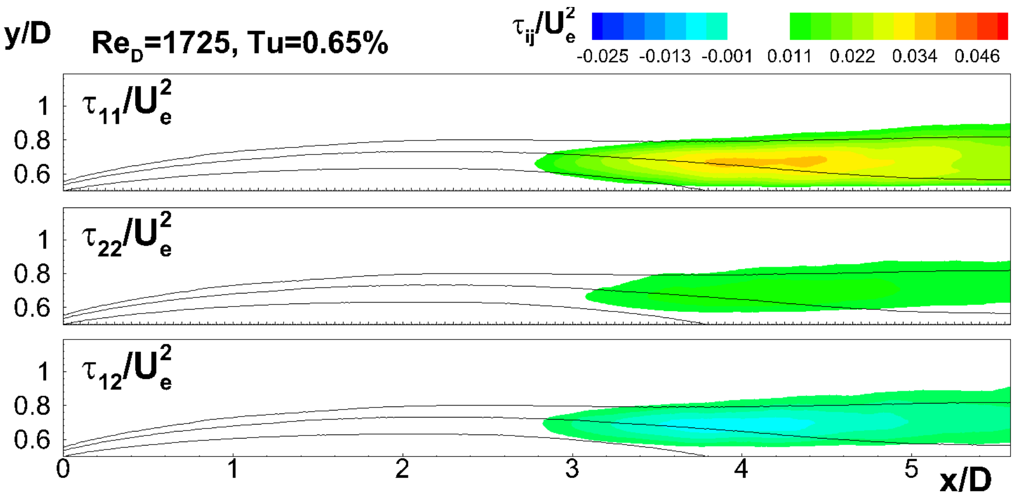

Figure 5.17: Normalized Reynolds stress tensor components for a LES-T3L condition at $Re_D = 1725$ and Tu = 0.65%. The contour lines correspond to U/Ue = 0, 0.5 and 0.9 (from the bottom to the top).

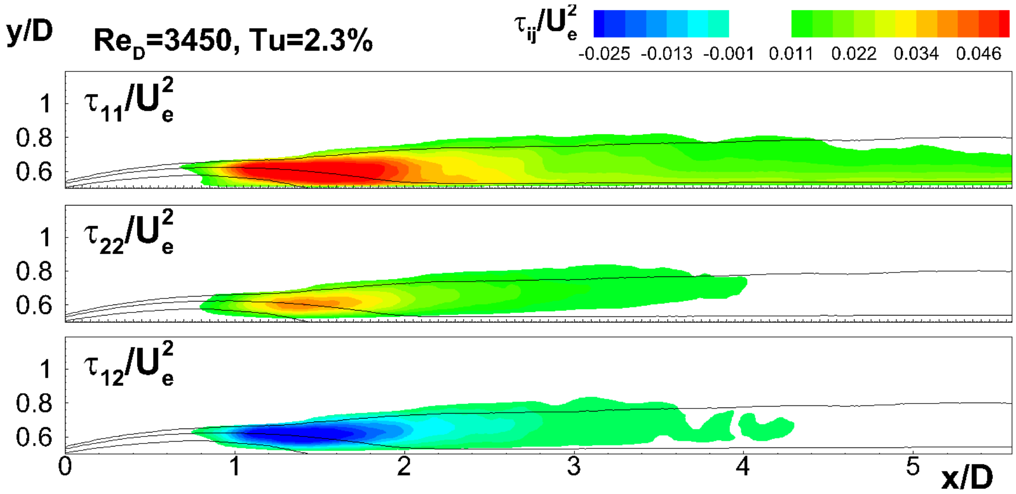

Figure 5.18: Normalized Reynolds stress tensor components for a LES-T3L condition at $Re_D = 3450$ and Tu = 2.3%. The contour lines correspond to U/Ue = 0, 0.5 and 0.9 (from the bottom to the top).

5.3 DNS compressor dataset (DNS-CDA)

The third dataset used in this work concerns with two DNS simulations performed by Pawel Przytarski within the research group of Prof. Richard Sandberg (University of Melbourne) [123]. They reproduce the flow passing by a controlled-diffusion airfoil (CDA) representative of a modern high-pressure-ratio compressor. This dataset were mainly used for validating the models trained on the EXP-FP and LES-CDA datasets. The cascade is characterized by a solidity of $\sigma = 1.7$, a diffusion factor of 0.45, and a nominal turning of $\theta = 27°$. These two simulations are characterized by relatively low Reynolds numbers of $Re = 34k$ and $Re = 68k$, with an inlet turbulence intensity of 8%. Under these operating conditions, a separation bubble develops on the suction side of the blade.

The simulations considered here are actually part of a broader dataset obtained by simulating higher Reynolds numbers of $Re = 125k$, $Re = 250k$, and $Re = 500k$. However, since these simulations exhibit either bypass transition or a separation too limited to be comparable with the other datasets, they were not included in the present work.

The simulations were performed using the high-order compressible multiblock structured flow solver HiP-STAR [124]. The dataset was generated using fourth-order accurate spatial and temporal discretizations with implicit subgrid-scale modelling. The fluid was modeled as a perfect gas with cold-air properties and a ratio of specific heats equal to 1.4. The $400M$-point mesh used, shown in Fig. 5.19, is composed of an O-grid overlaid on a Cartesian background mesh with an overset method [125].

The resolution of the conditions for $Re \leq 125k$ corresponds to a DNS level, with max-

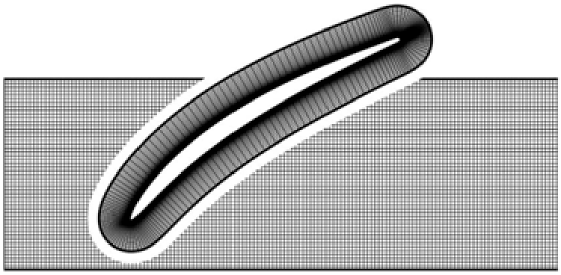

Figure 5.19: Example of the mesh used to generate the present dataset [126]

imum viscous wall units of $\Delta x^+ \leq 7$, $\Delta y^+ \leq 1$, and $\Delta z^+ \leq 7$, and with 95% of dissipation directly resolved. For the condition at $Re = 500k$, instead, the maximum viscous wall units are $\Delta x^+ \leq 25$, $\Delta y^+ \leq 3$, and $\Delta z^+ \leq 20$, with 65% of dissipation directly resolved, effectively providing a resolution equivalent to that of a wall-resolved LES.

For a more detailed description of this dataset, the reader is referred to [126], [127], where further LES simulations obtained using a coarser mesh consisting of 50 million cells are also presented.

To provide an overview of the main features of the separated conditions, Fig. 5.20 shows the loading coefficient for all five conditions included in the dataset by means of the pressure coefficient Cp as a function of the normalized streamwise coordinate. The lower curves, which correspond to the suction side of the blade, highlight a strong separation for the two conditions corresponding to the lowest Reynolds number, where the formation of a plateau can be observed. The laminar separation bubbles are shown in Fig. 5.21 through the streamwise mean-velocity component. On the left, the bubble developing on the blade is shown, while on the right, a zoom with straight axes provides a more detailed view of the separation. The separated region, identified by the white dashed line, is smaller in the case of the higher Reynolds number, as expected. The reduction in bubble size is due to both a downstream shift of the separation point and an upstream shift of the reattachment point. Figs. 5.22 and 5.23 report instead the corresponding distrubutions of the normalized Reynolds stress tensor components. As discussed earlier for the EXP-FP dataset, the maximum intensity of the components tends to increase with higher values of the Reynolds number. The anisotropy in the separated shear-layer is generally reduced compared to the experimental dataset, since the τ_{11} component tends to increase only moderately within the separated shear layer. Moreover, according to the behavior that was yet highlighted for the other two datasets, the peak value is reached just after the maximum height of the bubble. As a consequence, its location results to be shifted upstream for increasing values of the Reynolds number.

It is worth noticing that the databases here considered combines heterogeneous data for pressure and geometry induced separation bubbles (EXP-FP and LES-T3L) and an

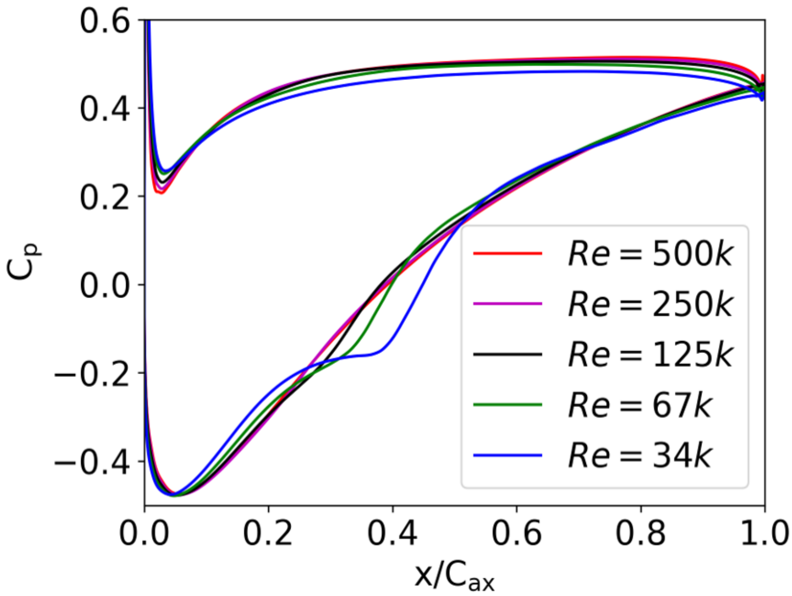

Figure 5.20: Loading coefficient for different Reynolds number

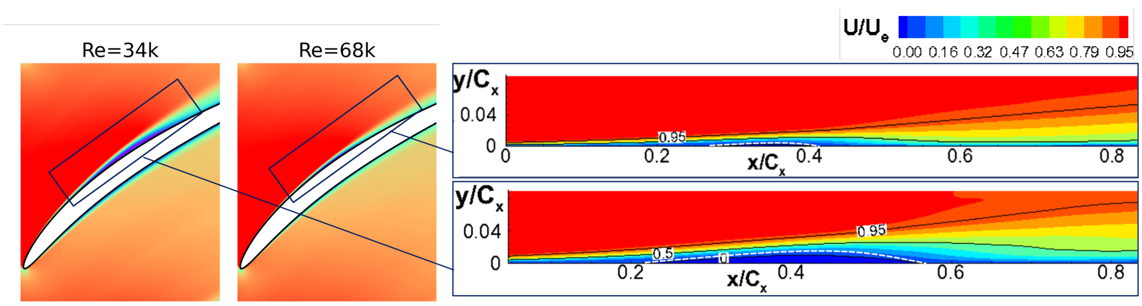

Figure 5.21: Streamwise mean-velocity component for the two DNS-CDA separated conditions

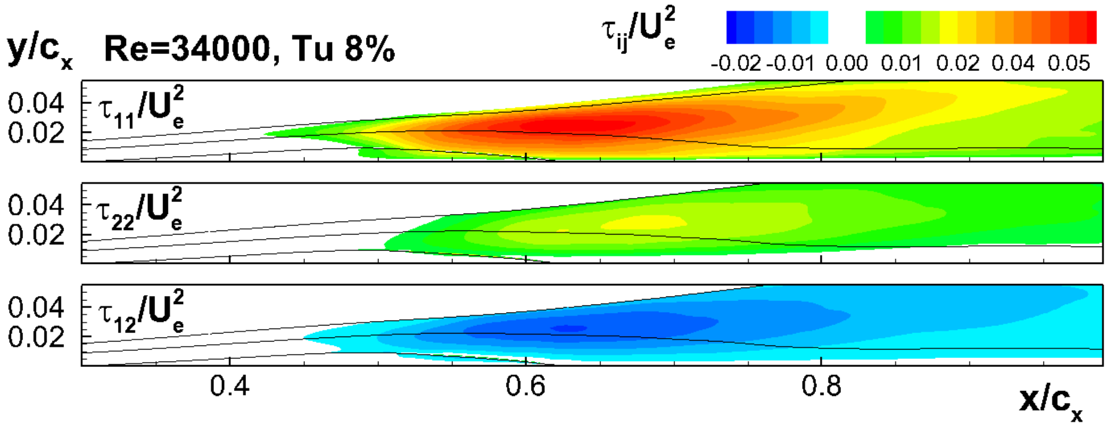

Figure 5.22: Distributions of the Reynolds stress tensor components for the DNS CDA case at Re = 34000 and $Tu = 8\%$.

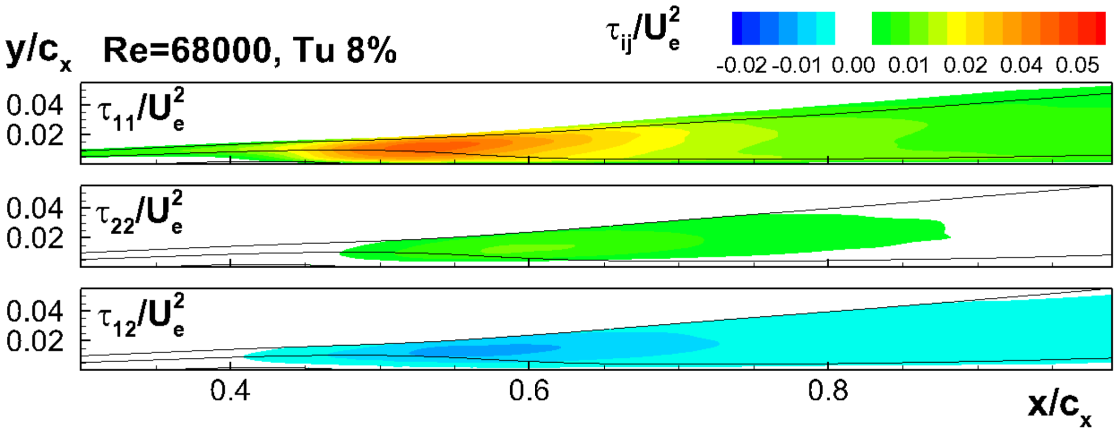

Figure 5.23: Distributions of the Reynolds stress tensor components for the DNS CDA case at Re = 68000 and $Tu = 8\%$.

applicative case of a separated shear layer along a curved surface (DNS-CDA). In order to properly classify the main characteristics of the separated shear layers with local variables, Fig. 5.24 reports the vorticity Reynolds number at the separation point $Re_{\Omega,sep}$ and the turbulent kinetic energy Reynolds number at the reattachment position $Re_{k,reatt}$, for different separation bubbles from the three datasets. The $Re_{\Omega,sep} = (||\Omega||y^2)/\nu$ (defined with the norm of the vorticity tensor Ω, the wall distance y and the kinematic viscosity ν) is a local indicator of the state of the separating boundary layer, since as shown in [94] it is directly correlated with the momentum thickness Reynolds number. Instead, the $Re_{k,reatt} = (\sqrt{k}y)/\nu$ (where k is the turbulent kinetic energy) expresses a measure of the relative importance of the velocity fluctuations promoting flow reattachment at a given wall distance with respect to viscous effects. The plot shows that separation bubbles in the LES-T3L dataset are characterized by values of $Re_{\Omega,sep}$ lower than in the EXP-FP dataset. The geometry-induced bubbles indeed originates at the leading edge of the plate with a very thin boundary layer, while in the EXP-FP cases the boundary layer continuously grows in the entire fore part of the plate before separation. The values of the $Re_{k,reatt}$ are also, on average, lower in the LES-T3L than in the EXP-FP dataset, but a partial overlap can be seen. Indeed, even if the boundary layer conditions at separation are different, the instability process characterizing the separated shear layer exhibits similar characteristics. Consequently, comparable values of $Re_{k,reatt}$ at reattachment position can be observed as a function of the external flow parameter, i.e., combinations of flow Reynolds number, freestream turbulence level and pressure gradient. The DNS-CDA cases are instead characterized by values of $Re_{\Omega,sep}$ and $Re_{k,reatt}$ close to lower bounds observed in the EXP-FP dataset.

In the studies presented in the following, the DNS-CDA dataset will be used for validation, in order to assess the predictive capabilities of the tuned models on a dataset representative of realistic turbomachinery applications.

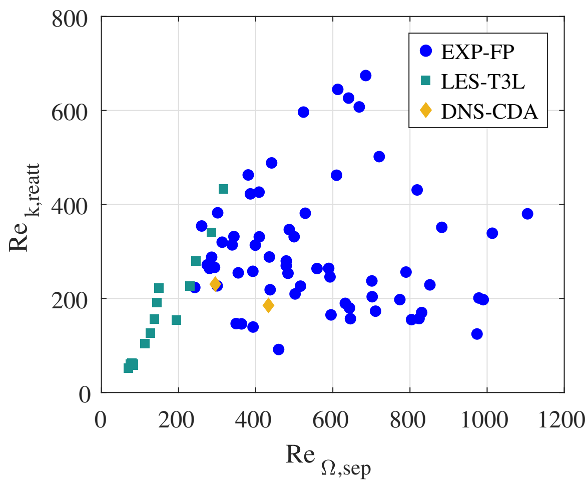

Figure 5.24: Vorticity Reynolds number at the separation point and turbulent kinetic energy Reynolds number at reattachment position for separation bubbles of different datasets.

Chapter 6

Sparse Bayesian Learning

The growing availability of data, however, calls for tools able to extract and interpreting the information embedded within it. Machine Learning (ML) techniques, which constitute the focus of this Chapter, have emerged as powerful instruments for identifying patterns, uncovering relationships, and developing predictive models from large and complex datasets. After a general introduction to the fundamental concepts and motivations behind machine learning, the discussion introduces to regression methodologies, which represent a core class of supervised learning approaches. Particular attention will be devoted to the Sparse Bayesian Learning algorithm, which is employed in this thesis due to its ability to produce sparse, interpretable, and physically meaningful models.

6.1 An Overview on Machine Learning

Machine Learning tools have become essential in engineering and data science, enabling applications ranging from face and image recognition to predicting flow separation over airfoils. In recent years, artificial intelligence has demonstrated enormous potential. As discussed in Mendez *et al.* [2], for example, ML is generally categorized into supervised and unsupervised learning. Supervised learning focuses on approximating an input-output map $f : \boldsymbol{x} \to \boldsymbol{t}$, where the algorithm is trained on known input-output pairs. This category includes regression and classification tasks: regression aims at learning continuous mappings from observations, while classification assigns categorical labels to data points. These approaches allow the modelling of system responses to parameter variations or the categorization of data into pre-defined classes. Unsupervised learning, instead, seeks to uncover patterns and structures in datasets without labeled outputs, effectively learning a map $f : \boldsymbol{x} \to \boldsymbol{x}$. Common techniques include dimensionality reduction, which finds compact representations of data (e.g., reduced order models for blade field reduction), and clustering, which partitions data into previously unknown groups based on inherent similarity. Unlike classification, the cluster labels are not provided a priori and must be inferred from the data itself.

In fluid dynamics, ML has been successfully applied in both regression, as provided by Sec. 4.5, and classification tasks. Manimaran *et al.* [128], for example, employed classification algorithms to distinguish between different fluid flow regimes in CFD simulations. Dimensionality-reduction methods, such as Proper Orthogonal Decomposition, have been widely used to identify coherent structures in turbulent flows [129], [130], while clustering techniques [131] have enabled the construction of reduced-order models based on the similarity of flow snapshots.

6.2 Regression Methods

Regression is the process of learning a continuous mapping $f : \boldsymbol{x} \to \boldsymbol{t}$ from observed data. The goal is to reproduce the behavior of a system while generalizing beyond the training samples. This approach aligns with the scientific method: collecting observations and seeking underlying laws. ML tools facilitate this process by automatically extracting functional relationships from data, allowing the modelling of complex systems with multiple variables and outputs.

The most intuitive machine learning techniques are based on linear regressions. Multiple Linear Regression (MLR), for example, is based on using multiple independent variables to predict a dependent variable through the calibration of a linear model. In general, the model function can be expressed as a linear combination of features:

$$f(\boldsymbol{x}) = \boldsymbol{C}(\boldsymbol{x}) \cdot \boldsymbol{w} \tag{6.1}$$

Here, $\boldsymbol{C}(\boldsymbol{x})$ is the matrix of features, also called predictors or basis functions, and $\boldsymbol{w}$ is the vector of coefficients, while $\boldsymbol{x}$ is the input space. For a dataset with N observations and M features, the feature matrix $\boldsymbol{C}$ can be explicitly written as:

$$\boldsymbol{C}_{N\times M} = \begin{bmatrix} c_1(\boldsymbol{x}_1) & c_2(\boldsymbol{x}_1) & \dots & c_M(\boldsymbol{x}_1) \\ c_1(\boldsymbol{x}_2) & c_2(\boldsymbol{x}_2) & \dots & c_M(\boldsymbol{x}_2) \\ \vdots & \vdots & \ddots & \vdots \\ c_1(\boldsymbol{x}_N) & c_2(\boldsymbol{x}_N) & \dots & c_M(\boldsymbol{x}_N) \end{bmatrix} \tag{6.2}$$

Each feature is a function of the input, defining a mapping from the original input space to a higher-dimensional feature space. Features can take many forms, such as polynomial expansions of the inputs, trigonometric functions, sigmoidal functions, or other transformations that encode prior knowledge or physical constraints. By choosing appropriate features, the model can capture complex relationships between inputs and outputs, even while the overall model remains linear in the coefficients $\boldsymbol{w}$.

Both the dependent variable $\boldsymbol{t}$ and the independent variables $\boldsymbol{x}$ are generally vectors. The model is considered calibrated once the values of the coefficients $\boldsymbol{w}$ are determined.

A common approach to solve this problem is the Least Squares Method (LSM). In LSM, for a training dataset $D(\boldsymbol{x},\boldsymbol{t})$, being $\boldsymbol{t} = [t_1,t_2,\dots,t_N]^T$ the observed output, the mean squared error is defined as:

$$S = (\boldsymbol{t} - \boldsymbol{C}\boldsymbol{w})^T(\boldsymbol{t} - \boldsymbol{C}\boldsymbol{w}) \tag{6.3}$$

Minimizing S with respect to $\boldsymbol{w}$ leads to the least squares solution:

$$\boldsymbol{w}_{LSM} = (\boldsymbol{C}^T\boldsymbol{C})^{-1}\boldsymbol{C}^T\boldsymbol{t} \tag{6.4}$$

Its limitation lies in the necessity to define the model structure beforehand, and in the fact that it assigns nonzero coefficients to all predictors forming the model, often leading to complex models prone to overfitting.

Other techniques can also be used to estimate the coefficients. Among different techniques available in the literature, LASSO, Ridge, and Elastic Net [132] introduce penalties on the ℓ_1 and ℓ_2 norms of the coefficients in the cost function, allowing regularization of complex models and preventing overfitting:

$$\boldsymbol{w} = \min_{w}\Big((\boldsymbol{t} - \boldsymbol{C}\boldsymbol{w})^T(\boldsymbol{t} - \boldsymbol{C}\boldsymbol{w}) + \lambda_1|\boldsymbol{w}|_1 + \lambda_2|\boldsymbol{w}|_2\Big) \tag{6.5}$$

Specifically, if only the ℓ_2 norm is penalized ($\lambda_1 = 0$), it is called Ridge regression [133], which avoids excessively large coefficients and stabilizes the model. If only the ℓ_1 norm is penalized ($\lambda_2 = 0$), it is called LASSO, which tends to produce parsimonious models where many coefficients are exactly zero, improving interpretability and generalization. Geometrically, the ℓ_1-norm constraint defines a square region in the coefficient space (e.g., $|w_1| + |w_2| < \lambda_1$), causing the solution to lie on one of its vertices (see Fig. 6.1). This property of LASSO, known as sparsity, is particularly useful when there are many predictors, as the method automatically selects the most relevant ones. When both penalties are applied, the method is called Elastic Net, combining the advantages of Ridge and LASSO.

If all these methods model the response as a linear combination of features, more flexible approaches can be employed to capture complex, non-linear relationships in the data. Gaussian Processes (or Kriging) provide flexible, non-linear regression capabilities, while artificial neural networks offer universal approximation potential, making them suitable for highly complex mappings. These methods do not require explicit specification of a feature space, allowing the model to learn interactions and non-linear dependencies directly from the data, although they typically require greater computational resources and careful hyperparameter tuning.

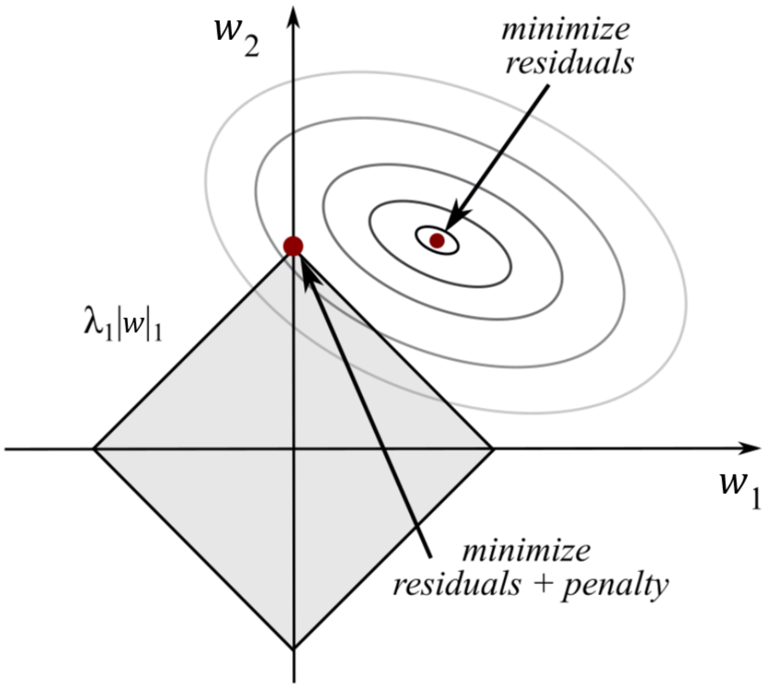

Figure 6.1: Sketch for the minimization problem in the Lasso regression.

6.3 Sparse Bayesian Learning Algorithm

Sparse Bayesian Learning (SBL) ([134]–[136]) is a probabilistic regression framework grounded in the Bayesian approach to inference. The idea behind the Bayesian framework is that model parameters are treated as random variables and prior knowledge is encoded through probability distributions, which are then updated using observed data to obtain posterior distributions via Bayes' theorem. Similarly to the LASSO technique, SBL promotes sparse models, thus to obtain compact formulations that could be implemented into CFD codes. Compared to traditional LASSO, however, SBL also provides an estimate of the uncertainty associated with each coefficient, which is a useful tool for model refinement.
Given a set of N observed data $D = (\boldsymbol{x}, \boldsymbol{t})$, with $\boldsymbol{t}$, for example, the measured components of the normalized anisotropy tensor a^*_{ij}, and $\boldsymbol{x}$ the ensemble of input parameters (e.g., the tensor invariants and flow features), the SBL aims at identifying the relation $\boldsymbol{t}(\boldsymbol{x})$. It is assumed to be expressed by a linear combination of the predictors $\boldsymbol{C}(\boldsymbol{x})\boldsymbol{w}$, with an additive noise ε to account for the deviation between modelled and measured data:

$$\boldsymbol{t} = \boldsymbol{C}(\boldsymbol{x})\boldsymbol{w} + \boldsymbol{\varepsilon} \tag{6.6}$$

The observed data can be considered in terms of probability distribution assigned to data given the model and the noise variance. This takes the form of a N-dimensional Gaussian distribution formulated with respect to the variable $\boldsymbol{t}$, centered in the model prediction $\boldsymbol{Cw}$ and characterized by a covariance $\sigma_n^2\boldsymbol{I}$, where σ_n is the noise variance:

$$p(\boldsymbol{t}|\boldsymbol{w},\sigma_n) = N(\boldsymbol{t};\boldsymbol{Cw},\sigma_n^2\boldsymbol{I}) = (2\pi\sigma_n^2)^{-\frac{N}{2}}\exp\Big(-\frac{1}{2\sigma_n^2}||\boldsymbol{t}-\boldsymbol{Cw}||^2\Big) \tag{6.7}$$

Maximizing Eq. 6.7, which corresponds to minimizing the least squared residual within the exponent, leads the model to overfitting (i.e., losing the capability to predict unseen data), especially if the predictor library is large. To overcome this issue, the idea is to assign a prior probability distribution to the coefficients that induces the less influential coefficients to have a null value. Thus, a prior normal distribution $p(\boldsymbol{w}|\boldsymbol{\alpha})$ centered in zero and with different dispersion α_i is introduced for the model coefficients:

$$p(\boldsymbol{w}|\boldsymbol{\alpha}) = N(\boldsymbol{w};0,\boldsymbol{A}^{-1}),\ \boldsymbol{A} = diag(\boldsymbol{\alpha}) \tag{6.8}$$

Since $\boldsymbol{w}=0$ is the most probable values according to Eq. 6.8, low value of $\boldsymbol{w}$ are promoted. Moreover, to obtain a set of coefficients even more sparse (i.e., only few coefficients different from zero) the demi-Bayesian LASSO technique introduced in [137] can be followed. Here, a further prior to the hyperparameters $\boldsymbol{\alpha}$ is added adopting a hierarchical approach. A Laplace probability distribution for $\boldsymbol{\alpha}$ is introduced (Eq. 6.9). The penalty term λ operates as further regularization promoter. Indeed, high values of λ increase the probability to obtain high values of $\boldsymbol{\alpha}$. Hence, the probability distribution of $\boldsymbol{w}$ becomes more tightly narrowed to zero, favoring even smaller values of $\boldsymbol{w}$.

$$p(\boldsymbol{\alpha}) = \prod_i \frac{\lambda}{2}\exp(-\frac{\lambda}{2\alpha_i}) \tag{6.9}$$

The model is tuned once the values of $\{\boldsymbol{w},\boldsymbol{\alpha},\sigma_n^2\}$ are obtained from data. The posterior distribution of the unknown given the data is:

$$p(\boldsymbol{w},\boldsymbol{\alpha},\sigma_n|\boldsymbol{t}) = \frac{p(\boldsymbol{t}|\boldsymbol{w},\boldsymbol{\alpha},\sigma_n)\,p(\boldsymbol{w},\alpha,\sigma_n)}{p(\boldsymbol{t})} \tag{6.10}$$

Then, the predictive distribution of a target t_*, corresponding to a new test point x_* can be expressed as:

$$p(t_*|\boldsymbol{t}) = \int p(t_*|\boldsymbol{w},\boldsymbol{\alpha},\sigma_n)p(\boldsymbol{w},\boldsymbol{\alpha},\sigma_n|t)d\boldsymbol{w}d\boldsymbol{\alpha}d\sigma_n \tag{6.11}$$

However, it is impossible to compute this integral analytically since the evaluation of the posterior joint probability distribution $p(\boldsymbol{w},\boldsymbol{\alpha},\sigma_n|\boldsymbol{t})$ would be necessary. The direct computation of such quantity, in turn, needs to solve an integral over all the coefficients and hyperparameters, thus it is computationally challenging for problems involving high-dimensional data (see [21] for details). To overcome this issue an alternative method is proposed in [134]. Here, the posterior probability distribution $p(\boldsymbol{w}, \boldsymbol{\alpha}, \sigma_n|\boldsymbol{t})$ is splitted into the product of two terms:

$$p(\boldsymbol{w}, \boldsymbol{\alpha}, \sigma_n|\boldsymbol{t}) = p(\boldsymbol{w}|\boldsymbol{t}, \boldsymbol{\alpha}, \sigma_n)\, p(\boldsymbol{\alpha}, \sigma_n|\boldsymbol{t}) \tag{6.12}$$

where:

- The term $p(\boldsymbol{w}|\boldsymbol{t}, \boldsymbol{\alpha}, \sigma_n)$ represents the posterior distribution for the coefficients $\boldsymbol{w}$ given the observed data and the hyperparameters. The Bayes' rule states that it is proportional to the product between Eqs. 6.7 and 6.8. As expressed in Eq. 6.13, this results in another Gaussian formulated with respect to the variable $\boldsymbol{w}$ with mean $\boldsymbol{\mu}$ and covariance $\boldsymbol{\Sigma}$ (see Eq. 6.14).

$$\begin{aligned} p(\boldsymbol{w}|\boldsymbol{t}, \boldsymbol{\alpha}, \sigma_n) \propto p(\boldsymbol{t}|\boldsymbol{w}, \sigma_n)\, p(\boldsymbol{w}|\boldsymbol{\alpha}) = \\ = N(\boldsymbol{t}; \boldsymbol{C}\boldsymbol{w}, \sigma_n^2\boldsymbol{I})\, N(\boldsymbol{w}; 0, \boldsymbol{A}^{-1}) = N(\boldsymbol{w}; \boldsymbol{\mu}, \boldsymbol{\Sigma}) \end{aligned} \tag{6.13}$$

$$\begin{cases} \boldsymbol{\Sigma} = \left(\boldsymbol{A} + \sigma_n^{-2}\boldsymbol{C}^T\boldsymbol{C}\right)^{-1} \\ \boldsymbol{\mu} = \sigma_n^{-2}\Sigma\boldsymbol{C}^T\boldsymbol{t} \end{cases} \tag{6.14}$$

- The term $p(\boldsymbol{\alpha}, \sigma_n|\boldsymbol{t})$ is assumed to be a multi-dimensional Dirac function centered at the most probable values of $\boldsymbol{\alpha}$ and σ_n. To find these most probable values, the Bayes' rule is again adopted to rewrite $p(\boldsymbol{\alpha}, \sigma_n|\boldsymbol{t})$ in the form provided by:

$$p(\boldsymbol{\alpha}, \sigma_n|\boldsymbol{t}) \propto p(\boldsymbol{t}|\boldsymbol{\alpha}, \sigma_n)\, p(\boldsymbol{\alpha})p(\sigma_n) \tag{6.15}$$

  If a uniform prior is considered for σ_n, the task of maximizing the righ hand term of Eq. 6.15 is equivalent to that of maximizing $p(\boldsymbol{t}|\boldsymbol{\alpha}, \sigma_n)\, p(\boldsymbol{\alpha})$. To this end, an analytical expression is obtained for the cost function L_{II}, i.e. the II-type marginal likelihood ([135], [136]). The maximization of such function with respect to $\boldsymbol{\alpha}$ and σ_n leads to find the most probable values of these hyperparameters. For this purpose, the iterative algorithm proposed in [134], here described by Eq. 6.17, is used.

$$\begin{aligned} L_{II} = \log\left(p(\boldsymbol{t}|\boldsymbol{\alpha}, \sigma_n)\, p(\boldsymbol{\alpha})\right) = \\ = -\frac{1}{2}\left[\log\left(\sigma_n^2\boldsymbol{I} + \boldsymbol{C}\boldsymbol{A}^{-1}\boldsymbol{C}^T\right) + \boldsymbol{t}^T\left(\sigma_n^2\boldsymbol{I} + \boldsymbol{C}\boldsymbol{A}^{-1}\boldsymbol{C}^T\right)\boldsymbol{t}\right] - \lambda\sum_i \frac{1}{\boldsymbol{\alpha}_i} \end{aligned} \tag{6.16}$$

$$\begin{cases} \alpha_i^{new} = \frac{1+\sqrt{1+8\lambda(\mu_i^2+\Sigma_{ii})}}{2(\mu_i^2+\Sigma_{ii})} \\ (\sigma_n^2)^{new} = \frac{||t-C\mu||^2}{N} \end{cases} \tag{6.17}$$

The algorithm determines the values of $\boldsymbol{\alpha}$ and $\boldsymbol{\sigma_n}$ that maximize Eq. 6.16 through the iterative cycle given by Eqs. 6.17. Then, the final values of $\boldsymbol{\mu}$ and $\boldsymbol{\Sigma}$ computed by Eq. 6.14 correspond to the coefficients $\boldsymbol{w}$ and their uncertainty, respectively. The resulting set of $\boldsymbol{w}$ will include a certain number of non-influential coefficients that the algorithm forces to be close to zero, which are then removed. Fig. 6.2 compares the prior and posterior probability distributions for two different coefficients during a cycle close to convergence. In the left panel, the prior distribution, although centered at zero, still exhibits a relatively wide Gaussian shape (low α values). This allows the posterior mean, μ, to deviate from zero, effectively corresponding to the nonzero coefficient. Conversely, in the right panel, the prior distribution is already centered at zero with a narrow Gaussian (high α values). As a result, the posterior follows a similar trend, leading to a vanishing coefficient. Moreover, the broader Gaussian of the posterior distribution indicates that the uncertainty associated with the retained coefficient is higher than that of the eliminated one. The number of these non-influential coefficients ultimately depends on the penalty term λ. Thus, the tuning is complete once λ, that plays in the cost function L_{II} the same role of an ℓ_1 penalty term of a LASSO regression ([138]), is defined. In the present work, the choice of λ is performed through a cross-validation procedure, looking for the best compromise between accuracy and sparsity.

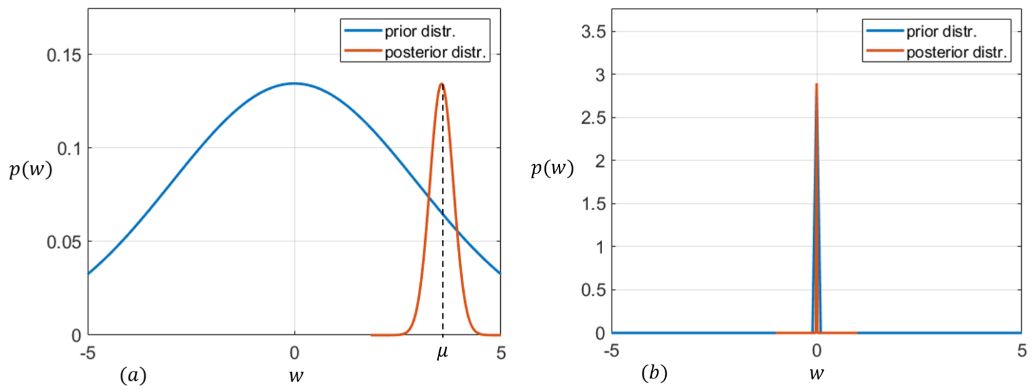

Figure 6.2: Prior and posterior probability distribution of a retained coefficient (a) and of a skipped one (b).

6.3.1 Cross-Validation

The procedure generally consists in testing the predictive capabilities of the model when it is required to predict data that are external to the training set, both in interpolation and extrapolation. Therefore, whenever a model is trained, the dataset must be divided into a training set, on which the model is effectively fitted, and a validation set, on which the model is tested. The proportion between the two datasets is generally around 70% for the training set and 30% for the validation set. Alternatively, a k-fold cross-validation can be employed, where the dataset is partitioned into k subsets. The model is trained on k-1 subsets and validated on the remaining one, repeating the process k times to ensure a more robust estimate of predictive performance. To complete the procedure, it is important to define an appropriate metric to evaluate the model accuracy. In this work, the mean squared error (MSE) was adopted. Although its definition may slightly vary depending on the case, it can generally be expressed as:

$$\text{MSE} = \sqrt{\frac{1}{N}\sum_{n=1}^{N}\left(y_{T,n} - y_{m,n}\right)^2} \tag{6.18}$$

where y_m represent the prediction of the models, y_T the corresponding observed data, while N is the number of the observations. Values of λ that are too high lead to models composed of only a few predictors, which exhibit excellent generalizability and interpretability but perform poorly in terms of error. A model that is too simple will, in fact, show a relatively high error even when applied to data within, or close to, the training set, although such error remains quite stable when predicting external data. Conversely, values of λ that are too low result in models composed of many predictors. These models exhibit low error on the training set but very high error on the validation set, indicating poor generalizability. The purpose of the cross-validation procedure is therefore to identify a model that lies within the green area of Fig. 6.3, corresponding to models characterized by the best trade-off between accuracy and generalizability.

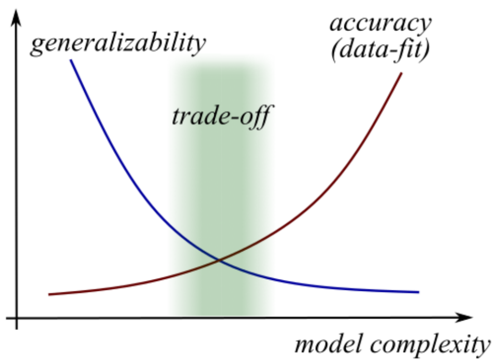

Figure 6.3: Accuracy and generalizability in function of the model complexity

Chapter 7

Results

In this Chapter, the results obtained by applying the theoretical framework previously introduced for the calibration of turbulence models in separated flows are presented. In particular, all the steps carried out will be shown, starting from the calibration of a preliminary model for the prediction of long separation bubbles, up to the calibration of an aggregated model suitable for the modelling of different datasets. The work will be concluded with the calibration of an intermittency model, which, when coupled with the turbulence model, aims to further improve the modelling of separation-induced transition.

7.1 Tuning of an Algebraic Model for the Prediction of Long Bubbles

The objective of this preliminary work [93] was to train a model able to reproduce the Reynolds stress tensor components in the case of long separation bubbles pertaining the EXP-FP dataset. To this end, a subset of data was chosen for the training procedure, while two additional conditions were selected for the validation and testing of the model, respectively. A summary of all the conditions used is provided in Tab. 7.1.

To define the entire predictor library for the SBL, a second-order combination of all the features listed in Tab. 7.2 was computed. In order to avoid too high values of the predictors (which would have resulted in too low coefficients), the features were divided by a power of ten of the same magnitude of their maximum value. In this way, ν_t', ν_t'', and ν_t''' (see Eq. 4.10) are each expressed as a function of 66 possible predictors, resulting in a function space of dimension 198. Using the four training conditions, the SBL algorithm was employed to train a series of models with varying values of the penalty term λ. The validation case was used to tune λ, in order to find the best trade-off between accuracy and generalizability. To guide the choice of the penalty term, the MSE computed as in Eq. 6.18 between the measured and modeled components of the Reynolds stress tensor was considered.

Table 7.1: Flow conditions adopted to train, validate and test the model

Training	Re_L	Tu	AP
	26304	NG	-0.41
	32865	NG	-0.41
	25882	LTU	-0.41
	38452	LTU	-0.41
Validation	Re_L	Tu	AP
	29522	HTU	-0.41
Test	Re_L	Tu	AP
	30663	LTU	-0.41

Table 7.2: Flow features for SBL

feature	definition	feature	definition
I_1	$S^*_{mn}S^*_{mn}$	Π_2	$\frac{\lVert\Omega\rVert y}{\lVert U\rVert}\cdot 10^{-1}$
I_2	$\Omega^*_{mn}\Omega^*_{mn}$	Π_5	$\frac{k}{\nu\lVert\Omega\rVert}\cdot 10^{-2}$
Re_k	$\frac{\sqrt{k}y}{\nu}\cdot 10^{-2}$	Π_6	$\frac{\lVert S\rVert y}{\lVert U\rVert}\cdot 10^{-2}$
Re_{k_x}	$\frac{\sqrt{k}x}{\nu}\cdot 10^{-3}$	Π_k	$\frac{\lVert S\rVert y}{\sqrt{k}}\cdot 10^{-1}$
Re_Ω	$\frac{\sqrt{I_2}y^2}{\nu}\cdot 10^{-1}$	Re_{Ω_x}	$\frac{\sqrt{I_2}x^2}{\nu}\cdot 10^{-3}$

The trend of the MSE as a function of λ is shown in Fig. 7.1. For clarity, nine values between 100 and 16000 have been analyzed to better show the region in the surround of the minimum MSE. As expected, the MSE is high for low values of λ, since in this case a model prone to overfitting is generated. Indeed, for $\lambda = 100$ a large number of predictors survives, generating models that are expected to reproduce with an high accuracy the training set but lose extrapolation capabilities. Viceversa, increasing the value of λ, a progressively more sparse solution is obtained, losing accuracy to mimic the training data but gaining generalizability (i.e., the MSE computed on the validation case decreases). For increasingly higher values of λ, the number of nonzero coefficients tends to decrease until the surviving predictors are no longer sufficient to ensure good performances (i.e., MSE increases again). Therefore, the cross-validation process allows the identification of the optimal λ corresponding to a model which is supposed to be the best to predict flow conditions outside the training set. The model corresponding to $\lambda = 3000$ was found to be the one with the minimum MSE. Moreover, Fig. 7.2 shows the number of survived predictors as a function of λ splitted in terms of the corresponding tensor base elements (see Eq. 4.10). In particular, the purple curve represents the overall number of the predictors that survive, while the other three curves are associated to a singular term of the Pope's expansion (blue T^1_{ij}, red T^2_{ij} and yellow T^3_{ij}). As expected, the plot reveals a decreasing trend since a high penalty coefficient value induces a sparse model.

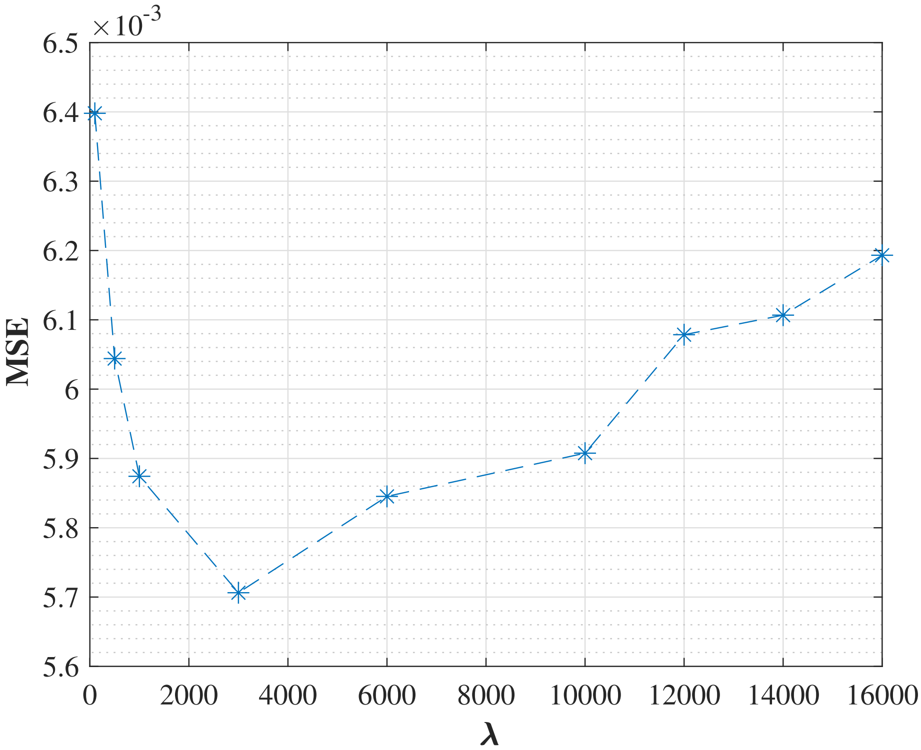

Figure 7.1: Mean Square Error (MSE) as a function of λ.

For the best model ($\lambda = 3000$), 37 predictors survives among the overall 198 considered. Table 7.3 reports the combinations of features that survive at the end of the sparsity promotion process at least in one of the three apparent viscosities. Their corresponding coefficients are also reported. The nonzero coefficients appear quite homogeneously spread over the three turbulent viscosities, with a slight predominance on ν_t'' (associated to T^2_{ij}) with 16 nonzero elements, while for ν_t' and ν_t''' (associated to T^1_{ij} and T^3_{ij}) they are respectively 10 and 11. It is also interesting to underline that I_2, Π_k, Re_Ω and Π_5 are the most recurrent features within the chosen combinations. In particular, Π_k appears in all the three apparent viscosities, highlighting the influence of S_{ij}, k, and the normal-to-wall coordinate in the separated flow transition process. Moreover, it is worth noting that I_2, Re_Ω, Π_5 are all related to the mean flow vorticity Ω_{ij}, emphasizing the importance of this term in modelling the transition induced by the flow separation (see Menter et al. [94] for instance).
The SBL algorithm also provides the estimation of the uncertainty of the model coeffi-

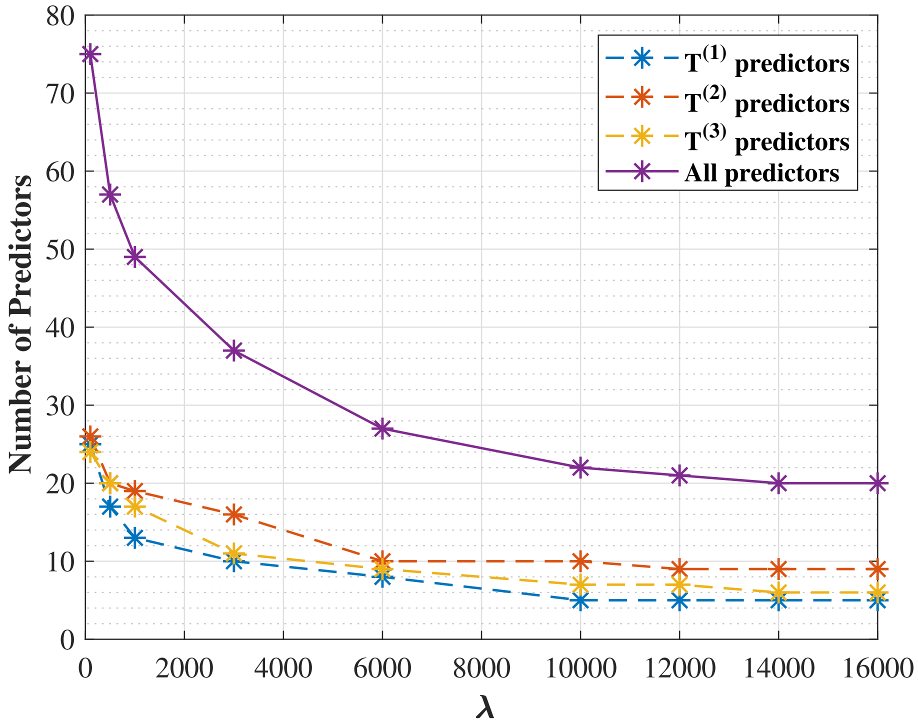

Figure 7.2: Number of predictors as a function of λ.

cients, that can be useful to others for fine adjustment of the presented coefficients once introduced into CFD codes. Figure 7.3 reports the trend of uncertainty σ_w for the 37 predictors of the selected model, expressed as percentage of the coefficient value. This distribution allow the identification of the most reliable predictors and the most questionable. Globally, the uncertainties range from approximately 0.5% to about 5% of the coefficient values. Particularly, the predictors 7 ($I_2\Pi_k$), 13 (Re_Ω) and 27 (I_2) show the lowest uncertainties for what concerns T^1_{ij}, T^2_{ij} and T^3_{ij}, respectively, with the coefficient 13 (Re_Ω) being the most reliable among all. On the other hand, the least confident coefficients for the three components of the tensor expansion are 10 (Π_k^2), 16 ($Re_k\Pi_6$) and 36 (I_2^2). In order to clearly show the capability of the tuned model in well capturing the anisotropic character of the turbulent field, Fig. 7.4 shows the temporal-averaged field of the Reynolds stress components for the validation case ($Re_L = 29552$ and $Tu = 3.5\%$), with the measured quantity on the left, and the modelled one on the right, respectively. Importantly, this represents an extrapolation case for the turbulence level ($Tu = 3.5\%$, HTU), that is higher than those considered in the training set. However, despite of the higher value of the Tu level, there is a good agreement between measured and modelled fields. Indeed, the modelled shear and normal-to-wall components of the Reynolds stress

Table 7.3: Coefficients and predictors of the best model.
(n) indicates the progressive number associated to the predictor.

	v'	v''	v'''
const.	0	-0.164 (11)	0
I_2	-0.0569 (1)	-1.87 (12)	3.45 (27)
Re_Ω	0	1.04 (13)	-0.760 (28)
$I_1 Re_{k_x}$	-0.0530 (2)	0	0
$I_1 Re_\Omega$	0.151 (3)	0	0
$I_1 \Pi_k$	0.191 (4)	0	0
$I_2 Re_k$	-0.0628 (5)	0	0
$I_2 Re_{k_x}$	0	0.0185 (14)	0
$I_2 Re_\Omega$	0	0	-1.12 (29)
$I_2 \Pi_5$	-0.0964 (6)	0	0
$I_2 \Pi_k$	-0.607 (7)	0	0.991 (30)
$Re_k \Pi_2$	0	0.0468 (15)	0
$Re_k \Pi_6$	0	0.0435 (16)	0
$Re_k \Pi_k$	0	-0.0625 (17)	0
$Re_{k_x} Re_\Omega$	-0.0146 (8)	0	0
$Re_{k_x} \Pi_k$	0	-0.224 (18)	0.482 (31)
$Re_\Omega \Pi_5$	0	-0.0680 (19)	0
$Re_\Omega \Pi_6$	0	2.42 (20)	0
$Re_\Omega \Pi_k$	-0.302 (9)	0	0
$Re_{\Omega_x} \Pi_5$	0	0	0.0187 (32)
$Re_{\Omega_x} \Pi_k$	0	-0.298 (21)	0.329 (33)
$\Pi_2 \Pi_5$	0	0	-0.552 (34)
$\Pi_2 \Pi_k$	0	-0.511 (22)	0.816 (35)
$\Pi_5 \Pi_6$	0	1.75 (23)	0
$\Pi_5 \Pi_k$	0	0.0958 (24)	0
I_2^2	0	0	0.616 (36)
$Re_{k_x}^2$	0	0.0062 (25)	-0.0145 (37)
Re_Ω^2	0	-0.0454 (26)	0
Π_k^2	-0.0396 (10)	0	0

tensor ($\overline{u'v'}$ and $\overline{v'^2}$) keep low into the separated shear layer. Downstream of the separation position only the streamwise component $\overline{u'^2}$ starts to increase, reaching its maximum value immediately after the position of bubble maximum displacement, as it occurs for the measured quantity. Downstream of this position both $\overline{u'v'}$ and $\overline{v'^2}$ start to increase due to the transition process dominating the flow evolution.
Furthermore, the model has been tested on a flow case that did not participate to the tuning,

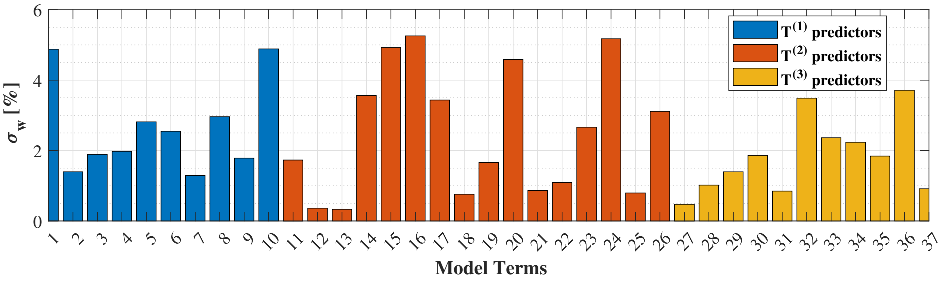

Figure 7.3: Uncertainty related to the coefficients of the survived predictors of the selected model.

characterized by $Re_L = 30663$ and $Tu = 2.5\%$ (LTU). Figure 7.5 reports the comparison between the measured and the modelled fields of the Reynolds stress components for this flow case. Here, as it can be observed by the contour line characterized by $U/Ue = 0$, the bubble size is slightly larger with respect to the validation case (previous Fig. 7.4). The Reynolds number is indeed similar, but the turbulence level is lower. As a consequence, flow separation is anticipated (it occurs at $x/L \approx 0.5$ vs $x/L \approx 0.55$ of the validation case), while the reattachement position is moved downstream ($x/L \approx 0.85$ vs $x/L \approx 0.82$ of the validation case). Nevertheless, all the components of the Reynolds stress tensor are correctly predicted both in terms of shape and intensity. Thus, considering again that the model has been trained on separation conditions characterized by flow parameters that are different from the test case, the predictive capability of the model looks promising for generally modelling the Reynolds stress tensor in the case of occurrence of long separation bubbles.
The main issue that emerged from this work was the large number of predictors characterizing the model. Although this is not necessarily a problem in terms of implementing the model within the CFD code, it limits the interpretability of the model itself and makes it more prone to overfitting when applied to data that differ from the training set. For this reason, one of the primary goals of the following studies was to reduce the number of predictors without drastically compromising the predictive capabilities of the model.

7.2 Tuning of Algebraic Models for the Prediction of Short and Long Bubbles

Building on the experience gained from the previous work, this second research activity [54] aimed at improving the tuning procedure to obtain sparser models. The procedure was again applied to the EXP-FP dataset, this time extended to train also a specific model able to predict short separation bubbles. The separation between long and short bubbles was conducted using the data-driven classification method proposed in [61]. The

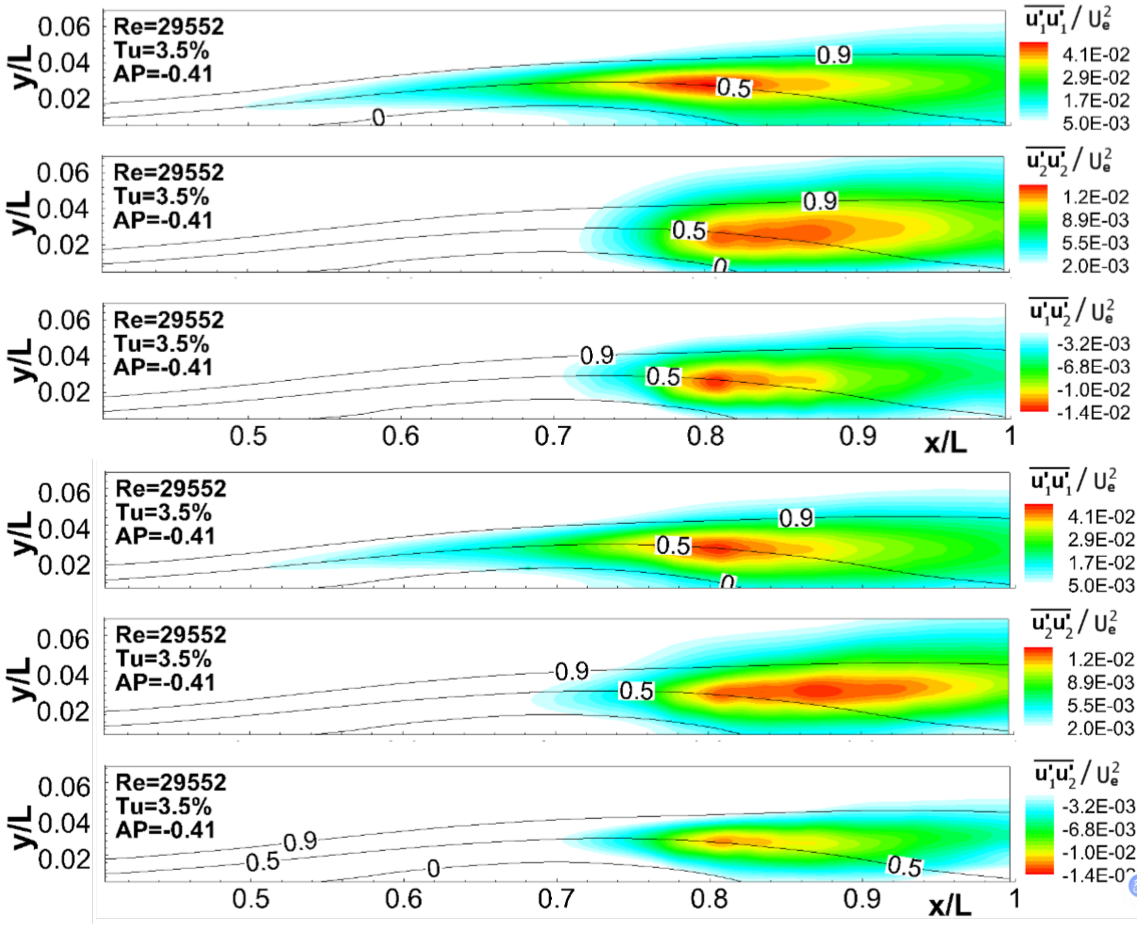

Figure 7.4: Measured (top) and modelled (bottom) components of Reynolds stress tensor for the Validation case (made dimensionless with the external velocity).

possibility of distinguishing between long and short separation bubbles allows for the training of specialized models. This makes it possible to analyze which predictors are selected for each of the two cases, thereby highlighting any potential differences and ultimately providing a deeper physical understanding of the phenomenon. The size of the bubbles is specified in Table 5.2. Differently from the previous work, model tuning was performed here excluding points in the freestream region (where $U/U_e \geq 0.95$). In this region the flow is fully turbulent, and the baseline models already exhibit satisfactory predictive capabilities. Excluding the freestream allows for training models specialized in the separated zone, which are not required to account for two regions with distinct physical characteristics. This makes it easier to obtain models that are sparse yet effective.
For each of the two models, a training dataset and a validation dataset were selected. Both datasets were expanded compared to the previous work, also because the removal of

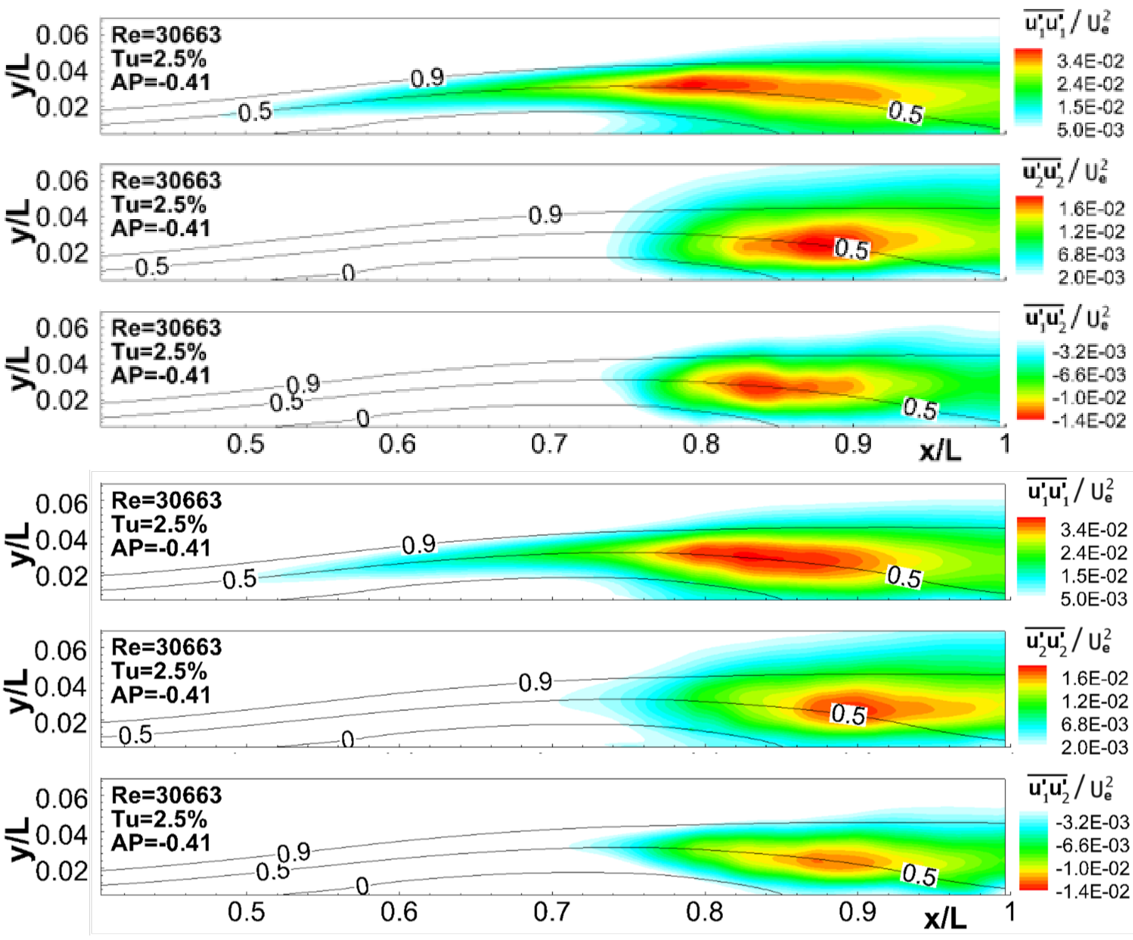

Figure 7.5: Measured (top) and modelled (bottom) components of Reynolds stress tensor for the Test case (made dimensionless with the external velocity).

the freestream allows for the inclusion of more cases without making the training phase computationally too demanding. A summary of all the condition used for validation is reported in Table 7.4.

Model performances were evaluated by computing the Mean Square Error (MSE) defined in Eq. 7.1, where N is the number of spatial points within the domain, a_{ij}^{M} indicates the modelled anisotropy tensor component and a_{ij} the measured one. The errors for the three components of the tensor have been differently weighted by means of the weighting tensor p_{ij}. In order to give a greater weight to the shear stress component, the tensor has been defined such that $p_{11,22} = 0.1$, while $p_{12} = 0.8$. The MSE defined in this way is equivalent to that calculated with respect to the components of the Reynolds stress tensor τ_{ij}, since the latter differs from the components of the anisotropy tensor only by the

Table 7.4: Validation cases used for long and short bubble models, ordered by increasing Re_L. The **bold** Re_L values correspond to long bubbles.

AP	Tu	Re_L	AP	Tu	Re_L
-0.41	1.5%	**22200**	-0.27	2.5%	**23800**
-0.41	3.5%	**29500**	-0.27	1.5%	**31800**
-0.41	2.5%	**34600**	-0.18	2.5%	43100
-0.27	3.5%	45000	-0.41	3.5%	38500
-0.27	2.5%	52200	-0.41	3.5%	61800

additive term $\frac{2}{3}k\delta_{ij}$ (see Eq. 4.7).

$$MSE = \sqrt{\frac{\sum_{n=1}^{N}(\sum_{i=1}^{2}(\sum_{j=1}^{2}(p_{ij}(a_{ij_n}^{M} - a_{ij_n})^2))}{N}} \tag{7.1}$$

To define a library of predictor suitable to be used in the SBL algorithm, features and invariants listed in Tab. 7.5 have been combined into a third-order polynomial expansion, to define a large predictor library. As can be observed, compared to the previous work, the predictors Re_{k_x} and Re_{ω_x} were excluded because they are not Galilean invariant, while, following further literature research, the predictors η_1 and η_2 were introduced. In particular, η_1 corresponds to the *Q-criterion*, while η_2 represents a local measure of turbulence intensity. Actually, not all combinations of mixed terms were considered. In particular, the cross terms between flow features and invariants were excluded. Indeed, some tests proved that, despite a significant increase in the number of predictors, the benefits in terms of model accuracy were negligible. Moreover, the baseline expressions of some of the model predictors have been replaced by their hyperbolic tangent functions, since it has been shown to increase model accuracy. The use of hyperbolic tangent functions allows the predictor values to be bounded between 0 and 1, preventing potential outliers from having an excessive influence. This procedure is particularly beneficial for the implementation of the models within a RANS code, where excessively large predictor values could otherwise compromise the robustness and stability of the simulation. The resulting predictor library $C(I_1, I_2, flowfeatures)$ is constituted by 56 predictors for each apparent viscosity, for a total of 168 predictors.

For the long bubble case, Fig. 7.6 reports the trend of MSE (on the left) and the number of survived predictors (on the right) as a function of λ computed on the validation set. An additional analysis was conducted to demonstrate the actual effectiveness of incorporating physics-based predictors. The red curves are related to the baseline EARSM models, for which the turbulent viscosities are only function of the invariants of the mean strain and rotation rate tensors (see Eq. 4.11). The blue curves, instead, correspond to the

Table 7.5: Invariants and flow features for SBL.

Feature	Definition	Feature	Definition
I_1	$S^*_{mn}S^*_{mn}$	Π_2	$\frac{\lVert\Omega\rVert y}{\lVert U\rVert}\cdot 10^{-1}$
I_2	$\Omega^*_{mn}\Omega^*_{mn}$	Π_5	$\frac{k}{\nu\lVert\Omega\rVert}\cdot 10^{-2}$
Re_k	$\frac{\sqrt{k}y}{\nu}\cdot 10^{-2}$	Π_6	$\frac{\lVert S\rVert y}{\lVert U\rVert}\cdot 10^{-2}$
Re_Ω	$\frac{\sqrt{I_2}y^2}{\nu}\cdot 10^{-1}$	Π_k	$\frac{\lVert S\rVert y}{\sqrt{k}}\cdot 10^{-1}$
η_1	$\frac{\lVert\Omega\rVert^2-\lVert S\rVert^2}{\lVert\Omega\rVert^2+\lVert S\rVert^2}$	η_2	$\frac{k}{0.5U_iU_i+k}$

models where flow features are also included (as for Eq. 4.12). The two curves follow a similar trend. For low values of λ, implying an high number of predictors, the models are characterized by high accuracy but they are not parsimonious. Increasing λ, the number of preditors drops down and the accuracy decreases (i.e., MSE increases). Comparing the two curves, it can be seen that the MSE of the features-including models is less than an half of that of the baseline EARSM models. Thus, the advantage of utilizing models that incorporate flow features in the predictor library is clear, both whether the comparison is made at fixed value of λ or with similar number of predictors. Indeed, for example, the baseline EARSM for $\lambda = 10$ defined by 23 survived predictors has a much higher MSE with respect to the features-including model for $\lambda = 30000$, for which non-zero predictors are 18. At the end, the features-including model tuned for $\lambda = 60000$ has been chosen as the best compromise between accuracy and sparsity. For this model, indicated by blue dot, only 13 predictors remain among the overall 168 of the predictor library. Fig. 7.7 shows the MSE and the number of survived predictors for various λ for the case of short bubbles. The trend of the curves follows the pattern previously observed for the case of long bubbles. Also in this case, the MSE related to the feature-including models is less than an half of that of the baseline EARSM. However, it can be observed that an accurate model for short bubbles is more challenging compared to the long bubble case, as the MSE values are generally higher particularly for high values of λ. The best trade-off has been identified in the feature-including model corresponding to $\lambda = 60000$, as for the previous case. The selected model (indicated by the blue dot) is constituted by 15 predictors.

7.2.1 Long and Short Bubble Models

The tuned models for short and long bubble types are here provided. Their capability of reproducing the distributions of the a_{ij} tensor components is shown on the validation set of data. Then, the proposed model accuracy is quantitatively compared with current models available from the literature.

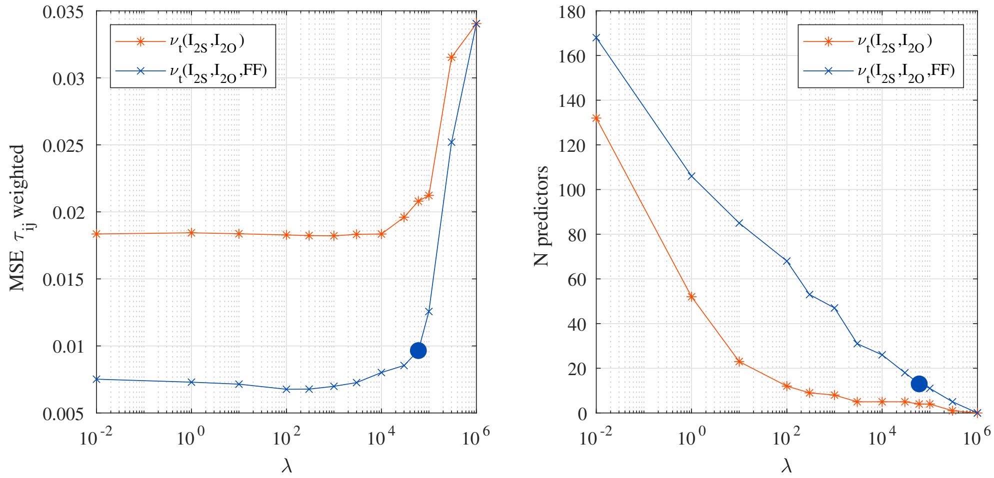

Figure 7.6: MSE (left) and number of the survived predictors (right) vs. λ for the long bubble models.

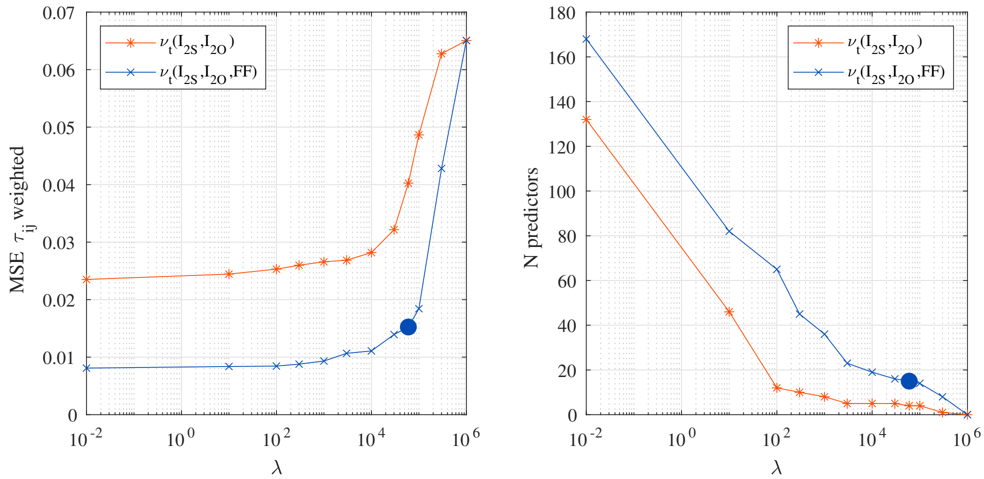

Figure 7.7: MSE (left) and number of the survived predictors (right) vs. λ for the short bubble models

7.2.1.1 Long Bubble Model

Table 7.6 lists the 13 model terms identified by the SBL algorithm and the related uncertainties for the long bubble type. The model terms are spread over the three turbulent viscosities with a prevalence on ν_t'' (associated to T_{ij}^2), where 6 predictors survive. The

other apparent viscosities ν_t' and ν_t''' (associated to T_{ij}^1 and T_{ij}^3) are reproduced by 3 and 4 non-zero predictors, respectively. The most recurrent feature is Π_k, highlighting the role of S_{ij}, k and the normal to wall coordinate in modelling long separation bubbles. Moreover, except for Re_k, all the other survived features (I_2, Re_Ω, Π_2 and Π_5) depends on the mean flow vorticity Ω_{ij}, whose importance in modelling transition induced by flow separation has been underlined also by [94], as discussed above. Table 7.6 also reports the uncertainties σ_w, expressed as a percentage of the coefficient value. In this case, the uncertainties are very low, being included between 0.12% and 1.1%, with the term $tanh\left(\frac{\Pi_5}{100}\right)$ the most confident and $\frac{Re_\Omega}{100}\frac{\Pi_k}{10}$ and $tanh\left(\frac{\Pi_2}{10}\right)\frac{\Pi_k}{10}$ the least.
Figures. 7.8 and 7.9 have been reported with the aim of showing the capability of the tuned model to correctly capture the spatial distributions of the anisotropy tensor components a_{ij}. The plots report the measured (on the left) and the modelled (on the right) anisotropy tensor components for two flow conditions selected from the validation set: the one in Fig. 7.8 is characterized by $Re_L = 34600$, $Tu = 2.5\%$ and $AP = -0.41$, while the one in Fig. 7.9 is characterized by $Re_L = 22200$, $Tu = 1.5\%$ and $AP = -0.41$. Although both the bubbles are included within the range of long bubbles, the second one is larger in size, in accordance with the lower Re_L and Tu. The isolines at $U/U_e = 0, 0.5$ and 0.9 have been superimposed again to the plot.
The diagonal components a_{11} (with positive sign) and a_{22} (negative) of the measured distributions point out the maximum anisotropy that has been observed for τ_{11} and τ_{22} (see section 5.1.6). The maximum is indeed along the isoline at $U/U_e = 0.5$ between the bubble maximum eight and the reattachment positions. The component a_{12} is instead equal to the shear stress by definition.
The model appears able to well reproduce all the three components, as it can be seen by comparing the left and the right plots of the figures. Especially, the normal component a_{11} starts to increase within the separated shear layer just downstream of the separation position, reaching its maximum value downstream of the bubble maximum thickness. A similar behaviour is shown by a_{22}, with an inverted sign. However, they are characterized by different magnitude, and this is captured thanks to the Pope's expansion which is able to model this asymmetry. Finally, a_{12} results to be different from zero only downstream of the bubble maximum height, as for the measured distribution. Also in this case the accordance between the measured and the modelled components is good.
The comparison between Figs. 7.8 and 7.9 provides the capability of the model to correctly locate the positions of the maximum intensity of both the normal and shear components, as well as to properly capture the increased magnitude with respect to the flow case characterized by an higher Reynolds number.

Table 7.6: Long bubble model predictors.

Predictor	Tensor	Coefficient	Uncertainty
cost.	T^1_{ij}	-0.24	0.46%
cost.	T^2_{ij}	-0.96	0.12%
cost.	T^3_{ij}	0.65	0.75%
I_2	T^3_{ij}	1.0	0.93%
$\tanh\left(\frac{\Pi_5}{100}\right)$	T^1_{ij}	-0.074	0.16%
$\frac{\Pi_k}{10}\tanh\left(\frac{\Pi_5}{100}\right)$	T^1_{ij}	-1.4	0.61%
$\frac{\Pi_k}{10}$	T^2_{ij}	-0.18	0.56%
$\frac{Re_k}{100}\tanh\left(\frac{\Pi_5}{100}\right)$	T^2_{ij}	0.16	0.31%
$\frac{Re_\Omega}{100}\frac{\Pi_k}{10}$	T^2_{ij}	-0.0082	1.1%
$\tanh\left(\frac{\Pi_2}{10}\right)\tanh\left(\frac{\Pi_5}{100}\right)$	T^2_{ij}	0.68	0.93%
$\tanh\left(\frac{\Pi_2}{10}\right)\frac{\Pi_k}{10}$	T^2_{ij}	-0.82	0.58%
$\frac{\Pi_k}{10}$	T^3_{ij}	0.62	0.77%
$\tanh\left(\frac{\Pi_2}{10}\right)\frac{\Pi_k}{10}$	T^3_{ij}	1.9	1.1%

7.2.1.2 Short Bubble Model

The model educated for the short bubble case is defined by the 15 terms provided in Table 7.7. The model terms are again homogeneously spread over the three turbulent viscosities. In particular, 5, 6 and 4 predictors survive into the definition of T^1_{ij}, T^2_{ij} and T^3_{ij}, respectively. Even if Π_k appears in 5 among the 15 survived predictors, the most recurrent feature results to be I_2, making the influence of the mean vorticity tensor Ω_{ij} even stronger than in the case of long bubbles. The values of coefficient uncertainties are slightly higher compared to the long bubble case, being in the range between 0.31% and 2.1%. The coefficients related to the $tanh\left(\frac{\Pi_2}{10}\right)\frac{\Pi_k}{10}$ term results to be the most reliable, while the $I_1 I_2^3$ coefficient the least.

Table 7.8 reports the predictors appearing in both short and long bubbles models. These predictors can thus be considered as the most relevant in the modelling of laminar separation bubbles, while the others improve the capability of the models to capture the difference between the bubble state.

Figs. 7.10 and 7.11 report the comparison between the measured (on the left) and the modelled (on the right) anisotropy tensor components for the flow cases at $Re_L = 61800$, $Tu = 3.5\%$ and $AP = -0.41$ (Fig. 7.10) and at $Re_L = 52200$, $Tu = 2.5\%$ and $AP = -0.27$ (Fig. 7.11). Contour lines at $U/U_e = 0, 0.5$ and 0.9 clearly show the reduced size of the

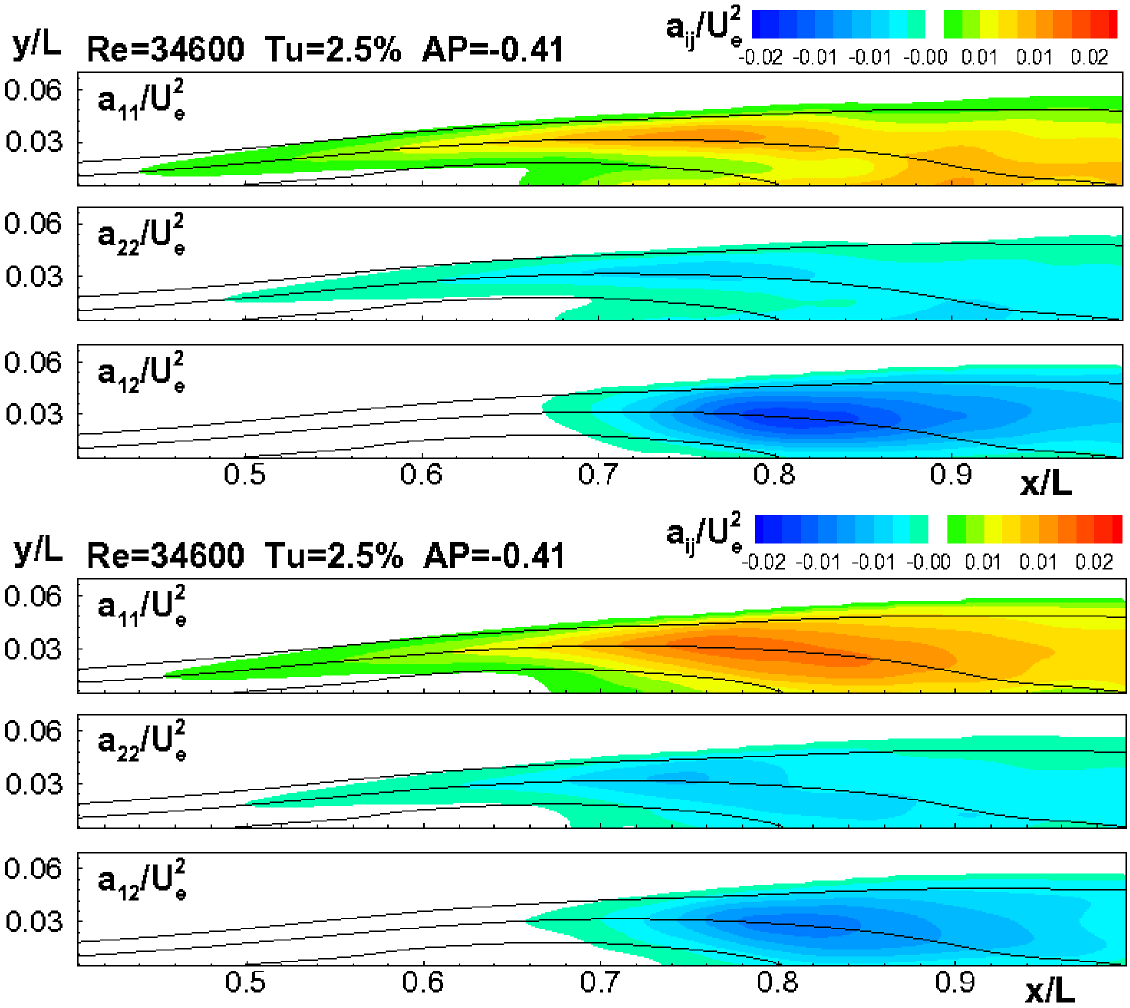

Figure 7.8: Comparison between the measured (on the top) and the modelled (on the bottom) anisotropy tensor components for the long bubble model for the condition $Re = 34600$, $Tu = 2.5\%$ and $AP = -0.41$. The contour lines correspond to $U/U_e = 0$, 0.5 and 0.9 (from the bottom to the top).

bubbles with respect to the cases shown in the previous section. The modelled components provide again a good agreement with the measured distributions, accurately reflecting the scale and size variation of the bubbles. This can be observed in Fig. 7.10 and Fig. 7.11. Interestingly, in these cases the bubble size is similar because the effects of reduced Tu and Re_L is compensated by a reduction of AP, but the bubble position is shifted downstream because of the reduced pressure gradient.

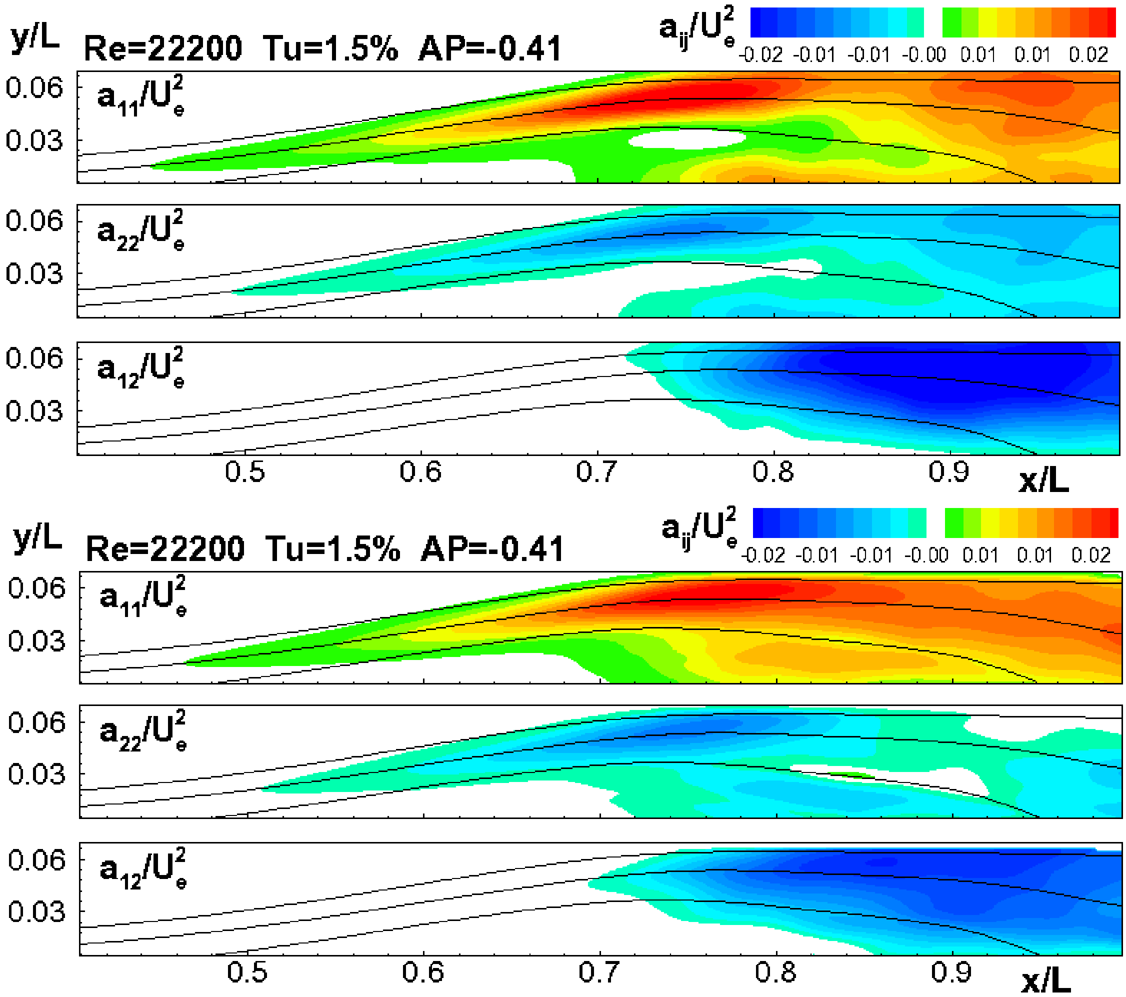

Figure 7.9: Comparison between the measured (on the left) and the modelled (on the right) anisotropy tensor components for the long bubble model for the condition $Re = 22200$, $Tu = 1.5\%$ and $AP = -0.41$. The contour lines correspond to $U/U_e = 0$, 0.5 and 0.9 (from the bottom to the top).

7.2.2 Comparison with the literature

The accuracy of the present model has been compared with previous models available in the literature to provide a quantitative estimation of their predictive capabilities. Particularly, the constitutive laws here defined have been compared with: (1) the linear law at the base of the $SST\ k-\omega$ from [7], the algebraic models of (2) [14] and (3) [18], and (4) with the algebraic closure scheme provided by [139]. The comparisons have been carried

Table 7.7: Short bubble model predictors.

Predictor	Tensor	Coefficient	Uncertainty
cost.	T_{ij}^2	-0.40	0.44%
I_2^2	T_{ij}^1	-0.29	1.5%
I_2^3	T_{ij}^1	-0.68	1.3%
$I_1 I_2^3$	T_{ij}^1	-0.65	2.1%
I_2	T_{ij}^2	-0.77	0.45%
I_2	T_{ij}^3	0.39	1.93%
I_2^2	T_{ij}^3	2.9	0.72%
$\tanh\left(\frac{\Pi_5}{100}\right)$	T_{ij}^1	-0.12	1.3%
$\frac{\Pi_k}{10}\tanh\left(\frac{\Pi_5}{100}\right)$	T_{ij}^1	-1.9	0.61%
$\frac{\Pi_k}{10}$	T_{ij}^2	-0.12	0.92%
$\frac{Re_k}{100}\tanh\left(\frac{\Pi_5}{100}\right)$	T_{ij}^2	0.024	1.7%
$\frac{Re_\Omega}{100}\tanh\left(\frac{\Pi_5}{100}\right)$	T_{ij}^2	0.0068	0.48%
$\tanh\left(\frac{\Pi_2}{10}\right)\frac{\Pi_k}{10}$	T_{ij}^2	-3.9	0.31%
$\frac{\Pi_k}{10}$	T_{ij}^3	0.37	1.4%
$\tanh\left(\frac{\Pi_2}{10}\right)\frac{\Pi_k}{10}$	T_{ij}^3	8.9	0.63%

Table 7.8: Common predictors for long and short bubble models.

Predictor	Tensor
cost.	T_{ij}^2
I_2	T_{ij}^3
$\tanh\left(\frac{\Pi_5}{100}\right)$	T_{ij}^1
$\frac{\Pi_k}{10}\tanh\left(\frac{\Pi_5}{100}\right)$	T_{ij}^1
$\frac{\Pi_k}{10}$	T_{ij}^2
$\frac{Re_k}{100}\tanh\left(\frac{\Pi_5}{100}\right)$	T_{ij}^2
$\tanh\left(\frac{\Pi_2}{10}\right)\frac{\Pi_k}{10}$	T_{ij}^2
$\frac{\Pi_k}{10}$	T_{ij}^3
$\tanh\left(\frac{\Pi_2}{10}\right)\frac{\Pi_k}{10}$	T_{ij}^3

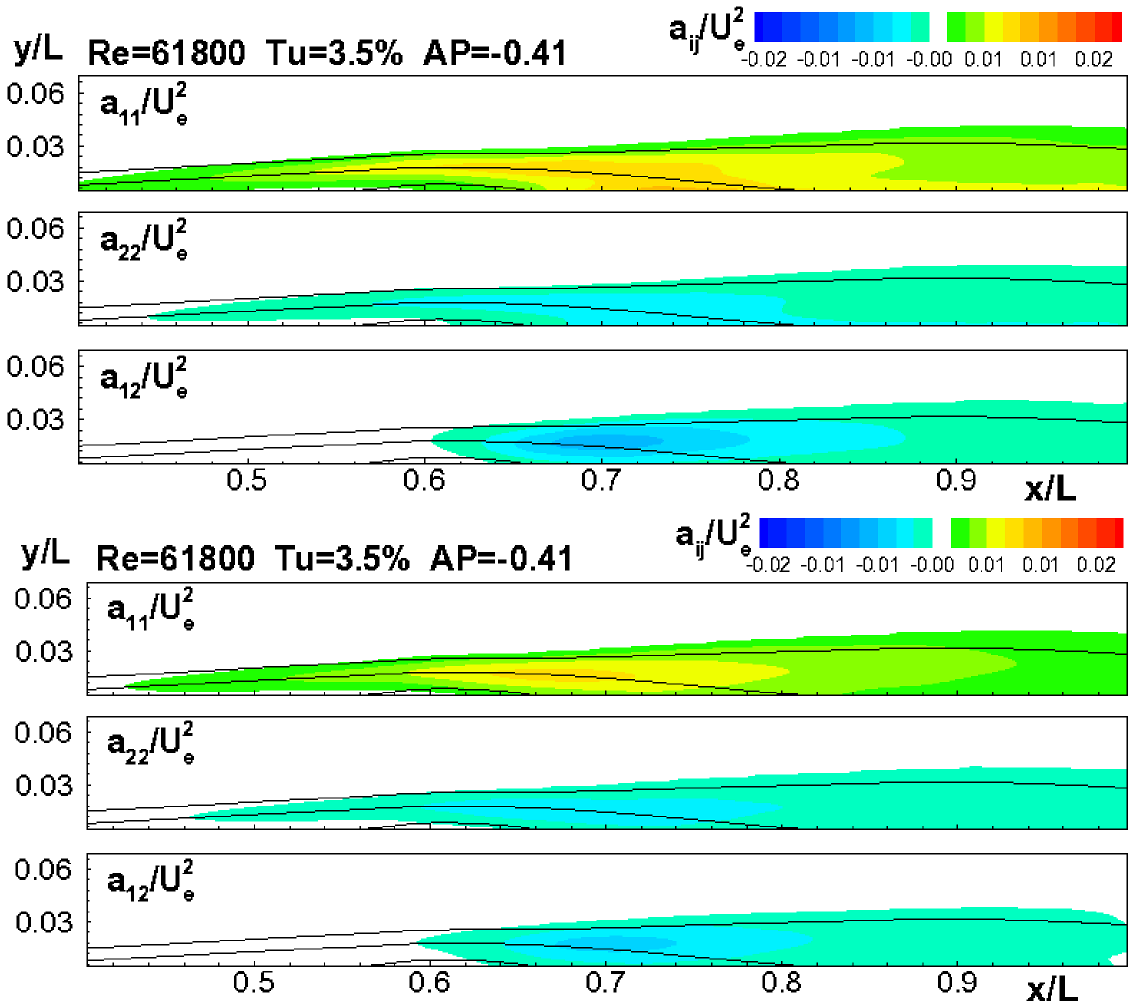

Figure 7.10: Comparison between the measured (on the left) and the modelled (on the right) anisotropy tensor components for the short bubble model for the condition $Re = 61800$, $Tu = 3.5\%$ and $AP = -0.41$. The contour lines correspond to $U/U_e = 0$, 0.5 and 0.9 (from the bottom to the top).

out evaluating the constitutive laws of the different models assuming a frozen experimental flow field (U_{exp}), the turbulent kinetic energy k here evaluated from experimental data (adopting the same assumption previously mentioned $\overline{u_3'^2} = \overline{u_2'^2}$), and the dissipation frequency replaced by the norm of the velocity gradient ($s = \omega$) for models (1), (2) and (3). The MSE computed on the normal and shear stress components has been evaluated independently and used as measure for the accuracy.
Figure 7.12 reports the bar plots of the MSE on the normal (blue bars) and on the tan-

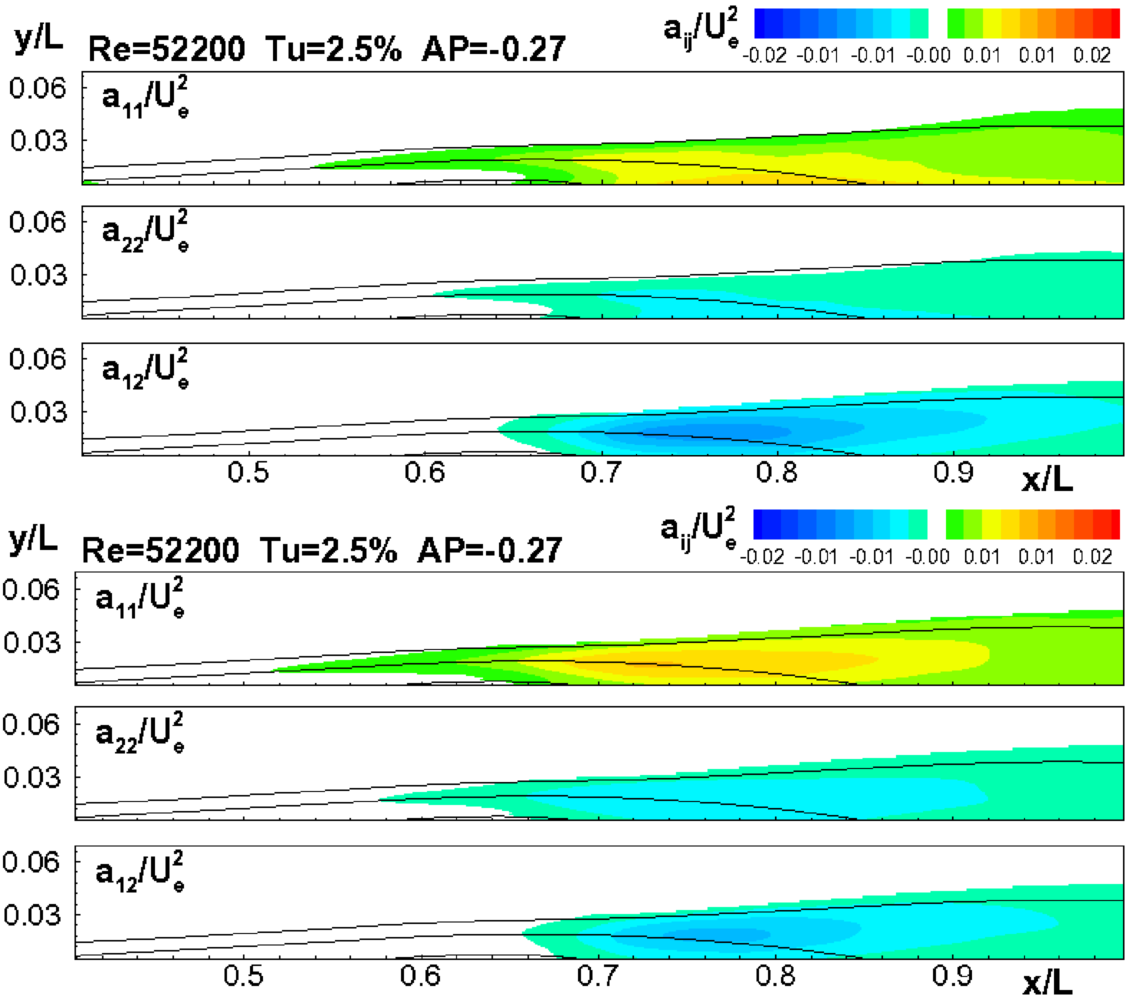

Figure 7.11: Comparison between the measured (on the left) and the modelled (on the right) anisotropy tensor components for the short bubble model for the condition $Re = 52200$, $Tu = 2.5\%$ and $AP = -0.27$. The contour lines correspond to $U/U_e = 0$, 0.5 and 0.9 (from the bottom to the top).

gential (red bars) components of the stress tensor. The five validation flow cases listed in Table 7.4 for the long (on the left) and short (on the right) bubble types have been used. The plots show that all the models provide good predictions of the shear stress component, as the red bars are quite low and not significantly different between the different models. In this sense, the present model performance are in line with current models. Slightly better predictions are obtained by the $SST\ k-\omega$ model, for which the linear term is properly tuned on the shear stress, and by the model described in [18]. Instead, the blue bars show the improvement that can be obtained by non-linear closure schemes, that evidently provide a better reproduction of the anisotropic characteristics of the turbulence along the separated shear layer. Indeed, the largest errors are here exhibited by the $SST\ k-\omega$ model, whose linear constitutive law tuned on the shear stress can not provide an accurate modelling of the diagonal components of the stress tensor. Improvements are shown, in sequence, by the algebraic models of [18], [14] and [139]. The present models provide the best prediction of the diagonal components. Any significant difference can be observed between the short and the long bubble sets of data.

To conclude, this work demonstrated that the models, aimed at predicting the turbulent field generated by long and short laminar separation bubbles, correctly reproduce both the asymmetry between the normal components of the tensor and the distribution of the shear stress term. In particular, model performance is in line with current models regarding the reproduction of the shear stress component, while it can improve the modelling of the diagonal terms of the stress tensor. The main limitation lies in the fact that the two models are specialized to reproduce a specific bubble size, without exploring the possibility of using an aggregation process to improve their generalizability. This second aspect was the main focus of the subsequent studies, which will be described below.

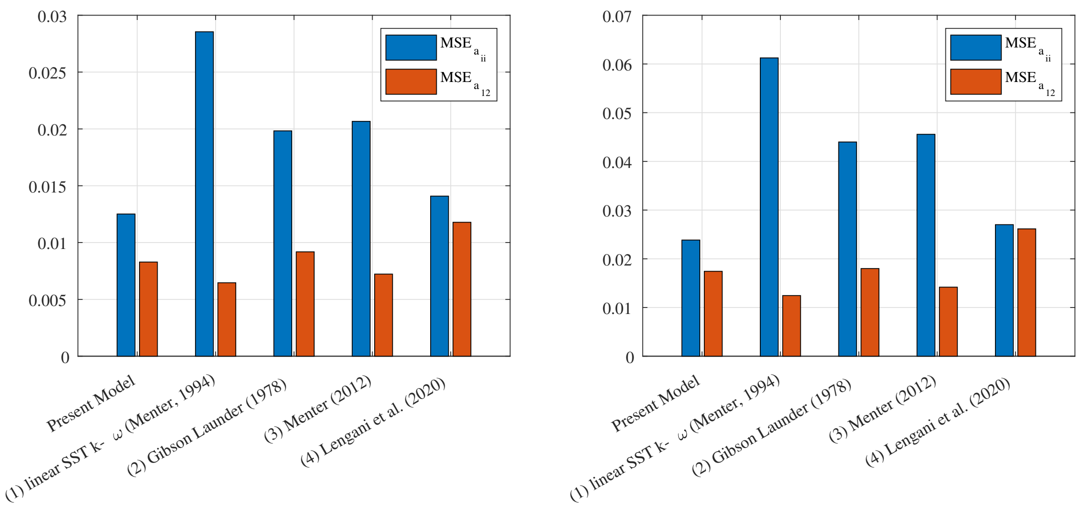

Figure 7.12: MSE on the diagonal components (blue bars) and MSE on the shear stress (red bars) for validation sets of long (left) and short (right) bubbles for different constitutive models.

7.3 Aggregated Model for Long and Short Bubbles

The main objective of this third research activity [140] is the development of a model aggregation procedure to enhance the generalizability of models specialized for a specific flow case. In particular, two models were specifically trained for the prediction of long and short bubbles, and then the X-MA technique was used to improve prediction in the case of mid-range bubbles.

7.3.1 Tuning of the Two Sub-models

In this section, the tuning process of the two sub-models for the prediction of long and short separation bubbles is presented. The training and the validation datasets have been created involving only long and short bubbles at the boundaries of the dataset, with the aim of optimizing the prediction of bubbles with extreme sizes. For this reason, the two datasets differ from those previously employed for the training procedures described in Sec. 7.2. Then, the prediction of mid-range bubbles is demanded to the merged model in the next section. The freestream region above $U/U_e = 0.95$ was removed for both training and validation processes. A mean square error (MSE) between the modelled and the measured non-dimensional anisotropy tensor components ($a^{*M}_{ij_n}$ and $a^{*}_{ij_n}$, respectively), defined as in Eq. 7.1, has been computed to evaluate the performance of the models for the three validation cases, which were selected outside the training set. As above, with the aim of favoring the models which well capture the a_{12} component, the coefficients p_{11} p_{22} and p_{12} have been set to 0.1, 0.1 and 0.8, respectively.
The apparent viscosities ν_t', ν_t'' and ν_t''' are represented through polynomial expansions of the invariants I_1 and I_2. To construct the turbulent viscosities, all combinations of I_1 and I_2 up to the fifth order were included, yielding a library of 132 candidate predictors. Although the previous work demonstrated the effectiveness of incorporating physics-based predictors, in this case the choice was that to adhere more closely to the literature on aggregated models (see [1]), where this limited set of predictors were only used for training the model for the weight. For this reason, and for the previously discussed motivation, namely, to account for particularly long and particularly short separation bubbles, a new training procedure was carried out instead of using the models previously described in Sec. 7.2.
The formulation exploits the SBL framework, enabling the algorithm to identify the most relevant terms directly from the data. Fig. 7.13 reports the trends of MSE for the long bubble (blue curve) and the short bubble (red curve) models as a function of λ. As expected, in both cases it is possible to see that for increasing values of λ, which correspond to fewer surviving predictors, the MSE increases. The increase remains limited up to a critical value of λ, beyond which it significantly rises. The critical value is around $\lambda = 3 \cdot 10^2$ for the short bubble model and $\lambda = 10^5$ for the long bubble model. The red and the blue dots, corresponding to $\lambda = 10^2$ and $\lambda = 6 \cdot 10^4$, respectively, indicate the models that have

been chosen as the best compromise between accuracy and sparsity.

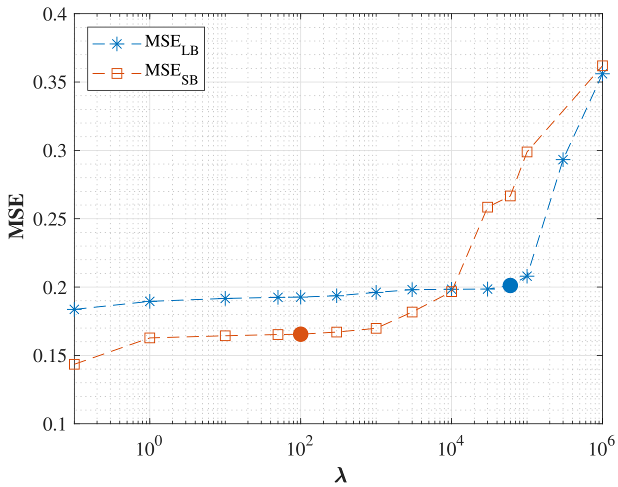

Figure 7.13: MSE of the long and short bubble models as functions of λ.

Among the overall 132 predictors introduced in the library, the surviving ones are only 4 in the case of the long bubble model and 7 in the case of the short bubble model. All the surviving predictors are listed in Tab. 7.9 and Tab. 7.10, along with their location in Pope's expansion, the value of the coefficient and the corresponding uncertainty expressed as a percentage of the coefficient. The predictors are homogeneously spread over the three turbulent viscosities, with a prevalence of ν_t''' for the long bubble model and of ν_t' for the short one. In the long bubble model, the constant term appears to be relevant, while in the short bubble model the most recurrent invariant among the predictors results to be I_2. The uncertainty appears to be generally higher for the short bubble model compared to the long bubble model. Finally, Fig 7.14 and Fig. 7.15 show the predictive capability of the two models by reporting the shear stress component a_{12} for a long and a short bubble case, respectively. The two flow cases reported here are part of the validation sets, so they have not been used to tune the models. The models are able to well capture the a_{12} distributions, which start to increase after the position of the bubble maximum height. Although both models slightly underestimate the a_{12} maximum value, which approximately occurs at the reattachment point, they appear able to capture the different magnitudes between the two types of bubbles.

7.3.2 Aggregation Procedure of Long and Short Bubble Sub-models

To achieve a space-dependent model aggregation the idea is to assign a high weight to the model which performs better in a single spatial point, and, consequently, a low weight to

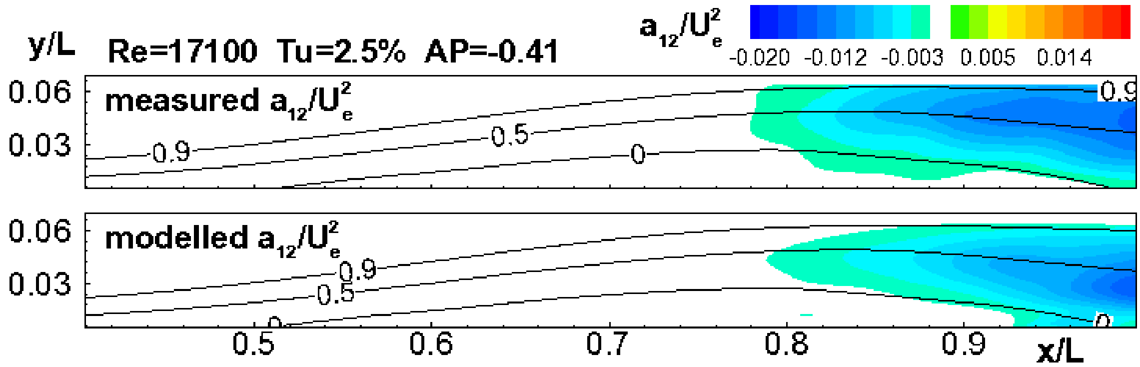

Figure 7.14: Comparison between the measured and the modelled shear stress component a_{12} for a long bubble case not used for training.

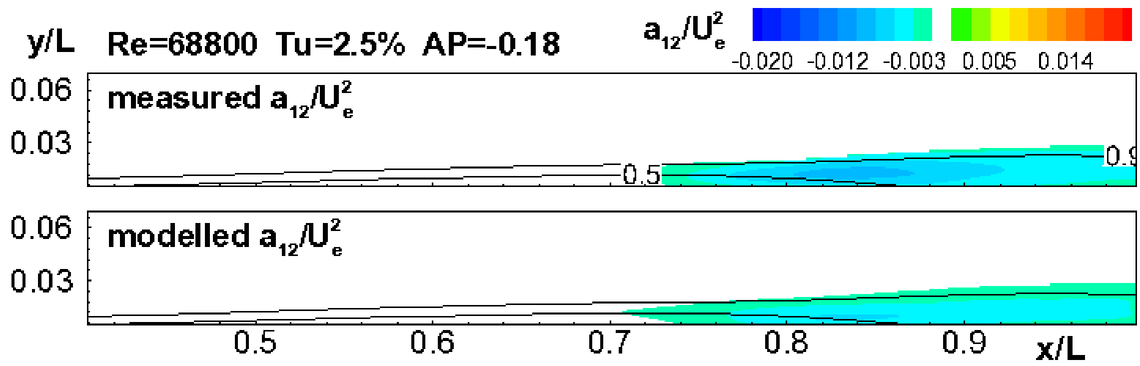

Figure 7.15: Comparison between the measured and the modelled shear stress component a_{12} for a short bubble case not used for training.

Table 7.9: Long bubble model predictors.

Predictor	Tensor	Coefficient	Uncertainty
const.	T^1_{ij}	-0.31	0.45%
const.	T^2_{ij}	-1.0	0.12%
const.	T^3_{ij}	0.32	1.4%
I_2	T^3_{ij}	2.6	0.53%

the other. Following the aggregation procedure yet described in Sec. 4.4, now applied to the case of two models ($N = 2$), the ensemble solution $a^{AG}_{ij}(x)$ is obtained by aggregating the individual predictions $a^{LB}_{ij}(x)$ and $a^{SB}_{ij}(x)$ provided by the long and short bubble

Table 7.10: Short bubble model predictors.

Predictor	Tensor	Coefficient	Uncertainty
const.	T_{ij}^2	-1.2	0.24%
I_1	T_{ij}^1	-0.38	4.2%
I_1^2	T_{ij}^1	-0.18	11%
I_2^5	T_{ij}^1	-5.8	3.8%
I_1^5	T_{ij}^2	2.2	2.6%
I_2	T_{ij}^3	1.1	6.9%
I_2^2	T_{ij}^3	6.7	2.3%

models, such that:

$$a_{ij}^{AG}(x) = w_{LB}(x)a_{ij}^{LB}(x) + w_{SB}(x)a_{ij}^{SB}(x) \tag{7.2}$$

where w_{LB} and w_{SB} indicate the weighting functions assigned to the long and short bubble models, respectively. With the aim of defining a training set to tune the weighting functions, the long and the short bubble models have been used to predict a set of conditions including some mid-range bubbles. Then, the Exponentially Weighted Average (EWA) has been computed for the short bubble model prediction error with respect to the measured anisotropy tensor components a_{ij}:

$$\tilde{w}_{SB}(x,\sigma_w) = \frac{g_{SB}(x,\sigma_w)}{g_{SB}(x,\sigma_w) + g_{LB}(x,\sigma_w)} \tag{7.3}$$

where:

$$g_{SB,LB} = \exp\Big(-\frac{1}{2}\frac{\sum_{i=1}^{2}\sum_{j=1}^{2}(p_{ij}(a_{ij}^{SB,LB} - a_{ij})^2)}{\sigma_w^2}\Big) \tag{7.4}$$

From this point on, the training weight distribution, i.e., the distribution calculated from the predictions of the individual models, will be denoted by $\widetilde{w}$, in order to distinguish it from w, which represents the weighting function reconstructed by the model. The weight distribution of the long bubble model has not been subject to a training process since, as provided by Eq. 4.14, $w_{LB} = 1 - w_{SB}$. Before proceeding with the tuning of the weight model, it was necessary to determine a value for the parameter σ_w. The effect of this parameter on the weight distribution is summarized in Fig. 7.16. For values of σ_w close to 0 (top plot of Fig 7.16), the better model at a given point in the domain is forced to dominate the other, making the weight distribution practically binarized. It is important to note the presence of a blanked white region, mainly in correspondence of the region where the short bubble model outperform the long one (i.e, the red area of the plot). Indeed, for very low values of σ_w, the distribution of the gating functions tends to be a Dirac centered in 0. It may therefore generate regions where both g_{SB} and g_{LB} are close to 0, making the ratio defined in Eq. (7.3) indeterminate and the resulting weight unable to be used for the merging purpose. Conversely, for increasing values of σ_w (see the second and third plots of Fig 7.16), the weight distribution becomes increasingly uniform, finally becoming constant and equal to 0.5. In this work, after several attempts, a value of $\sigma = 0.005$ has been chosen as the best compromise between the usability of the weighting function and its effectiveness. The flow features adopted to tune the weighting function are listed in Table 7.11. These features have been combined to define the predictor library for the SBL. This approach resulted in a library consisting of 45 predictors. The SBL algorithm capability allows us to retain only the truly influential predictors by assigning them non-zero coefficients. Developing a parsimonious model not only simplifies code implementation but also enhances our physical understanding of the key terms involved in the separation-induced transition process.

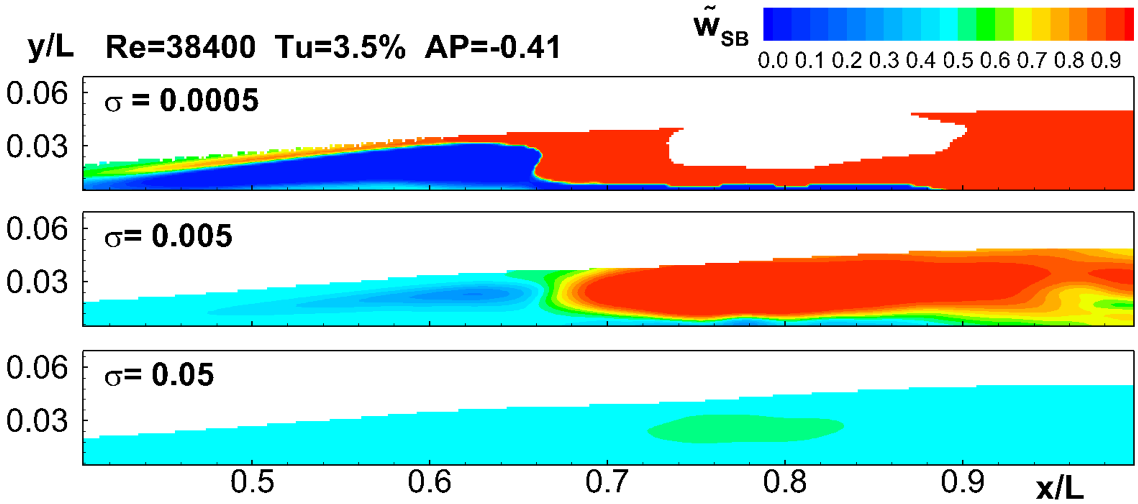

Figure 7.16: Measured distributions of $\tilde{w}_{SB}$ varying σ.

7.3.3 Results of Model Aggregation

The results from the merging process are shown here, with five "mid-range" conditions outside of the training set that are selected for validation. Then, the models provided by short and long bubbles have been aggregated according to Eq. 7.2 through the weights trained for different λ. With the aim of identifying the best compromise between accuracy and sparsity (i.e., choosing an optimal value of λ), the MSE between the measured and the modelled anisotropy tensor components has been computed. Figure 7.17 shows, for one flow case among the validation set, the comparison between the measured weight

Table 7.11: Flow features for SBL.

feature	definition	feature	definition
Re_k	$\frac{\sqrt{k}y}{\nu} \cdot 10^{-2}$	Π_6	$\frac{\lvert\lvert S\rvert\rvert y}{\lvert\lvert U\rvert\rvert} \cdot 10^{-2}$
Re_Ω	$\frac{\sqrt{I_2}y^2}{\nu} \cdot 10^{-1}$	Π_k	$\frac{\lvert\lvert S\rvert\rvert y}{\sqrt{k}} \cdot 10^{-1}$
Π_2	$\frac{\lvert\lvert\Omega\rvert\rvert y}{\lvert\lvert U\rvert\rvert} \cdot 10^{-1}$	η_1	$\frac{\lvert\lvert\Omega\rvert\rvert^2-\lvert\lvert S\rvert\rvert^2}{\lvert\lvert\Omega\rvert\rvert^2+\lvert\lvert S\rvert\rvert^2}$
Π_5	$\frac{k}{\nu\lvert\lvert\Omega\rvert\rvert} \cdot 10^{-2}$	η_2	$\frac{k}{0.5U_iU_i+k}$

distribution (i.e., the target of the training process) and the modelled ones obtained for $\lambda = 0$, which does not induce sparsity, $\lambda = 10^3$ and $\lambda = 10^5$. The accuracy in reproducing the weight distribution is clearly higher exploiting the model for $\lambda = 0$. However, as can be observed in Tab. 7.12, the improvement in terms of MSE between this model and the SBL model obtained for $\lambda = 10^3$ are limited, but the number of surviving predictors decreases from 45 to 8. Moreover, since the MSE increases for values of $\lambda > 10^3$, the model obtained for $\lambda = 10^3$ has been considered the best compromise between accuracy and sparsity. Focusing on the weighting distributions provided by Fig. 7.17, one can see that the short bubble model outperforms the long bubble one in the separated shear layer downstream of the bubble maximum height, while the long bubble model performs well in the fore part of the bubble. The presented flow case has been taken as example for brevity, but the other validation cases also show a similar behaviour. In particular, the location where the long or the short bubble models perform better than the other is nearly the same, while the magnitude of the weighting function changes according to the characteristics of the bubble at hand. The short bubble model hence appears to be more suitable for capturing the flow dynamics in the rear part of the bubble, while the long bubble model is better in capturing those in the front portion.
The surviving predictors defining the weight model, along with the corresponding coefficient and uncertainty, are reported in Tab. 7.13. The Π-groups and η_2 are the most recurrent features among the surviving predictors. However, it can be observed that the uncertainty related to some of these terms is high, while the most confident predictors are the constant term and Re_k. Finally, Fig. 7.18 shows the measured time-mean anisotropy tensor components for the same validation case adopted in Fig. 7.17, while Fig. 7.19, 7.20 and 7.21 show the prediction of the long bubble, short bubble and merged models, respectively. All models are able to well predict the three distributions. In particular, the normal components a_{11} and a_{22} behave similarly but with a reverse sign. They start to increase just downstream of the separation position, reaching their maximum downstream of the bubble maximum height. A slight tendency to shift the peak region backward and to overestimate the maximum magnitude can be observed. The shear component a_{12} be-

comes nonzero only downstream of the bubble maximum displacement. The positioning of the peak region of a_{12} is well captured, though with a slight underestimation of the maximum intensity.
The predictions provided by the long bubble, short bubble and merged models are very similar, as can be noticed also looking at the MSE values provided in Tab. 7.12. This result highlights that, despite the apparent differences between long bubbles and short bubbles, the underlying physical phenomena that govern them are not significantly different. This allows both long bubble and short bubble models to produce similar predictions when it comes to model a bubble within the mid-range set. The merged model still proves to be the best with respect to the selected dataset. By comparing Figs. 7.19, 7.20 and 7.21, it can be observed that the short bubble model slightly overestimates the maximum of a_{11} more than the long bubble one, while the opposite occurs for a_{12}. The merged model offers an intermediate solution between the two, making it the best compromise in terms of MSE. However, it is worth noticing that the benefit obtained by model aggregation is small. This, from one side, confirms the capabilities of the MA technique of merging different flow cases, but at the same time suggests that it is not decisive in the modelling of short and long bubbles, while accurate predictions can also be obtained by each single model alone. For this reason, the main outcome of this research activity can be considered the development of a robust procedure for aggregating different models. This suggests that such a procedure could be more effective if applied to models trained on more heterogeneous datasets, i.e., datasets that differ markedly from one another in terms of the physical dynamics governing the phenomena they describe. By doing so, the results of the aggregated model could be improved, at least in terms of the generalizability.

Table 7.12: Comparison between MSE values.

Model	MSE
Long bubble model	0.215
Short bubble model	0.222
Aggregated model ($\lambda = 0$)	0.207
Aggregated model ($\lambda = 1000$)	0.209
Aggregated model ($\lambda = 100000$)	0.225

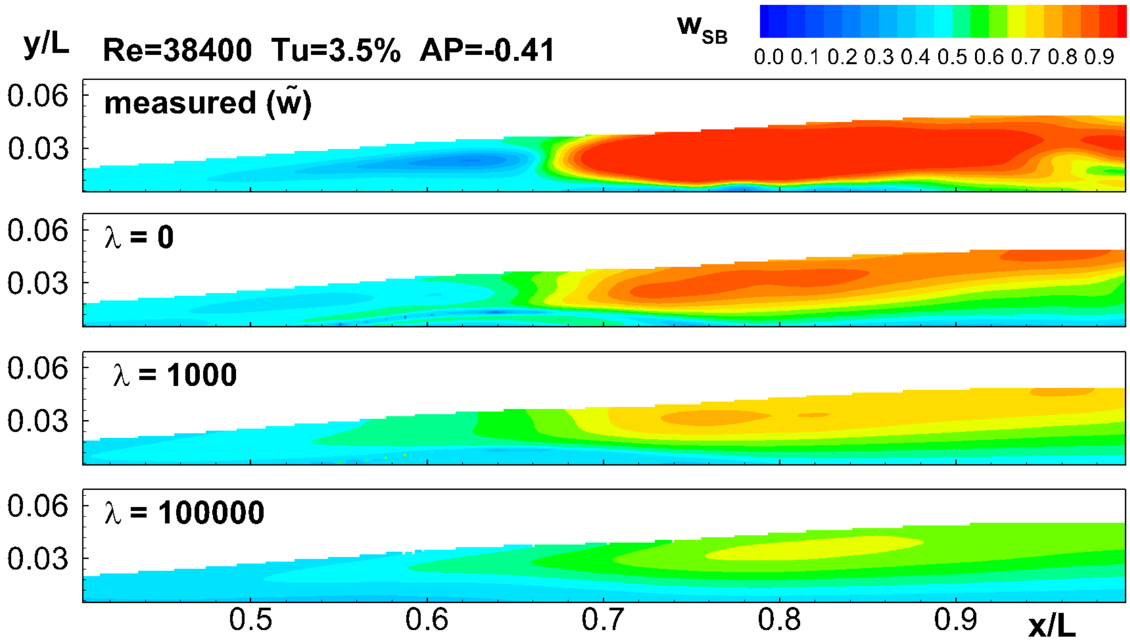

Figure 7.17: Modelled distributions of w_{SB} varying λ.

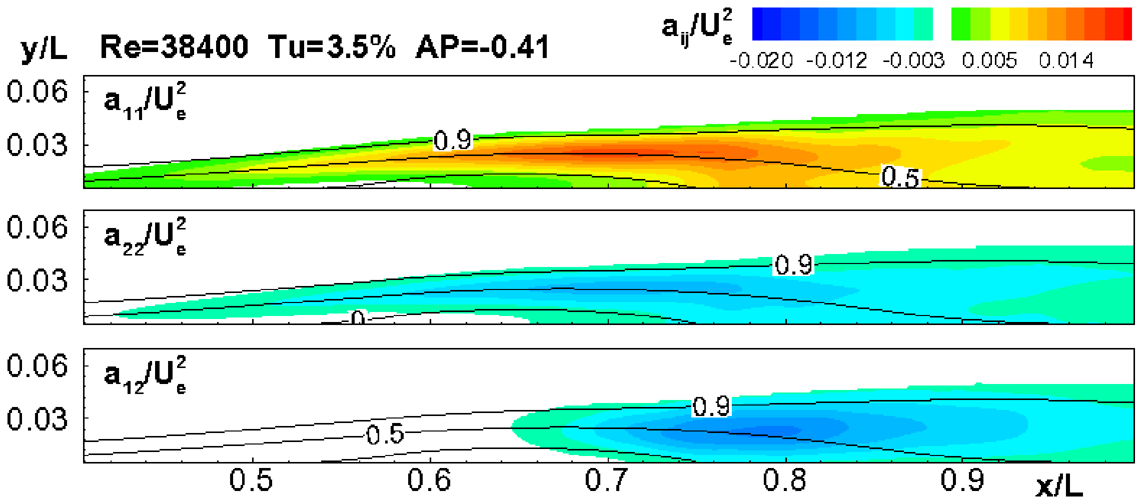

Figure 7.18: Measured time-mean anisotropy tensor components.

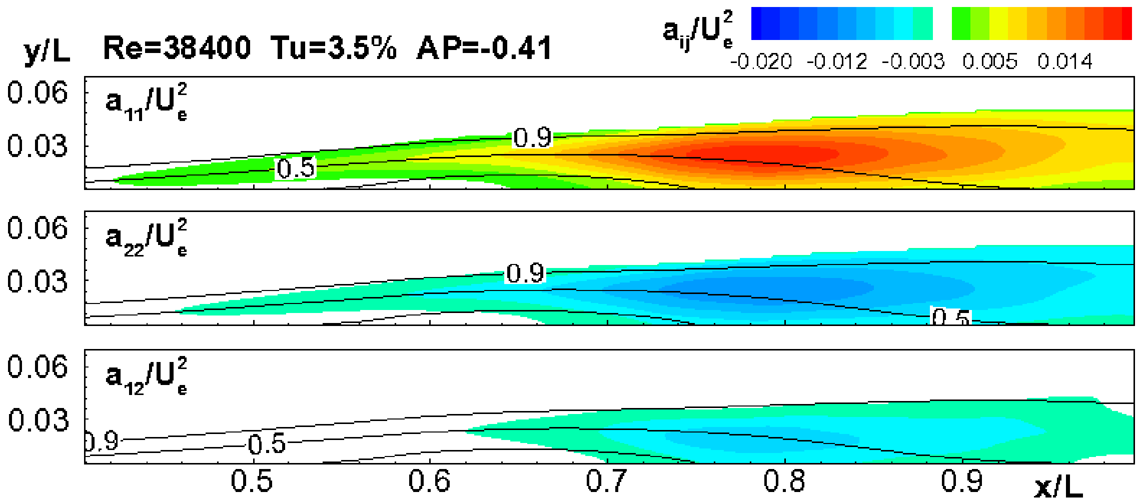

Figure 7.19: Time-mean anisotropy tensor components modelled with the long bubble model.

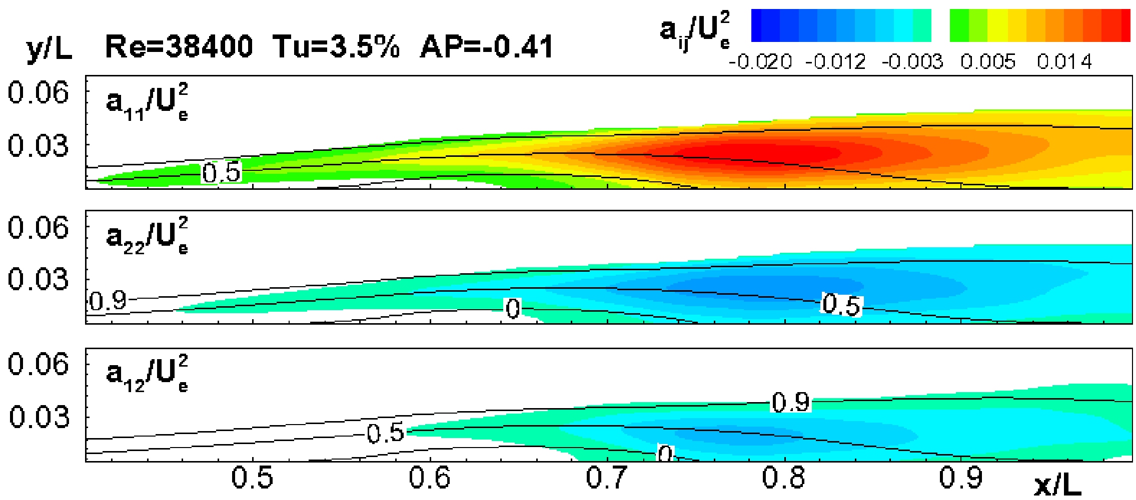

Figure 7.20: Time-mean anisotropy tensor components modelled with the short bubble model.

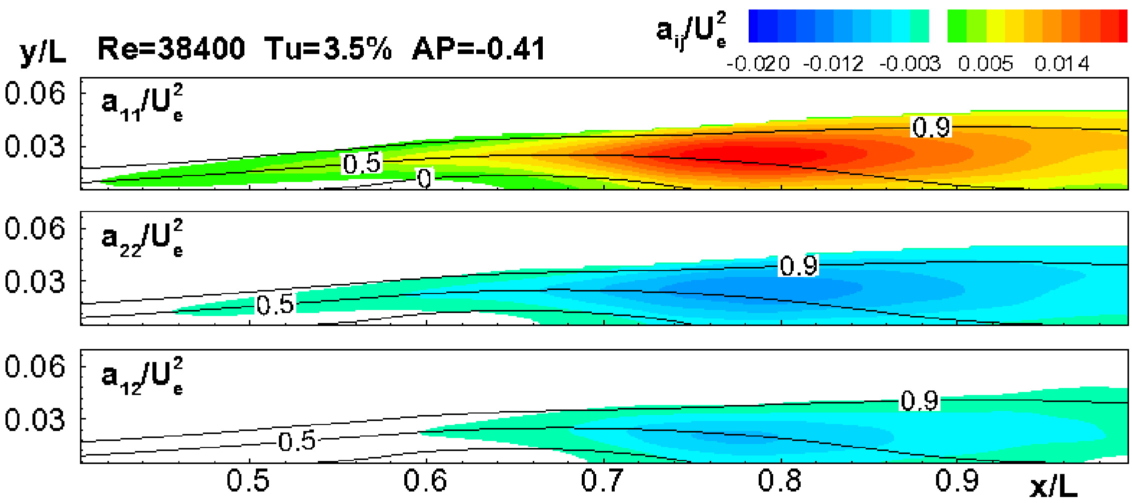

Figure 7.21: Time-mean anisotropy tensor components modelled with the merged model.

Table 7.13: Weighting function model predictors

Predictor	Coefficient	Uncertainty
cost.	0.45	0.26%
Re_k	0.11	0.5%
Π_2	0.025	4.2%
$Re_\Omega \Pi_6$	-0.015	3.5%
$\Pi_2 \Pi_5$	-0.046	4.2%
$\Pi_5 \Pi_k$	0.29	1.9%
$\Pi_k \eta_2$	0.052	9.2%
η_2^2	-0.085	2.7%

7.4 Tuning of Aggregated Turbulence Model for Separated Flows from Different Datasets

Leveraging the experience gained from previous work, this research effort sought to fully exploit the model aggregation process. The aim is to obtain an aggregated model that provides improved accuracy in modelling flow cases characterized by different dynamics, in this case pressure-induced and geometry-induced laminar separation bubbles.

7.4.1 Methodology

First of all, two independent sub-models for the prediction of the Reynolds stress tensor components were tuned with the pressure-induced separation bubble dataset (EXP-FP) and with the geometry-induced one (LES-T3L), respectively. They can be regarded as specialized for two different separated-flow scenarios, namely, a pressure-induced and a geometrically-induced condition.

In contrast to the previous works here presented, where the target of the tuning process was the normalized anisotropy tensor a^*_{ij}, the present work focused on tuning the correction to the Boussinesq hypothesis. The choice of varying the objective function was made to achieve better alignment with the literature and to assess whether fitting not the entire tensor, but rather the correction to the Boussinesq's hypothesis, could help obtain a sparser model. Consequently, the tuning target was:

$$b^*_{ij} = \frac{\tau_{ij} - \frac{2k}{3}\delta_{ij} + 2\nu_t S_{ij}}{k} \tag{7.5}$$

The turbulent viscosity ν_t was defined according to the $k-\omega$ SST model implemented in the software OpenFOAM, which is based in turn on the alternative definition presented by Menter in [141].

$$\nu_t = \frac{a_1 k}{\max(a_1 s, b_1 F_2 \sqrt{S_2})} \tag{7.6}$$

Where:

$$S_2 = 2I_1, \tag{7.7}$$

$$F_2 = \tanh(\arg_2^2), \quad a_1 = 0.31, \qquad b_1 = 1 \quad and \tag{7.8}$$

$$\arg_2 = \min\left(\max\left(\frac{2}{0.09}\cdot\frac{\sqrt{k}}{sy}, \frac{500\cdot 1.5\cdot 10^{-5}}{y^2 s}\right), 100\right) \tag{7.9}$$

Applying the Pope's expansion, b^*_{ij} can be expressed as:

$$b^*_{ij} = \nu'_t T^1_{ij} + \nu''_t T^2_{ij} + \nu'''_t T^3_{ij} \tag{7.10}$$

The modelling approach adopted in this work focuses on the tuning of the apparent viscosities ν', ν'' and ν'''. Differently from the previous work, in this study the predictor library used for training the sub–models was generated by including not only combinations of strain and rotation tensor invariants, but also Galilean–invariant physically–based flow features, as listed in Tab. 7.14. In particular, the invariants were combined up to the fourth order, while a set of linear and pairwise terms of the other features were considered. Numerical scaling factors were applied to selected features, and a hyperbolic tangent was used (for all features except η_1 and η_2) to ensure that predictor values remain bounded between 0 and 1. Following the approach proposed in Cherroud et al. (2022), the SBL algorithm was employed to identify the coefficients related to each predictor, taking advantage of its capability to identify a sparse representation of the model. Different models were tuned by imposing an increasing level of sparsity promoting coefficient. The accuracy was evaluated through the MSE computed as follows:

$$MSE = \sqrt{\frac{1}{N}\sum_{n=1}^{N}\Big(\sum_{i,j=1}^{2}\big(p_{ij}\Big(\frac{b^{*M}_{ij_n} - b^{*}_{ij_n}}{U_e^2}\Big)^2} \tag{7.11}$$

Where N is the number of spatial points in the domain, while p_{ij} is the weighting matrix defined as $p_{11} = p_{22} = 0.1$ and $p_{12} = 0.8$. This weighting matrix helps to promote models that can capture the a_{12} component, as described above for the MSE metric based on a_{ij}.

Table 7.14: Flow features for SBL.

Feature	**Definition**	**Feature**	**Definition**
Re_k	$\frac{\sqrt{k}y}{\nu}\cdot\frac{1}{500}$	Π_6	$\frac{\lvert\lvert S\rvert\rvert y}{\lvert\lvert U\rvert\rvert}\cdot$
Re_Ω	$\frac{\sqrt{I_2}y^2}{\nu}\cdot\frac{1}{10^3}$	Π_k	$\frac{\lvert\lvert S\rvert\rvert y}{\sqrt{k}}\cdot\frac{1}{10}$
Π_2	$\frac{\lvert\lvert\Omega\rvert\rvert y}{\lvert\lvert U\rvert\rvert}\cdot$	η_1	$\frac{\lvert\lvert\Omega\rvert\rvert^2-\lvert\lvert S\rvert\rvert^2}{\lvert\lvert\Omega\rvert\rvert^2+\lvert\lvert S\rvert\rvert^2}$
Π_5	$\frac{k}{\nu\lvert\lvert\Omega\rvert\rvert}\cdot\frac{1}{10^2}$	η_2	$\frac{k}{0.5U_iU_i+k}$

7.4.2 Flow Features Analysis

To provide a detailed view of the features role in the different scenarios, Fig. 7.22 shows the probability density function (pdf) of each of them computed in the separated shear layer (excluding the freestream region). They have been separately computed for the three different datasets: EXP-FP, LES-T3L and DNS-CDA. The plots highlight the range of variation of each feature and its recurrence among the different datasets.
The invariants I_1 and I_2 show similar distributions with a peak value around 0.125. A larger variance is observed in the EXP-FP with respect to the LES-T3L case, while for the DNS-CDA case distributions are not symmetric, almost mirrored between I_1 and I_2. A similar trend is shown by η_1 since it is a direct combination of the invariants. It is centered in zero for the EXP-FP and LES-T3L cases ($||S|| \approx ||\Omega||$), while it is slightly unbalanced toward positive values ($||\Omega|| > ||S||$) in DNS-CDA case, probably as effect of the flow turning imposed by the blade. The pdf of the other physics-based features (plotted in log scale because of the large range of variation) is characterized by similar distributions among the different datasets. Only minor differences can be noticed. The values of Re_k and Re_Ω appear to be lower in the LES-T3L than in the EXP-FP case, accordingly with what observed in Fig. 5.24. This may be related to the different initial conditions of the separating shear layer between pressure and geometry induced separation bubbles. Similar considerations can be done looking at the distributions of Π_2, Π_5 and Π_6. Instead,

the features Π_K, that exploits the ratio between the turbulent kinetic energy and the wall distance, and η_2, expressing the local turbulence intensity, exhibit similar most recurrent values.

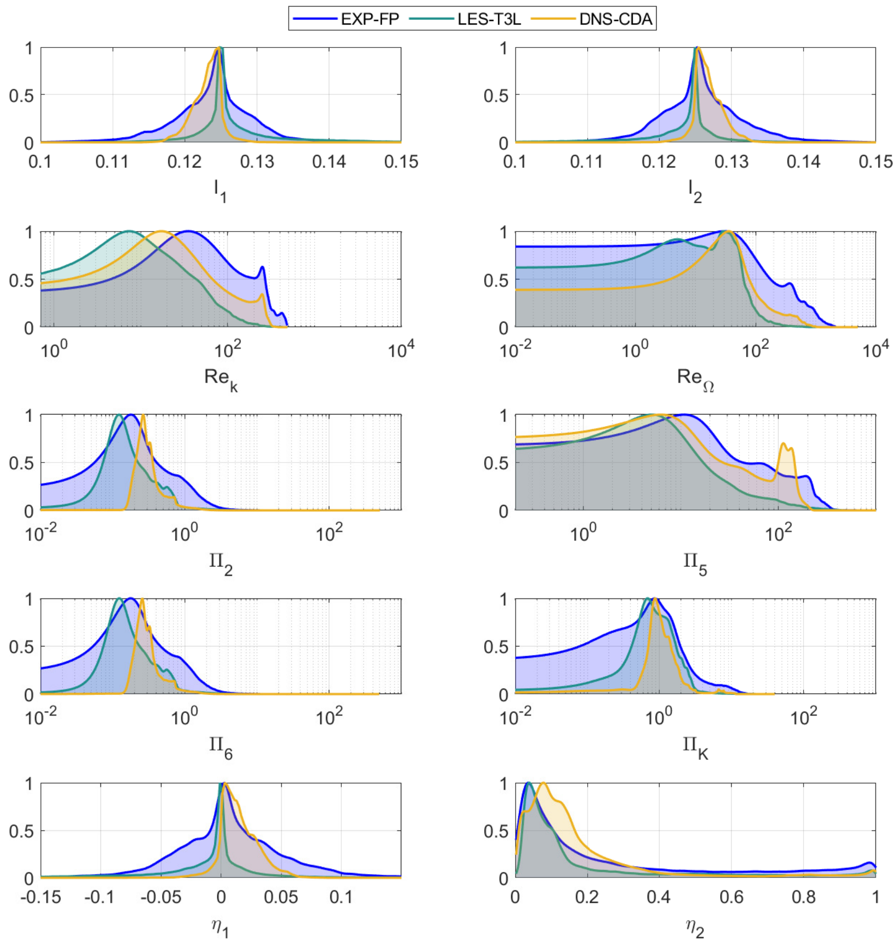

Figure 7.22: Probability density functions of the values assumed by flow features in the separated shear layer region for the different datasets.

The spatial distributions of the flow features showed many similarities between different cases of the different datasets, remarking a common behavior of the separated shear layer. For example, Fig. 7.23 reports the Re_Ω distributions (normalized with their maximum value) for two cases from EXP-FP dataset: (a) Re=56700, Tu=3.5%, AP=-0.41, (b) Re=44000, Tu=2.5%, AP=-0.41 and two cases from LES-T3L dataset (c) Re=3450, Tu=0.65%, (d) Re=6900, Tu=2.3%. Isolines at $U/U_e = 0, 0.5, 0.9$ are used to trace the time-mean separation bubble. It can be seen that, despite the magnitude depends on the flow condition (e.g., Reynolds number, freestream turbulence), normalized distributions conserves similarities between different datasets. Indeed, the Re_Ω distributions follow the mean shape of the bubble, growing in the fore part of the boundary layer and reaching a maximum almost in correspondence of the bubble maximum height in between the isolines at U/U_e=0.5 and 0.9, both for pressure and geometry induced separation bubbles. Similar considerations were found also for other flow features (not shown here for brevity).

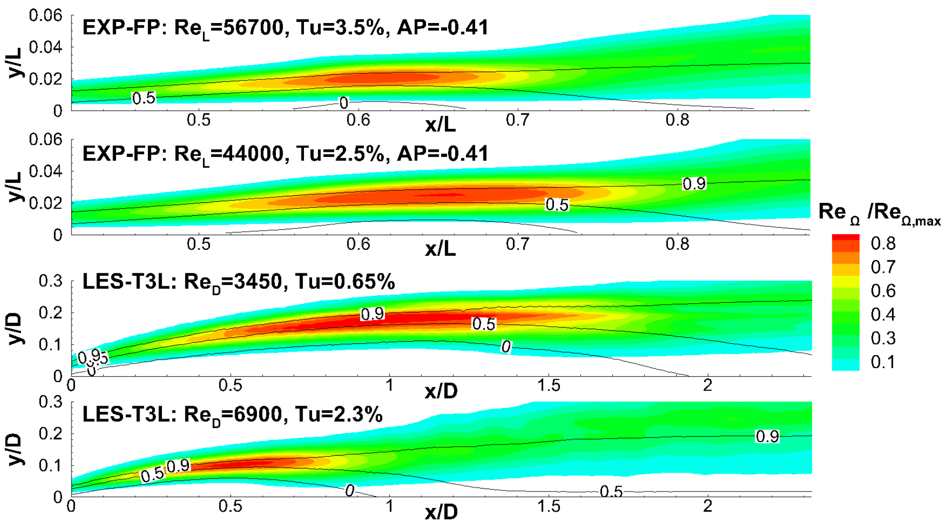

Figure 7.23: Spatial distribution of Re_Ω for four different cases from EXP-FP and LES-T3L datasets

7.4.3 EXP-FP and LES-T3L Models

For the EXP-FP dataset, the results of the tuning process are summarized in Fig. 7.24. The plot on the left shows predictors and coefficients that define models with an increasing number of terms (i.e., N=1,2,4,8). The bar plot on the right reports related performance on the training dataset in terms of deviation between modeled and measured b^*_{ij}. Bars are stacked by errors on shear and diagonal components. The first bar reports the errors when any b^*_{ij} model is used (that corresponds to the error of the linear closure). The model composed by N=8 predictors was found to provide the best performance on the EXP-FP dataset, while more complex models are prone to overfitting. The terms includes a constant (negative) correction on T^2_{ij}, a positive constant on T^3_{ij}, and further terms (mainly involving Re_Ω, Π_6 and Π_k) almost homogeneously spread over the three tensors T^1_{ij}, T^2_{ij} and T^3_{ij}. Increasing sparsity to force the model to leave only one term, it can be observed that the $const \cdot T^2_{ij}$ term is the most explicative one, as also previously observed in [21]. This term is able to capture the largest part of anisotropy along the separated shear layer, reducing the error on the diagonal components with respect to the linear closure. With increasing number of terms, further predictive improvements can be obtained on both diagonal and shear components.

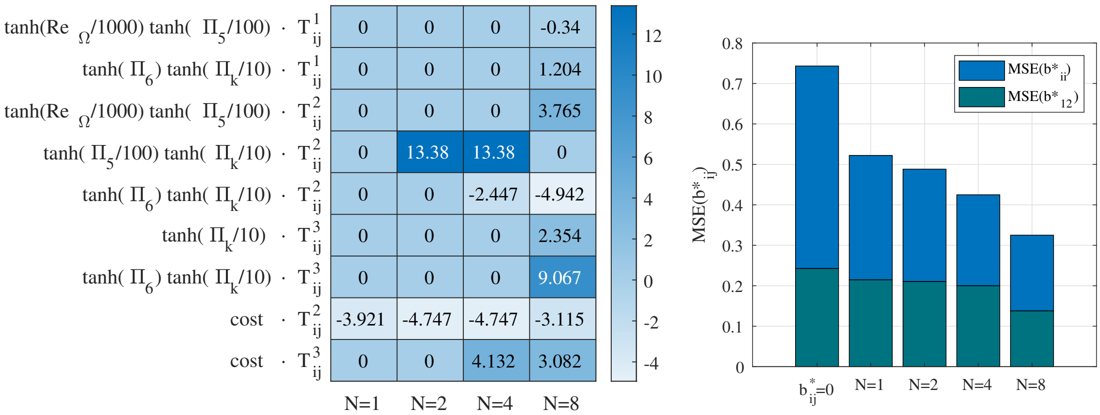

Figure 7.24: Model terms and coefficients (on the left) and reconstruction errors (on the right) for EXP-FP models with different levels of sparsity.

The same procedure was applied on the LES-T3L database. Figure 7.25 reports coefficients and performance on the LES-T3L dataset of the tuned models with N=1,2,4,8 predictors. The model with N=8 predictors again provide the best fitting, with improving predictions on the tensor diagonal components. Interestingly, the constant terms on T_{ij}^2 (negative) and T_{ij}^3 (positive) are again pointed out, together with a slight different combination of other terms (again mainly involving Re_Ω, Π_5 and Π_k). Increasing sparsity, the constant term on T_{ij}^2 leads again the model, further confirming that this correction to the linear case is dominant also for the case of geometry induced separation.

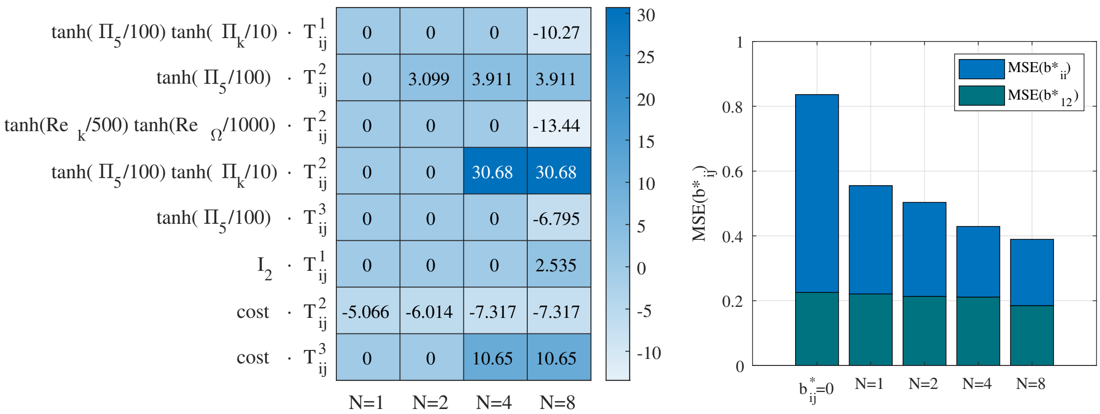

Figure 7.25: Model terms and coefficients (on the left) and reconstruction errors (on the right) for LES-T3L models with different levels of sparsity.

7.4.4 Aggregation Procedure of the EXP-FP and LES-T3L Sub-models

Model aggregation was then exploited to merge the models. This time the weights were defined in two different ways: if the true value of the extra-anisotropy tensor in a datum spatial position lies outside the predictions of the two sub-models, the best model (i.e. the one predicting a values closer to the real one) is selected, and a weight equal to 1 is assigned to the best model and 0 to the other. Otherwise, if the true value lies inside the values predicted by the two models, the weights were estimated by local predictive Gaussian gating functions, as defined in Eq. 4.15. The gating functions were defined by the residual between the stress components predicted by the k^{th} model M_k and the stress components from the experimental/numerical data b^*_{ij}. The hyperparameter σ_w, which controls the sensitivity to error estimation, was independently tuned through cross-validation.

$$\begin{cases} g_k = \exp\Big(-\frac{1}{2\sigma_w^2}\sum_{i=1}^{2}\sum_{j=1}^{2} p_{ij}(\frac{b_{ij}^{*M_k}-b^*_{ij}}{U_e^2})^2\Big) \\ w_k(x,\sigma_w) = \frac{g_k(x,\sigma_w)}{g_1(x,\sigma_w)+g_2(x,\sigma_w)} \end{cases} \tag{7.12}$$

A set of flow cases extracted from the EXP-FP and LES-T3L datasets and not included in the training process were selected to train the model for the weights. The tuning was performed on $w_1(x)$, i.e., the weight assigned to the sub-model predicting the EXP-FP dataset. The weight $w_2(x)$ can be computed from Eq. 4.13. In order to compute the weight distribution according to Eq. (4.13), the models of the EXP-FP and LES-T3L cases with 8 predictors were used. SBL was then applied to define the weighting function $w_1(x)$. For the weighting model, a second-order polynomial expansion of the only physics-based features were used to define the predictor library. The invariants I_1 and I_2 were excluded since they did not provide evidence for clustering the two stress models. Also in this step, as done in many classification problems [142], outputs were pre and post-processed with a sigmoid function $\sigma(z)$ to ensure $w_m(x) \in [0,1]$. The tradeoff between accuracy and generalizability was again discovered by cross-validation. Eq. (7.13) reports the equation learned for $w_1(x)$, defined through the sigmoid function $\sigma(z)$, whose sensitivity ℓ_s was determined within the cross-validation process. The model involves a combination of three features: Re_Ω, Π_5 and Π_6. Accordingly with the distributions of Fig. 7.22, $w_1(x) \to 1$ when Re_Ω, Π_5 and Π_6 assumes large values (as observed in the EXP-FP dataset). Thus, the aggregated model tends to prefer the model trained on EXP-FP dataset for large values of such features, while it favors the LES-T3L model where these features are small.

$$\begin{cases} w_1(x) = \sigma\Big(-0.38 + 0.36\,tanh\Big(\frac{Re_\Omega}{10^3}\Big) + 0.34\,tanh\Big(\frac{\Pi_5}{10^2}\Big) + 0.19\,tanh(\Pi_6)\Big) \\ \sigma(z) = \dfrac{1}{1+exp(-\ell_s z)}; \quad \ell_s = 10 \end{cases} \tag{7.13}$$

Figure 7.26 presents the comparison between the estimated weight, indicated here as

$\widetilde{w}_1$, and the modeled distributions $w_1(x)$ for two cases belonging to different databases. On the top, the weights for the EXP-FP case at $Re = 45000$, $Tu = 3.5\%$ and $AP = -0.27$ are presented, while the LES-T3L case at $Re_D = 6900$, $Tu = 5.6\%$ is shown at the bottom. Both the conditions belong to the validation set in their database (thus, they were not used for training). Contour lines of $U/U_e = 0, 0.5, 0.9$ are again reported to show the time-mean separation bubble structure. The distributions of the estimated weights are almost binarized due to the conditional scheme adopted for weight evaluation. As expected, in the first case, the EXP-FP model provides the best predictions, and $\widetilde{w}_1$ is close to 1 over almost the entire shear layer. However, there are some regions (e.g., close to the wall downstream of bubble reattachment) where the LES-T3L model locally provides better predictions. Conversely, in the second case, the $\widetilde{w}_1$ distribution is close to zero for large domain extension (the LES-T3L model provides the best predictions), except in the fore upper part of the separated shear layer. Indeed, even if the models are expected to have, on average, a lower prediction error when predicting a bubble belonging to its own dataset, this is not necessarily true across the entire domain. In this way, the predictions of the aggregated model may still have room for improvement compared to that of the two sub-models. The modelled distributions $w_1(x)$ capture the distributions of the estimated weights, smoothing the sharp passage between the models.
The weighting function was then tested on the DNS-CDA dataset, in order to evaluate its distribution with respect to input data of the compressor blade scenario. The plots in Fig. 7.27 shows that $w_1(x)$ tends to 1 in the separated shear layer on the blade suction side, for both the cases characterized by different Reynolds numbers. Thus, in the compressor blade application, the aggregated model tends to prefer the model educated with the EXP-FP data, accordingly with the greater similarity exhibited with the pressure-induced separation bubbles (see Fig. 5.24). Also in this case, a near-wall region downstream of bubble reattachment where the LES-T3L model provides a better accuracy is present. This is due to the fully turbulent condition of the boundary layer developing downstream of the reattachment position, which is a process well described in LES database (it is embedded into the data) while it is not well resolved by the PIV data.

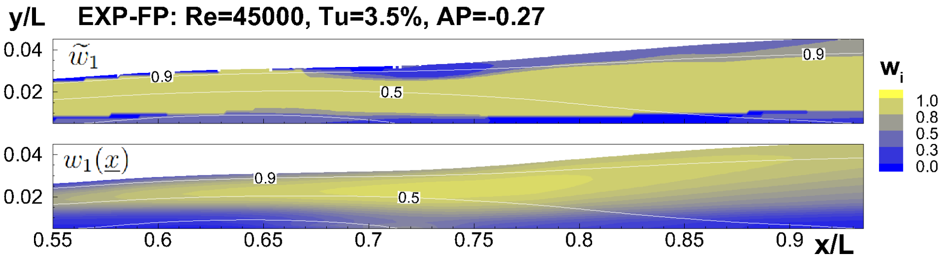

(a) EXP-FP case at $Re = 45000$, $Tu = 3.5\%$ and $AP = -0.27$

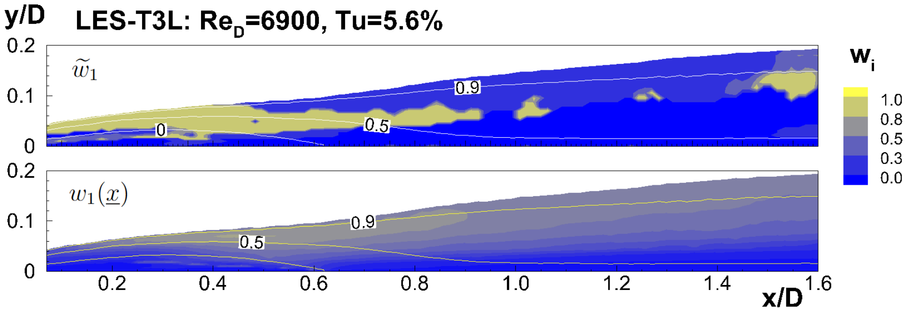

(b) T3L case at $Re_D = 6900$, $Tu = 5.6\%$

Figure 7.26: Comparison between estimated and modelled distributions of the weighting function for two cases among the EXP-FP and T3L datasets.

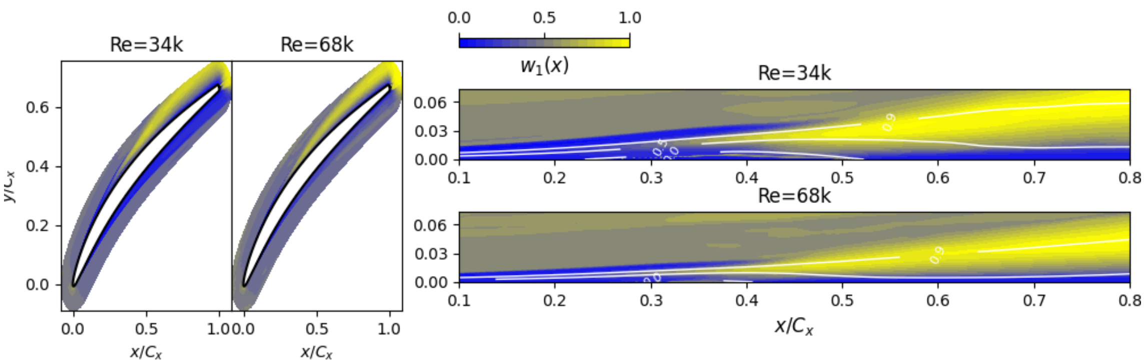

Figure 7.27: Modelled weight distributions $w_1(\underline{x})$ for the CDA cases at different Reynolds numbers.

7.4.5 Distribution of the Modelled Weighing Functions and Reynolds Stress Tensor Components

The aggregated model was used to predict the spatial distributions of the stress component for both with the validation set of the EXP-FP and LES-T3L datasets and the DNS-CDA data. Figure 7.28 shows the measured and modeled components of the anisotropy part of the Reynolds stress tensor (a_{ij}) for the EXP-FP case at $Re = 45000$, $Tu = 3.5\%$ and $AP = -0.27$, respectively. The aggregated model can accurately reproduce the anisotropy characteristics of the separated shear layer. This is made possible by the non-linear tensor expansion that allows for the misalignment of the principal axes of the stress and the strain tensors. The diagonal components a_{11} and a_{22} grow in the separated shear layer along the $U/U_e = 0.5$ isoline. The anisotropy character of the Reynolds stress tensor, represented by their different magnitude, appears to be well reproduced. Moreover, the modelled off-diagonal element a_{12} exhibits a maximum value that is correctly located approximately behind the axial position that corresponds to the bubble reattachment.
Figure 7.29 shows the analogous comparison between measured and modelled components of the Reynolds stress tensor for the LES-T3L case at $Re_D = 6900$, $Tu = 5.6\%$. The normal component a_{11} grows in the for part of the separated shear layer away from the wall. Also in this case, the strong anisotropy character is exhibited by the negative sign of the component a_{22}, while the shear stress component shows its peak almost in correspondence of the reattachment position. Both the magnitude and position of the high-stress region appear to be well reproduced by the modeled quantities. Moreover, in the bubbles belonging to the LES-T3L dataset, the high spatial resolution and the extended domain downstream of the bubble make it possible to observe the turbulent boundary layer that develops after the reattachment of the separated shear layer. This results in a region of high intensity of the a_{11} and a_{22} components near the wall downstream of the bubble. The model is also able to correctly capture this behavior.
Finally, the model has been tested on the two flow conditions belonging to the DNS-CDA dataset. Figs. 7.30 and 7.31 report the corresponding high-fidelity and modelled anisotropy tensor components. The aggregated model is again capable of accurately reproducing the Reynolds stress tensor components. In particular, the diagonal components a_{11} and a_{22} show very good agreement, highlighting the strongly anisotropic nature of the flow. The a_{12} component, which reaches its peak downstream of the maximum height of the bubble, is also well captured by the model. The contribution of the geometry-induced model near the wall allows the turbulent boundary layer downstream of the bubble reattachment to be correctly modelled. The model is also able to correctly reproduce the variations in the intensity of the components and in the location of their peak values as the Reynolds number changes.
To quantitatively assess the effectiveness of the merging process, Fig. 7.32 shows the MSE computed for the two validation subsets of the EXP-FP and LES-T3L datasets and for the test dataset that includes the DNS-CDA flow conditions. The prediction error was

computed with both the two sub-models and the aggregated one. The values of the MSE have been normalized by the maximum error computed for each dataset. As expected, the pressure-induced model outperforms the geometry-induced model when evaluated on flow cases from the EXP-FP dataset, whereas the opposite trend is observed for the LES-T3L dataset. However, the aggregated model provides the best overall performance across both the two cases. Instead, considering the DNS-CDA dataset, it can be noticed that the best performing sub-model is the EXP-FP model. This is in agreement with the weighting distribution (see Fig. 7.27), where the model educated with data of pressure-induced separated cases not only has a wider spatial dominance, but also performs better in the shear region. That region, indeed, is characterized by higher turbulent kinetic energy, and the absolute error carries a greater influence. The aggregated model effectively combines the two sub-models and provides the most accurate predictions, even with a margin of improvement over either sub-model.

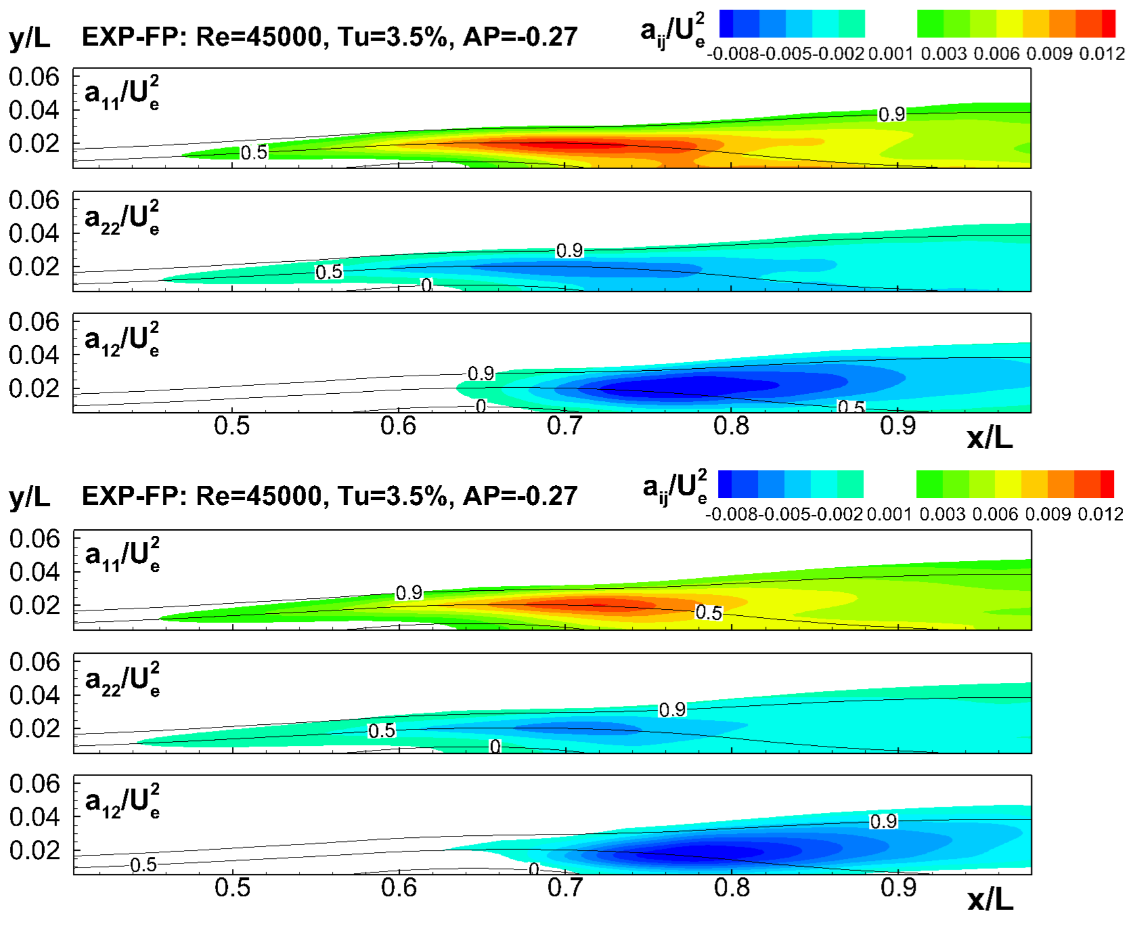

Figure 7.28: Comparison between measured (top) and modelled (bottom) distributions of the Reynolds stress tensor components for a validation case of the EXP-FP dataset.

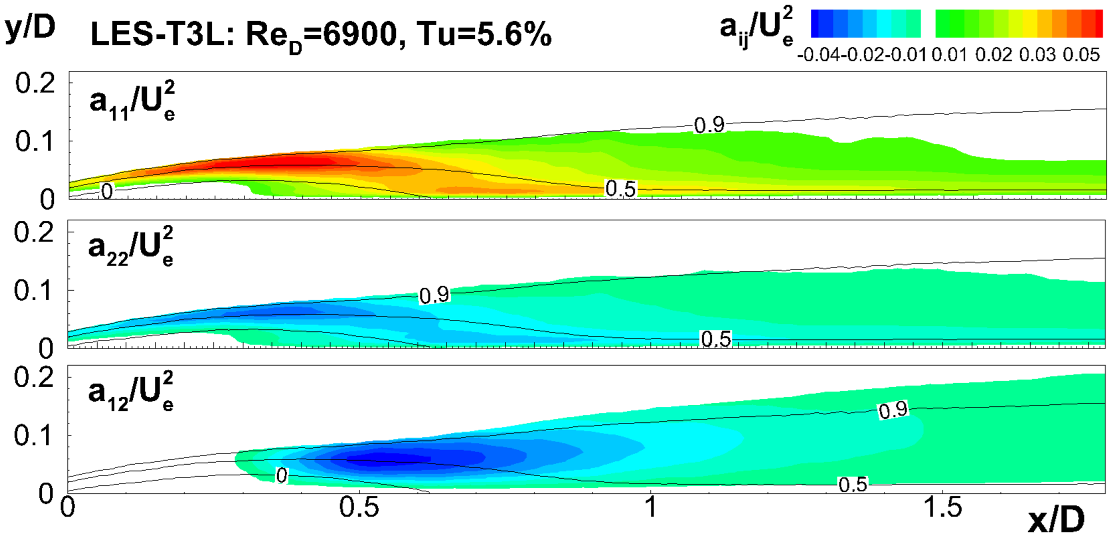

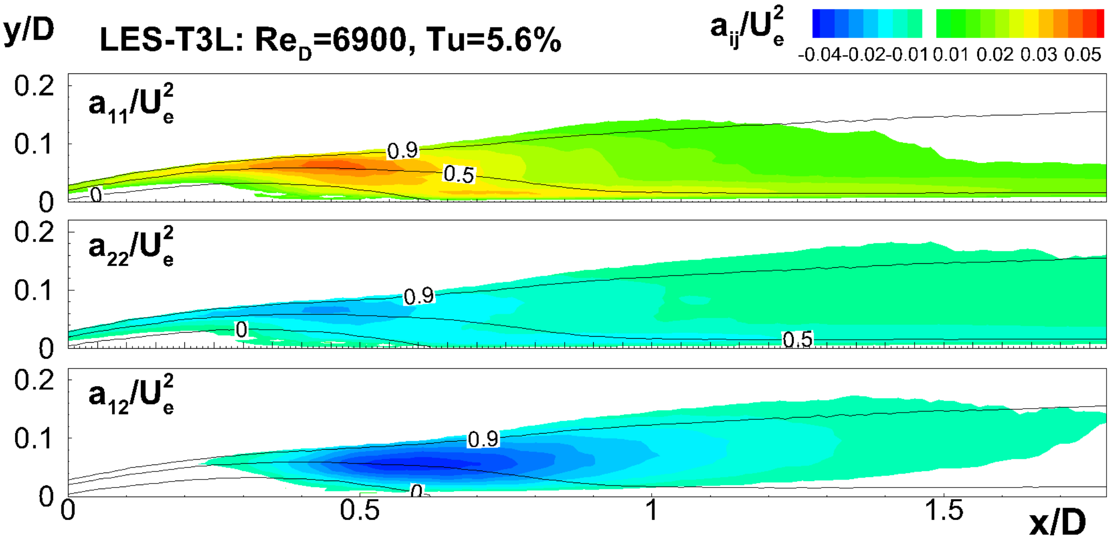

Figure 7.29: Comparison between high fidelity (top) and modelled (bottom) distributions of the Reynolds stress tensor components for a validation case of the LES-T3L dataset.

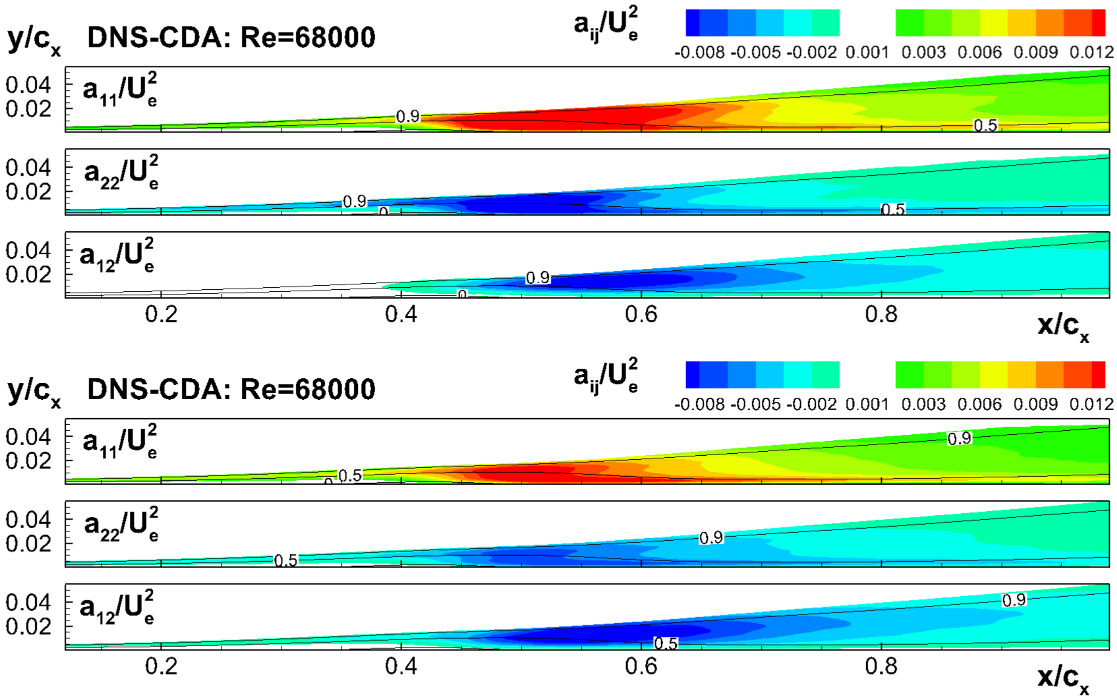

Figure 7.30: Comparison between high fidelity (top) and modelled (bottom) distributions of the Reynolds stress tensor components for the DNS-CDA case at $Re = 68000$.

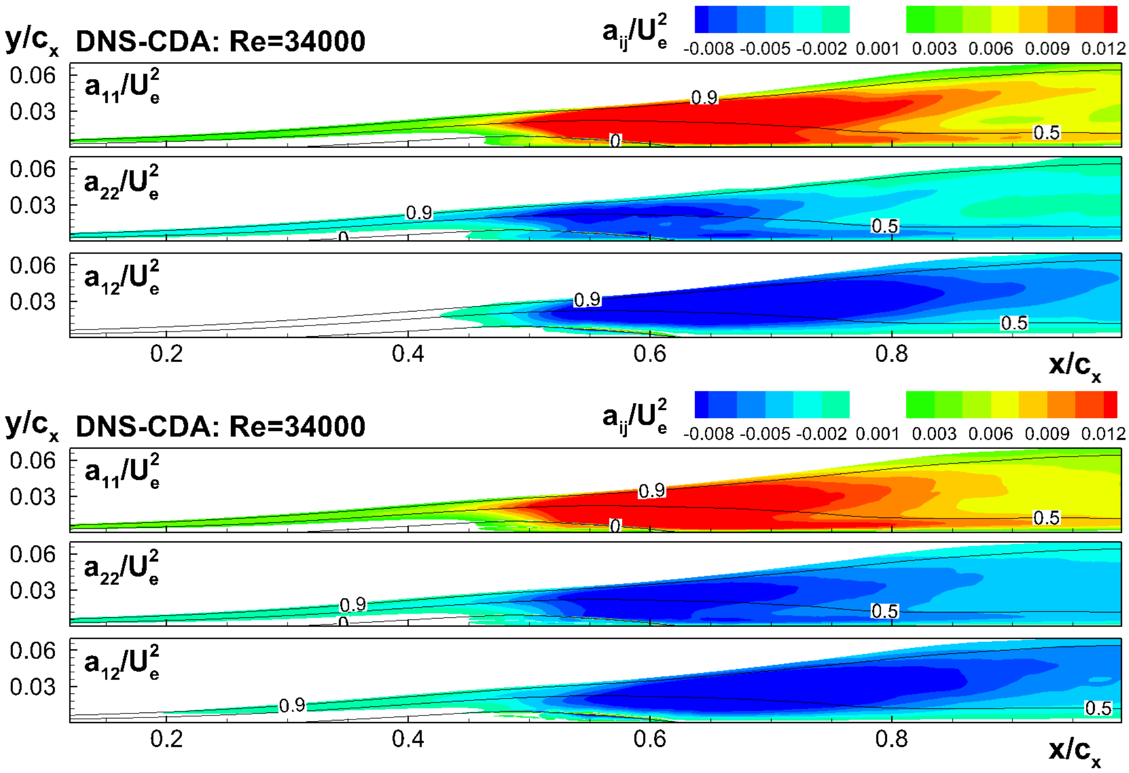

Figure 7.31: Comparison between high fidelity (top) and modelled (bottom) distributions of the Reynolds stress tensor components for the DNS-CDA case at $Re = 34000$.

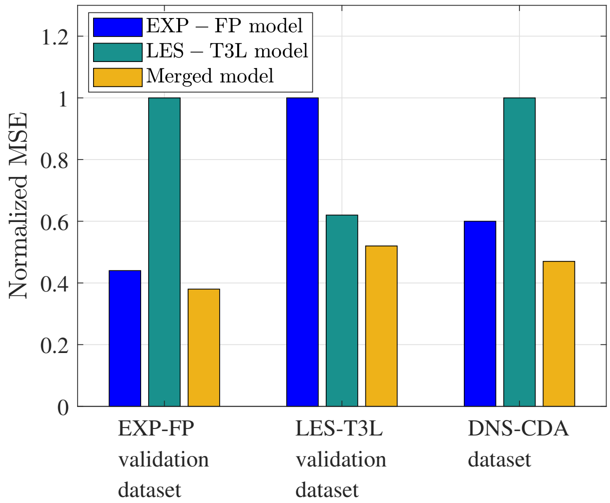

Figure 7.32: MSE computed applying the two sub-models and the aggregated model on a set of validation conditions for the three datasets.

7.5 Intermittency-Weighted Model

After exploring the possibility of aggregating different models, this final part of the work instead focuses on coupling a model suitable for predicting the Reynolds stress tensor with an algebraic model able to describe intermittency. As observed in Figs. 5.12, 5.13 and 5.14, the τ_{11} component begins to increase already within the separated shear layer. This behaviour is linked to the formation of streaky structures and low-frequency bubble oscillations, which, however, are not genuinely turbulence-related fluctuations. The associated risk is that, once the model is implemented in a RANS solver, it may trigger an artificially early transition due to excessive production of TKE in the upstream portion of the bubble. The intermittency model, once coupled with the turbulence model, is therefore tasked with dumping these oscillations.

7.5.1 Intermittency Function

To enable the training of the model, the two-dimensional intermittency field was first computed for all the different flow conditions. The availability of snapshots from the two databases (EXP-PIV and DNS-CDA) made it possible to statistically determine whether a spatial point belongs to a laminar, transitional, or turbulent state. An in-house code, based on the method proposed by [143], [144], was therefore applied to compute a 2D distribution, i.e., to assign a state value between 0 and 1 to each spatial position in the domain. Fig. 7.33 shows the distribution of γ obtained for the five conditions varying the flow parameter. Specifically, moving from the first to the second plot, the flow exhibits a higher level of turbulence. From the second to the third case, the main change is an increase in the Reynolds number. The transition from the third to the fourth plot highlights instead the effect of a reduced adverse pressure gradient, while the Reynolds number remains nearly unchanged. Finally, the last case is characterized by simultaneous increases in both Reynolds number and turbulence intensity compared to the previous configuration, accompanied by a weaker adverse pressure gradient. The isolines characterized by $U/U_e = 0, 0.5, 0.9$ are superimposed to the plot to highlight the position of the separation bubble. As expected, the intermittency value is zero within the laminar boundary layer and approaches unity in the free stream. In the separated shear layer, γ remains low until vortex formation triggers transition. This occurs around the location of maximum bubble height, downstream of which the intermittency rapidly becomes uniformly equal to 1. The last condition, which differs from the others since it corresponds to a very short bubble with a transition mode approaching the bypass process, exhibits a more extended laminar region. Furthermore, as can be seen by comparing the second and fourth plots from the top in Fig. 7.33 with the corresponding tensor components shown in Fig. 7.34 and Fig. 7.35, the magnitude of the streamwise component of the tensor begins to increase while the intermittency is still close to zero. This indicates that the mechanisms responsible for this growth are linked to low-frequency oscillations of the bubble and to the formation of streaky structures. These effects should therefore be filtered out to avoid an excessive production of TKE in the upstream portion of the bubble.

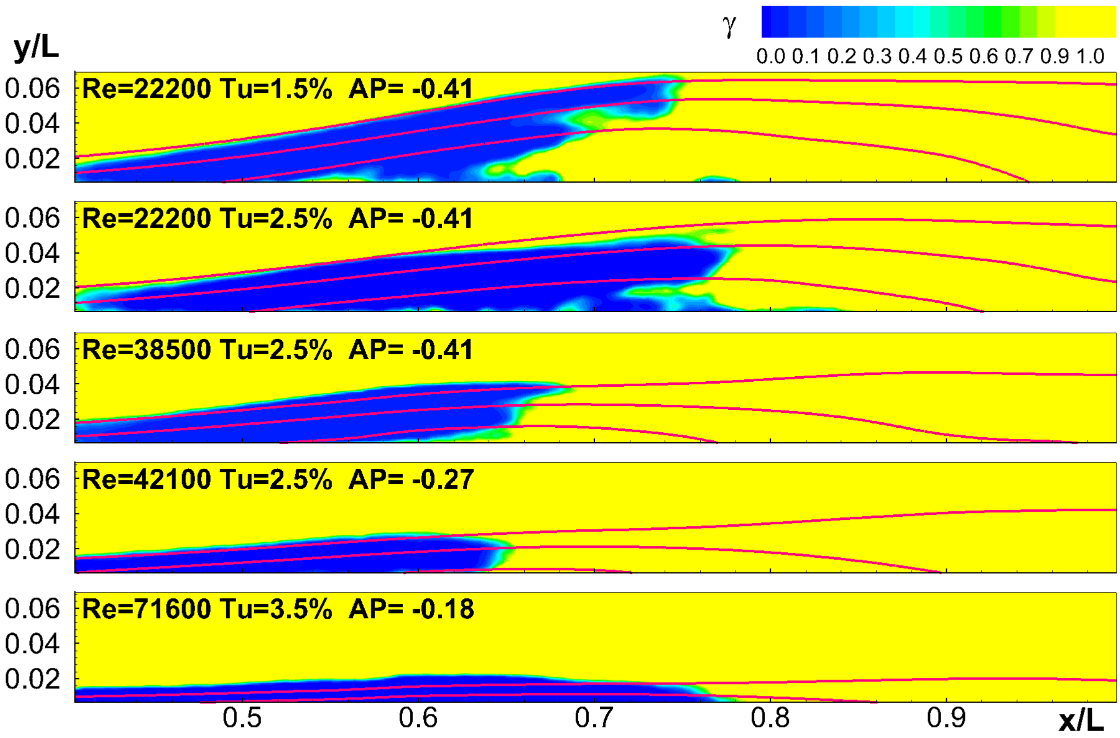

Figure 7.33: Intermittency distribution for different flow conditions.

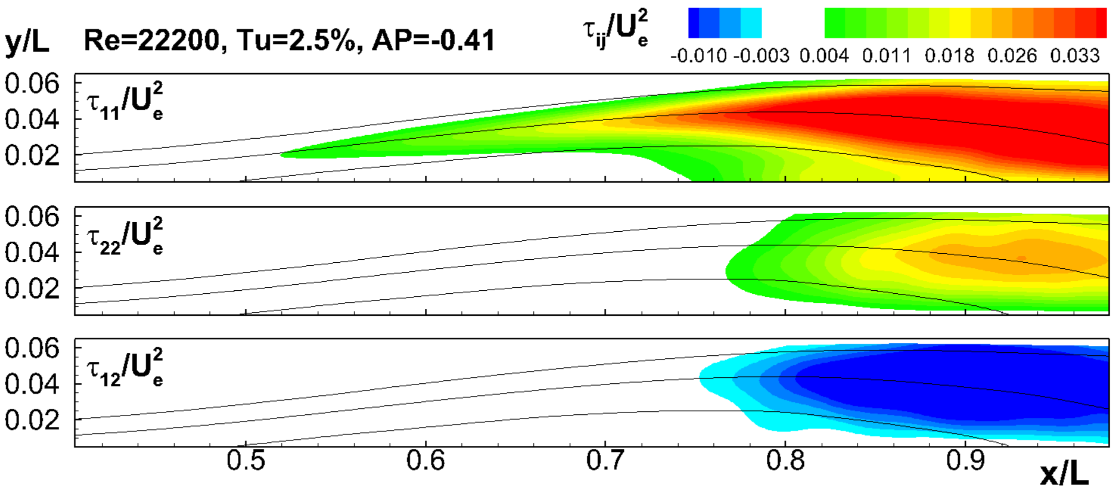

Figure 7.34: Time-mean Reynolds stress tensor components for a long bubble case. The black lines correspond to the isolines at $U/U_e = 0, 0.5, 0.9$ (from the bottom to the top).

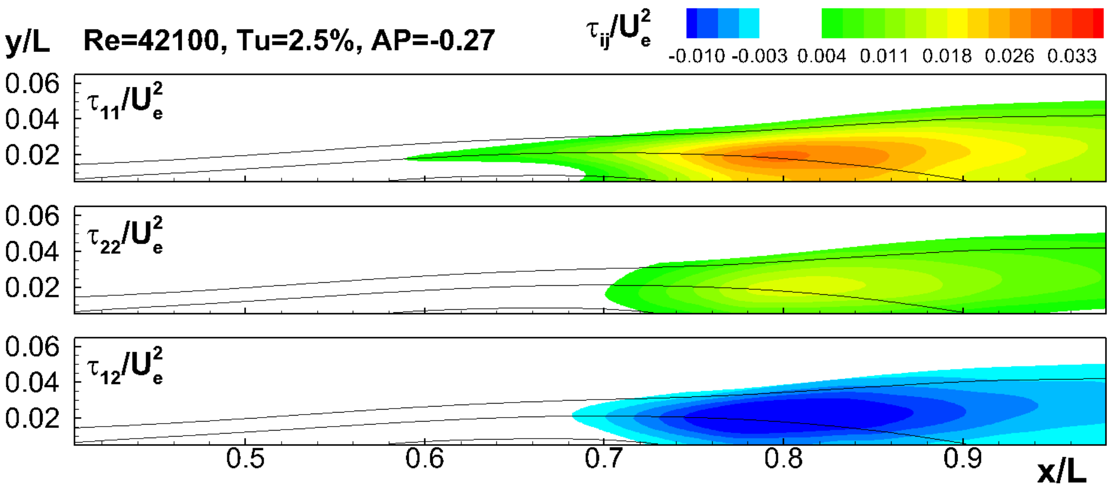

Figure 7.35: Time-mean Reynolds stress tensor components for a short bubble case. The black lines correspond to the isolines at $U/U_e = 0, 0.5, 0.9$ (from the bottom to the top)

7.5.2 Reynolds Stress Tensor Model

Before calibrating a model specifically designed for intermittency, an EARSM model for the prediction of the Reynolds stress tensor was first tuned. The tuning procedure was carried out as described in Sec. 7.4. Thus, after defining a training set and a validation set with a 70–30 split, the SBL algorithm was applied to fit the extra-anisotropy tensor b^*_{ij} (see Eq. 7.5). The calibration of a new model is justified by the fact that it is coupled with an intermittency model. Compared to the procedure followed previously, indeed, in addition to the regions corresponding to the free stream (identified where $U/U_e \geq 0.95$) also the laminar and transitional portions of the flow (identified where $\gamma \leq 0.95$) were excluded from the domain. This exclusion was intended to avoid forcing the model to fit points where an enhanced predictive capability is not required. In the turbulent freestream, baseline turbulence models already provide sufficient predictive accuracy, while in the laminar region, the intermittency function deactivates the turbulence model, making accurate prediction unnecessary. This approach allows the model to focus solely on the turbulent region downstream of the bubble, enhancing both its predictive performance and its simplicity. In this case as well, a comprehensive library was defined, consisting of combinations of invariants and flow features. Several models were trained by progressively increasing the sparsity-promoting coefficient. The higher the value of this coefficient, the more the algorithm produces models composed of a smaller number of predictors. The model accuracy was then evaluated by testing the obtained models on the validation set, adopting the Mean Square Error (MSE) as a metric for model performance. The model showing the best trade-off between accuracy and sparsity were selected. Tab. 7.15 reports the predictors that define the selected models, the associated coefficients, and the corresponding uncertainties. The model is formed by six predictors spread over the three tensor elements, but mainly associated to the tensor element T_{ij}^2. In particular, three physic-based predictors survive: η_2 associated to T_{ij}^1, $tanh(\Pi_5)tanh(\Pi_k)$ and $tanh(\Pi_6)tanh(\Pi_k)$ associated to T_{ij}^2. Moreover, the two constant terms associated to T_{ij}^2 and T_{ij}^3 are found to be relevant, as well as I_2 associated to T_{ij}^2.

Table 7.15: Pressure-induced laminar separation bubbles model predictors.

Tens.	**Feature**	**Coeff.**	**Unc.(%)**
T_{ij}^1 {	η_2	0.27	0.87
	const	−2.6	0.13
T_{ij}^2 {	I_2	−1.7	1.1
	$\tanh(Re_\Omega)\tanh(\Pi_5)$	2.4	0.24
	$\tanh(\Pi_6)\tanh(\Pi_k)$	−1.1	0.93
T_{ij}^3 {	*const*	2.1	0.64

7.5.3 Tuning of the Intermittency Model

Once tuned the Reynolds stress tensor model, similar steps were also applied to calibrate a coupled transition model, dedicated to reproduce the intermittency function among different separated flow cases. Also in this case, a training set and a validation set were defined, with a 70/30 split. The intermittency function has been pre-processed applying it the inverse of the hyperbolic tangent function *atanh* to define the target. In this way, the objective function is no longer restricted to the 0–1 interval. It has been observed that this pre-processing step enhances the predictive capabilities of the model. Let now G denote the output of the fitting, i.e., the function aimed at modelling the experimental distribution of $atanh(\gamma)$. The function G is therefore expressed as a linear combination of flow features. The predictor library was defined by combining the flow features listed in Tab 7.14, up to the second order, with the addition of two additional features:

$$Tu_L = min\left(100 \cdot \frac{\sqrt{2k/3}}{sy}, 100\right) \tag{7.14}$$

$$\lambda_{\theta_L} = -7.57 \cdot 10^{-3} \frac{dV}{dy}\frac{y^2}{\nu} + 0.0128 \tag{7.15}$$

These two features are derived from the intermittency transport equation introduced in the $\gamma - Re_\theta$ model by Menter [96], and represent an alternative formulation of the turbulence intensity and a local quantification of the adverse pressure gradient, respectively. The SBL algorithm was applied again to obtain different models by varying the sparsity-promoting parameter. All the tuned models were later applied to the validation set, thus allowing the identification of the best trade-off between accuracy and sparsity. In order to obtain the modelled distribution of γ_{mod}, i.e., rescale the output values within the 0–1 interval, the inverse of the *atanh* function must be applied to model. However, instead of using *tanh*, a sigmoid function was adopted. The advantage of the sigmoid is that it is bounded between 0 and 1, whereas *tanh* ranges from -1 to 1. When modelling experimental points for which $atan(\gamma) \approx 0$, the model, being inherently imperfect, may return slightly negative values, which would remain negative if *tanh* were applied. Hence, the final expression of the modelled intermittency is:

$$\gamma(x)_{mod} = \frac{1}{1+e^{-h(G-m_0)}}, \tag{7.16}$$

Where the function G is the actual output of the tuning. The selected model for G consists of only four predictors. Besides the constant term, the surviving predictors are $tanh(Re_k)$, $tanh(\Pi_5)$ and $tanh(\Pi_k)Tu_L$. Interestingly, Π_5 survives, since it acts as a sensitive function for transition. Similarly, Tu_L (multiplied by Π_k) also survives, as it is primarily sensitive to the local turbulence intensity. The expression of G therefore is:

$$\begin{aligned} G = 0.18 &+ 0.23 \cdot \tanh(Re_k) \\ &+ 3.94 \cdot \tanh(\Pi_5) \\ &+ 0.32 \cdot \tanh(\Pi_k) Tu_L \end{aligned} \tag{7.17}$$

The introduction of the sigmoid function brings the two additional hyperparameters h and m_0. In particular, h controls the sensitivity of the intermittency to the function G, while m_0 represents the threshold of G at which the intermittency equals 0.5. In this work, $h = -10$ and $m_0 = 2$ were chosen as the set of parameters. These values were obtained after an additional iterative process aimed at minimizing the prediction error.
As it will be further confirmed later, this equation should consequently provide accurate results only based on mean flow quantity related features, thus avoiding applying time-consuming γ-function detection techniques that also require availability of instantaneous fields.

7.5.4 Validation on the Flat-Plate Dataset

This section presents the results concerning the predictive capabilities of the models of both the intermittency and Reynolds tensor models once applied to the validation set. It is worth stressing that this set of data did not participate in the tuning but should be considered an interpolation set. Figs. 7.36 and 7.37 show the measured and predicted intermittency distributions for three conditions belonging to the validation set. The first case (on top of Fig. 7.36 and 7.37) features a medium–low Reynolds number, an intermediate turbulence level, and a strong adverse pressure gradient, which together lead to the formation of a long separation bubble. The second case is characterized by higher Reynolds number and turbulence intensity, resulting in a shorter bubble size. The third case corresponds to an even shorter bubble, primarily due to the weaker adverse pressure gradient. The comparison between Figs. 7.36 and 7.37 reveals that, irrespective of the bubble size produced by the different combinations of the flow parameters, the intermittency model accurately reproduces the observed behavior. The extent of the laminar region, associated with $\gamma = 0$, is consistent with the mean bubble shape, highlighted by the $U/U_e = 0, 0.5, 0.9$ isolines. Indeed, the flow is predicted in a laminar condition in the recirculating flow region as well as in the fore part of the separated shear layer, prior to the bubble maximum height position. The onset of transition, i.e. the streamwise location where the intermittency starts rising from 0 within the separated shear layer, is accurately captured in all three conditions close to the bubble maximum height, with only the intermediate case showing a slightly delayed transition process. The freestream region is also correctly predicted with $\gamma = 1$. Downstream of the bubble maximum height, where vortex formation has already rendered the flow fully turbulent, the model appropriately returns $\gamma = 1$ even throughout the rear part of the separated shear layer.

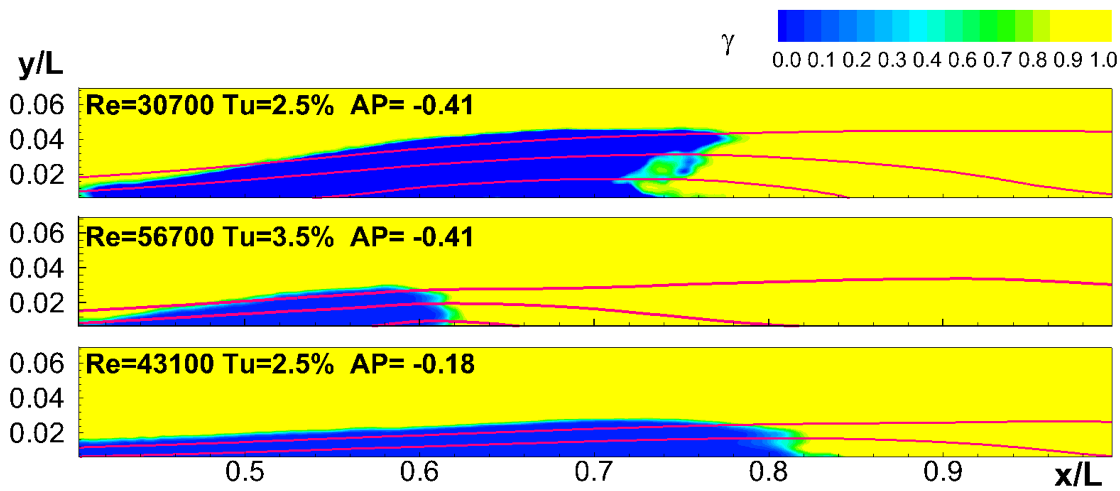

Figure 7.36: Measured distribution of the Intermittency function for three flow conditions within the validation set

In all three cases the model dumps fluctuations at the edge of the boundary layers, as made evident by a thicker blue area characterizing the modelled distribution as compared with the measured one. However, once adopted in RANS applications this discrepancy

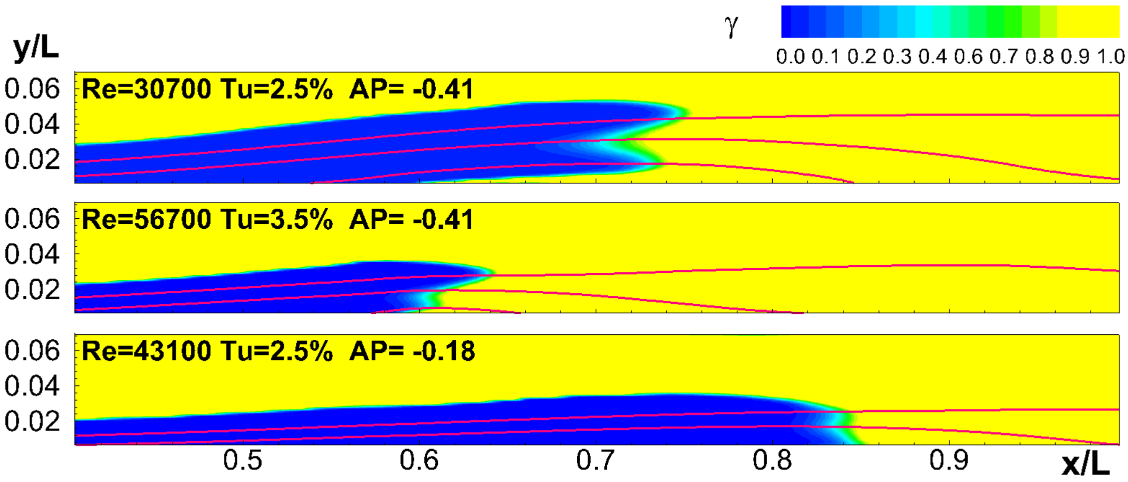

Figure 7.37: Modelled distribution of the Intermittency function for three flow conditions within the validation set

is expected to induce a relatively minor impact compared with accurately predicting the separation location.
The predictive capabilities regarding the Reynolds stress tensor components are illustrated through the representation of the product between the intermittency γ and the tensor components themselves. This approach makes it possible to assess the model ability to filter out streamwise velocity fluctuations associated with streak formation and pre-transitional low-frequency oscillations. For this purpose, the top plots of Fig. 7.38, 7.39 and Fig. 7.40 show the measured components of the product $\gamma \cdot \tau_{ij}$ for the three conditions in the validation set just shown in Figs. 7.36 and 7.37, while the bottom plots present the corresponding modelled components. In this way, the intermittency function activates the turbulence model prediction only in the rear part of the separated flow region in accordance with what discussed from Fig. 7.37. Comparing the modelled and measured component of the Reynolds stress tensor sheds light on the model accuracy. In particular, the spatial distribution of all three components of the tensor is correctly reproduced for all three conditions. Specifically, it can be observed that they reach their maximum downstream of the region corresponding to the bubble maximum height. The three components are correctly scaled relative to each other, and the peak intensity values are in good agreement with the experimental measurements. In addition, the model can respond appropriately to the variation of flow parameters, adjusting the component distributions accordingly. The model is also able to effectively limite velocity fluctuations in the pre-transitional region of the shear layer, thereby preventing the tensor effect from being activated too early.

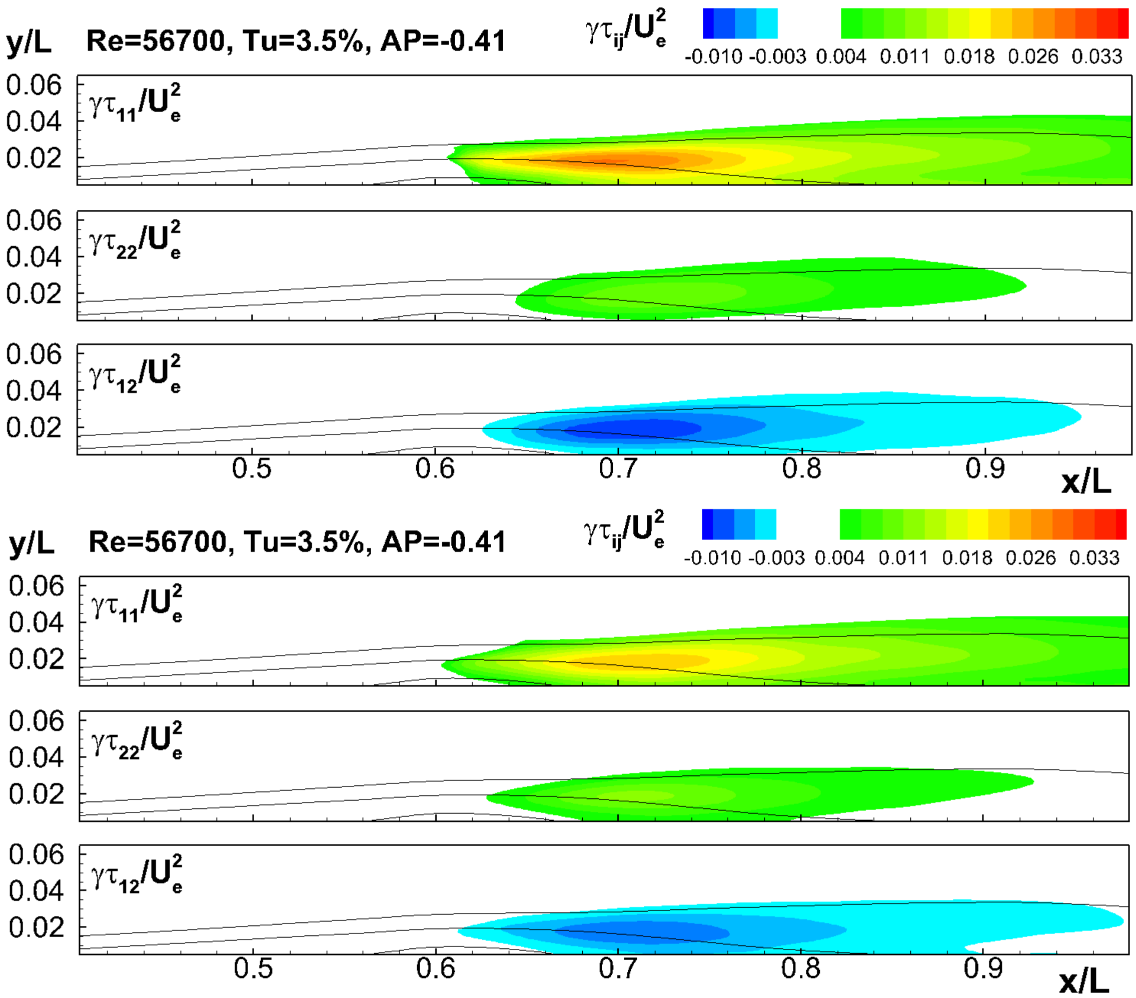

Figure 7.38: Comparison between measured (top) and modelled (bottom) distributions of the Reynolds stress tensor components for the experimental case at Re = 56700, Tu = 3.5% and AP = −0.41.

7.5.5 Test on CDA

The predictive capabilities of the model were finally assessed by applying it to the two DNS compressor-blade conditions (see Sec. 5.3). Since these cases lie outside the datasets used for training and validation, they allow evaluating the model performance in extrapolation. Specifically, Fig. 7.41 shows the comparison between the measured (top) and modelled (bottom) product of intermittency and Reynolds stress components for the low Reynolds number condition ($Re = 34k$), while Fig. 7.42 presents the same comparison for the high Reynolds number condition ($Re = 68k$). An increase in Reynolds number results in a shorter separation bubble, as expected. Since the Reynolds stress components

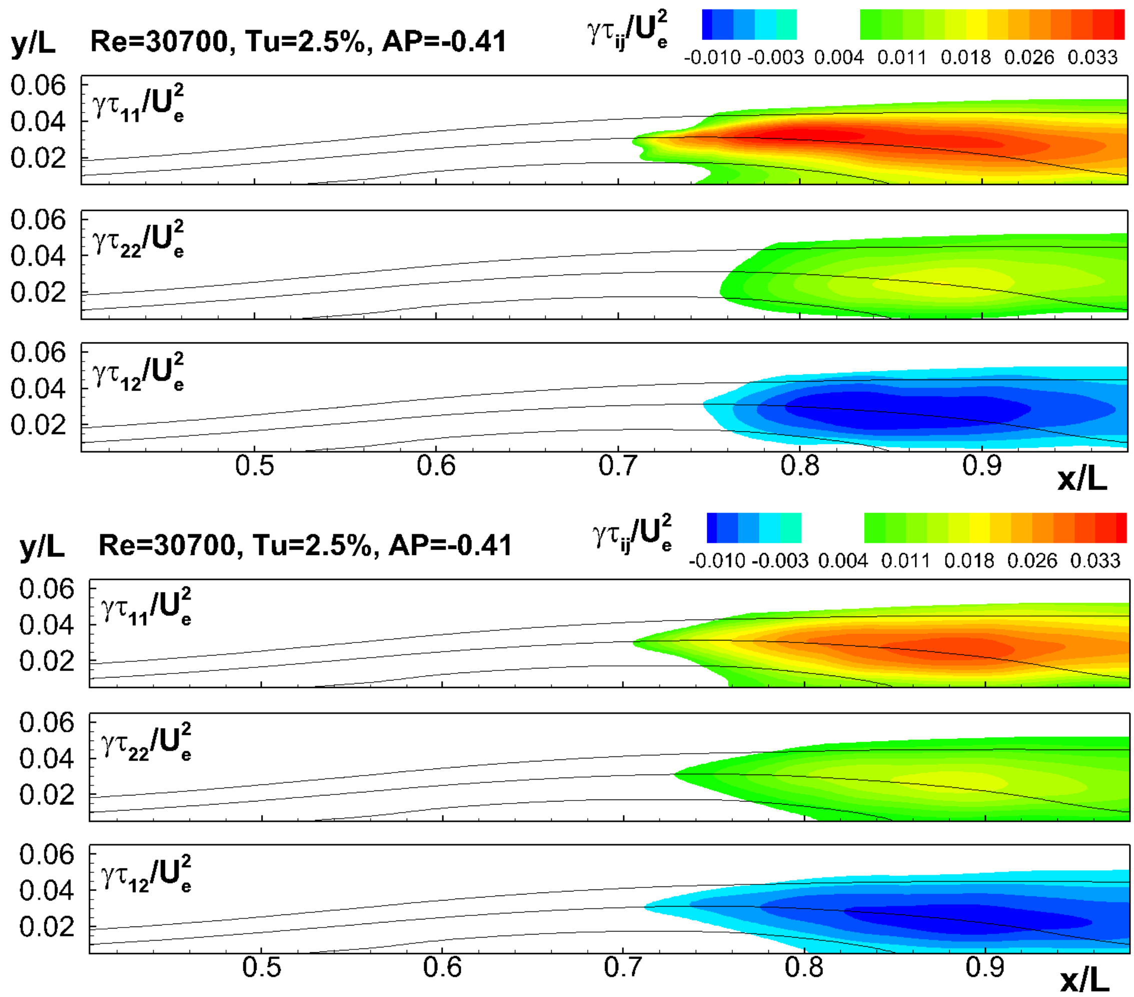

Figure 7.39: Comparison between measured (top) and modelled (bottom) distributions of the Reynolds stress tensor components for the experimental case at Re = 30700, $Tu =$ 2.5% and AP = -0.41.

reach their maximum just downstream of the bubble maximum height position, the peak displayed by the model responds accordingly: both normal and shear stress peaks in Fig. 7.41 are localized downstream of the peaks observable in Fig. 7.42. Consistently with what was observed for the experimental dataset, the normalized components exhibit a higher peak value at lower Reynolds numbers, or, equivalently, for larger separation bubbles. In both cases, the predictions are good for all three components, both in terms of the location of the peak and its magnitude. A slight underestimation of the maximum values is generally observed, but the model still succeeds in effectively scaling the components as a consequence of the variation of the flow Reynolds number in a real application that

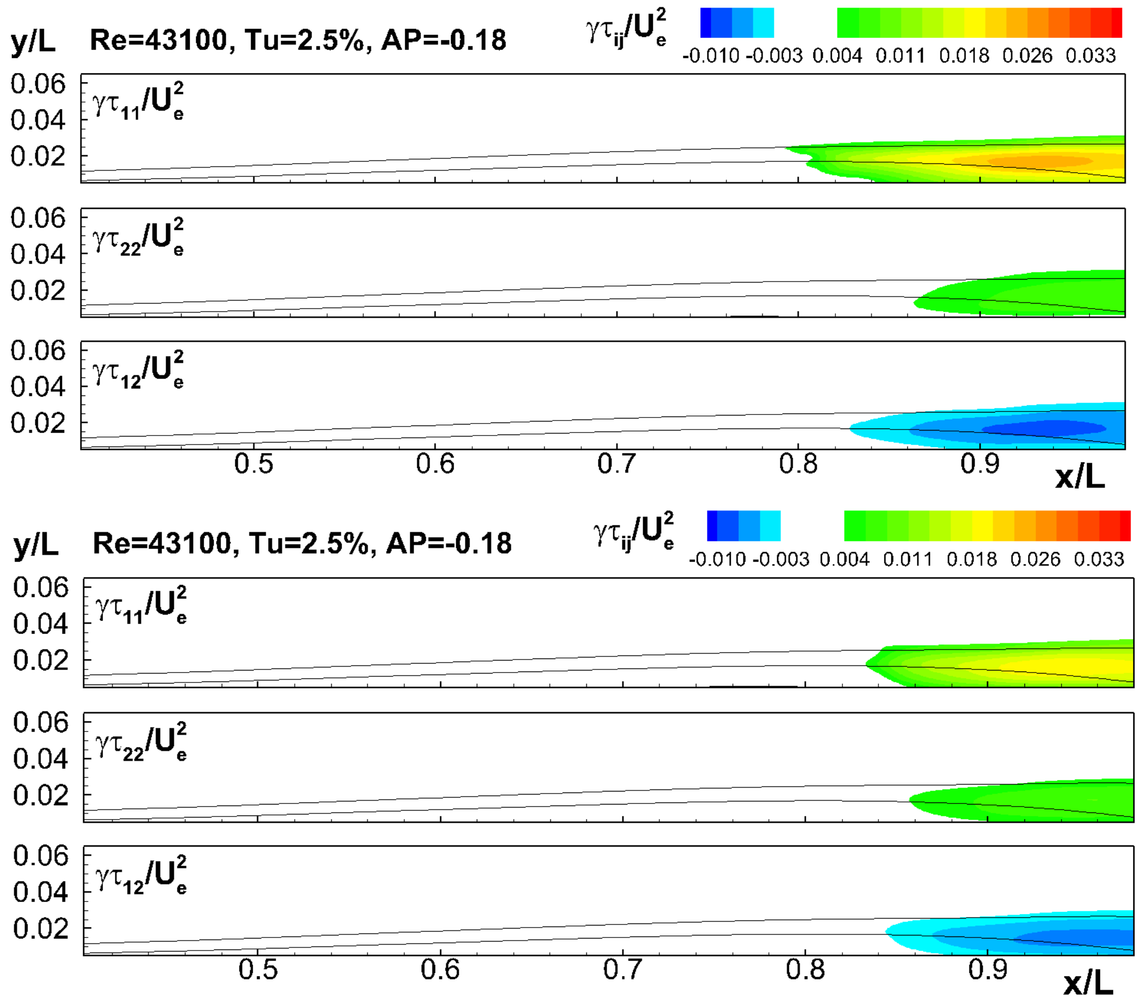

Figure 7.40: Comparison between measured (top) and modelled (bottom) distributions of the Reynolds stress tensor components for the experimental case at Re = 43100, Tu = 2.5% and AP = −0.18.

did not participate to the tuning. Finally, even in this case the model is able to prevent premature growth of the streamwise component of the tensor within the front part of the separated shear layer, thus further strengthening the ability of the model in adequately capturing the transition onset position. This makes the model also a usefull 0-D tool for the inspection of the propagation of the transition process (with the algebraic relation easily provided for the intermittency by Eq. 7.17) or the complete turbulent field.

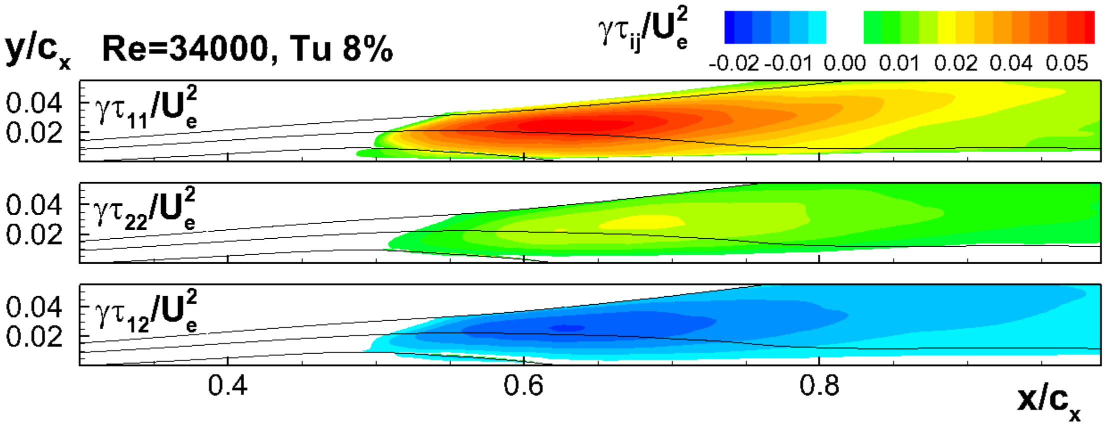

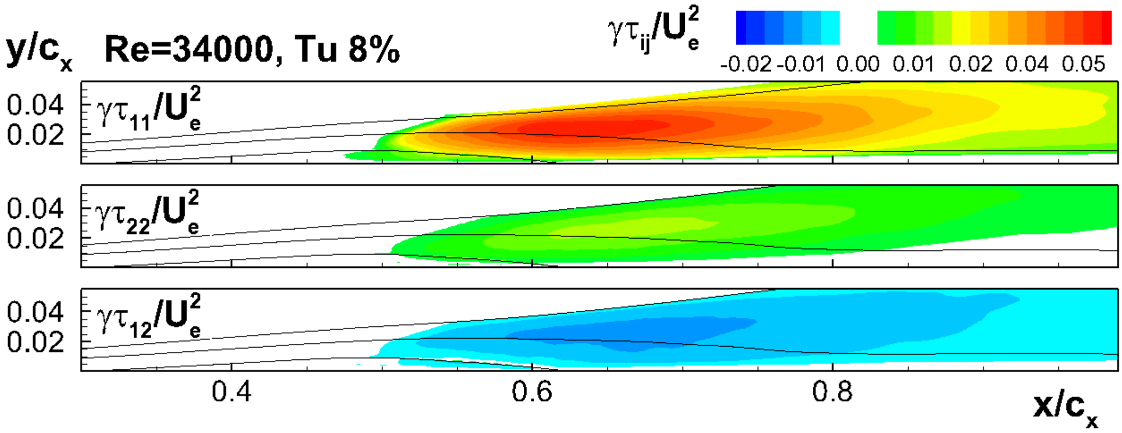

Figure 7.41: Comparison between measured (top) and modelled (bottom) distributions of the Reynolds stress tensor components for the DNS CDA case at Re = 34000 and $Tu = 8\%$.

7.6 Comparison with Existing Constitutive Models

To further assess the predictive performance of the present model, a quantitative comparison was carried out against several turbulence closures available in the literature. In particular, the proposed constitutive relation was evaluated against:

- The long-bubble model previously described in Sec. 7.2.1.1 [54];
- The linear eddy-viscosity formulation underlying the SST k–ω model by Menter [94];
- Pope's EARSM model [10];
- The implicit algebraic model proposed by Launder et al. [145];

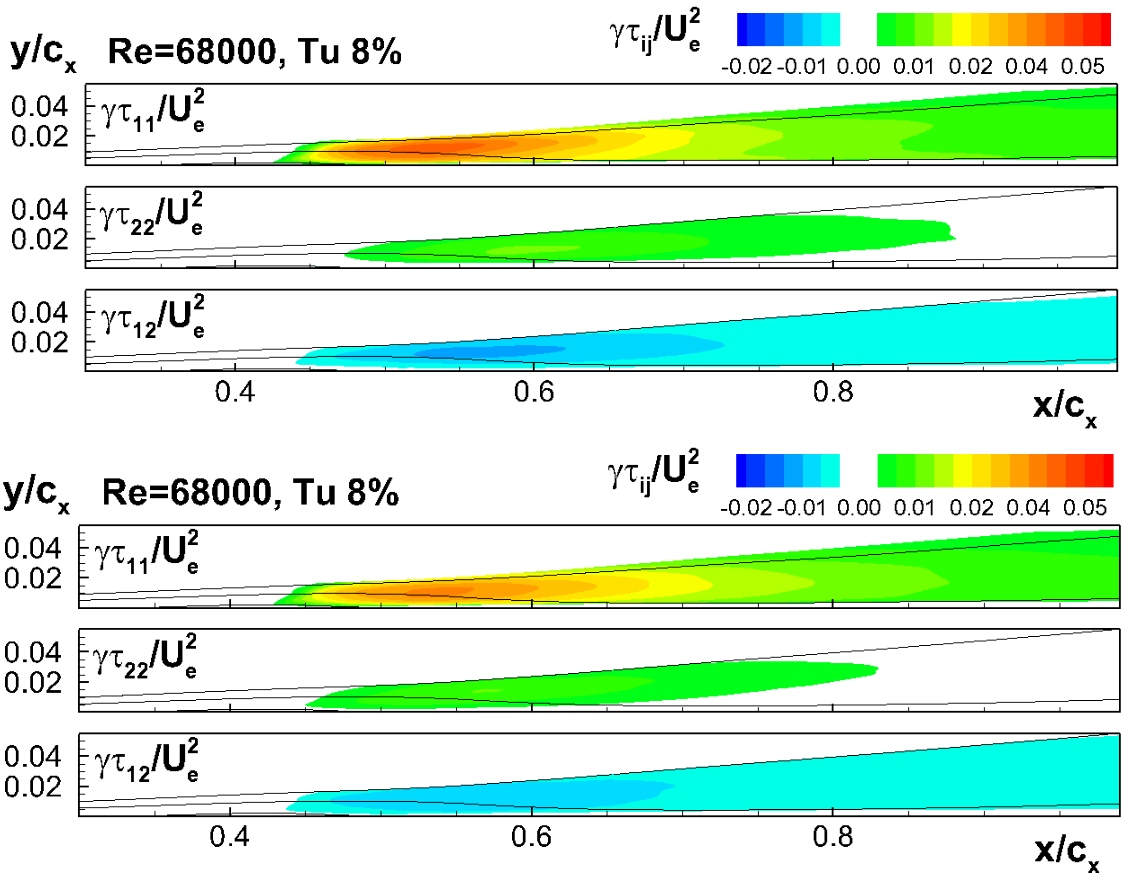

Figure 7.42: Comparison between measured (top) and modelled (bottom) distributions of the Reynolds stress tensor components for the DNS CDA case at Re = 68000 and $Tu = 8\%$.

- The EARSM formulation proposed by Wallin and Johansson [17].

All comparisons were performed by evaluating the constitutive relations on the frozen high-fidelity mean flow field obtained from the DNS simulations. Model accuracy was quantified through the mean squared error (MSE), computed separately for the normal and shear components of the Reynolds stress tensor in the region corresponding to $\gamma > 0.95$.
Figure 7.43 reports the MSE values for the normal (blue bars) and shear (red bars) components for the two DNS-CDA cases. The results indicate that all models provide comparable predictions of the shear stress component, as shown by the relatively small values of the corresponding MSE. In this respect, the present model performs at a level comparable to the best-performing approaches. A clearer distinction emerges for the normal stress components. The largest errors are observed for the SST k–ω model, whose linear constitutive relation, primarily calibrated for shear stress prediction, does not accurately

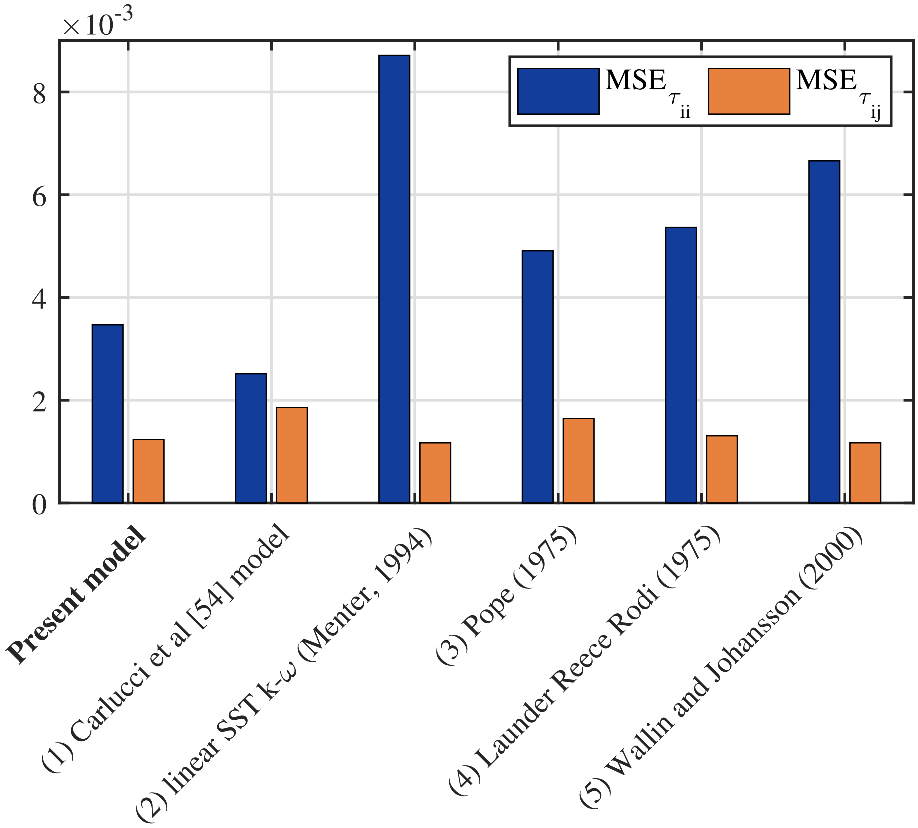

Figure 7.43: MSE of the diagonal (blue) and shear (red) Reynolds stress components for the CDA DNS dataset for different constitutive models.

reproduce the diagonal components of the Reynolds stress tensor. Improved predictions are obtained with nonlinear algebraic closures, including the models of Launder et al. (1975), Pope (1975), and Wallin and Johansson (2000). Both the present model and the formulation proposed in [54] yield reduced MSE on the normal stress components relative to the other models considered for comparison. Nevertheless, accurate prediction of the shear component remains particularly important, as it predominantly contributes to the production term in the RANS schemes. In this respect, the present model achieves accurate predictions of the τ_{12} component while relying on less than half of the predictors used in [54]. The diagonal components exhibit somewhat larger errors compared with the previous model calibrated in [54]. This behaviour is consistent with the reduced number of predictors, which tends to drive the model closer to the Boussinesq hypothesis and, given the definition of ν_t, makes the formulation resemble the SST k–ω model [94]. Despite this, the present model provides a balanced compromise, maintaining satisfactory predictive capability across all three Reynolds stress components while retaining a com-

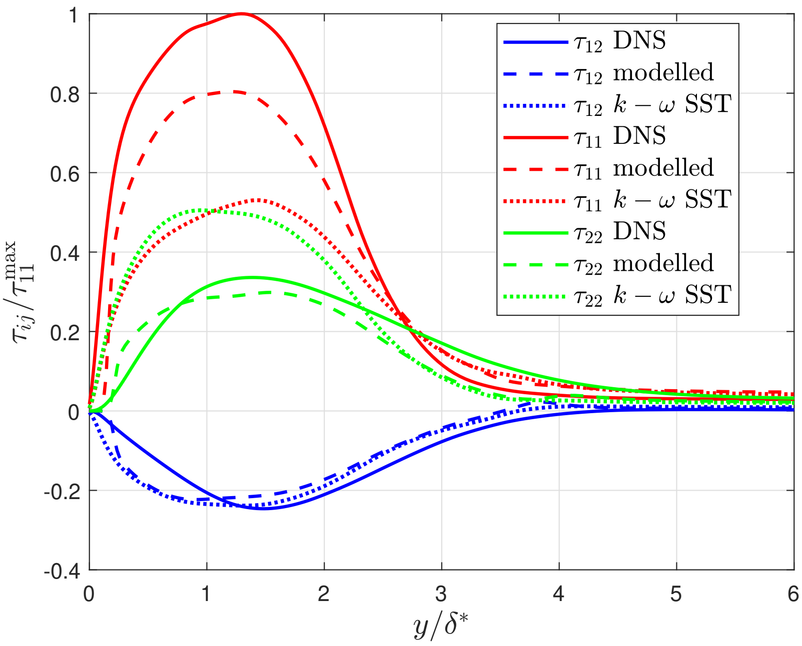

Figure 7.44: Normalized Reynolds stress profiles at a fixed streamwise location for the DNS-CDA case at $Re = 68k$.

pact formulation.

Additional insight into the predictive behaviour of the model is provided in Fig. 7.44, which shows the profiles of the three Reynolds stress components (normalized by their streamwise maximum value) evaluated at the streamwise location where each component reaches its absolute peak. The profiles are plotted as a function of the wall-normal coordinate normalized by the boundary-layer thickness δ^* for the CDA case at $Re = 68k$. The distributions display the characteristic anisotropic structure across the separated shear layer (see [75]), and compare the predictions of the present model with those obtained using the widely adopted k–ω SST model against the DNS reference. The comparison shows that the present model significantly improves the prediction of the diagonal stress components relative to the SST formulation, while maintaining good agreement with the DNS data also for the shear stress component. The successful test of the present model against the DNS-CDA cases suggests a satisfactory level of robustness. Nevertheless, these flow conditions remain relatively close to those used for calibration, as separation is primarily driven by an adverse pressure gradient.

Chapter 8

Conclusions

This thesis addressed the challenge of improving the predictive capabilities of RANS simulations for separated-transitional flows, with particular focus on laminar separation bubbles relevant to turbomachinery applications. By leveraging data-driven methodologies and high-quality experimental and numerical datasets, the work demonstrated how machine learning techniques can be effectively integrated into turbulence modelling frameworks while preserving physical consistency. The main object of this research is the development and calibration of data-driven Explicit Algebraic Reynolds Stress Models (EARSM) using Sparse Bayesian Learning (SBL) algorithm. The proposed approach enabled the identification of compact, sparse, and physically interpretable models able to accurately reproduce the magnitude and spatial distribution of the Reynolds stress tensor components across a wide range of flow conditions. The use of SBL has been proven to be particularly effective in balancing model complexity and generalization, providing insight into the dominant flow features governing stress anisotropy in separated flows.
The first study presented here focused on the calibration of a data-driven EARSM for the prediction of long laminar separation bubbles. The tuning was performed using a TR-PIV experimental dataset of separation bubbles developing over a flat plate with adverse pressure gradient. SBL algorithm was employed to identify the leading features from an extensive library of predictors defined by combinations of tensorial invariants and phisycal-based ingredients. The resulting formulation, composed by 37 predictors, demonstrated the ability of the model to accurately reproduce the spatial distribution and anisotropy properties of the Reynolds stress tensor components. Building upon this experience, the second study extended the EARSM calibration to short separation bubbles. Two models were trained on the experimental dataset to predict long and short separation bubbles, respectively. The calibration process was optimized with the target of obtaining sparser models, which led to the identification of only 13 predictors for the long-bubble model and 15 for the short-bubble one. A comparison with models defined solely through combinations of invariants demonstrated the effectiveness of including flow features in the predictor library. Finally, the predictive capabilities of the two models were compared

with those of models available in the literature showing good performance, particularly in the diagonal components of the Reynolds stress tensor. In the successive study, the limitations associated with regime-specific models were addressed through the introduction of a space-dependent Model Aggregation strategy. This approach combined the predictions of the long- and short-bubble EARSMs using spatially varying weights identified via SBL. The aggregated model successfully extended predictive capabilities to mid-range separation bubbles, demonstrating improved generalization across different flow conditions without accuracy penalties in the regimes for which the individual models were optimized. The fourth study further expanded the aggregation framework by combining compact models trained on heterogeneous datasets, including experimental flat-plate measurements and numerical LES data of separation bubbles induced by leading-edge geometry. This extension enabled the aggregated model to capture fundamentally different separation mechanisms driven by pressure gradients and geometric effects. Validation against DNS cases of compressor cascade flows that did not participated to the tuning showed improved accuracy, confirming the robustness of the approach and its potential for extrapolative applications relevant to turbomachinery. Finally, in the last study attention has been focused on the problem of correctly activating the turbulence models when needed. To this aim, an algebraic model for the intermittency function was tuned through the experimental separation-bubble dataset. When coupled with the trained EARSM, the intermittency formulation effectively suppresses non-turbulent low-frequency oscillations in the upstream part of the separated shear layer and ensured that Reynolds stresses are activated only in regions of fully developed turbulence. This coupling provides a more physically consistent representation of transition and mitigates the risk of premature turbulence generation when implemented in a RANS framework. This work also provides a useful 0-D tool for the definition of intermittency solely based on statistical properties of the flow, without the need for instantaneous flow field snapshots to be further elaborated and processed. Overall, this work demonstrates the strong potential of machine-learning-assisted turbulence modelling to bridge the gap between high-fidelity simulations and industrial RANS solvers. The developed models provide improved accuracy in the prediction of separated and transitional flows while remaining computationally affordable and physically interpretable. Future work will focus on the full implementation of the proposed models within a RANS solver, building upon preliminary tests conducted in OpenFOAM, and on further extending the framework to other flow configurations. It's author's hope that this work could represent a step toward next-generation data-informed tools for aerodynamic design and turbomachinery analysis.

Bibliography

[1] S. Cherroud, X. Merle, P. Cinnella, and X. Gloerfelt, “Space-dependent aggregation of data-driven turbulence models,” *arXiv preprint arXiv:2306.16996*, 2023. DOI: 10.48550/arXiv.2306.16996.

[2] M. A. Mendez, J. Dominique, M. Fiore, F Pino, P Sperotto, and J Berghe, “Challenges and opportunities for machine learning in fluid mechanics,” *arXiv preprint arXiv:2202.12577*, 2022.

[3] B. Graver, K. Zhang, and D. Rutherford, “Emissions from commercial aviation, 2018,” *International Council on Clean Transportation*, 2019.

[4] International Civil Aviation Organization, *Report of the 41st icao assembly*, 2022. [Online]. Available: https://www.icao.int/Meetings/a41/Pages/assembly-report-and-minutes.aspx.

[5] P. Spalart and S. Allmaras, “A one-equation turbulence model for aerodynamic flows,” *AIAA*, vol. 439, 1992. DOI: https://doi.org/10.2514/6.1992-439.

[6] B. Launder and D. Spalding, “The numerical computation of turbulent flow computer methods,” *Computer Methods in Applied Mechanics and Engineering*, vol. 3, pp. 269–289, Mar. 1974. DOI: 10.1016/0045-7825(74)90029-2.

[7] F. Menter, “Two-equation eddy-viscosity turbulence models for engineering applications,” *AIAA Journal*, vol. 32, no. 8, pp. 1598–1605, 1994. DOI: 10.2514/3.12149.

[8] D. Wilcox, *Turbulence Modeling for CFD*, 3rd. La Cañada, California: DCW Industries, 2006.

[9] F. G. Schmitt, “About boussinesq’s turbulent viscosity hypothesis: Historical remarks and a direct evaluation of its validity,” *Comptes Rendus Mécanique*, vol. 335, no. 9, pp. 617–627, 2007, ISSN: 1631-0721. DOI: 10.1016/j.crme.2007.08.004.

[10] S. Pope, “A more general effective-viscosity hypothesis,” *J. Turbomach. 72(2)*, 1975. DOI: 10.1017/S0022112075003382.

[11] W Rodi, "A new algebraic relation for calculating the reynolds stresses," *ZAMM - Journal of Applied Mathematics and Mechanics / Zeitschrift für Angewandte Mathematik und Mechanik*, vol. 56, no. S1, T219–T221, 1976. DOI: 10.1002/zamm.19765613093.

[12] T. H. Shih, J. Zhu, and J. L. Lumley, *A realizable Reynolds stress algebraic equation model*. Cleveland, Ohio: NASA Lewis Research Center, 1993, vol. 105993.

[13] F.-S. Lien, "Low-reynolds-number eddy-viscosity modelling based on non-linear stress-strain/vorticity relations," *Proc. 3rd Symposium On Engineering Turbulence Modelling and Measurements*, pp. 1–10, 1996. DOI: 10.1016/B978-0-444-82463-9.50015-0.

[14] M. M. Gibson and B. E. Launder, "Ground effects on pressure fluctuations in the atmospheric boundary layer," *Journal of Fluid Mechanics*, vol. 86, no. 3, 491–511, 1978. DOI: 10.1017/S0022112078001251.

[15] T. B. Gatski and C. G. Speziale, "On explicit algebraic stress models for complex turbulent flows," *Journal of Fluid Mechanics*, vol. 254, 59–78, 1993. DOI: 10.1017/S0022112093002034.

[16] T. Craft, B. Launder, and K. Suga, "Development and application of a cubic eddy-viscosity model of turbulence," *International Journal of Heat and Fluid Flow*, vol. 17, pp. 108–115, Apr. 1996. DOI: 10.1016/0142-727X(95)00079-6.

[17] S. Wallin and A. V. Johansson, "An explicit algebraic reynolds stress model for incompressible and compressible turbulent flows," *Journal of Fluid Mechanics*, vol. 403, 89–132, 2000. DOI: 10.1017/S0022112099007004.

[18] F. Menter, A. Garbaruk, and Y Egorov, "Explicit algebraic reynolds stress models for anisotropic wall-bounded flows," *Progress in Flight Physics*, vol. 3, pp. 89–104, 2012. DOI: 10.1051/eucass/201203089.

[19] R. Pacciani, M. Marconcini, F. Bertini, S. Rosa Taddei, E. Spano, Y. Zhao, H. D. Akolekar, R. D. Sandberg, and A. Arnone, "Assessment of machine-learned turbulence models trained for improved wake-mixing in low-pressure turbine flows," *Energies*, vol. 14, no. 24, p. 8327, 2021.

[20] M. Schmelzer, R. P. Dwight, and P. Cinnella, "Discovery of algebraic reynolds-stress models using sparse symbolic regression," *Flow, Turbulence and Combustion*, vol. 104, no. 2–3, 579–603, Dec. 2019, ISSN: 1573-1987. DOI: 10.1007/s10494-019-00089-x. [Online]. Available: http://dx.doi.org/10.1007/s10494-019-00089-x.

[21] S. Cherroud, X. Merle, P. Cinnella, and X. Gloerfelt, "Sparse bayesian learning of explicit algebraic reynolds-stress models for turbulent separated flows," *International Journal of Heat and Fluid Flow*, vol. 98, p. 109 047, 2022. DOI: 10.1016/j.ijheatfluidflow.2022.109047.

[22] H. D. Akolekar, J. Weatheritt, N. Hutchins, R. D. Sandberg, G. Laskowski, and V. Michelassi, "Development and use of machine-learnt algebraic reynolds stress models for enhanced prediction of wake mixing in low-pressure turbines," *Journal of Turbomachinery*, vol. 141 (4), 2019. DOI: 10.1115/1.4041753.

[23] H. Akolekar, F. Waschkowski, Y. Zhao, R. Pacciani, and R. Sandberg, "Transition modeling for low pressure turbines using computational fluid dynamics driven machine learning," *Energies*, vol. 14, p. 4680, 2021. DOI: 10.3390/en14154680.

[24] Y. Fang, Y. Zhao, H. D. Akolekar, A. Ooi, R. D. Sandberg, and R. Pacciani, "A data-driven approach for generalizing the laminar kinetic energy model for separation and bypass transition in low-and high-pressure turbines," *Journal of Turbomachinery*, vol. 146, pp. 091 005–1, 2024. DOI: 10.1115/GT2023-102902.

[25] Y. Marioni, E. A. de Toledo Ortiz, A. Cassinelli, F. Montomoli, P. Adami, and R. Vazquez, "A machine learning approach to improve turbulence modelling from dns data using neural networks," *International Journal of Turbomachinery, Propulsion and Power*, vol. 6, no. 2, p. 17, 2021. DOI: 10.3390/ijtpp6020017.

[26] J.-X. Wang, J.-L. Wu, and H. Xiao, "Physics-informed machine learning approach for reconstructing reynolds stress modeling discrepancies based on dns data," *Physical Review Fluids*, vol. 2, no. 3, p. 034 603, 2017.

[27] S. Yazdani and M. Tahani, "Data-driven discovery of turbulent flow equations using physics-informed neural networks," *Physics of Fluids*, vol. 36, no. 3, 2024.

[28] F. Pioch, J. H. Harmening, A. M. Müller, F.-J. Peitzmann, D. Schramm, and O. e. Moctar, "Turbulence modeling for physics-informed neural networks: Comparison of different rans models for the backward-facing step flow," *Fluids*, vol. 8, no. 2, p. 43, 2023.

[29] Y. Patel, V. Mons, O. Marquet, and G. Rigas, "Turbulence model augmented physics-informed neural networks for mean-flow reconstruction," *Physical Review Fluids*, vol. 9, no. 3, p. 034 605, 2024.

[30] R. Sandberg, R. Tan, J. Weatheritt, A. Ooi, A. Haghiri, V. Michelassi, and G. Laskowski, "Applying machine learnt explicit algebraic stress and scalar flux models to a fundamental trailing edge slot," *Journal of Turbomachinery*, vol. 140 (10), 2018. DOI: 10.1115/1.4041268.

[31] L. Davidson, "Using neural network for improving an explicit algebraic stress model in 2d flow," *CUSF, Murray Edwards College, Cambridge, UK*, 2024.

[32] R. Pacciani, M. Marconcini, A. Arnone, F. Bertini, E. Spano, S. Rosa Taddei, and R. D. Sandberg, "Improvements in the prediction of steady and unsteady transition and mixing in low-pressure turbines by means of machine-learnt closures," *Journal of Turbomachinery*, vol. 146, no. 5, 2024. DOI: https://doi.org/10.1115/1.4064312.

[33] S. E. Yuksel, J. N. Wilson, and P. D. Gader, "Twenty years of mixture of experts," *IEEE transactions on neural networks and learning systems*, vol. 23, no. 8, pp. 1177–1193, 2012.

[34] G. Stoltz, "Agrégation séquentielle de prédicteurs: Méthodologie générale et applications à la prévision de la qualité de l'air et à celle de la consommation électrique," *Journal de la Société française de Statistique*, vol. 151, no. 2, pp. 66–106, 2010.

[35] R. Deswarte, V. Gervais, G. Stoltz, and S. Da Veiga, "Sequential model aggregation for production forecasting," *Computational Geosciences*, vol. 23, no. 5, pp. 1107–1124, 2019.

[36] M. Devaine, P. Gaillard, Y. Goude, and G. Stoltz, "Forecasting electricity consumption by aggregating specialized experts: A review of the sequential aggregation of specialized experts, with an application to slovakian and french country-wide one-day-ahead (half-) hourly predictions," *Machine Learning*, vol. 90, no. 2, pp. 231–260, 2013.

[37] W. Edeling, P. Cinnella, and R. P. Dwight, "Predictive rans simulations via bayesian model-scenario averaging," *Journal of Computational Physics*, vol. 275, pp. 65–91, 2014.

[38] M. De Zordo-Banliat, G. Dergham, X. Merle, and P. Cinnella, "Space-dependent turbulence model aggregation using machine learning," *Journal of Computational Physics*, vol. 497, p. 112 628, 2024, ISSN: 0021-9991. DOI: 10.1016/j.jcp.2023.112628.

[39] R. Langtry and F. Menter, "Correlation-based transition modeling for unstructured parallelized computational fluid dynamics codes," *AIAA Journal*, vol. 47, pp. 2894–2906, Dec. 2009. DOI: 10.2514/1.42362.

[40] F. R. Menter, A. Matyushenko, R. Lechner, A. Stabnikov, and A. Garbaruk, "An algebraic lctm model for laminar–turbulent transition prediction," *Flow, Turbulence and Combustion*, vol. 109, no. 4, pp. 841–869, 2022.

[41] S. Kubacki and E. Dick, "An algebraic intermittency model for bypass, separation-induced and wake-induced transition," *International Journal of Heat and Fluid Flow*, vol. 62, pp. 344–361, 2016. DOI: https://doi.org/10.1016/j.ijheatfluidflow.2016.09.013.

[42] S. Kubacki, D. Simoni, D. Lengani, and E. Dick, "An extended version of an algebraic intermittency model for prediction of separation-induced transition at elevated free-stream turbulence level," *International Journal of Turbomachinery, Propulsion and Power*, vol. 5, no. 4, p. 28, 2020.

[43] M. M. Rahman, "Predicting transition with algebraic intermittency function," *Physics of Fluids*, vol. 34, no. 3, p. 034 113, Mar. 2022. DOI: 10.1063/5.0077513.

[44] S. Vallinayagam Pillai and S. Lardeau, “Extending one-equation local correlation-based transition model for spalart-allmaras turbulence model,” *AIAA AVIATION 2023 Forum*, p. 3556, 2023. DOI: `10.2514/6.2023-3556`.

[45] D. Petronio, M. Dellacasagrande, D. Simoni, and D. Lengani, “A new empirical correlation for transition in both short and long separation bubbles,” ser. Turbo Expo: Power for Land, Sea, and Air, vol. 13C, 2023. DOI: `https://doi.org/10.1115/GT2023-103021`.

[46] D. Petronio, P. Paliotta, M. Dellacasagrande, D. Lengani, and D. Simoni, “Local correlations for predicting the transition process in separated flows tuned with a large experimental database,” *International Journal of Heat and Fluid Flow*, vol. 107, p. 109 392, 2024, ISSN: 0142-727X. DOI: `https://doi.org/10.1016/j.ijheatfluidflow.2024.109392`.

[47] ERCOFTAC, *Machine learning for fluid dynamics: Workshop test cases*, 2023. [Online]. Available: `https://www.ercoftac.org/events/machine-learning-for-fluid-dynamics/workshop-test-cases/`.

[48] F. Bonnet, J. A. Mazari, P. Cinnella, and patrick gallinari, “AirfRANS: High fidelity computational fluid dynamics dataset for approximating reynolds-averaged navier–stokes solutions,” in *Thirty-sixth Conference on Neural Information Processing Systems Datasets and Benchmarks Track*, 2022. [Online]. Available: `https://openreview.net/forum?id=Zp8YmiQ_bDC`.

[49] A. Towne, S. T. Dawson, G. A. Brès, A. Lozano-Durán, T. Saxton-Fox, A. Parthasarathy, A. R. Jones, H. Biler, C.-A. Yeh, H. D. Patel, *et al.*, “A database for reduced-complexity modeling of fluid flows,” *AIAA journal*, vol. 61, no. 7, pp. 2867–2892, 2023.

[50] J. Bridges and M. Wernet, “Establishing consensus turbulence statistics for hot subsonic jets,” in *16th AIAA/CEAS aeroacoustics conference*, 2010, p. 3751.

[51] J. Bridges and M. P. Wernet, “The nasa subsonic jet particle image velocimetry (piv) dataset,” NASA Glenn Research Center, Cleveland, Ohio, Tech. Rep., 2011.

[52] J. Naughton, S. Viken, and D. Greenblatt, “Wall shear stress measurements on the nasa hump model for cfd validation,” *24th AIAA Aerodynamic Measurement Technology and Ground Testing Conference*, p. 2607, 2004. DOI: `10.2514/6.2004-2607`.

[53] C. Laurent, I. Mary, V. Gleize, A. Lerat, and D. Arnal, “Dns database of a transitional separation bubble on a flat plate and application to rans modeling validation,” *Computers & Fluids*, vol. 61, pp. 21–30, 2012, ”High Fidelity Flow Simulations” Onera Scientific Day, ISSN: 0045-7930. DOI: `https://doi.org/10.1016/j.compfluid.2011.07.011`.

[54] A. Carlucci, D. Petronio, M. Dellacasagrande, D. Simoni, and F. Satta, "Data-driven algebraic models tuned with a vast experimental database of separated flows," *Flow, Turbulence and Combustion*, pp. 1–28, 2024.

[55] R. E. Mayle, "The Role of Laminar-Turbulent Transition in Gas Turbine Engines," *Turbo Expo: Power for Land, Sea, and Air*, vol. Volume 5, V005T17A001, Jun. 1991. DOI: 10.1115/91-GT-261.

[56] O. Marxen and D. S. Henningson, "The effect of small-amplitude convective disturbances on the size and bursting of a laminar separation bubble," *Journal of Fluid Mechanics*, vol. 671, pp. 1–33, 2011. DOI: https://doi.org/10.1017/S0022112010004957.

[57] A. E. Von Doenhoff, "A preliminary investigation of boundary-layer transition along a flat plate with adverse pressure gradient," Tech. Rep., 1938.

[58] P. Owen and L Klanfer, "On the laminar boundary layer separation from the leading edge of a thin aerofoil," 1955.

[59] L. Crabtree, *The formation of regions of separated flow on wing surfaces*. University Park, PA, USA: Citeseer, 1957.

[60] M. Gaster, *The structure and behaviour of laminar separation bubbles*. University Park, PA, USA: Citeseer, 1967.

[61] M. Dellacasagrande, D. Lengani, D. Simoni, and S. Yarusevych, "A data-driven analysis of short and long laminar separation bubbles," *Journal of Fluid Mechanics*, vol. 976, R3, 2023. DOI: 10.1017/jfm.2023.960.

[62] R. Howard, M. Alam, and N. Sandham, "Two-equation turbulence modelling of a transitional separation bubble," *Flow Turbul. Combust.*, vol. 63(1-4), pp. 175–191, 2000. DOI: 10.1023/A:1009992406036.

[63] I. Hadžić and K. Hanjalić, "Separation-induced transition to turbulence: Second-moment closure modelling," *Flow Turbul. Combust.*, vol. 63(1-4), p. 153, 2000. DOI: 10.1023/A:1009980119240.

[64] M. Dellacasagrande, D. Lengani, D. Simoni, and M. Ubaldi, "An experimental database for the analysis of bursting of a laminar separation bubble," *International Journal of Turbomachinery, Propulsion and Power*, vol. 9, no. 1, 2024. DOI: 10.3390/ijtpp9010003.

[65] M. Leschziner, *Statistical turbulence modelling for fluid dynamics-demystified: an introductory text for graduate engineering students*. World Scientific, 2015.

[66] A. Kolmogorov, *The local structure of turbulence in incompressible viscous fluids for very large reynolds numbers. c. r. acad. sci ussr, 30, 301-305*, 1941.

[67] H. Schlichting and K. Gersten, *Boundary-layer theory*. springer, 2016.

[68] J. JD, *Anderson, fundamentals of aerodynamics, forth edittion*, 2010.

[69] B. Abu-Ghannam and R Shaw, "Natural transition of boundary layers—the effects of turbulence, pressure gradient, and flow history," *Journal of Mechanical Engineering Science*, vol. 22, no. 5, pp. 213–228, 1980.

[70] E. Dick and S. Kubacki, "Transition models for turbomachinery boundary layer flows: A review," *International Journal of Turbomachinery, Propulsion and Power*, vol. 2, no. 2, p. 4, 2017.

[71] P. Andersson, M. Berggren, and D. S. Henningson, "Optimal disturbances and bypass transition in boundary layers," *Physics of Fluids*, vol. 11, no. 1, pp. 134–150, 1999.

[72] P. Luchini, "Reynolds-number-independent instability of the boundary layer over a flat surface: Optimal perturbations," *Journal of Fluid Mechanics*, vol. 404, pp. 289–309, 2000.

[73] I Currie, *6. 1974. fundamental mechanics of fluids*.

[74] S Sarkar, "Identification of flow structures on a lp turbine blade due to periodic passing wakes," *Journal of fluids engineering*, vol. 130, no. 6, p. 061 103, 2008.

[75] S. Lardeau, M. Leschziner, and T. Zaki, "Large eddy simulation of transitional separated flow over a flat plate and a compressor blade," *Flow, turbulence and combustion*, vol. 88, no. 1, pp. 19–44, 2012.

[76] D. Simoni, M. Ubaldi, P. Zunino, D. Lengani, and F. Bertini, "An experimental investigation of the separated-flow transition under high-lift turbine blade pressure gradients," *Flow, turbulence and combustion*, vol. 88, no. 1, pp. 45–62, 2012.

[77] M. Alam and N. D. Sandham, "Direct numerical simulation of 'short' laminar separation bubbles with turbulent reattachment," *Journal of Fluid Mechanics*, vol. 410, pp. 1–28, 2000.

[78] D Simoni, M Ubaldi, and P Zunino, "Experimental investigation of flow instabilities in a laminar separation bubble," *Journal of Thermal Science*, vol. 23, no. 3, pp. 203–214, 2014.

[79] S. Burgmann and W Schröder, "Investigation of the vortex induced unsteadiness of a separation bubble via time-resolved and scanning piv measurements," *Experiments in fluids*, vol. 45, no. 4, pp. 675–691, 2008.

[80] S. Hosseinverdi and H. F. Fasel, "Numerical investigation of laminar–turbulent transition in laminar separation bubbles: The effect of free-stream turbulence," *Journal of Fluid Mechanics*, vol. 858, pp. 714–759, 2019. DOI: https://doi.org/10.1017/jfm.2018.809.

[81] L. L. Pauley, P. Moin, and W. C. Reynolds, "The structure of two-dimensional separation," *Journal of fluid Mechanics*, vol. 220, pp. 397–411, 1990.

[82] M. Langari and Z. Yang, "Numerical study of the primary instability in a separated boundary layer transition under elevated free-stream turbulence," *Physics of Fluids*, vol. 25, no. 7, 2013.

[83] J Coupland and D Brierley, "Transition in turbomachinery flows," *Final Report, BRITE/EURAM Project AERO-CT92-0050*, 1996.

[84] Y. Cengel and J. Cimbala, *Ebook: Fluid mechanics fundamentals and applications (si units)*. McGraw Hill, 2013.

[85] M. Russo, A. Carlucci, M. Dellacasagrande, D. Petronio, D. Lengani, D. Simoni, J. Bellucci, M. Giovannini, A. A. Granata, M. Gily, *et al.*, "Optimization of low-pressure turbine blade by means of fine inspection of loss production mechanisms," *Journal of Turbomachinery*, vol. 147, no. 4, p. 041 005, 2025.

[86] D. C. Wilcox, "Reassessment of the scale-determining equation for advanced turbulence models," *AIAA journal*, vol. 26, no. 11, pp. 1299–1310, 1988.

[87] S. Pope, *Turbulent flows*. Cambridge, UK: Cambridge university press, 2000.

[88] W. Balzer and H. F. Fasel, "Numerical investigation of the role of free-stream turbulence in boundary-layer separation," *Journal of Fluid Mechanics*, vol. 801, pp. 289–321, 2016.

[89] M. Hack and T. Zaki, "Streak instabilities in boundary layers beneath free-stream turbulence," *Journal of fluid mechanics*, vol. 741, pp. 280–315, 2014.

[90] J. Verdoya, M. Dellacasagrande, D. Lengani, D. Simoni, and M. Ubaldi, "Inspection of structures interaction in laminar separation bubbles with extended proper orthogonal decomposition applied to multi-plane particle image velocimetry data," *Physics of Fluids*, vol. 33, p. 043 607, Apr. 2021. DOI: 10.1063/5.0047347.

[91] A. Miró Jané, S. Wallin, A. Colombo, L. Temmerman, D. Wunsch, and O. Lehmkuhl Barba, "Towards a machine learning model for explicit algebraic reynolds stress modelling using multi-expression programming," in *14th International ERCOFTAC Symposium on Engineering, Turbulence, Modelling and Measurements*, 2023.

[92] F. Menter, P. Smirnov, T. Liu, and R. Avancha, "A one-equation local correlation-based transition model," *Flow, Turbulence and Combustion*, vol. 95, pp. 1–37, Jul. 2015. DOI: 10.1007/s10494-015-9622-4.

[93] A. Carlucci, D. Petronio, D. Barsi, M. Dellacasagrande, and D. Simoni, "Tuning of an algebraic model for separated flows by means of bayesian lasso," in *Turbo Expo: Power for Land, Sea, and Air*, American Society of Mechanical Engineers, vol. 88070, 2024, V12CT32A046.

[94] F. R. Menter, R. Langtry, S. Likki, Y. Suzen, P. Huang, and S. Volker, "A correlation-based transition model using local variables: Part i—model formulation," *Turbo expo: power for land, sea, and air*, vol. 41693, pp. 57–67, 2004. DOI: 10.1115/1.2184352.

[95] R. B. Langtry and F. R. Menter, "Correlation-based transition modeling for unstructured parallelized computational fluid dynamics codes," *AIAA journal*, vol. 47, no. 12, pp. 2894–2906, 2009.

[96] F. R. Menter, P. E. Smirnov, T. Liu, and R. Avancha, "A one-equation local correlation-based transition model," *Flow, Turbulence and Combustion*, vol. 95, no. 4, pp. 583–619, 2015.

[97] D. K. Walters and D. Cokljat, "A three-equation eddy-viscosity model for reynolds-averaged navier–stokes simulations of transitional flow," 2008.

[98] R. Pacciani, M. Marconcini, A. Arnone, and F. Bertini, "A cfd study of low reynolds number flow in high lift cascades," in *Turbo Expo: Power for Land, Sea, and Air*, vol. 44021, 2010, pp. 1525–1534.

[99] Y. Liu, P. Li, and K. Jiang, "Comparative assessment of transitional turbulence models for airfoil aerodynamics in the low reynolds number range," *Journal of Wind Engineering and Industrial Aerodynamics*, vol. 217, p. 104 726, 2021.

[100] X. Hao, X. He, Z. Zhang, and J. Li, "A review of simulations and machine learning approaches for flow separation analysis.," *Aerospace (MDPI Publishing)*, vol. 12, no. 3, 2025.

[101] L. Jiang, G. Tabor, and G. Gao, "A new turbulence model for separated flows," *International Journal of Computational Fluid Dynamics*, vol. 25, no. 8, pp. 427–438, 2011.

[102] A. P. Singh, S. Medida, and K. Duraisamy, "Machine-learning-augmented predictive modeling of turbulent separated flows over airfoils," *AIAA journal*, vol. 55, no. 7, pp. 2215–2227, 2017.

[103] C. Yan, H. Li, Y. Zhang, and H. Chen, "Data-driven turbulence modeling in separated flows considering physical mechanism analysis," *International Journal of Heat and Fluid Flow*, vol. 96, p. 109 004, 2022.

[104] X. Shan, Y. Liu, W. Cao, X. Sun, and W. Zhang, "Turbulence modeling via data assimilation and machine learning for separated flows over airfoils," *AIAA Journal*, vol. 61, no. 9, pp. 3883–3899, 2023.

[105] A. Ferrero, A. Iollo, and F. Larocca, "Field inversion for data-augmented rans modelling in turbomachinery flows," *Computers & Fluids*, vol. 201, p. 104 474, 2020.

[106] P. S. Volpiani, M. Meyer, L. Franceschini, J. Dandois, F. Renac, E. Martin, O. Marquet, and D. Sipp, "Machine learning-augmented turbulence modeling for rans simulations of massively separated flows," *Physical Review Fluids*, vol. 6, no. 6, p. 064 607, 2021.

[107] J. Ho, N. Pepper, and T. Dodwell, "Probabilistic machine learning to improve generalisation of data-driven turbulence modelling," *Computers & Fluids*, vol. 284, p. 106 443, 2024.

[108] S. Choi, J. Lee, Y. Kim, and S. Lee, "Machine learning-based prediction of turbulent flows over backward-facing steps with varying step angles using large eddy simulation data," *Physics of Fluids*, vol. 37, no. 6, 2025.

[109] J. Wu, J. Li, X. Qiu, and Y. Liu, "A comparative analysis of multi-machine learning algorithms for data-driven rans turbulence modelling," in *Journal of Physics: Conference Series*, IOP Publishing, vol. 1684, 2020, p. 012 043.

[110] J. Weatheritt and R. Sandberg, "A novel evolutionary algorithm applied to algebraic modifications of the rans stress–strain relationship," *Journal of Computational Physics*, vol. 325, pp. 22–37, 2016.

[111] Y. Fang, M. Reissmann, R. Pacciani, Y. Zhao, A. Ooi, M. Marconcini, H. D Akolekar, and R. D. Sandberg, "Accelerating cfd-driven training of transition and turbulence models for turbine flows by one-shot and real-time transformer integration," *Computers & Fluids*, p. 106 927, 2025.

[112] M. Schmelzer, R. P. Dwight, and P. Cinnella, "Discovery of algebraic reynolds-stress models using sparse symbolic regression," *Flow, Turbulence and Combustion*, vol. 104, no. 2, pp. 579–603, 2020.

[113] Y. Frey Marioni, E. A. de Toledo Ortiz, A. Cassinelli, F. Montomoli, P. Adami, and R. Vazquez, "A machine learning approach to improve turbulence modelling from dns data using neural networks," *International Journal of Turbomachinery, Propulsion and Power*, vol. 6, no. 2, p. 17, 2021.

[114] Y. Frey Marioni, P. Adami, R. Vazquez Diaz, A. Cassinelli, S. J. Sherwin, and F. Montomoli, "Development of machine-learnt turbulence closures for wake mixing predictions in low-pressure turbines," *Journal of Turbomachinery*, pp. 1–14, 2024.

[115] D. Dabiri, "Cross-correlation digital particle image velocimetry–a," *University of Washington, Department of Aeronautics and Astronautics, Seattle, WA*, vol. 98195,

[116] P. Roach, "The generation of nearly isotropic turbulence by means of grids," *International journal of heat and fluid flow*, vol. 8, no. 2, pp. 82–92, 1987. DOI: 10.1016/0142-727X(87)90001-4.

[117] M. S. Istvan and S. Yarusevych, "Effects of free-stream turbulence intensity on transition in a laminar separation bubble formed over an airfoil," *Experiments in Fluids*, vol. 59, no. 3, p. 52, 2018. DOI: `https://doi.org/10.1007/s00348-018-2511-6`.

[118] T. Jaroslawski, M. Forte, O. Vermeersch, J.-M. Moschetta, and E. Gowree, "Influence of roughness-generated streaks on laminar separation bubbles," *Experiments in Fluids*, vol. 65, no. 7, pp. 1–16, 2024. DOI: `https://doi.org/10.1007/s00348-024-03837-6`.

[119] T. M. Kirk and S. Yarusevych, "Vortex shedding within laminar separation bubbles forming over an airfoil," *Experiments in Fluids*, vol. 58, pp. 1–17, 2017. DOI: `10.1007/s00348-017-2308-z`.

[120] M. Dellacasagrande, D. Barsi, D. Lengani, and D. Simoni, "Instability processes in short and long laminar separation bubbles," *Experiments in Fluids*, vol. 65, no. 7, pp. 1–12, 2024. DOI: `https://doi.org/10.1007/s00348-024-03847-4`.

[121] F. Bassi, A. Colombo, A Crivellini, M Franciolini, A Ghidoni, G Manzinali, and G. Noventa, "Under-resolved simulation of turbulent flows using ap-adaptive discontinuous galerkin method," in *iTi Conference on Turbulence*, Springer, 2018, pp. 157–162.

[122] M. Franciolini, L. Botti, A. Colombo, and A. Crivellini, "P-multigrid matrix-free discontinuous galerkin solution strategies for the under-resolved simulation of incompressible turbulent flows," *Computers & Fluids*, vol. 206, p. 104 558, 2020.

[123] P. J. Przytarski and A. P. Wheeler, "Accurate prediction of loss using high fidelity methods," *Journal of Turbomachinery*, vol. 143, no. 3, p. 031 008, 2021.

[124] R. D. Sandberg, V. Michelassi, R. Pichler, L. Chen, and R. Johnstone, "Compressible direct numerical simulation of low-pressure turbines—part i: Methodology," *Journal of Turbomachinery*, vol. 137, no. 5, p. 051 011, 2015.

[125] M. Deuse and R. D. Sandberg, "Implementation of a stable high-order overset grid method for high-fidelity simulations," *Computers & Fluids*, vol. 211, p. 104 449, 2020.

[126] P. J. Przytarski, D. Lengani, and R. Sandberg, "The impact of inflow unsteadiness on loss prediction," *Journal of Turbomachinery*, vol. 147, no. 4, p. 041 014, 2025.

[127] P. J. Przytarski, D. Lengani, D. Simoni, and A. P. Wheeler, "The role of turbulence transport in mechanical energy budgets," *Journal of Turbomachinery*, vol. 146, no. 10, p. 101 008, 2024.

[128] R Manimaran, P. T. Krishnan, C. C. Columbus, and T. S. Kumar, "Accurate and efficient fluid flow regime classification using localized texture descriptors and machine learning," *IEEE Access*, 2025.

[129] M. Berrino, F. Satta, D. Simoni, M. Ubaldi, P. Zunino, and F. Bertini, "Aerodynamic loading distribution effects on the overall performance of ultra-high-lift lp turbine cascades," *Journal of Thermal Science*, vol. 23, no. 1, pp. 1–12, 2014.

[130] P. J. Holmes, J. L. Lumley, G. Berkooz, J. C. Mattingly, and R. W. Wittenberg, "Low-dimensional models of coherent structures in turbulence," *Physics Reports*, vol. 287, no. 4, pp. 337–384, 1997.

[131] E. Kaiser, B. R. Noack, L. Cordier, A. Spohn, M. Segond, M. Abel, G. Daviller, J. Östh, S. Krajnović, and R. K. Niven, "Cluster-based reduced-order modelling of a mixing layer," *Journal of Fluid Mechanics*, vol. 754, pp. 365–414, 2014.

[132] T. Hastie, R. Tibshirani, and M. Wainwright, "Statistical learning with sparsity," *Monographs on statistics and applied probability*, vol. 143, no. 143, p. 8, 2015.

[133] A. E Hoerl and R. Kennard, "Ridge regression: Biased estimation for nonorthogonal problems," *Technometrics*, vol. 12, no. 1, pp. 55–67, 1970.

[134] M. E. Tipping, "Sparse bayesian learning and the relevance vector machine," *Journal of machine learning research*, vol. 1, no. Jun, pp. 211–244, 2001.

[135] D. MacKay, "A practical bayesian framework for backpropagation networks," *Neural computation*, vol. 4, no. 3, pp. 448–472, 1992. DOI: 10.1162/neco.1992.4.3.448.

[136] J. O. Berger, "Bayesian analysis," in *Statistical Decision Theory and Bayesian Analysis*. New York, NY: Springer New York, 1985, pp. 118–307, ISBN: 978-1-4757-4286-2. DOI: 10.1007/978-1-4757-4286-2_4.

[137] S. Balakrishnan and D. Madigan, "Priors on the variance in sparse bayesian learning: The demi-bayesian lasso," *Frontiers of statistical decision making and Bayesian analysis: in honor of James O. Berger*, pp. 346–359, 2010. DOI: 10.7916/D88P65TH.

[138] R. Tibshirani, "Regression shrinkage and selection via the lasso," *Journal of the Royal Statistical Society. Series B (Methodological)*, vol. 58, no. 1, pp. 267–288, 1996, ISSN: 00359246. DOI: https://doi.org/10.1111/j.2517-6161.1996.tb02080.x. (visited on 12/18/2023).

[139] D. Lengani, D. Simoni, S. Kubacki, and E. Dick, "Analysis and modelling of the relation between the shear rate and reynolds stress tensors in transitional boundary layers," *International Journal of Heat and Fluid Flow*, vol. 84, p. 108 615, 2020.

[140] A. Carlucci, D. Petronio, M. Dellacasagrande, D. Simoni, and F. Satta, "An aggregated turbulence model for the prediction of short and long separation bubbles," in *Proceedings of the European Turbomachinery Conference*, 2025.

[141] F. R. Menter, M. Kuntz, R. Langtry, *et al.*, "Ten years of industrial experience with the sst turbulence model," *Turbulence, heat and mass transfer*, vol. 4, no. 1, pp. 625–632, 2003.

[142] C. Williams and C. Rasmussen, "Gaussian processes for regression," *Advances in neural information processing systems*, vol. 8, 1995.

[143] M. Dellacasagrande, J. Verdoya, D. Barsi, D. Lengani, D. Simoni, and F. Bertini, "Effects of streamwise oriented riblets on spot nucleation in free-stream turbulence induced transition," *Experimental Thermal and Fluid Science*, vol. 139, p. 110 738, 2022.

[144] M. Dellacasagrande, D. Lengani, D. Simoni, J. Pralits, K. Durović, A. Hanifi, and D. Henningson, "A procedure for computing the spot production rate in transitional boundary layers," *Experiments in Fluids*, vol. 63, no. 8, p. 136, 2022.

[145] B. E. Launder, G. J. Reece, and W Rodi, "Progress in the development of a reynolds-stress turbulence closure," *Journal of fluid mechanics*, vol. 68, no. 3, pp. 537–566, 1975.